

# Critical and sustainable fluxes of mixed and flocculated feeds during membrane filtration

Zhang, Yanpeng

2009

Zhang, Y. (2009). Critical and sustainable fluxes of mixed and flocculated feeds during membrane filtration. Doctoral thesis, Nanyang Technological University, Singapore.

<https://hdl.handle.net/10356/15153>

<https://doi.org/10.32657/10356/15153>



**NANYANG  
TECHNOLOGICAL  
UNIVERSITY**

**CRITICAL AND SUSTAINABLE FLUXES OF MIXED  
AND FLOCCULATED FEEDS DURING MEMBRANE  
FILTRATION**

**ZHANG YANPENG**

**SCHOOL OF CIVIL AND ENVIRONMENTAL ENGINEERING**

**2009**

# **Critical and Sustainable Fluxes of Mixed and Flocculated Feeds during Membrane Filtration**

**Zhang Yanpeng**

School of Civil and Environmental Engineering

A thesis submitted to the Nanyang Technological University  
in fulfillment of the requirement for the degree of  
Doctor of Philosophy

**2009**

## **Acknowledgement**

First of all, I would like to thank my supervisor, Professor Anthony Gordon Fane, for bringing me into the field of membrane science. He is not only my mentor who provides me with invaluable guidance throughout this project, but also a model for me to learn from his work ethics and his attitudes towards life. I am very grateful for his patience and trust in me. It is a great honour for me to have such a wonderful opportunity to work with him.

Secondly, I'd like to express my gratitude towards Associate Professor Adrian Law, as my co-supervisor, who has continuously offered me his generous help and constructive suggestions.

Dr. Wong Fook Sin, Dr. Chua Hwee Chuan and Dr. Li Hongyu are colleagues who I once worked with. I want to thank them for their professional assistance and support they contributed during my research process.

My life in NTU would not have been so fun had I not met the TP program members who have accompanied me all the way along through the challenges.

Also, I should say thank you to my family, especially my wife Yang, for her understanding and love.

GrahamTec Singapore is acknowledged for providing the EMF devices.

Finally, financial support from A\*Star Singapore for this program is greatly acknowledged.

## Table of contents

|  |      |
|--|------|
| Acknowledgement.....                                     | i    |
| Table of contents.....                                   | ii   |
| Summary.....   | vi   |
| List of tables.....                                      | vii  |
| List of figures.....                                     | viii |
| List of symbols.....                                     | xiii |
| List of abbreviations.....                               | xvi  |
| Chapter 1. Introduction.....                             | 1    |
| 1.1 Background.....                                      | 1    |
| 1.2 Objectives and scope of this research.....           | 2    |
| 1.3 Organization of this thesis.....                     | 3    |
| Chapter 2. Literature review.....                        | 5    |
| 2.1 Introduction.....                                    | 5    |
| 2.2 Basic concept.....                                   | 5    |
| 2.2.1 Microfiltration (MF).....                          | 5    |
| 2.2.2 Crossflow microfiltration (CFMF).....              | 7    |
| 2.2.3 Concept of critical flux.....                      | 10   |
| 2.2.4 Strategies to alleviate flux decline.....          | 13   |
| 2.3 Theories of microfiltration.....                     | 14   |
| 2.3.1 Darcy's law.....                                   | 14   |
| 2.3.2 Membrane resistance.....                           | 16   |
| 2.3.3 Cake resistance.....                               | 17   |
| 2.3.4 Concentration polarization model (Film model)..... | 18   |
| 2.3.5 Shear-induced diffusivity model (SID).....         | 20   |
| 2.3.6 Inertial lift model.....                           | 21   |
| 2.4 Factors influencing the permeate flux.....           | 23   |
| 2.4.1 Influence of crossflow velocity (CFV).....         | 24   |
| 2.4.2 Influence of filtration pressure.....              | 26   |
| 2.4.3 Influence of feed concentration.....               | 27   |
| 2.4.4 Influence of temperature.....                      | 28   |

|  |    |
|--|----|
| 2.4.5 Influence of membrane pore size.....   | 29 |
| 2.4.6 Influence of surface charge.....   | 30 |
| 2.4.7 Influence of particle size and particle size distribution.....                 | 31 |
| 2.4.8 Influence of particle shape.....   | 34 |
| 2.5 Flocculation of particles.....   | 35 |
| 2.5.1 Introduction to flocculation.....  | 36 |
| 2.5.2 Mechanisms of flocculation.....  | 37 |
| 2.5.3 Fractal concept.....   | 38 |
| 2.5.4 Properties of floc .....   | 40 |
| 2.6 Topics of interest for further study.....  | 41 |
| Chapter 3. Materials and methodology.....  | 42 |
| 3.1 Experimental approaches.....   | 42 |
| 3.2 Experimental materials.....  | 45 |
| 3.2.1 Polystyrene latex particles .....  | 45 |
| 3.2.2 Washed baker's yeast.....  | 46 |
| 3.2.3 Membrane for filtration experiments.....                                       | 46 |
| 3.3 Analysis and measurement.....  | 49 |
| 3.3.1 Particle size distribution and fractal dimension.....                          | 49 |
| 3.3.2 pH measurement.....  | 51 |
| 3.3.3 Particle surface charge.....   | 51 |
| 3.3.4 Membrane surface charge.....   | 53 |
| 3.3.5 Image analysis.....  | 55 |
| 3.4 Hematite particle preparation and flocculation experiments.....                  | 57 |
| 3.4.1 Preparation of hematite particles.....   | 57 |
| 3.4.2 Flocculation for hematite flocs.....   | 59 |
| 3.5 Filtration experiments.....  | 61 |
| 3.5.1 Experimental setup.....  | 61 |
| 3.5.2 Experimental protocol.....   | 61 |
| 3.6 Electromagnetic field (EMF).....   | 63 |
| 3.6.1 EMF cell winding.....  | 64 |
| 3.6.2 EMF upstream.....  | 65 |
| Chapter 4. Investigations of factors influencing filtration behavior of single-sized |    |

|   |     |
|---|-----|
| particles.....  | 67  |
| 4.1 Critical flux measurement of single-sized particles.....  | 68  |
| 4.2 Influence of crossflow velocity (CVF).....  | 70  |
| 4.3 Influence of feed concentration.....  | 76  |
| 4.4 Influence of surface charge (pH).....   | 80  |
| 4.5 Influence of ionic strength.....  | 84  |
| 4.6 Influence of particle size.....   | 87  |
| 4.7 Influence of flow channel height.....   | 89  |
| 4.8 Summary.....  | 92  |
| Chapter 5. Critical flux and particle deposition of bidisperse suspensions during crossflow microfiltration.....  | 94  |
| 5.1 Critical fluxes of bidisperse latex feeds.....  | 97  |
| 5.2 Evidence from image analysis for the improved critical flux.....  | 103 |
| 5.3 Discussion.....   | 106 |
| 5.4 Effect of the relative composition of larger particles in mixed latex feeds.....                              | 111 |
| 5.5 Factors influencing the critical fluxes of bidisperse latex feeds...113                                       |     |
| 5.5.1 Influence of CFV on critical flux of bidisperse latex feeds..113  |     |
| 5.5.2 Influence of pH on critical flux of bidisperse latex feeds....114   |     |
| 5.5.3 Influence of channel height on critical flux of bidisperse latex feeds.....115                              |     |
| 5.6 Summary.....  | 118 |
| Chapter 6. Critical flux and particle deposition of flocculated suspensions during crossflow microfiltration..... | 120 |
| 6.1 Polydispersity of suspensions in membrane separation.....   | 121 |
| 6.2 Fractal concept in membrane separation.....   | 122 |
| 6.3 Flocculation of hematite particle.....  | 124 |
| 6.3.1 Effect of hematite concentration.....   | 125 |
| 6.3.2 Effect of ionic strength.....   | 126 |
| 6.3.3 Effect of pH.....   | 127 |
| 6.3.4 Effect of shear rate.....   | 128 |

|   |     |
|---|-----|
| 6.3.5 Conclusions on particle flocculation.....   | 129 |
| 6.4 Critical/Sustainable fluxes of hematite flocs.....                                      | 129 |
| 6.5 Membrane fouling by hematite polydisperse suspensions.....                              | 134 |
| 6.6 Membrane fouling by fractal hematite flocs.....   | 137 |
| 6.7 Summary.....  | 139 |
| Chapter 7. Determination of critical flux by mass balance technique combined with DOTM..... | 141 |
| 7.1 Comparison of critical flux measurement techniques.....                                 | 141 |
| 7.1.1 Transmembrane (TMP) monitoring.....   | 141 |
| 7.1.2 Direct observation.....   | 143 |
| 7.1.3 Mass balance.....   | 144 |
| 7.2 Mass balance combined with observation technique.....                                   | 145 |
| 7.3 Mass balance equation developing.....   | 148 |
| 7.4 Results.....  | 155 |
| 7.5 Summary.....  | 166 |
| Chapter 8. Effect of electromagnetic field on critical flux of particles using DOTM.....    | 167 |
| 8.1 Introduction and objectives.....  | 167 |
| 8.2 Results.....  | 169 |
| 8.2.1 Hematite flocs with EMF winding.....  | 169 |
| 8.2.2 Yeast cells with EMF winding.....   | 170 |
| 8.2.3 Latex particles with EMF winding.....   | 178 |
| 8.2.4 Yeast cells with EMF upstream.....  | 179 |
| 8.3 Discussion.....   | 181 |
| 8.4 Summary.....  | 182 |
| Chapter 9. Conclusions and Recommendations.....   | 184 |
| 9.1 Conclusions.....  | 184 |
| 9.2 Recommendations.....  | 186 |
| References.....   | 188 |



## Summary

The main disadvantage of membrane microfiltration processes is the fact that the filtration flux declines with time due to the cake layer of deposit formed or the blockage in the membrane pores. This thesis presents the study of particle deposition on membrane surface during separating mixed and flocculated feeds using the Direct Observation Through Membrane (DOTM) technique.

This study was aimed to find sub-critical strategies and to identify practical methods to increase sustainable flux of mixed and flocculated feeds. Uniform and mixed latex particle solutions were selected as the mono- and bi-disperse suspensions and flocculated hematite flocs were used as the polydisperse suspensions. The investigation was focused on measuring the critical fluxes of the suspensions under various operating conditions in crossflow microfiltration mode. The concept of critical flux showed the capability of optimizing the filtration processes. The most commonly used methods of measuring the values of critical flux were also compared and evaluated.

The mechanisms of particle deposition of mixed and flocculated feeds were observed using the DOTM. Enhancement in critical flux was found in the presence of larger particles due to the increased back diffusions. Another enhancement induced by electro-magnetic field (EMF) was also discussed in this thesis.

Two parameters (particle size distribution and fractal dimension) describing the floc properties were introduced into crossflow microfiltration, which is innovative for the conventional filtration theories where assumed that the particles were compact and spherical. The relationships between floc characteristics (floc size and structure) and experiment conditions (pH, concentration, ionic strength and shear rate) were also studied.

## List of tables

|   |     |
|---|-----|
| Table 2.1 Classification of strategies of controlling flux decline.....   | 14  |
| Table 3.1 Specifications of the Anopore inorganic membrane.....   | 48  |
| Table 4.1 Back transport mechanisms for different particle size ranges.....   | 75  |
| Table 4.2 Critical flux measurements under different CFVs using two membrane cells with different flow channel heights at concentration 0.05 %.....   | 90  |
| Table 4.3 Normalized critical fluxes for the latex particles.....   | 92  |
| Table 5.1 Critical fluxes of latex particles suspensions.....   | 102 |
| Table 5.2 Critical flux measurements under different CFVs using two membrane cells with different flow channel heights at a latex particle concentration of 0.05 % each.....  | 117 |
| Table 7.1 Comparison of $J_{crit}(\text{DOTM})$ and $J_{crit}(\text{MB})$ (mass balance) for the filtration of 3.0 $\mu\text{m}$ latex particles (0.05 vol. %) suspension at CFV of 0.2m/s but different pH values..... | 161 |
| Table 7.2 Comparison of $J_{crit}(\text{DOTM})$ and $J_{crit}(\text{MB})$ (mass balance) for the filtration of 5.0 $\mu\text{m}$ latex particles (0.05 vol. %) suspension at pH 8 but different CFVs.....               | 161 |
| Table 7.3 Comparison of $J_{crit}(\text{DOTM})$ and $J_{crit}(\text{MB})$ (mass balance) for the filtration of 10.0 $\mu\text{m}$ latex suspensions at constant CFV of 0.2m/s, pH 8 but different concentrations.....   | 162 |
| Table 8.1 Increase in critical flux with EMF.....   | 175 |
| Table 8.2 Increase in critical flux with EMF.....   | 177 |
| Table 8.3 Increase in critical flux with EMF.....   | 177 |

## List of figures

|  |    |
|--|----|
| Figure 1.1 Study method of this work.....  | 2  |
| Figure 2.1 Pore and particle size ranges of membrane applications (Li, 1996).....  | 6  |
| Figure 2.2 Schematic of dead-end and crossflow operation configurations.....   | 8  |
| Figure 2.3 Schematic of TMP vs. Flux profiles when limiting flux is reached.....   | 12 |
| Figure 2.4 Critical flux vs. limiting flux.....  | 13 |
| Figure 2.5 Schematic of concentration polarization boundary layer.....   | 18 |
| Figure 2.6 Critical flux vs. crossflow observed in the filtration of yeast and latex particles using DOTM technique (Li <i>et al.</i> , 1998)..... | 24 |
| Figure 2.7 Interactions between particles and membrane pores.....  | 29 |
| Figure 2.8 A schematic diagram of the effect of the double layer thickness on cake layer structure.....  | 31 |
| Figure 2.9 Permeate flux vs. particle radius in CFMF according to three back transport mechanisms.....   | 32 |
| Figure 2.10 Streamlines of creeping flow in the neighborhood of a porous sphere (Chellam <i>et al.</i> , 1993).....                                | 39 |
| Figure 3.1 Filtration set-up including DOTM facilities.....  | 43 |
| Figure 3.2 Schematic of the membrane module.....   | 44 |
| Figure 3.3 FESEM images of Anopore membrane.....   | 47 |
| Figure 3.4 Membrane template.....  | 48 |
| Figure 3.5 Overview of the system components.....  | 49 |
| Figure 3.6 Optical unit array schematic-top view.....  | 50 |
| Figure 3.7 A typical plot of log(Intensity) vs. log(Angle) from a measurement of hematite floc for the determination of fractal dimension.....     | 51 |
| Figure 3.8 Zeta potential of latex particles.....  | 52 |
| Figure 3.9 Zeta potential of washed baker's yeast.....   | 52 |
| Figure 3.10 Total zeta potential between PMMA plate and membrane ( $\zeta_{\text{total}}$ ).....   | 54 |
| Figure 3.11 Zeta potential of the PMMA plate ( $\zeta_{\text{PMMA}}$ ).....  | 54 |
| Figure 3.12 The net zeta potential of the membrane ( $\zeta_{\text{Sample}}$ ).....  | 54 |
| Figure 3.13 Determination of fractional surface coverage.....  | 56 |
| Figure 3.14 Scanning electron micrograph of hematite particles (adapted from   |    |

|   |    |
|---|----|
| (Petteys <i>et al.</i> , 1998).....   | 58 |
| Figure 3.15 Hematite floc preparation flowchart.....  | 60 |
| Figure 3.16 Schematic of the electromagnetic field produced by an electric current<br>flowing through a coil.....   | 64 |
| Figure 3.17 Picture of EMF cell winding working with DOTM.....  | 65 |
| Figure 3.18 Integrated DOTM system with a circulating line.....   | 66 |
| Figure 4.1 DOTM images of particle deposition during the filtration of 3.0 $\mu\text{m}$ latex<br>(0.05 %vol.) at CFV = 0.2 m/s.....  | 69 |
| Figure 4.2 Critical flux vs. crossflow velocity during filtration of latex particles at a<br>concentration 0.05% vol. and membrane isoelectric point pH 8.....                                      | 71 |
| Figure 4.3 Schematic of crossflow velocity distribution in the flow channel.....  | 71 |
| Figure 4.4 Particles removal during the filtration of 3.0 $\mu\text{m}$ latex particles at<br>concentration 0.05% vol. and pH 8.....  | 74 |
| Figure 4.5 $J_{crit}$ vs. CFV in CFMF according to the back transport mechanisms:<br>Brownian diffusion (Brownian), Shear-induced diffusion (SID) and<br>Inertial lift (IL).....                    | 75 |
| Figure 4.6 Critical flux vs. latex particle concentration at CFV 0.2 m/s.....   | 77 |
| Figure 4.7 Critical flux vs. log(particle concentration) in filtration of latex and yeast<br>at CFV 0.2 m/s.....  | 78 |
| Figure 4.8 Critical flux vs. yeast particle concentration at CFV 0.2 m/s.....   | 79 |
| Figure 4.9 Images captured during filtration of washed yeast at concentration 0.525<br>g/l and CFV 0.2 m/s. (a) operated at 45 l/m <sup>2</sup> h and (b) operated at 60<br>l/m <sup>2</sup> h..... | 80 |
| Figure 4.10 Critical flux vs. solution pH in filtration of latex at CFV 0.2 m/s.....  | 82 |
| Figure 4.11 Critical flux vs. solution pH in filtration of yeast at CFV 0.2 m/s.....  | 83 |
| Figure 4.12 3.0 $\mu\text{m}$ latex particles attached to the membrane before filtration had<br>started when flux was zero at pH 5.....   | 83 |
| Figure 4.13 Critical flux vs. ionic strength in the filtration of latex at 0.2 m/s.....   | 85 |
| Figure 4.14 Critical flux vs. ionic strength in the filtration of yeast at 0.1 m/s.....   | 85 |
| Figure 4.15 $J_{crit}$ vs. size of latex particles at pH 8, CFV 0.2 m/s and concentration<br>0.05 % vol.....  | 88 |
| Figure 4.16 Crossflow velocity distribution in the flow channel .....   | 91 |

|   |     |
|---|-----|
| Figure 5.1 DOTM images of particle deposition during filtration of 3.0 and 5.0 $\mu\text{m}$ latex particles (0.05 and 0.01 %vol. respectively) at CFV = 0.2 m/s.....       | 98  |
| Figure 5.2 Critical flux of single and mixed feeds of 3.0 (0.05%vol.) and 5.0 $\mu\text{m}$ latex particles at CFV = 0.2 m/s.....   | 99  |
| Figure 5.3 Critical flux of bidisperse feed of 5.0 (0.025%vol.) and 10.0 $\mu\text{m}$ latex particles at CFV = 0.2 m/s.....  | 100 |
| Figure 5.4 Critical flux of bidisperse feed of 3.0 (0.05%vol.) and 10.0 $\mu\text{m}$ latex particles at CFV = 0.2 m/s.....   | 101 |
| Figure 5.5 Critical flux improvement by the addition of big particles during the filtration of the mixed latex particles at CFV = 0.2 m/s.....                              | 101 |
| Figure 5.6 Comparison of membrane coverage between 3.0 $\mu\text{m}$ only and 3.0 + 5.0 $\mu\text{m}$ mixed system.....   | 104 |
| Figure 5.7 Comparison of membrane coverage between 3.0 $\mu\text{m}$ only and 3.0 + 10.0 $\mu\text{m}$ mixed system.....  | 105 |
| Figure 5.8 Critical fluxes of mixed latex particles 3+5 and 5+10 $\mu\text{m}$ at various composition ratios but a fixed total concentration 0.1 % vol. at CFV 0.2 m/s..... | 112 |
| Figure 5.9 Increase in the critical fluxes of mixed latex particles 3+5 and 5+10 $\mu\text{m}$ as the composition ratio of the bigger particles increased.....              | 113 |
| Figure 5.10 Critical fluxes of 3.0+5.0 $\mu\text{m}$ mixed latex feeds at various CFV.....  | 114 |
| Figure 5.11 Critical fluxes of 3.0+5.0 $\mu\text{m}$ mixed latex feeds vs. pH.....  | 115 |
| Figure 6.1 Size evolution with different concentration of hematite particles.....   | 125 |
| Figure 6.2 Size evolution with different concentration of KCl.....  | 126 |
| Figure 6.3 Size evolution with different pH.....  | 127 |
| Figure 6.4 Size evolution with different shear rate.....  | 128 |
| Figure 6.5 Schematic of membrane fouling by polydisperse suspensions.....   | 130 |
| Figure 6.6 Schematic of fouling development by polydisperse suspensions.....  | 131 |
| Figure 6.7 DOTM images during filtration of flocculated hematite flocs.....   | 132 |
| Figure 6.8 Particle size distribution evolution of the deposited flocs on the membrane shown in Figure 6.7.....   | 133 |
| Figure 6.9 Critical fluxes of hematite flocs under different CFVs.....  | 134 |

|   |     |
|---|-----|
| Figure 6.10 CFV exponents, $n$ for the hematite flocs.....  | 135 |
| Figure 6.11 Critical fluxes of different sizes of the hematite flocs.....   | 136 |
| Figure 6.12 Particle size exponents, $m$ for the hematite flocs.....  | 136 |
| Figure 6.13 Critical fluxes of hematite flocs with different fractal dimensions but<br>similar mean particle size at CFV 0.1 m/s (data points at $d_F=3.0$ are<br>extrapolated from the latex results)..... | 137 |
| Figure 7.1 Schematic plot of coverage rate vs. permeate flux.....   | 151 |
| Figure 7.2 $J_{covered}$ vs. $J_{open}$ where $J = 30 \text{ l/m}^2\text{h}$ and $A_{open}=A_{covered}$ .....   | 153 |
| Figure 7.3 Membrane coverage development in the filtration of $3.0 \mu\text{m}$ latex<br>at a concentration of 0.05 % vol., pH 8.0 and a CFV of 0.2 m/s.....  | 156 |
| Figure 7.4 Membrane coverage development in the filtration of $5.0 \mu\text{m}$ latex<br>at a concentration of 0.05 % vol., pH 8.0 and a CFV of 0.2 m/s.....  | 156 |
| Figure 7.5 Membrane coverage development in the filtration of $10.0 \mu\text{m}$ latex<br>at a concentration of 0.05 % vol., pH 8.0 and a CFV of 0.2 m/s.....   | 157 |
| Figure 7.6 An example of second layer build-up during the filtration of $5.0 \mu\text{m}$<br>(0.05 % vol.) latex suspension at pH 8 and CFV 0.05m/s.....  | 158 |
| Figure 7.7 Membrane coverage development in the filtration of $5.0 \mu\text{m}$ latex<br>at a concentration of 0.05 % vol., pH 8.0 and CFV 0.2 m/s.....   | 159 |
| Figure 7.8 Particle deposition rate vs. permeate flux.....  | 160 |
| Figure 7.9 Fractional deposition of the $3.0 \mu\text{m}$ latex particles vs. pH with a<br>concentration of 0.05 % vol. at CFV 0.2 m/s.....   | 163 |
| Figure 7.10 Fractional deposition of the $5.0 \mu\text{m}$ latex particles vs. CFVs with a<br>concentration of 0.05 % vol. at pH 8.....   | 163 |
| Figure 7.11 Fractional deposition of the $10.0 \mu\text{m}$ latex particles vs. concentrations<br>with a CFV of 0.2 m/s at pH 8.....  | 164 |
| Figure 7.12 Amount of deposited $10.0 \mu\text{m}$ latex particles vs. concentrations with a<br>CFV of 0.2 m/s at pH 8.....   | 165 |
| Figure 8.1 Hematite particle deposition pattern with and w/o EMF winding.....   | 170 |
| Figure 8.2 Critical flux of baker's yeast with EMF at CFV 0.1 m/s, Concentration<br>0.525g/l, pH 7.....   | 171 |
| Figure 8.3 Critical flux of baker's yeast with EMF at CFV 0.1 m/s, Concentration<br>0.525g/l, pH 7.....   | 172 |

|  |     |
|--|-----|
| Figure 8.4 Critical flux of baker's yeast with EMF at CFV 0.1 m/s, Concentration 0.525g/l, pH 7.....   | 174 |
| Figure 8.5 Comparison of two images on gray scale from Figures 8.3 and 8.4....   | 175 |
| Figure 8.6 Critical flux of 0.525 g/l yeast with EMF at various pH, CFV = 0.2 m/s.....   | 176 |
| Figure 8.7 Critical flux of 0.525 g/l yeast at various salt concentrations, at pH = 7, CFV = 0.2 m/s.....  | 176 |
| Figure 8.8 Critical flux of yeast at different concentrations with presence of 2 g/l salt but with and without EMF at pH = 7, CFV = 0.2 m/s..... | 177 |
| Figure 8.9 Critical flux of 3.0 $\mu\text{m}$ latex in brackish water.....   | 178 |
| Figure 8.10 Critical flux of 3.0 $\mu\text{m}$ latex at various pHs.....   | 179 |
| Figure 8.11 Critical fluxes of 0.525 g/l yeast at different pH values without salt at CFV = 0.2 m/s.....   | 180 |
| Figure 8.12 Critical fluxes of 0.525 g/l yeast at different salt concentrations at pH = 7, CFV = 0.2 m/s.....                                    | 180 |

## List of symbols

|           |  |
|-----------|--|
| $A$       | membrane area, $\text{m}^2$  |
| $a$       | particle radius, $\mu\text{m}$   |
| $c$       | particle concentration, $\text{kg}/\text{m}^3$                                 |
| $D$       | diffusion coefficient  |
| $d$       | particle diameter, $\mu\text{m}$   |
| $d_F$     | fractal dimension  |
| $H_o$     | half channel height, $\text{m}$  |
| $K$       | Boltzmann's constant, $\text{g}\cdot\text{cm}^2/\text{s}^2\cdot^\circ\text{K}$ |
| $k$       | constant   |
| $J$       | permeate flux, $\text{m}/\text{s}$   |
| $l$       | membrane thickness, $\mu\text{m}$  |
| $L$       | filter length, $\text{m}$  |
| $m$       | particle size exponent   |
| $n$       | velocity exponent/particle number  |
| $n_p$     | number of pores per unit   |
| $Q$       | volumetric flow rate/scattering vector quantity                                |
| $r$       | radius, $\mu\text{m}$  |
| $R$       | hydraulic resistance, $\text{m}^{-1}$  |
| $Re_p$    | particle Reynolds number   |
| $r_p$     | membrane pore size, $\mu\text{m}$  |
| $s$       | cake compressibility   |
| $S$       | specific surface area, $\text{m}^2$  |
| $t$       | filtration time, $\text{h}$  |
| $T$       | absolute temperature, $\text{K}$   |
| $U$       | velocity, $\text{m}/\text{s}$  |
| $v_{L,o}$ | inertial lift velocity, $\text{m}/\text{s}$                                    |
| $V$       | permeate volume, $\text{L}$  |
| $V_E$     | dielectrophoretic enhancement velocity   |
| $w$       | channel width, $\text{m}$  |
| $y$       | distance, $\text{m}$   |



## Greek letters

$\alpha_c$  specific resistance of cake layer

$\alpha_o$  constant

$\beta$  fraction of the membrane surface covered

$\Gamma$  velocity gradient(s)

$\gamma$  shear rate,  $s^{-1}$

$\delta$  cake layer thickness,  $\mu m$

$\varepsilon$  void fraction

$\zeta$  zeta potential, mV

$\eta_o$  viscosity of solution, g/cm\*sec

$\theta$  fraction deposition

$\kappa$  Boltzmann's constant

$\mu$  viscosity of permeate, g/cm\*sec

$\nu$  kinematic viscosity of fluid,  $m^2/s$

$\xi$  fraction of membrane area covered

$\pi$  osmotic pressure, kPa

$\rho$  fluid density,  $kg/m^3$

$\Delta p$  transmembrane pressure, kPa

$\phi$  concentration, fraction volume

$\omega$  mass of cake, g

## Subscript list

- $b$  bulk
- $c$  cake layer
- $E$  electric field
- $f$  fouling
- $i$  species
- $m$  membrane
- $p$  membrane pore
- $s$  shear-induced
- $w$  wall

## List of abbreviations

|       |   |
|-------|---|
| CFMF  | crossflow microfiltration                   |
| CFV   | crossflow velocity                          |
| CP    | concentration polarization                  |
| CRIT  | critical                                    |
| DOTM  | direct observation through the membrane     |
| EMF   | electro-magnetic field                      |
| FESEM | field emission scanning electron microscopy |
| IEP   | iso-electric point                          |
| MF    | microfiltration                             |
| PSD   | particle size distribution                  |
| SEM   | scanning electron microscopy                |
| SID   | shear-induced diffusion                     |
| TEM   | transmission electron microscopy            |
| TMP   | transmembrane pressure                      |
| UNSW  | University of New South Wales               |

## Chapter 1 Introduction

### 1.1 Background

Since the first synthetic membranes were fabricated several decades ago, membrane separation technology has been used more and more intensely. Membrane fouling, the buildup of cake layers in microfiltration, is still a major obstacle to the development of its applications. The problems to be addressed here are to better understand how foulants deposit on microfiltration membrane surface in crossflow filtration mode, how the deposited particles are removed by crossflow shear force by controlling the operating conditions, and how to optimize the operating conditions to minimize membrane fouling and therefore maximize permeate flux.

Much research was conducted on crossflow microfiltration (CFMF) with respect to the effects of crossflow velocity, filtration pressure, operating temperature, feed concentration, and membrane morphology as well as membrane pore size using all kinds of model particles with different particle sizes. A lot of techniques were invented and developed to study the mechanisms of membrane fouling. Based on the findings on membrane fouling by the research techniques, many cleaning techniques were proposed accordingly. Meanwhile, a fair amount of work was performed on the theoretical models to predict membrane fouling and transmembrane pressure transient.

However, little research has been pursued on the understanding of the mechanisms of membrane fouling caused by polydisperse suspensions using non-invasive visual techniques to make it more comprehensive and easier. In order to tackle this problem, a simplified simulation is a must. Based on the knowledge in filtrations of mono-sized particles, a possible way could be starting from mixed feeds of two or more mono-sized particles to flocculated feeds with controlled size distributions and structures, and finally to real industrial feeds. The results will also have a deep meaning for membrane bio-reactors (MBR).

Figure 1.1 shows the method of this study for the fouling mechanisms. First, the critical fluxes of mono- (Chapter 4), bi- (Chapter 5) and poly-disperse suspensions (Chapter 6) were experimentally measured respectively using the direct observation through membrane (DOTM) technique. Then the DOTM images were analyzed and the critical fluxes based on the mass balance were estimated (Chapter 7). Last, the fouling mechanisms were revealed.

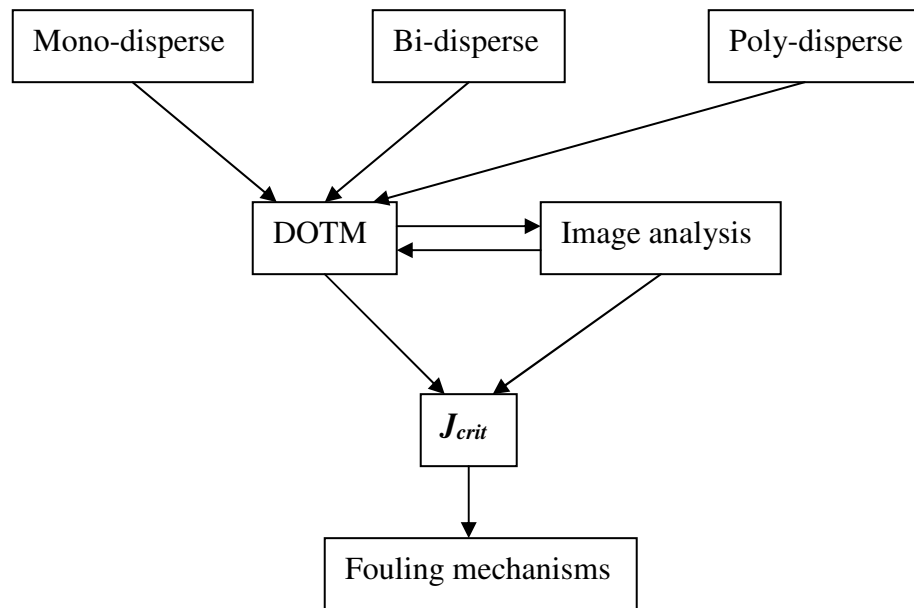


**Figure 1.1 Study method of this work.**

## 1.2 Objectives and scope of this research

- To obtain flocs with certain particle size distributions (PSD) and structures. Hematite particles were selected and flocculated under different conditions (Chapter 3);
- To investigate the interactions between different-sized particles during CFMF. Two single-sized latex particles were mixed and used as the mixed feeds. The Direct Observation Through Membrane technique was used to determine the critical fluxes and examine deposition phenomena (Chapter 5);

- To simulate fouling pattern of real polydisperse suspensions. Flocculated hematite flocs with controlled PSD and structure were used to study the particle deposition on the membrane surface (Chapter 6);
- To investigate the effects of operating conditions, such as crossflow velocity (CFV) and suspension concentration *etc.* on the filtration rate of polydisperse suspensions. Filtrations of hematite flocs were conducted (Chapter 6);
- To develop techniques to increase the sustainable flux and make long term membrane operation possible for real feeds (Chapter 6);
- To compare the critical flux of non-ideal feeds with the conventional filtration theories for micron-sized particles such as the film model, shear-induced diffusion (SID) model and inertial lift model (Chapter 6);
- To use two non-invasive techniques, the DOTM and image analysis for qualitative and quantitative assessment of deposited mass (Chapter 7);
- To apply the non-invasive DOTM technique to evaluate an industrial technology developed by GrahamTek that used Electro Magnetic Field (EMF) in RO. In particular, to examine the effect of EMF on critical flux of model foulants. The baker's yeast was selected as the model particulates (Chapter 8);
- To find strategies to identify sustainable flux conditions for a given complex feed (such as bioflocs) based on the preliminary work (Chapter 9).

### 1.3 Organization of this thesis

This thesis consists of nine chapters. In Chapter 1, a brief background as well as the objectives and scope of this research were given. The literature related to this study

was reviewed in Chapter 2. In this chapter, the relevant basic concepts and applications referring to microfiltration and crossflow microfiltration were introduced. Then concentration polarization and membrane fouling as the main limits to microfiltration were also discussed. The dominant factors influencing permeate flux in microfiltration such as operating conditions, membrane morphology as well as pore size, and nature of particle suspensions were summarized in this chapter according to the literature. In the last part of this review, knowledge on flocculation processes and the properties evaluating flocculation results were introduced. Experimental materials and methodologies as well as the experimental protocols were included in Chapter 3. Experimental setups used in this study were described in detail in this chapter as well. A comprehensive study of the factors influencing the critical fluxes of the mono-disperse latex and yeast suspensions at various conditions was presented in Chapter 4. The results in Chapter 4 were compared with those reported in Chapter 5 where the critical fluxes of the bidisperse latex suspensions were measured. In Chapter 6, a study on the relationship between floc characteristics (floc size and structure characterized as fractal dimension) and the experimental conditions (pH, concentration, ionic strength and shear rate) was performed. Further, the fouling mechanisms of the polydisperse hematite suspensions were tackled in Chapter 6. A concept of fractal dimension was introduced into the filtration process. The effect of the fractal dimension on the critical flux was studied in this part as well. A new quantitative method to determine the critical flux using the DOTM image data combined with the mass balance equation was developed in Chapter 7. A project testing the electromagnetic field (EMF) application in membrane filtration for an industry company was enclosed in Chapter 8. Finally, conclusions obtained from this study were drawn and recommendations for future research on this topic were proposed in Chapter 9.

## **Chapter 2 Literature review**

### **2.1 Introduction**

This chapter is a review relating to this topic in the literature. This study was aimed to investigate the fouling mechanisms during crossflow microfiltration process. The development of microfiltration and crossflow microfiltration processes was reviewed and compared at the beginning of this chapter. The concept of ‘critical flux’ was introduced as a powerful method in studying particle deposition in crossflow microfiltration. A summary on the strategies of fouling control was also given. The theories of microfiltration were surveyed in this chapter. The mathematical equations developed from these filtration theories predicting permeate flux were listed correspondingly. Typical factors influencing the filtration rate were discussed in detail. The experimental works studying these factors were also referred. Apart from the studies on the fouling by model particles, which were solid, spherical and uniform in particle size, the studies on particle size distribution and porous structure of flocs were also included in this project. Therefore, some knowledge on particle flocculation was necessary. A concept of geometry, ‘fractal dimension’ was introduced to show how the porous structure of flocs would influence membrane filtration processes.

### **2.2 Basic concepts**

#### **2.2.1 Microfiltration (MF)**

When pressure-driven flow through a membrane or other filter media is used to separate micro-sized particles from suspensions, the process is called microfiltration. Membrane separation is commonly used in mass separation processes nowadays. Compared with the conventional separation techniques such as distillation, crystallization and extraction, the membrane separation has been favored due to its many benefits. Membrane filtration can be easily achieved at the ambient temperature which allows temperature sensitive solutions to be filtered without



damage. Membrane filtration is also a potentially “green” process since it needs no additional chemicals except for membrane cleaning and produces no extra waste sludge to the environment. The process can be designed and performed competitively according to specific requirements. During microfiltration, the driving force, transmembrane pressure forces the suspending fluid through the filter medium. The particulates to be filtered are dragged toward the filter under the convective force and finally rejected by the membrane. The main mechanism of separation is the sieving effect. Compared with ultrafiltration and reverse osmosis filtration, microfiltration has an advantage of small pressure drop, typically 10 to 300 kPa. During the last few decades, MF has been increasingly used to separate fine particles, colloids and macromolecules in a range of 0.02-10  $\mu\text{m}$  (Figure 2.1). Typical particles falling in this size range include colloidal silica, clay silt, metal hydroxides, carbon black, latex emulsion, paint pigment, bacteria and yeast cells. Most of the contaminants in water and wastewater treatment fall into this size range.

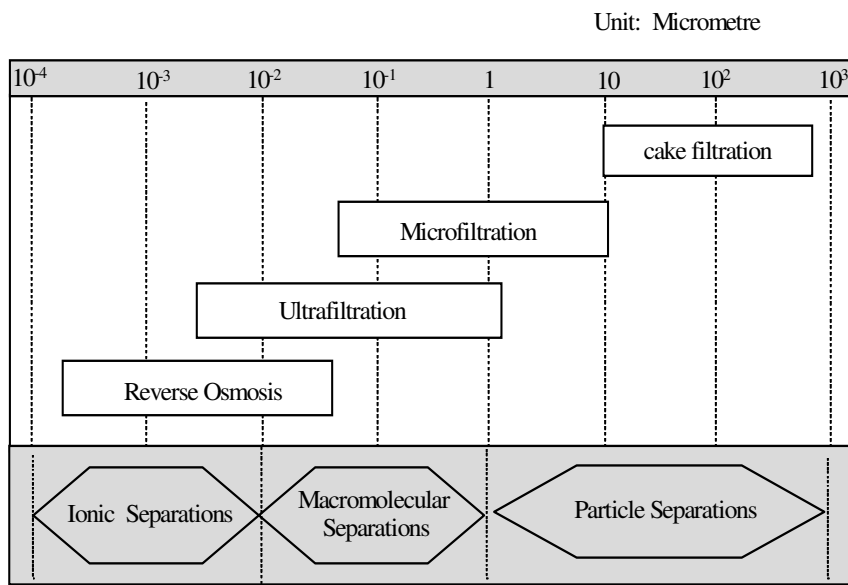


**Figure 2.1 Pore and particle size ranges of membrane applications (Li, 1996).**

The first synthetic microporous membranes were fabricated at the beginning of the last century and made the MF process possible. The membranes used in MF have a high porosity and a microporous structure which separate fine particles from suspensions. One of the criteria for selecting a membrane process depends on the

size of the particles to be separated. Particles larger than the MF membrane pores will be rejected. Particles smaller than the membrane pores will penetrate or block the membrane. Meanwhile, the membranes are required to have high strength as well as chemical and thermal stability. The membranes are also demanded to have a reasonable cost/benefit ratio. The membrane properties are largely determined by the producing methods and the materials. The commonly used types are polymer and inorganic membranes which include polypropylene, polyethylene, polycarbonate, ceramic, zirconium oxide, borosilicate glass, stainless steel, silver, poly pure cellulose acetate, regenerated cellulose, acrylic polymers, polyamide and polysulfone (Belfort *et al.*, 1994). Some of these types are solvent cast while the others are produced by a radiation track-etched process.

### 2.2.2 Crossflow microfiltration (CFMF)

In MF, there are two operation configurations, dead-end and crossflow filtrations. In dead-end filtration (Figure 2.2 a), the fluid flow is predominantly perpendicular to the membrane surface. The particles continue to deposit on the membrane surface and form a very thick cake layer rapidly until the driving force is counteracted by the resistance and then the filtration has to be ceased. Alternatively, if the flux is to be maintained, the pressure has to be increased continuously until a limit is reached.

In 1907, it was first found that the filtration rate was enhanced using a stirred filtration cell to create a shear flow across the filter when separating colloidal and fine particles. The membrane fouling was alleviated by a shear fluid flowing parallel to the membrane surface.

In crossflow filtration, the fluid flows tangentially to the membrane surface and the growth of cake layer can be controlled by the shear flow at a low level so that continuous operation is possible. Hence, crossflow filtration has many advantages, such as a thin or negligible cake layer, a high permeate flux on lower operating pressure and a continuous operation mode compared with the conventional dead-

end filtration. However, dead-end filtration consumes much less energy than crossflow filtration since hydraulic flow equipments have to be provided to produce shear flow. CFMF makes it possible to maintain a steady and long-term operation with a low level of membrane fouling if operated properly. However, the optimal operating conditions for CFMF without frequent membrane cleaning and replacement are still unclear and worthy of further study.

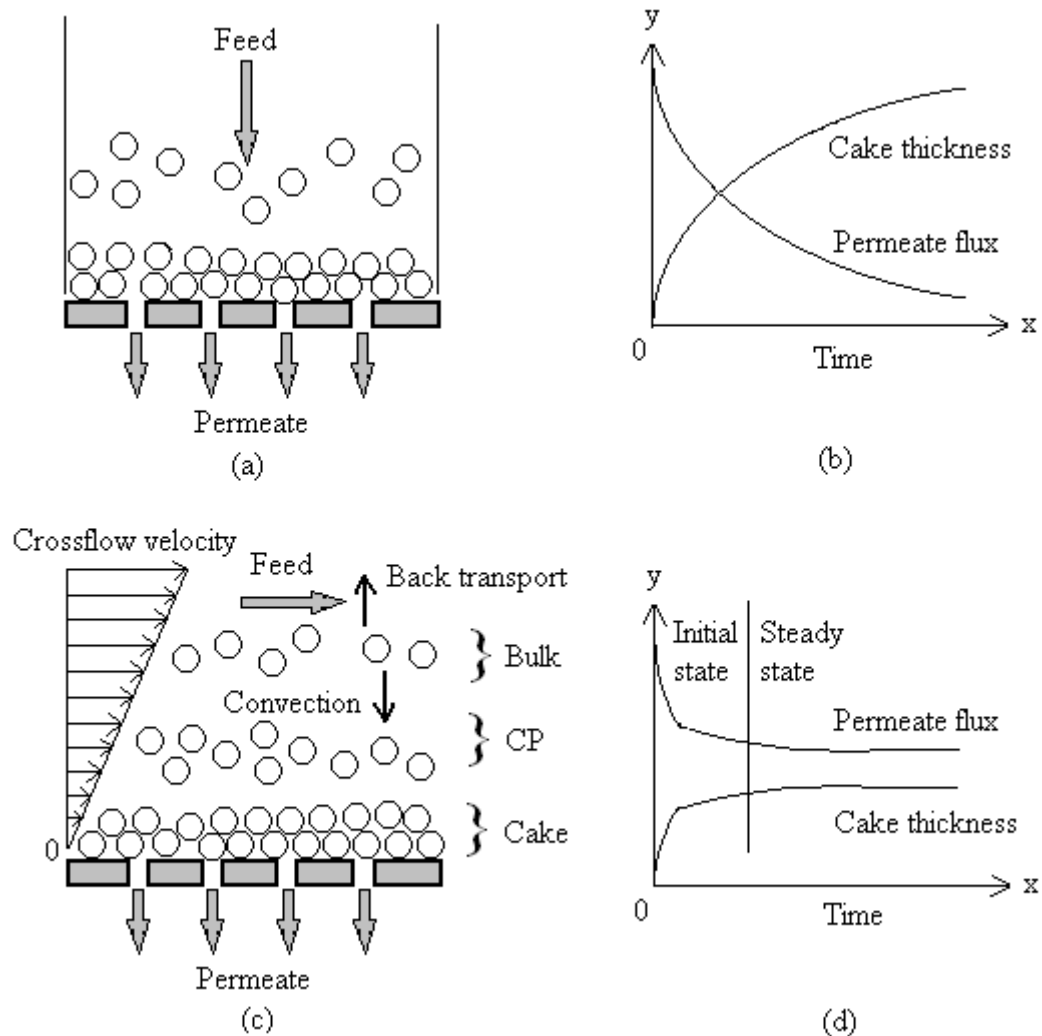


**Figure 2.2 Schematic of dead-end and crossflow operation configurations. (a) and (c) illustrate dead-end and crossflow configurations respectively. (b) and (d) show their corresponding permeate flux and cake thickness curves against time. (CP: Concentration Polarization).**

At the beginning of CFMF in constant pressure mode, as fluids permeate through the membrane pores, particles to be separated are dragged to the membrane to form a cake layer by the convective force due to the permeate flow. During this period, the permeate flux drops due to the additional resistance generated by the concentration polarization and the growing cake layer. At the same time, some of the deposited particles are removed from the membrane due to the tangential shear stress, the so-called re-entrainment. The movement of the particles is balanced between the convection and the back transport. The particle back transport mechanisms are particle size dependent. Brownian diffusion is dominant when the particle size is smaller than 0.5  $\mu\text{m}$ . Inertial lift has a major role in the filtration mechanism when the particle size is larger than 30 micron. In between, shear-induced diffusion is the main back transport mechanism (Belfort *et al.*, 1994). The rate of particle deposition decreases with the permeate flux. A steady state without further decline in permeate flux can be reached gradually when the amount and the size of the depositing particles are the same as the removed particles.

In constant flux mode when operated below ‘critical flux’ (Section 2.2.3 below), there is no or negligible fouling on the membrane. There is no transmembrane pressure (TMP) increase in this period. However, when operated above critical flux, particles start to deposit due to the increased convective force and TMP increases gradually. From then on, cake layer thickness keeps on increasing until the permeate flux cannot be kept constant.

Ripperger *et al.* (2002) summarized the applications of the CFMF technique for:

- Clarification of fruit juice, wine, cider and vinegar;
- Separation of fat and bacteria removal from milk;
- Removal of beer yeast;
- Filtration of fermentation broths;
- Pretreatment of other membrane filtration steps in water/wastewater treatment;
- Purification of potable water without chemical conditioning;

- Upgrading of cleaning solutions in food and metalworking industries.

### 2.2.3 Concept of critical flux

Recently, the concept of critical flux is often used to describe the conditions where fouling occurs. Field *et al.* (1995) first proposed the concept of critical flux from their experiments in the filtration of yeast suspensions in constant flux mode.

Field *et al.* (1995) stated that: **“There exists a flux below which a decline of flux with time does not occur; above this flux, fouling is observed. This flux is termed as the critical flux and its value depends on the hydrodynamics and probably also on the other variables.”**

This concept means that the critical flux of a given suspension should be equal to the corresponding clean water flux at the same TMP. Wu *et al.* (1999) defined a ‘strong form’ of critical flux if the flux of a suspension was equal to the water flux at the same TMP. A ‘weak form’ of critical flux existed correspondingly if the relationship between TMP and flux was linear but with a different slope from that for pure water. They conducted experiments to investigate the strong and weak forms of critical flux using colloidal suspensions and bovine serum albumin (BSA) solutions with three types of membranes. They measured the flux and TMP profiles using sensitive pressure transducers that could monitor a TMP increase of 0.1 kPa to compare with the profiles for pure water. Theoretically, the water flux is directly proportional to the applied TMP.

Therefore, below a certain flux known as critical flux, particles never deposit on membrane surface and the relationship between flux and TMP for solutions or suspensions should be linear. The concept of critical flux allows a long-term operation. Filtration above the critical flux causes membrane fouling. Increasing TMP only increases flux for a transient period with the flux eventually falling back to the critical value. Continuous increase in TMP is required to maintain flux above critical value, but it is unsustainable in the long term. When operated at sub-critical

flux in the range right below the critical flux, long term and zero fouling operation could be achieved (Howell, 1995). It is more important to control permeate flux from a low level at the beginning than pressure. Membrane cleaning and replacement will be much less frequent then. So it is feasible to operate below the critical flux although the flux is relatively low.

Many experiments and theories showed that the value of critical flux is a function of numerous parameters such as suspension properties (particle size and concentration), surface interactions (pH and zeta potential) and hydrodynamic operating conditions (tangential velocity) (Bacchin, 2004). The effects of these factors will be discussed in detail in Sections 2.3 and 2.4.

There are several ways to measure the critical flux. TMP monitoring is the most commonly used method to determine critical flux. In this method, critical flux is defined as the flux below which increase in TMP could not be observed since membrane fouling would not occur below the critical flux. The measurement is usually conducted in constant flux mode in crossflow filtration. If the imposed flux is below the critical flux, only the membrane dominates the filtration resistance. The TMP should not change with time, and if it is above the critical flux, a cake layer grows until the constant flux cannot be maintained. The TMP increases eventually because of the additional resistance. To do the measurement, a simple flux-stepping test can be conducted. For each step, the permeate flux is controlled constant by a pump in permeate side. The permeate flux starts from a low value and is increased upwards after a certain duration of time until TMP starts to rise. The highest flux where there is no steady TMP increase is regarded as the critical flux. Although TMP monitoring is a simple method to determine critical flux, there is no standard protocol so far. Researchers are operating their systems with different constant flux durations and increments (Bacchin *et al.*, 2006; Le Clech *et al.*, 2003). This makes it difficult to compare the results. The results often have to be normalized correctly. Besides, it is often limited by the sensitivity of the pressure transducers as well as the specific resistance of the foulants.

Another method is based on mass balance principal (Kwon *et al.*, 2000). Critical flux is defined as the flux below which there is no decrease in particle concentration due to particle deposition. Membrane fouling can be expressed in terms of the rate of particle deposition at an imposed flux. There are also some other visualization techniques to observe the commencement of membrane fouling. Among them, the non-invasive, in situ visual techniques provide direct insights on membrane fouling studies. Among these techniques, Direct Observation Through Membrane (DOTM), were used in this study (Chapter 3, Section 3.1). Further comparison of the critical flux determination methods can be found in Chapter 7.

Critical flux is often misunderstood with limiting flux, although they may be equivalent or related under some circumstances. Limiting flux is the maximum stationary permeate flux that can be achieved when TMP increases (Bacchin, 2004) (Figure 2.3). Figure 2.4 shows the typical flux *vs.* TMP relationship for microfiltration with a transition from membrane control (pressure dependent flux) to cake control (pressure independent flux – limiting flux). Limiting flux represents the flux beyond which long-term operation is not possible. However, critical flux is a transit parameter between concentration polarization and membrane fouling. Before critical flux is reached, permeate flux should be linear with TMP. A cake layer will build up increasingly on membrane surface until limiting flux is reached. After that, a dynamic equilibrium can be established and permeate flux does not increase with TMP increasing. Therefore, flux is independent of TMP.

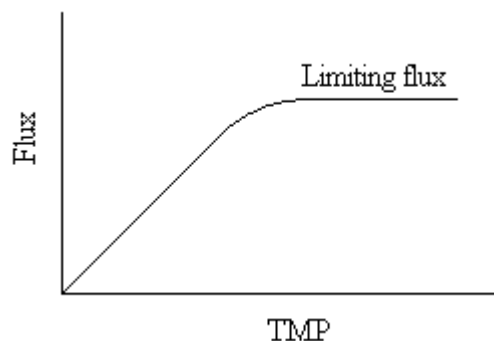


**Figure 2.3 Schematic of TMP *vs.* Flux profiles when limiting flux is reached.**

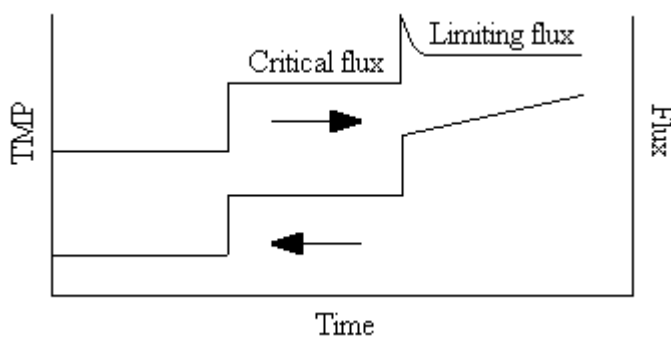


**Figure 2.4 Critical flux vs. limiting flux.**

Bacchin (2004) suggested a simple model that limiting and critical fluxes could be theoretically linked and critical flux had a value of two-thirds of limiting flux. This model was based on certain assumptions *i.e.* cake deposition was taken as the main fouling phenomenon and osmotic pressure was neglected, the flux had a strong form of critical flux and the membrane channel had a constant critical Péclet number *etc.* He proposed that a way to avoid fouling could be never to exceed two-thirds of the limiting flux. However, in practice this might be difficult due to the varying conditions of velocity, concentration and TMP in the system.

#### 2.2.4 Strategies to alleviate flux decline

Rather than sub-critical flux operation, there are several strategies that prevent permeate flux from declining. According to the factors controlling flux in different applications, they can be summarized into three main classifications: membrane modification, feed pretreatment and hydrodynamic conditions (Winzeler *et al.*, 1993). Table 2.1 gives a summary of the proven techniques (Tragardh, 1989; Wakeman *et al.*, 2002). They can be achieved by either physical or chemical processes. Hydrodynamic and operational controls are of interest in this study.



**Table 2.1 Classification of strategies for controlling flux decline**

| <b>Strategies:</b>              | <b>Techniques:</b>   |
|---------------------------------|--|
| Control of membrane properties  | Alteration of hydrophobicity<br>Alteration of surface charge   |
| Pretreatment of the feed        | Prefiltration/Centrifugation/Sedimentation<br>Flocculation/Coagulation/Precipitation<br>Ion exchange   |
| Control of operating conditions | Optimization of crossflow velocity<br>Use of rotating membrane modules<br>Generation of secondary flows<br>Design of inserts/protuberances<br>Ultrasonic/Electric/Magnetic field<br>Pulsation/Bubbling/Backwash <i>etc.</i><br>Membrane cleaning |

## 2.3 Theories of microfiltration

### 2.3.1 Darcy's Law

In MF where the sieving mechanism applies, the overall filtration rate (known as permeate flux) can be expressed as a ratio of pressure driving force to filtration resistance. The driving force is the transmembrane pressure. The filtration resistance includes the membrane hydraulic resistance due to the membrane microporous structure as well as the cake layer resistance due to the particle deposition in or on the membrane. The general relationship between permeate flux and filtration driving force as well as filtration resistance is described by Darcy's law:

$$J \equiv \frac{1}{A} \frac{dV}{dt} = \frac{\Delta p}{\mu(R_m + R_c)} \quad (2-1)$$

where  $J$  is permeate flux,  $V$  is the total volume of permeate,  $A$  is membrane area,  $t$  is filtration time,  $\Delta p$  is pressure drop imposed across the cake layer and the membrane,  $\mu$  is the viscosity of permeate,  $R_m$  is membrane hydraulic resistance which increases with time due to membrane fouling and compaction and  $R_c$  is cake resistance which increases with time due to the cake build-up and compression (Ho *et al.*, 2001).

According to the types of resistance, deposition or fouling, Darcy's law has following different forms:

(a) Solvent only flux:

$$J = \frac{\Delta p}{\mu R_m} \quad (2-2)$$

(b) Flux in the presence of solute that exerts a significant osmotic pressure,  $\Delta\pi$ :

$$J = \frac{\Delta p - \Delta\pi}{\mu R_m} \quad (2-3)$$

(c) Flux in the presence of a reversible cake or deposit or polarization ( $R_c$ ):

$$J = \frac{\Delta p}{\mu(R_m + R_c)} \quad (2-4)$$

(d) Flux due to a combination of resistances including fouling ( $R_f$ ):

$$J = \frac{\Delta p - \Delta\pi}{\mu(R_m + R_f)}, J = \frac{\Delta p}{\mu(R_m + R_f)} \text{ or } J = \frac{\Delta p}{\mu(R_m + R_c + R_f)} \quad (2-5)$$

where  $R_f$  is the resistance due to membrane fouling.

### 2.3.2 Membrane resistance

Membrane resistance is the hydraulic resistance of membrane capillary pores to permeate flow. It is a function of membrane thickness, nominal pore size, pore distribution and pore density, and various morphological features such as tortuosity and porosity. Membrane resistance can be estimated using the Hagen-Poiseuille equation with the assumption that the permeate through the membrane pores is laminar Newtonian flow (Li, 1996).

$$R_m = \frac{8l}{n_p \pi r_p^4} \quad (2-6)$$

where  $l$  is membrane thickness,  $n_p$  is the number of pores per unit area and  $r_p$  is the assumed pore size. This equation only applies to a membrane that has cylindrical capillary pores with uniform radius which are perpendicular to the membrane surface.

From this equation one can see that membrane resistance increases with increasing membrane thickness and decreasing pore size and number density. It may also increase with time if membrane fouling and compaction occur.

For convenience, the Hagen-Poiseuille equation can be simplified by defining membrane porosity ( $\varepsilon_m$ ) and specific surface area ( $S_m$ ) (Mores *et al.*, 2001).

$$R_m = \frac{k(1-\varepsilon_m)^2 S_m^2 l}{\varepsilon_m^3} \quad (2-7)$$

where  $k$  is a constant varying with membrane morphology and pore structure ( $k = 2$  for membranes with uniform cylindrical pores), the void fraction is  $\varepsilon_m$  = membrane void volume/total volume ( $\varepsilon_m = n_p \pi r_p^2$ ), and the specific surface area is  $S_m$  = pore surface area/solids volume ( $S_m = 2\pi r_p n_p / (1 - \varepsilon_m)$ ).

The resistance of the membranes used in this study (Chapter 3, Section 3.2.3) could be calculated according to the Hagen-Poiseuille equation. According to the properties of the Anopore membrane listed in Table 3.1, this kind of membrane had a thickness of 60  $\mu\text{m}$  and porosity 25-50 %. For 0.2  $\mu\text{m}$  membranes with porosity 50 % for example, the membrane resistance was estimated to be  $9.6 \times 10^{10} \text{ m}^{-1}$ .

### 2.3.3 Cake resistance

For an incompressible cake layer, its porosity and resistance is independent of the imposed pressure drop. The resistance can be estimated by the Carman-Kozeny equation (Belfort *et al.*, 1994; Mores *et al.*, 2002):

$$R_c = \frac{k(1-\varepsilon_c)^2 S_c^2 \delta_c}{\varepsilon_c^3} \quad (2-8)$$

where  $\varepsilon_c$  is the void fraction of the cake layer,  $S_c$  is the solid surface area per unit volume of solids in the cake and  $\delta_c$  is the thickness of the cake layer. For rigid spherical particles with a radius of  $r$ , the specific surface area is  $S_c = 3/r$ , the void fraction of a randomly packed cake layer is  $\varepsilon_c \approx 0.4$  and the constant  $k$  is  $\sim 5.0$ .

The resistance of a single cake layer formed by 3.0  $\mu\text{m}$  rigid and spherical particles was calculated to be  $3.375 \times 10^8 \text{ m}^{-1}$  according to the Carman-Kozeny equation. Compared with the estimated membrane resistance ( $9.6 \times 10^{10} \text{ m}^{-1}$ ) used in this study, a single cake layer formed by 3.0  $\mu\text{m}$  particles only contributed a limited effort to the total filtration resistance. If the particle size was reduced to 0.3  $\mu\text{m}$ , the cake resistance increased dramatically up to  $3.375 \times 10^9 \text{ m}^{-1}$ . This was because the relationship  $R_c \propto (1/r)$ . A cake of multiple layers of 0.3  $\mu\text{m}$  particles, 8.53  $\mu\text{m}$  thick would have a similar resistance to the membrane, which means that the membrane resistance was equivalent to 28 fouling layers of 0.3  $\mu\text{m}$  particles.

It is often convenient to define the specific resistance of a cake on a mass basis:

$$\alpha_c = R_c / \omega \quad (2-9)$$

where  $\alpha_c$  is the specific resistance of the cake and  $\omega$  is the mass of cake deposited per unit area of membrane.

However, the cake layer formed by foulants, such as flocculated particles and cells, is highly compressible (Belfort *et al.*, 1994). The cake voidage decreases and the specific resistance increases when the imposed pressure drop is increased due to the effect of  $\varepsilon_c$  on  $R_c$ . In this case, the specific resistance of a compressible cake is estimated as a power-law function of the imposed pressure drop:

$$\alpha_c = \alpha_o (\Delta p)^s \quad (2-10)$$

where  $\alpha_o$  is a constant related to the size and shape of the fouling particles and  $s$  is the cake compressibility which varies from zero for a rigid cake layer to a value near one for a highly compressible cake layer.

### 2.3.4 Concentration polarization model (Film model)

Concentration polarization refers to a boundary layer where the ‘particles’ to be separated are rejected by the membrane. When concentration polarization occurs, the ‘particle’ concentration decreases exponentially from the membrane surface to the bulk solution (Figure 2.5).

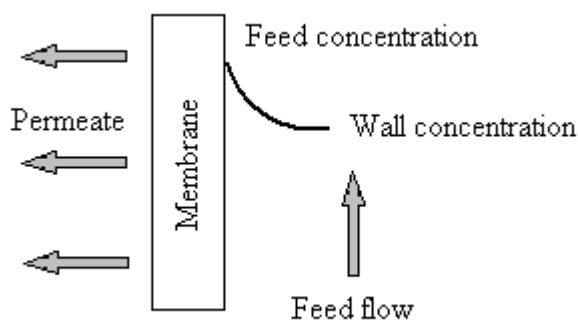


**Figure 2.5 Schematic of concentration polarization boundary layer.**

In the concentration polarization model, the convection of particles towards the cake layer is balanced by the diffusion of particles away from the cake layer. To describe the balance:

$$-D \frac{\partial \phi}{\partial y} = J \phi \quad (2-11)$$

where  $D$  is a diffusion coefficient and  $y$  is the coordinate normal to the membrane surface. Equation (2-11) assumes no particles pass through the membrane.

If the diffusion coefficient is constant, Equation (2-11) can be integrated:

$$J = \frac{D}{\delta} \ln\left(\frac{\phi_w}{\phi_b}\right) = k \ln\left(\frac{\phi_w}{\phi_b}\right) \quad (2-12)$$

where the boundary conditions are  $\phi = \phi_w$  (the wall concentration) when  $y = 0$  (the cake surface) and  $\phi = \phi_b$  (the bulk concentration) when  $y = \delta$ . Constant  $k = D/\delta$  is defined as mass transfer coefficient (Ho *et al.*, 2001).

The concentration polarization model is also called as the film model. This is the first model to include the effect of bulk concentration ( $\phi_b$ ) successfully on permeate flux. By integrating the conventional correlations, such as the L  v  que solution for laminar flow, the dependence of flux on crossflow velocity is evident.

For laminar flow, length-averaged mass transfer coefficient is calculated by the L  v  que solution (Ho *et al.*, 2001):

$$\langle J \rangle = 0.807 \left( \frac{\gamma_o D^2}{L} \right)^{1/3} \ln\left(\frac{\phi_w}{\phi_b}\right) \quad (2-13)$$

where  $\gamma_o$  is the shear rate in the boundary layer and  $L$  is the length of the filter tube or channel. Note that this equation is based on the assumption that the flux is

constant. This equation shows that the steady state permeate flux is independent of the imposed pressure drop. This is because the concentration polarization layer controls the cake layer thickness and hence the permeate flux.

The diffusivity can be calculated as the Brownian diffusivity of a particle with a radius  $r$  given by the Stokes-Einstein equation:

$$D_b = \frac{KT}{6\pi\mu r} \quad (2-14)$$

where  $K = 1.38 \times 10^{-16} \text{ g}\cdot\text{cm}^2/\text{s}^2\cdot^\circ\text{K}$  is the Boltzmann's constant and  $T$  is the absolute temperature. Note that the Brownian diffusivity is independent of the shear rate.

Integrating Equation (2-14) into (2-13), the permeate flux can be obtained:

$$\langle J \rangle = 0.114 \left( \frac{\gamma_o K^2 T^2}{\mu^2 a^2 L} \right)^{1/3} \ln \left( \frac{\phi_w}{\phi_b} \right) \quad (2-15)$$

Note that when the Brownian diffusion is dominant, the permeate flux increases with one-third power of the shear rate or the crossflow velocity and decreases with two-third power of the particle radius. Hence, the Brownian diffusivity is important for sub-micron particles ( $< 0.5 \text{ }\mu\text{m}$  in diameter) in low shear rate fluids. However, this model predicts fluxes much lower than those observed in experiments (Belfort *et al.*, 1994). This difference is the so-called “flux paradox”. Therefore, there might be other back transport mechanisms for larger particles, such as shear-induced diffusion and inertial lift which will be discussed in the following sections.

### 2.3.5 Shear-induced diffusivity model (SID)

When it comes to particulates larger than  $0.5 \text{ }\mu\text{m}$ , the concentration polarization model cannot predict the flux properly since the Brownian diffusion is no longer significant for such large particles. Zydney and Colton (1986) replaced the

Brownian diffusivity with a shear-induced diffusivity first measured by Eckstein *et al.* in 1977. They observed that the shear-induced diffusivity increased with increasing shear rate and concentration. Depending on the concentration, the shear-induced diffusivity had the following forms:

$$D_s \approx 0.1\phi r^2 \gamma \quad \text{For } 0 < \phi < 0.2 \quad (2-16)$$

$$D_s \approx 0.025r^2 \gamma \quad \text{For } 0.2 < \phi < 0.5 \quad (2-17)$$

Zydney and Colton (1986) substituted  $D = 0.03r^2 \gamma_o$  into Equation (2-13) and got:

$$\langle J \rangle = 0.078 \left( \frac{r^4}{L} \right)^{1/3} \gamma_o \ln \left( \frac{\phi_w}{\phi_b} \right) \quad (2-18)$$

From Equation (2-18), the permeate flux increased linearly with the shear rate and proportionally to  $r^{4/3}$  where  $r$  was the particle radius. Both the concentration polarization model and the SID model predicted that the flux decreased when the bulk concentration increased.

To determine the wall concentration ( $\phi_w$ ), many assumptions have to be made. In Li's work (2000), they used the membrane area coverage by the deposited particles to calculate  $\phi_w$ . They proposed for spherical particles  $\phi_w = 2/3\xi$ , where  $\xi$  was the fraction of membrane area covered by the deposited particles. They found that the shear-induced diffusion model predicted reasonable fluxes of 6.4 and 11.9  $\mu\text{m}$  latex particles and under-predicted the critical flux of 3  $\mu\text{m}$  latex. They also provided a modified shear-induced diffusion model which was more applicable for 5-12  $\mu\text{m}$  model particles.

### 2.3.6 Inertial lift model

It was observed that a neutrally buoyant particle migrated across the fluid streamlines in a duct in laminar flow (Altena *etc.*, 1984). Particles were transported



laterally to the membrane due to the tangential flow across the membrane. Altena and Belfort (1984) studied the lateral migration of spherical particles in crossflow filtration in porous flow channels. In their model, the forces on the particles were balanced between the drag force due to the convection flow into the membrane pores and the inertial force due to the lateral migration away from the membrane. They obtained for migration velocity  $v_{L,o}$ ,

$$v_{L,o} = \frac{\rho_o r^3 \gamma_o^2 f(y')}{16\mu} \quad (2-19)$$

where  $\rho_o$  was the fluid density,  $\gamma_o$  was the shear rate at the wall of the tube or channel and  $y'$  was the dimensionless distance of the particle from the wall of the tube or channel.  $f(y')$  reached its maximum value at the wall. It was estimated that  $f(y') \approx 1.6$  for a two-dimensional channel and  $f(y') \approx 1.3$  for a tube. However, this equation was only valid under the conditions:

$$\text{Re}_p = \frac{U_o r}{\nu} \ll 1 \text{ and } \frac{r}{2H_o} \ll 1$$

where  $\text{Re}_p$  was the particle Reynolds number. Hence, it only applied to small particles in low flow.

However, in crossflow filtration, the velocity often exceeded this range. When  $\text{Re}_p \ll 1$ ,  $f(y')$  was found to be 0.577 by Drew *et al.* (1991) for a two-dimensional channel. Then:

$$v_{L,o} = 0.577 \frac{\rho_o r^3 \gamma_o^2}{16\eta_o} \quad (2-20)$$

Compared with the shear-induced diffusion model, the permeate flux predicted by the inertial lift model is independent of particle concentration. The inertial lift

velocity increases with the square of the shear rate and the cube of the particle radius, inertial lift tends to become important for particles larger than 10  $\mu\text{m}$ .

In typical applications where the cake resistance dominates the permeate flux is assumed to equal to the inertial lift velocity:

$$J = v_{L,o} = 0.036 \frac{\rho_o r^3 \gamma_o^2}{\eta_o} \quad (2-21)$$

The permeate flux increases inversely with the solution viscosity and is independent of the filter length and the bulk concentration of the particles. The predicted flux is more sensitive to particle size and shear rate using this model compared with the shear-induced diffusion model. When applying the inertial lift velocity to crossflow filtrations, the particles are believed to deposit on the membrane surface only when the permeate flux is larger than the maximum value of the inertial lift velocity.

## 2.4 Factors influencing the permeate flux

As mentioned above, the value of permeate flux is known to be a function of particle size, hydrodynamics and membrane-colloid interactions. It is reported that there are numerous parameters that may influence the permeate flux. They can be classified into three groups:

- (i) Parameters relating to the operating conditions such as CFV, TMP, the solution concentration and the operational temperature;
- (ii) Membrane characteristics such as the membrane morphology, membrane pore size, membrane wettability and membrane surface charge;

- (iii) Nature of the particulate suspensions such as the particle size and particle size distribution, charge of particle surface and particle shape.

### 2.4.1 Influence of crossflow velocity (CFV)

In CFMF, deposited particles can be removed by tangential shear flow. Therefore, cake layer can be controlled and an equilibrium state or a quasi-steady state can be achieved within a relatively short period after the beginning of the filtration. It is accepted that CFV is one of the key controlling parameters in membrane fouling and permeate flux. The concentration polarization model (Equation (2-13)), the SID model (Equation (2-18)) and the inertial lift model (Equation (2-21)) all predict that the permeate flux increases with CFV. However, the degree of its effect is different. Many studies on crossflow velocity are available in the literature. Shown in Figure 2.6 is an example indicating the effect of CFV on critical permeate flux measured by the DOTM (Li *et al.*, 1998).

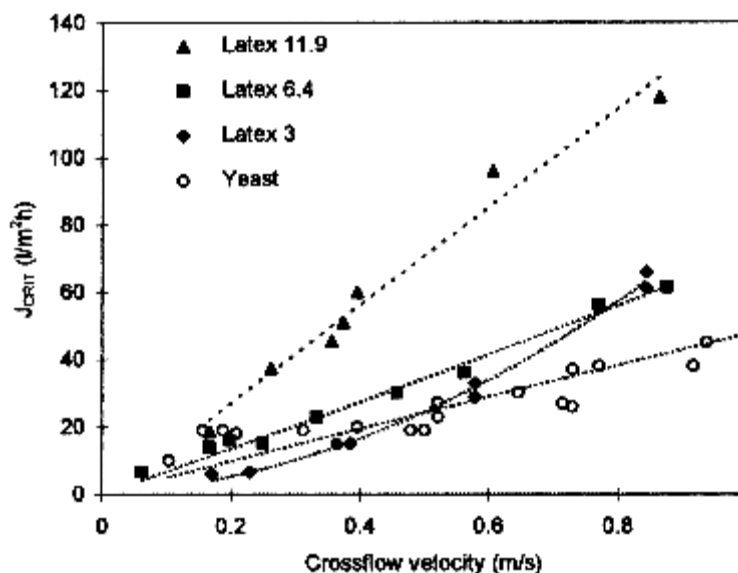


Figure 2.6 Critical flux vs. crossflow observed in the filtration of yeast and latex particles using the DOTM technique (Li *et al.*, 1998).

Below critical flux, whenever CFV is increased, permeate flux remains constant. This is because there is no or negligible fouling on membrane surface below the

critical flux. Membrane resistance is the dominant filtration resistance and permeate flux has a simplified form of Equation (2-1). Above critical flux, permeate flux increases with CFV until it reaches a steady state. When increasing CFV, the deposited particles migrate back to the bulk solution due to the velocity gradient in flow channel, and hence the mass coefficient increases and the thickness of the cake layer decreases both resulting in a low cake resistance.

Wakeman and Tarleton (1991) tested the influence of CFV on flux decline using calcite suspensions with two different sizes. Their data showed that the filtration flux increased with the CFVs for the particles which had a narrow particle size distribution. However, the permeate flux decreased with the CFV for the particles which had a large size distribution. They proposed that this was probably due to the particle classification at higher CFVs. In this mechanism, it was easier for the larger particles to be migrated away from the membrane surface than the smaller ones caused by the velocity gradient in the flow channel if the particle suspensions had a wide particle size distribution (Altena *et al.*, 1984). The negative effect of CFV on permeate flux was also found despite the formation of a very thin cake layer formed at a higher CFV (Mackley *et al.*, 1992). This could be explained in terms of the preferential deposition of the fine particles at the higher CFV. The resistance of the cake layer formed by the fine particles was higher than that formed by the larger particles due to the small particle size (Equation (2-8)). Li *et al.* (1998) directly observed this phenomenon using the DOTM technique. They found that the deposited particles at the high CFV were smaller than those at the low CFV while the total numbers of deposited particles at the two CFV values were almost the same.

Also, according to Darcy's law, the permeate flux depends on the resistance both of membrane ( $R_m$ ) and cake layer ( $R_c$ ), if the specific resistance of the cake layer cannot be neglected. When particle classification occurs, a thin cake layer with high cake resistance is formed by the smaller particles deposited at the high CFV. Therefore the filtration flux decreases instead even when CFV is increased.

Choi *et al.* (2005) studied the influence of crossflow velocity on the filtration of biological suspensions using MF and UF membranes but made of the same material. Their results showed that the relationships between permeate flux and CFV were linear for both MF and UF membranes, and the permeate flux was much higher for the MF membrane than for UF membrane at higher CFVs, which means increasing CFV was much more effective for MF than for UF.

On top of that, the influence of crossflow velocity diminished as the CFV went higher when there was no fouling layer at all formed under such a high tangential shear. The influence of CFV on permeate flux was dependent on the particle size and distribution of the feed suspension. Increasing CFV had no or negligible effect on the flux above a critical particle size distribution when all the particles were migrated by such a high shear rate. Below that, higher CFV produced higher permeate (Wakeman *et al.*, 1991).

#### **2.4.2 Influence of filtration pressure**

Permeate flux generally increases with filtration pressure. However in CFMF, when a cake layer forms, permeate flux is no longer proportional to TMP as described by Darcy's law (Equation (2-1)). Often, a substantial increase in TMP can produce only a small increase in flux after the critical flux has been reached. This can be ascribed to the formation of cake layers on membrane and the relationship between TMP and flux is no longer linear due to the additional cake resistance.

In constant pressure mode in CFMF, it is accepted that a high filtration pressure produces a high initial permeate flux and this permeate flux decreases to a lower steady state value in a short period of time. According to the concept of critical flux (Field *et al.*, 1995), it is possible that there exists a critical pressure below which flux decrease does not occur while above which permeate flux decreases rapidly. However, Field *et al.* (1995) found a contradictory result. In their filtrations of dodecane-water emulsion, a high pressure (0.7 bar) produced a lower flux than at a low pressure (0.4 bar) after 50 minutes filtration. In this case, the permeate flux was

not improved by the high filtration pressure. They explained that this might be due to membrane 'over-fouling' at the high pressure. The particles were deposited in the membrane pores and produced irreversible membrane fouling during the transition time. From this case one could see that when the filtration resistance increased proportionally with increasing pressure, the permeate flux did not change even when the pressure was increased.

In conclusion, permeate flux increases proportionally with TMP according to Equation (2-2) when there is no cake layer on membrane (below the critical flux) and when membrane resistance dominates filtration resistance. When operated above critical flux, particles start to deposit and a cake layer forms on membrane. Increasing driving force will be offset by a higher resistance deposit or a thicker cake (Equation (2-4)). Beyond limiting flux, permeate flux reaches its maximum whenever increasing filtration pressure (Figure 2.3). Permeate flux can be enhanced by increasing filtration pressure until cake resistance increases in proportion to the  $s$  power of transmembrane pressure (Equation (2-10)), where  $s$  is the cake compressibility and equals to 0 and 1 for incompressible and highly compressible cakes respectively.

### 2.4.3 Influence of feed concentration

Many experimental data and theoretical simulations show that permeate flux can be strongly affected by feed concentration, and permeate flux decreases with increasing feed concentration (Li *et al.*, 1998). This may be due to the higher probability of particle deposition at higher feed concentrations. The number of particles that tend to deposit on membrane is larger at a higher feed concentration for the same volume of permeation. Both the concentration polarization model (Equation (2-13)) and the SID model (Equation (2-18)) indicate the effect of bulk concentration and permeate flux decreases as feed concentration increases. Although the inertial lift model (Equation (2-21)) does not reflect the effect of concentration directly in the equation, permeate flux is inversely proportional to feed viscosity. For dilute suspensions containing particles, suspension viscosity

increases with particle concentration (Smith *et al.*, 2004). Since the viscosity is dependent on the concentration, the concentration affects the flux consequently.

An experimental study on the influence of feed concentration with latex particles was performed by Kwon *et al.* (2000). They suggested that the mechanisms of particle deposition onto the membrane might be different for low and high concentrations. At higher concentrations, the cake was observed to grow rapidly. Hence, an equilibrium flux was established more rapidly. There was also a preference for the particles bridging the membrane pores instead of plugging them at higher concentrations (Kwon *et al.*, 2000; Wakeman *et al.*, 1991). At low feed concentrations however, there might be a significant influence on the fouling resistance at a relative low concentration due to the pore plugging.

#### **2.4.4 Influence of temperature**

Operating temperature also has an effect on flux although its effect cannot be seen directly from Darcy's law. When temperature increases, filtration resistance may be unchanged but viscosity decreases and thus flux increases according to Equation (2-1). Chang *et al.* (1995) conducted experiments to study the effect of temperature on latex suspensions. The results showed that the increased temperature enhanced the permeate flux. In addition, they pointed out that the temperature of suspensions could affect the permeate flux due to the intense Brownian motion of particles at high temperature. When the Brownian motion increased, the wall concentration decreased, and hence the permeate flux increased. This effect would only occur for fine colloids (typically < 0.1 micron) where Brownian diffusion dominates the back-transport (Equations (2-11) to (2-15)). It should be noted that although operating at a higher temperature improves filtration performance, the associated higher capital investment and energy cost have to be balanced.

### 2.4.5 Influence of membrane pore size

The influence of membrane pore size on filtration rate depends on the interactions between the relative sizes of the particles to be filtered and membrane pores (Figure 2.7). The steady-state flux was found to be highest when the membrane pore size was within the same order of magnitude as the particle size (Kawakatsu *et al.*, 1993).

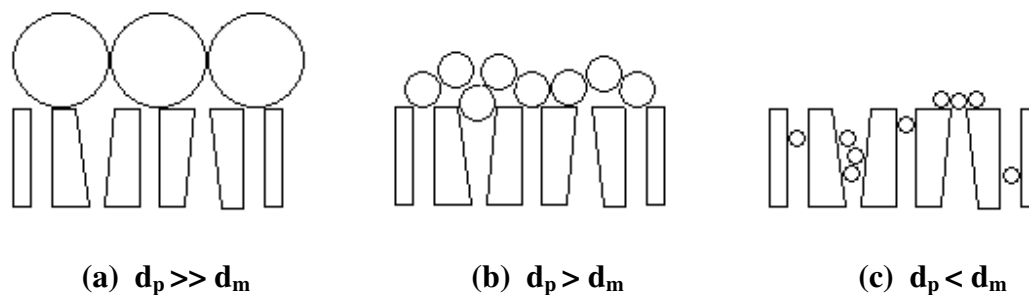


**Figure 2.7 Interactions between particles and membrane pores.**

When filtering particles that are much larger than the membrane pores, increasing the membrane pore size results in a lower membrane resistance and thus an increase in permeate flux. However, due to the higher permeate flux, cake layer grows more rapidly for membranes with a larger pore size. It should be noted that for filtration systems where particles are significantly larger than membrane pores, no or negligible internal fouling in the membrane pores occurs and thus there is limited influence of membrane pore size on flux, as observed by Kwon *et al.* (2000).

When particle sizes are slightly larger than pore sizes, the particles plug the membrane throats and a dynamic membrane forms on the membrane surface with a low voidage. In this situation, the resistance of the cake layer is the controlling reason for the flux decline. Thus increasing membrane pore sizes does not have a great effect on permeate flux.

In the case when particle sizes are smaller than membrane pores, permeate flux and quality are usually low. Some particles will penetrate the membrane pores or together plug the pores. The permeate flux will be eventually controlled by the



formation of a thin cake layer which has a low voidage. The permeate flux is influenced by both membrane pore plugging and fouling layers, rather than the cake layer formation only.

It can be concluded that it is the interactions between larger membrane pores and smaller particles in feed solutions that control the filtration performance in CFMF. Thus it is a good tip when choosing a membrane that the membrane pores should be small enough to prevent particles plugging the membrane pores internally and also large and numerous enough so that a low membrane resistance can be achieved. This requires detailed knowledge on the feed particle size distribution.

#### **2.4.6 Influence of surface charge**

It was found that permeate flux and membrane fouling were also dependent on the charges of membrane and particle surfaces (Childress *et al.*, 1996; Nazzal *et al.*, 1994). The influence of membrane surface charges is to repel ions of the same charge or attract particles with the opposite charge. An electrical double layer forms between membrane surfaces and electrolyte solutions. According to the DLVO theory, the net forces between two charged surfaces are the sum of the attractive van der Waals forces and the repulsive electric double layer forces. However, in some cases it was found that the membrane zeta potential played only a relatively minor role in the permeate flux even when the membrane charge was changed from negative to positive (Huisman *et al.*, 1999).

The measurement of electrical potentials is called zeta potential ( $\zeta$ , mV). Tests on the influence of zeta potentials of feed solutions on microfiltration could be conducted by altering pH values or electrolyte concentrations of the solutions to be filtered. It was found that increasing the zeta potential by controlling the pH or by decreasing the electrolyte concentration would increase the permeate flux (Nazzal *et al.*, 1994). This could be explained by the double layer repulsion force. Double layer thickness and repulsion force increase when zeta potential increases. High repulsion force prevents the particles in cake layers from getting close to each other.

Thus permeate flux increases are ascribed to the high voidage of the cake layer (Figure 2.8). However, in the case of particles aggregating at low zeta potentials ( $\pm 10$  mV), the particles become larger and this also results in permeate flux increases due to the influence of 'particle size' on cake resistance. McDonogh *et al.* (1989) showed this experimentally and theoretically.

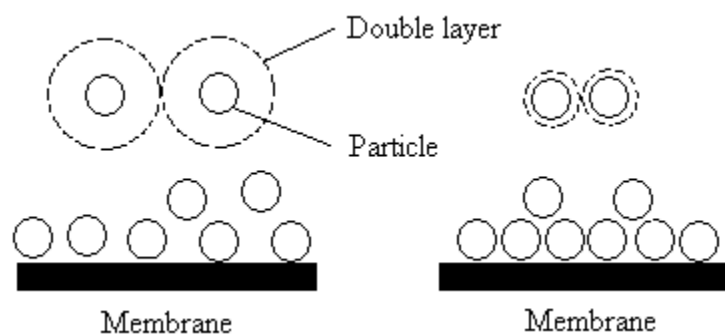


**Figure 2.8** A schematic diagram of the effect of the double layer thickness on cake layer structure.

It should be pointed out that the zeta potential values of many membranes might be influenced by the pH of the feed solutions. In some cases, the influence of the zeta potential of membrane surfaces and particle surfaces has to be considered together.

#### **2.4.7 Influence of particle size and particle size distribution**

Theoretical models based on the Carman-Kozeny equation and more recently developed by Bacchin *et al.* (2004) suggest that permeate flux depends strongly on particle size. Generally, an increase in particle size can produce a higher permeate flux. This is because of the fact that the lateral lift velocity and the shear-induced diffusion increase as the particle size is increased according to the theoretical analyses (Equations (2-18) and (2-21)). Large particles are more easily migrated away from membrane surface. As a result, cake thickness decreases with increasing particle size or the cake layer has a high porosity, and thus a higher permeate flux is achievable for suspensions containing larger particles with uniform or narrow distribution sizes.

Figure 2.9 shows the predicted fluxes of mono-disperse suspensions as a function of particle size according to three dominant back transport mechanisms, Brownian diffusion (Equation (2-15)), shear-induced diffusion (Equation (2-18)) and inertial lift (Equation (2-21)). From this figure, it can be seen that the Brownian diffusion is dominant for small particles and the inertial lift is important to large particles. The shear-induced diffusion is important for median particles with diameters in the range of 0.5 to 30  $\mu\text{m}$ . Since MF is often used to separate the particles in the range of 0.02 to 20  $\mu\text{m}$ , the shear-induced diffusion is the dominant back transport for particles in this size range. It is not hard to see that permeate flux increases with particle size according to the shear-induced diffusion model in MF. It is also evident that there is a minimum flux for particles around 0.2 to 0.5  $\mu\text{m}$ .

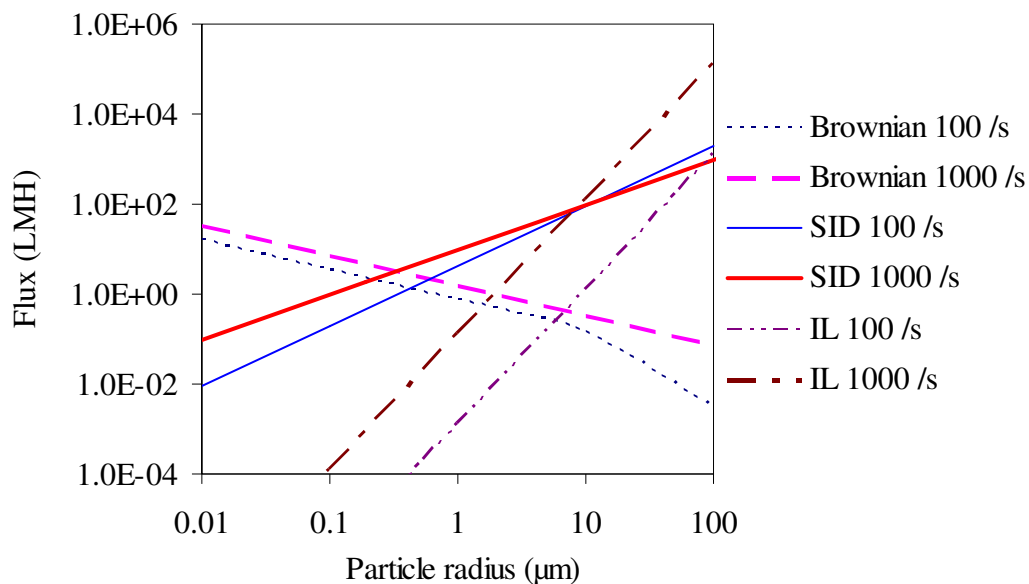


**Figure 2.9** Permeate flux vs. particle radius in CFMF according to three back transport mechanisms. Brownian diffusion (Brownian) (Equation (2-15)), Shear-induced diffusion (SID) (Equation (2-18)) and Inertial lift (IL) (Equation (2-21)). Conditions:  $L = 0.11 \text{ m}$ ,  $\phi_b = 0.0005$ ,  $\phi_w = 0.6$ ,  $\gamma_o = 100 \text{ s}^{-1}$  (lower lines) or  $1000 \text{ s}^{-1}$  (upper lines), Boltzmann's constant  $K = 1.38\text{e-}23 \text{ J/molK}$ ,  $T = 293 \text{ K}$ ,  $\mu = 0.001 \text{ kg/m}$ , and  $\rho_o = 1,000 \text{ kg/m}^3$ .

For mixed suspensions containing particles with a wide particle size distribution, the scenario will be different. Cake layers formed on membrane surface are often of different structures and compositions. For the feed suspensions containing a high proportion of large particles, the fine particles in the suspensions introduce a classification effect and deposit selectively on the membrane surface. It was reported that when operated at a high crossflow velocity, the composition of the cake layer on the membrane surface consisted mainly of small particles (Li *et al.*, 1998). According to the SID model (Equation (2-18)), the permeate flux is proportional to four-third power of the particle size. For an imposed flux, when shear rate is increased the deposited particles should be preferentially smaller accordingly. Thus, the small particles in a mixed system deposit first at a high crossflow velocity.

It was found that the permeate flux actually decreased with increasing the crossflow velocity for the mixed feed of calcite containing more large particles (Wakeman *et al.*, 1991). This might be due to the different structure and composition of the cake layers formed under relatively high and low crossflow velocities.

For feed suspensions containing a high proportion of small particles, the resistance of the cake layer is very high and increasing crossflow velocity has a greater effect on decreasing cake thickness rather than on increasing cake resistance. The high resistance of the cake layer formed by small particles can be explained by the specific resistance in the Carman-Kozeny equation (Equation (2-8)). The resistance of the cake layer increases with decreasing particle size and cake porosity.

Chang *et al.* (1996) investigated the effect of particle size distribution on microfiltration by mixing two and three different sizes of latex particles. One of their interesting results showed that the large particles were beneficial to the permeate flux if all the components were larger than the membrane pore size, and the larger particles were not beneficial to the permeate flux when the small particles were smaller than the membrane pore size.

The preliminary work showed that smaller particles in mixed feeds were predominantly responsible for membrane fouling and thus for flux decline. However, a question that has not been addressed in the previous work is whether critical fluxes in a mixture are the same as the critical fluxes of mono-sized particles. This question is to be addressed in this thesis.

#### **2.4.8 Influence of particle shape**

Particle shape is found to have an effect on the equilibrium flux due to the different structure of the cake layer formed on membrane surface. The differences in particle shape may lead to different mechanisms of membrane fouling.

Connell *et al.* (1998; 1999) studied the effect of particle shape on permeate flux. They used particles of glass beads, silica, silt, carbon and aluminium with similar density and size distribution to study the effect of particle shape on crossflow filtration flux. In their study, the particle shapes were characterized by a particle size analyzer and were confirmed by scanning electron microscope (SEM) images. The results showed that the glass beads had a spherical shape and the silica had a roughly spherical shape with rough irregular edges. The silt was described to be angular while the carbon was branched and the aluminum was platelet shaped. In order to eliminate other factors, particle surface charges were also measured. Most of the particles had similar zeta potentials of about  $-20$  mV. The difference in the surface charge was regarded as negligible due to the relatively large particle size. They found that highly irregular-shaped particles such as the branched carbon particles had the highest flux. The SEM image showed that these particles deposited on the membrane surface and formed a bridging structured cake layer. The platelet aluminium particles gave higher flux than expected due to the substantial space between the platelet particles. Since this type of particle could bridge themselves far from each other, the cake layer had a high voidage and thus gave a low filtration resistance. Increasing pressure produced an increased flux due to the less compressible bridging cake structure, and since highly irregular particles formed a cake layer with low compressibility, the filtration resistance was dominated by the

membrane resistance and internal fouling rather than the cake resistance. Increasing crossflow velocity or decreasing feed concentration had a minimal effect on improving the filtration rate. A thinner cake layer with low specific resistance would not help the filtration rate significantly. The more regularly shaped glass beads produced a relatively low flux due to the organized cake structure. More regularly shaped particles such as spheres tended to form a more compact structure since they could pile closer together. In Connell's experiments (1998; 1999), the flux decreased with decreasing CFV, increasing pressure and feed concentration. The operating parameters had more significant effects especially on small regularly shaped particles because of their higher tendency for plugging the membrane pores. However, previous work did not examine the effect of particle shape on the critical flux.

As described earlier in Section 2.4.7, critical flux increases with particle size due to the effect of shear-induced diffusion. It can be anticipated that the shear-induced effect would also vary with particle shape, particularly with fractal dimension (see Section 2.5.3). This topic is also to be addressed in this thesis.

## **2.5 Flocculation of particles**

Coagulation/flocculation of particles is often performed as a pre-treatment of microfiltration processes in order to achieve enhanced permeate flux. The alterations in particle size distribution contribute to the improvement in permeate flux. Flocculated feeds usually have a wider particle size distribution than unaggregated feeds. Moreover, aggregated particles are typically irregular in shape and have porous structures (characterized as "fractal dimension"). The fractal properties probably have an influence on the critical flux during tangential flow filtration. This section outlines the relevant flocculation theories as well as the fractal concept as a background to the component of work in this thesis on filtration of flocs.

### 2.5.1 Introduction to flocculation

It is well known that colloidal particles in water are often too fine to be removed by conventional water treatment methods without any assistance of other pretreatment processes. Flocculation/coagulation is a physicochemical process during which fine particles agglomerate to form large flocs that are much easier to be separated from liquid-solid systems. Hence, flocculation/coagulation of particles is frequently conducted as a pretreatment to sedimentation or separation to separate these fine colloidal particles in order to fulfill the ever more stringent requirements in water and wastewater treatment. The enhancement of microfiltration with flocculation are reported in the literature (Kim *et al.*, 2001; Mietton *et al.*, 1992).

The terms “flocculation” and “coagulation” are often confused. They are two essential but not necessarily independent steps in water and wastewater treatment processes. It is accepted that flocculation is the aggregation of particles by the addition of polymeric substances to reduce the repulsive forces between particles. The purpose of a polymeric flocculant is to bridge the neutralized coagulated particles into larger flocs. Coagulation can be accomplished by adding inorganic salts for the same purpose. In fact, “flocculation” and “coagulation” are widely used without discrimination in colloidal chemistry (Lee, 2003). In this study, the terminologies “flocculation/flocculant” and “coagulation/coagulant” are used interchangeably and refer to particle aggregation.

Flocculation is a critical step in many solid-liquid separation processes. In practice, it can be achieved by changing the pH value of solutions or changing the concentration of existing ions in the solution in order to reduce the zeta potential ( $\zeta$ ) of the colloidal particles. Counter ions with a higher charge are commonly added to achieve this effect. Inorganic salts containing  $\text{Al}^{3+}$ ,  $\text{Fe}^{2+}$ ,  $\text{Fe}^{3+}$  and  $\text{Ca}^{2+}$  are often used in aggregation of fine particles. Polymers, polyelectrolytes and surfactants are also used both as flocculants and dispersants. Blending or mixing is often used to disperse the flocculants and thus accelerate the flocculation process.

### 2.5.2 Mechanisms of flocculation

The flocculation process has been widely studied both theoretically and experimentally. Aggregations of fine particles in aqueous suspensions can be achieved by flocculation. In order to accomplish flocculation, particle collision and particle attachment are necessary. Flocculation of particles can be influenced by a number of factors, namely pH, turbidity, concentration, temperature, duration and strength of stirring, as well as the characteristics of flocculants. However, the mechanisms of flocculation and the significance of the various factors affecting flocculation rate are still not very clear.

In aqueous suspensions, particles frequently interact with one another because of Brownian motions and particle motions due to fluid velocity gradients. When the inter-particle collisions occur due to Brownian motions, perikinetic flocculation happens. The initial perikinetic flocculation rate can be described as the change of particles in the total concentration ( $J_B$ ) (Yusa, 1977):

$$J_B = -\frac{4\eta K T c^2}{3\mu} \quad (2-22)$$

where  $\eta$  is a collision efficiency factor,  $K$  is the Boltzmann's constant,  $T$  is the absolute temperature,  $c$  is the total concentration of particles in the suspension and  $\mu$  is the fluid viscosity.

In addition, settling particles may collide due to the differences in settling velocities of the particles of different size and density. Due to the intense collisions between the particles, the attachment of the particles occurs due to the attractive forces between them. When the inter-particle collisions are induced by the velocity gradients produced, such as by stirring, this flocculation process is termed as orthokinetic flocculation. The initial flocculation rate ( $J_G$ ) of mono-disperse



suspensions containing primary particles depends on velocity gradients according to Yusa (1977):

$$J_G = -\frac{2\eta\Gamma d^3 c^2}{3} \quad (2-23)$$

where  $\Gamma$  is the velocity gradient(s) and  $d$  is the diameter of colloidal particles.

Flocculation of particles can be accomplished by various mechanisms, such as approaching to iso-electric point (IEP) by pH adjustment, electrical double layer compression by electrolyte addition, electrostatic interaction with inorganic coagulants, hydrophobic interaction with surfactants, polymer bridging with polymeric flocculants and coagulants, charge-patch neutralization and depletion effects, *etc.* Note that more than one mechanism may take effect at the same time during the flocculation processes, depending on the nature of particle surfaces.

### 2.5.3 Fractal concept

Since the introduction of fractal geometry by Mandelbrot in 1977, the concept of fractals has been used increasingly in floc structure studies (Chakraborti, 2003). The fractal dimension ( $d_F$ ) is one of the most important parameters in fractal geometry. It is a non-integral value describing the space filling capacity of a fractal object. In three-dimensional space, the fractal dimensions of a straight line, sheet and compact sphere or totally compact object are 1.0, 2.0 and 3.0 respectively. Salt-induced perikinetic coagulation and polymer-induced bridging flocculation are the most commonly used mechanisms in industry. The fractal dimensions for these two cases range from 1.75 to 2.1 and 1.7 to 2.5 respectively (Yan *et al.*, 2000). The effect of the floc porous structure could be seen from the permeability of fluid passing through and the drag force of fluid on flocs. Chellam *et al.* (1993) studied the fluid flow mechanisms for fractal aggregates and found that as the fractal dimension

decreased, the permeability increased and thus the drag force on the flocs decreased (Figure 2.10).

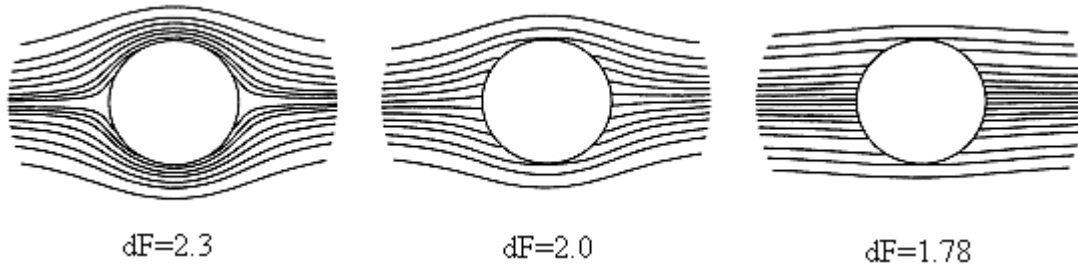


**Figure 2.10** Streamlines of creeping flow in the neighborhood of a porous sphere (Chellam *et al.*, 1993).

The classic Euclidean geometry assumes that the properties of a compact spherical object follow a power law relationship, *i.e.*

$$A_{sphere} = \frac{1}{4} \pi d^2 \quad (2-24)$$

$$V_{sphere} = \frac{1}{6} \pi d^3 \quad (2-25)$$

Equation (2-25) shows that the volume of an object is in a power of three of the diameter. However, most of the real objects do not follow the Euclidean geometry due to their amorphous shape. Similarly in the fractal geometry, the volume of an amorphous object could be expressed in a power relationship (Meakin, 1987). Usually, the exponent is a non-integer digit and less than 3 and this exponent is defined as the fractal dimension.

One of the interests of this study is the effect of floc structure, as characterized by fractal dimension, on the observed critical flux. This has not been reported before. It is anticipated that there will be a relationship of the form:

$$J_{crit} = f(d_{Floc}, d_F, \gamma, \text{etc.})$$

where  $J_{crit}$  is dependent not only on size and shear rate, but also on floc shape, characterized by fractal dimension.

Among the methods of measuring fractal dimension (image analysis, settling velocity data and light scattering), light scattering is widely used compared with the other two methods which are time consuming. In the light scattering theory, scattered light intensity and fractal dimension have the relationship:

$$I(Q) \propto Q^{-d_F} \quad (2-26)$$

where  $d_F$  is the fractal dimension,  $Q$  is the scattering vector quantity and  $I(Q)$  is the intensity of scattered light at a certain angle. Thus a log-log plot of  $I$  vs.  $Q$  provides a measure of  $d_F$  from the slope of the plot (details are available in Section 3.3.1).

#### 2.5.4 Properties of floc

Depending on the applications, different measurements are employed to evaluate the flocculation efficiency, such as flocs settling rate, percentage of solids settled, sediment volume/weight, moisture content and flocs strength, as well as viscosity and turbidity of suspensions. However, these parameters only reflect the flocculation effectiveness indirectly. Since flocculation is an aggregation process of fine particles, the most proper and direct reflection should be floc size distribution. Floc structure is also an important parameter reflecting the compressibility of cake layer formed in MF. In this study, floc size and size distribution are to be measured using the light scattering theory to determine the flocculation efficiency and the fractal dimension of flocs is used to describe the floc structure.

## **2.6 Topics of interest for further study**

Crossflow microfiltration has been increasingly employed for the solid-liquid separation purpose due to the ability of cake controlling. However, the fouling mechanisms have not been fully understood and the optimum operating conditions are yet to be disclosed. The difficulty lies in the fact that numerous factors influencing the filtration rate are involved during the fouling process. In addition, it is still unclear on the fluid flow complexion in the region adjacent to membrane surface. Theoretical models have been greatly developed to predict permeate flux of crossflow microfiltration. However, almost all the mathematical models are only applicable to model particles which are incompressible, spherical and with uniform sizes. Seldom attention has been paid to complicated suspensions. They could be mixtures with a single species with a wide size distribution or even different species. The particulates contained could have different shapes and inner porous structures as characterized in terms of fractal dimension.

The problems stated above are of interest in this thesis. The experimental results addressing these problems will be presented in the following chapters and brief reviews in the literature are also provided on the corresponding topics. Some knowledge in the literature on the hydrodynamics in the closed flow channel and particle sedimentation in terms of fractal dimension as well as the fluid flow through the porous particles will be helpful to this study.

## Chapter 3 Materials and methodology

### 3.1 Experimental approaches

Many techniques have been developed to study the mechanisms of membrane fouling. Among these techniques, the most direct method to observe particle deposition and the interactions between particle and membrane is visualization using optical instruments. The DOTM technique is one of the first applications of optical techniques to observe particle deposition on membrane developed by Li *et al.* (1998). The experimental rigs used in this study were built according to the DOTM set-up in the University of New South Wales (UNSW) in Australia.

Some modifications were introduced (Figure 3.1) in this study. The original DOTM set-up used a television camera to transfer the observing view to a black and white TV monitor for live preview and utilized a super-VHS video recorder for taping. The images of interest were then post captured using editing software. In the current setup, the observation is viewed via a digital CCD camera which is connected directly to a PC. The images can be captured at pre-determined time intervals and stored in the PC and the preview is available simultaneously. The captured images have true color and high resolution. Image analysis can be carried out easily (Section 3.3.5).

The dimensions of the membrane cell were also modified in order to use a microscopic objective with a higher magnification but inevitably with a small working distance. The permeate flow channel height was reduced to make the objective as close as possible to the membrane in the cell. The glass in the observation hole was replaced by a piece of optical glass with a lower refractive index to reduce focusing distance. Both of the modifications made the use of the objective possible. A digital peristaltic pump was introduced into the permeate line allowing inching adjustment in flux stepping which made the measured critical flux more precise.

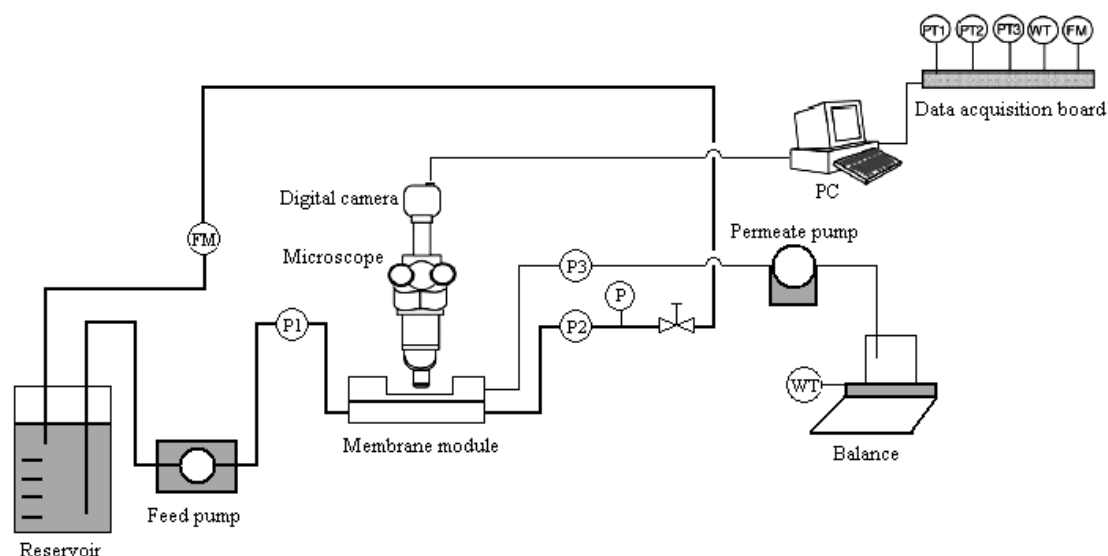


**Figure 3.1 Filtration set-up including DOTM facilities. P1, P2 and P3 denote pressure transducers. FM denotes flowmeter. WT denotes electric balance.**

The membrane module used in the DOTM was a crucial component as it had to be as transparent as the membrane. A membrane module was specially designed and fabricated from perspex to allow the transmission of light (Figure 3.2). The membrane module consisted of two parts, permeate channel and feed channel, with a transparent membrane in between. An observation window in the permeate half allowed the objective to move close to the membrane in the module. A piece of thin optical glass was used for the window. The gasket in the feed channel half prevented any leakage and held the pressure in the flow channel. The feed flow channel was 110 mm in length, 40 mm in width and 2 mm in height. A perforated plate with 3 mm holes made of stainless steel was placed in the permeate channel to support the membrane preventing membrane breakage. An objective lens with 32 times magnification (Carl Zeiss, Germany) could be mounted on the permeate side of the module. Another two objectives with 10x and 20x magnifications were also available for observing larger particles. The images observed by the microscope (Axiolab Zeiss, Carl Zeiss, Germany) could be viewed via a digital camera (MicroPublisher 5.0 RTV, QImaging, Canada) and previewed on a computer monitor.

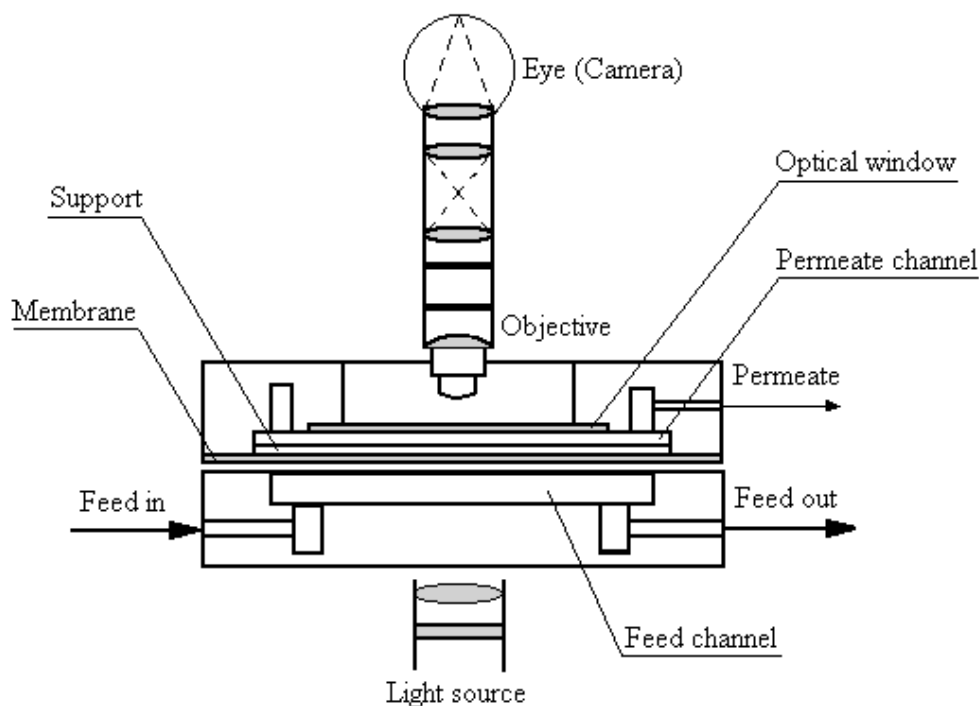


**Figure 3.2 Schematic of the membrane module.**

To make the observation possible and to avoid the turbidity of feed solutions, the feed channel was fabricated as the lower part, which means the feed solution flowed below the membrane, and the gravity force on the particles was opposite to that due to convection by the permeate flow. However, this effect was theoretically proven (for the particles of interest) to be negligible (Li *et al.*, 2000). In addition, the latex and yeast particles had a density similar with water, making them almost neutrally buoyant.

It should be noted that a potential limitation of the DOTM technique was that when the observation area was totally covered by a single fouling layer, individual particle in the following layers could not be seen clearly because of the lack of light transmission. The DOTM could only distinguish the second layer due to the different darkness. In addition, due to the limitation in the magnification, particles only larger than 1  $\mu\text{m}$  could be observed clearly by the DOTM. Particles smaller than 1  $\mu\text{m}$  had to be fluorescent-dyed in order to make them distinguishable.

## 3.2 Experimental materials

### 3.2.1 Polystyrene latex particles

Polystyrene latex particles are one of the mostly used model colloidal particles for membrane fouling mechanism studies in microfiltration and ultrafiltration processes. They have several advantages which are well-suited for fouling studies, such as their stability in solution, neutral buoyancy, spherical shape and narrow particle size distribution. Particle sizes ranging from 100 nm to 10  $\mu\text{m}$  were used in previous studies (Blake *et al.*, 1992; Li *et al.*, 1998).

Micro particles based on polystyrene (Fluka, Sigma-Aldrich, U.S.A.) which are commonly called latex particles, were used as the model particles in this study. Polystyrene latex beads were negatively charge-stabilized colloidal particles. Latex beads were produced by the polymerization of styrene under conditions that induced spontaneous coalescence bead formation. Normally they were supplied as aqueous suspensions with a solids content of 10% with a similar density ( $1.05 \times 10^3 \text{ kg/m}^3$ ) to pure water, and consisted mainly of the polymer particles and water, with small amounts of surfactant, sodium bicarbonate and potassium sulfate.

The 3.0 and 5.0  $\mu\text{m}$  latex particles used in this study had a standard deviation no larger than 0.1  $\mu\text{m}$ , and the 10.0  $\mu\text{m}$  latex particles had a standard deviation no larger than 0.2  $\mu\text{m}$ . Latex suspension with a specified concentration was diluted and re-dispersed in MilliQ<sup>®</sup> water to make a feed solution for filtration. The solution pH was adjusted using 0.1 molar acid or alkaline solutions. The salinity was controlled by introducing sodium chloride to the solutions. Latex particles larger than 0.6  $\mu\text{m}$  tended to settle down slowly in the suspensions. Thus, the prepared feed suspensions were stirred continuously using a magnetic stirring bar in this study. The latex supplies and reused suspensions were stored in a refrigerator at 4 °C for sterilization.



### 3.2.2 Washed baker's yeast

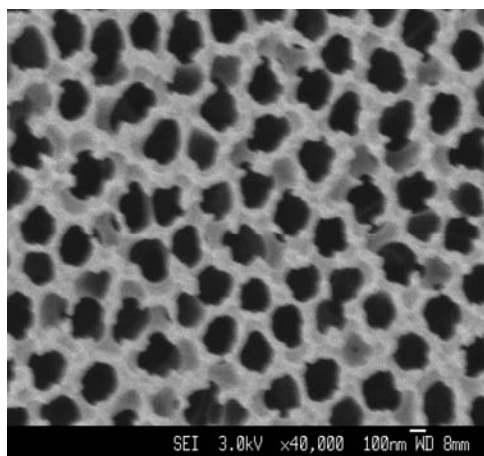
Yeast is another type of model particle which was often used in microfiltration studies (Field *et al.*, 1995; Howell *et al.*, 1993). Proteins extracted from yeast were also used to study protein fouling and adsorption (Richard Bowen *et al.*, 1993). Unlike latex suspensions, yeast suspensions were usually selected as the substitute for bio-suspensions to study microbial fouling in microfiltration. Yeast cells were not as spherical as latex particles. However, its elliptic shape was often regarded approximately as spherical.

Baker's yeast (*Saccharomices cerevisiae*) was used in this study. In order to keep the yeast properties constant, only one product of yeast (Saf-instant, France) was used to prepare the yeast suspensions. The yeast powder was washed before use to remove the extra-cellular polymeric substances (EPS) attached to the yeast cells. The washing process was similar to the work by Mores *et al.* (2001). 0.25 gram of powder with 50 ml MilliQ<sup>®</sup> water was mixed in a 50 ml centrifuge tube and then centrifuged at 2500 rpm for 10 minutes. The supernatant liquor was discarded before the yeast was re-dispersed in 50 ml fresh MilliQ<sup>®</sup> water and centrifuged again. This washing procedure was repeated three times before a yeast suspension was ready. Some of the mass would be lost during washing. The washed yeast was dried at a temperature of 105 °C for 24 hours to calculate the loss in weight. The loss of mass was about 30 % after washing and only 70 % of the final product was re-dispersed to make the feed solution. The particle size distribution was quantified by Malven Mastersizer (Section 3.3.1), and the distribution showed a mean size ( $d_{50}$ ) around 5.0  $\mu\text{m}$  with a narrow distribution. Fresh yeast suspensions were prepared for each run just before the filtration and discarded within 4 hours to prevent any fermentation.

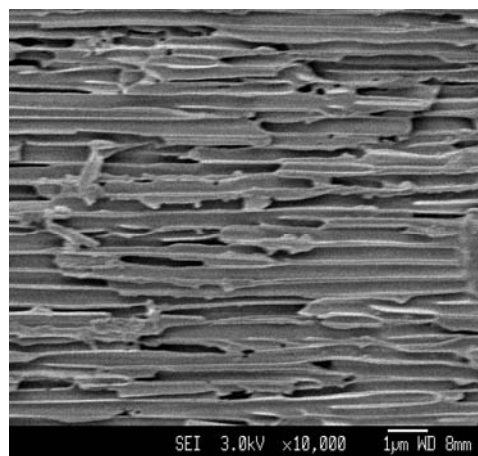
### 3.2.3 Membranes for filtration experiments

The selection of membrane was the key to this study. The membrane to be used in the DOTM had to be transparent to allow light transmission. The Anopore inorganic

membrane (Anodisc, Whatman, UK) fulfilled this requirement. It had a high pore density (25-50%), and was highly hydrophilic. However, due to the nature of its material, it tended to crack easily. Therefore, the applied pressure on the membrane could not be too high. Anopore membranes could not endure strong and frequent pulsations caused by pumping or pressure fluctuations. The field emission scanning electron microscopy (FESEM) images of the Anopore membrane are shown in Figure 3.3. According to the front view in Figure 3.3 (a), the Anodisc had a narrow pore size distribution. Additional specifications on the Anopore membranes are listed in Table 3.1. This product was available in three pore sizes (0.02, 0.1 and 0.2  $\mu\text{m}$ ). Anodisc 47 (Cat. N0. 6809-5022) with a pore size 0.2  $\mu\text{m}$  and 47 mm in diameter was used in all of the experiments in this study. From the cross-sectional image (Figure 3.3 (b)), this kind of membrane had a very low pore tortuosity. The membranes were visually transparent when wet because the non-deformable honeycomb pore structure allowed the transmission of light. This property made the observation under a regular lab microscope possible.



(a) Front



(b) Cross section

**Figure 3.3 FESEM images of Anopore membrane.**

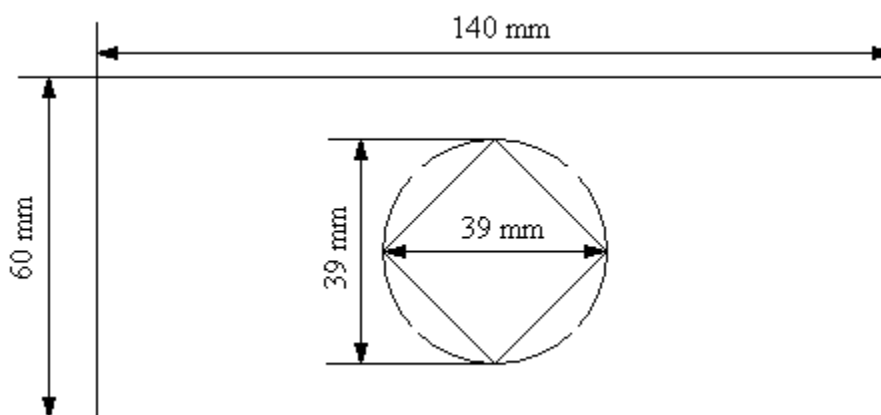
The permeability of the membrane was experimentally determined by measuring the TMP with a range of permeate flux steps using MilliQ<sup>®</sup> water. Following the Hagen-Poiseuille equation (Equation (2-6)), the permeability of the membrane was calculated to be  $96.0 \pm 3.8 \text{ l/m}^2 \cdot \text{h} \cdot \text{kPa}$ .

**Table 3.1 Specifications of the Anopore inorganic membrane**

| Material          | Pore size<br>( $\mu\text{m}$ ) | Thickness<br>( $\mu\text{m}$ ) | Porosity<br>% | Hydrophilic | Protein<br>binding | Strength<br>(psi) |
|-------------------|--------------------------------|--------------------------------|---------------|-------------|--------------------|-------------------|
| Aluminum<br>oxide | 0.2                            | 60                             | 25-50         | Yes         | Low                | 65-110            |

Due to its fragility, the Anopore membrane had to be handled with care before it could be used in the membrane cell. Two templates made from printing paper were used to hold the membrane (Figure 3.4). The circle indicates where the membrane was glued. A 28.3 x 28.3mm square ( $8 \times 10^{-4} \text{ m}^2$ ) was removed as the working area. Each side of the template was applied with a thin layer of glue using a spatula. The membrane was glued between the two halves of the template using a slow drying araldite (Huntsman, UK). The finished membranes with templates were pressed under weight over night until the glue was dry. The finished membranes were stored in a refrigerator to prevent contamination.

The working square was placed as a diamond instead of a rectangle. This was because the particles in the feed could be stopped at the edge of the template paper since the thickness of the printing paper (100  $\mu\text{m}$ ) was much higher than the particles used in this study (10  $\mu\text{m}$ , the biggest particles used). The effect of retained particles was reduced in the diamond configuration as shown in Figure 3.4.

**Figure 3.4 Membrane template.**

### 3.3 Analysis and measurements

#### 3.3.1 Particle size distribution and fractal dimension

Both particle size distribution and fractal dimension were measured by Malvern Mastersizer 2000 (Malvern Instruments Ltd, UK). The Mastersizer 2000 is a particle size analyzer using low angle laser light scattering as well as wide angle laser light scattering and back scattering to determine particle size distributions. It allowed measurements of a broad particle size range from 0.02 to 2,000 microns. When floc particles were analyzed, their fractal dimensions could be calculated by a separate Excel spreadsheet using the data obtained from Mastersizer.

The whole system consisted of an optical unit, a combination of one or more sample dispersion units (Hydro 2000 SM was used in this study), a color printer and a computer running the Mastersizer 2000 software (Figure. 3.5).

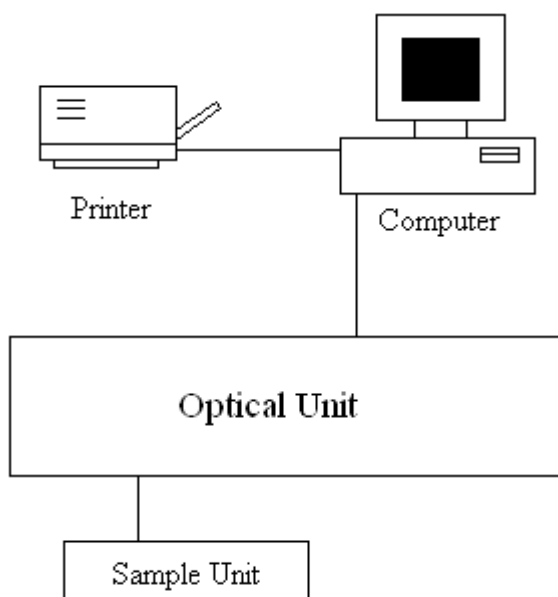


**Figure 3.5 Overview of the Mastersizer system components.**

The optical unit comprised a helium neon laser light producer, a Fourier lens, a sample cell, a number of photosensitive detectors (back scatter detectors, large angle detectors and forward angle detectors) and a focal plane (Figure. 3.6).

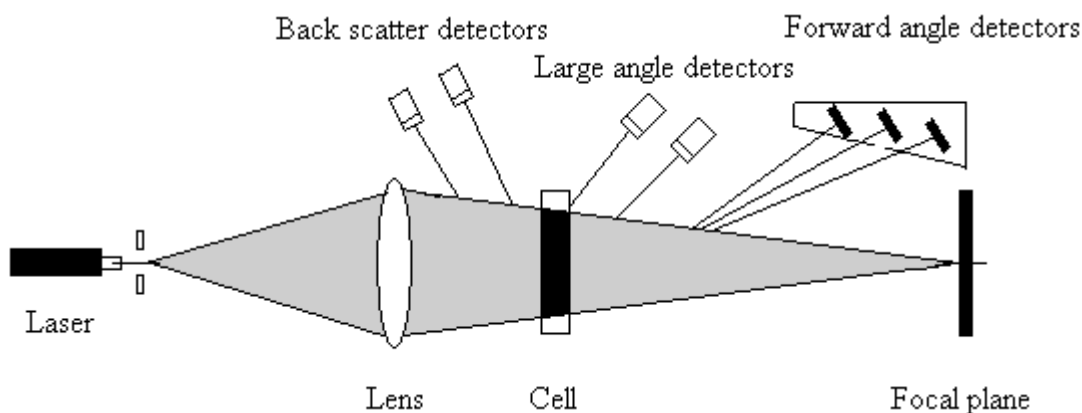


**Figure 3.6 Optical unit array schematic-top view.**

The particle size distribution was calculated from the scattered light intensity obtained from the detectors in the optical unit using the Malvern software installed in the computer. The calculation was based on one of light scattering theories (Mie theory) assuming that 100% of the volume lies within the measurable range. The volume median diameter,  $D(v,0.5)$ , (50 percentile of the particle size is above this value) was used to describe the result instead of number, surface area or length scale size distributions.

To compute the fractal dimension, the raw data were exported into a specially designed Excel spreadsheet to obtain the scattering intensities and the corresponding light angles measured by each light detector. The exported data were then automatically plotted into a  $\log(\text{Intensity})$  (Y axis) vs.  $\log(\text{Angle})$  (X axis) plot (Figure. 3.7) (Equation (2-26)), and a slope and R-squared number were determined using the Excel trendline function. The slope value that had the highest R-squared number was taken as the fractal dimension.

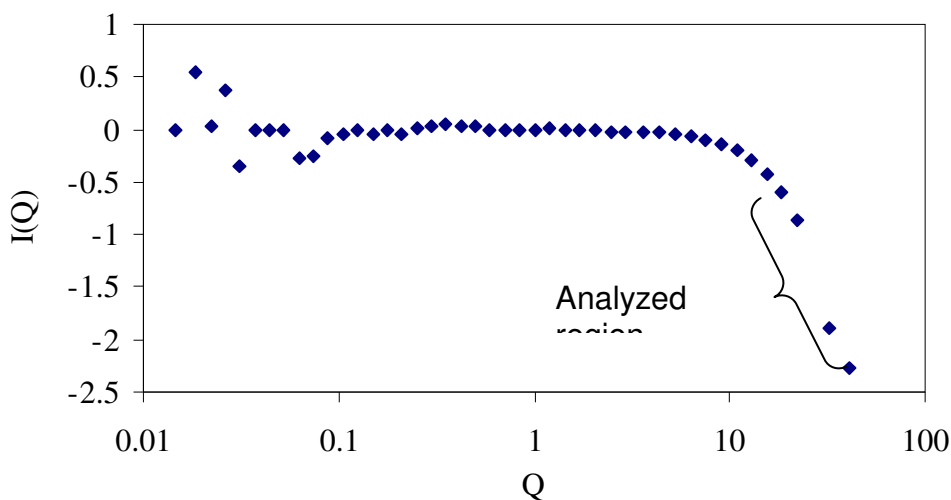


**Figure 3.7** A typical plot of  $\log(\text{Intensity})$  vs.  $\log(\text{Angle})$  from a measurement of hematite floc for the determination of fractal dimension.

### 3.3.2 pH measurement

0.1 molar of hydrochloric acid and sodium hydroxide solutions were used to adjust the pH of all the solutions and suspensions in the filtration and flocculation experiments. The pH values were monitored using a portable pH meter (SevenGo<sup>TM</sup>, Mettler Toledo, US).

### 3.3.3 Particle surface charge

Dispersed particles in suspensions acquire an electrical charge which is balanced by counter ions in the electrolyte solution. Hence, there exists a potential difference between the particle surface and the electrolyte solution. This potential is the so-called zeta potential ( $\zeta$ , mV), and can be determined by measuring the particle electrophoretic mobility. The value of zeta potential depends on the electrolyte pH and also on the solution ionic strength. The zeta potentials of the particles (latex and yeast) used in this study were measured at various pH values in an electrolyte of 1 millimolar KCl. The ZetaPALS, Zeta Potential Analyzer (Brookhaven, USA) was used for the determination of the particle surface charge.

Figure 3.8 is a summary of the zeta potential measurements for the three sizes of latex particles used in this project. The error bar shows the standard deviation of three repeated measurements. As shown in this figure, the iso-electric point (IEP) of these particles was around pH 3.

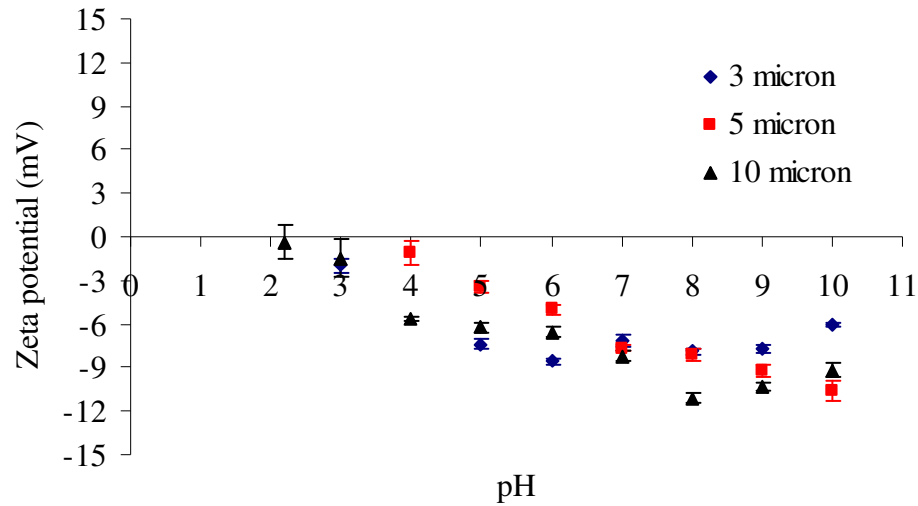


**Figure 3.8 Zeta potential of latex particles.**

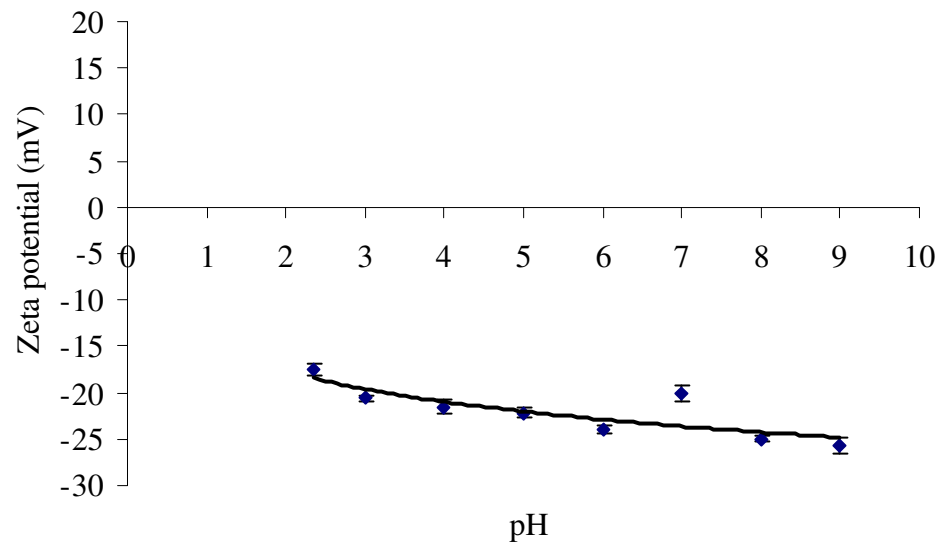


**Figure 3.9 Zeta potential of washed baker's yeast.**

Figure 3.9 shows the results of the zeta potential for washed baker's yeast which were negative over a wide range of pH values. The IEP of yeast cells was reported as pH 3 in the literature (Kang *et al.*, 2004).

### 3.3.4 Membrane surface charge

The zeta potential ( $\zeta$ , mV) of the Anopore membrane was determined at various pH values in an electrolyte of 1 millimolar KCl. The measurements were conducted using the Electro Kinetic Analyzer (EKA) (Anton Paar, Austria). The clamping cell was used for the determination of the zeta potential due to the small sample area available. Due to the construction of the clamping cell, the zeta potential measured by the analyzer was actually a sum surface charge between a plate made of polymethyl methacrylate (PMMA) and the sample,

$$\zeta_{total} = \frac{1}{2}\zeta_{PMMA} + \frac{1}{2}\zeta_{Sample} \quad (3.1)$$

where  $\zeta_{total}$  is the sum zeta potential which was measured by the analyzer,  $\zeta_{PMMA}$  is the zeta potential of the PMMA plate and  $\zeta_{Sample}$  is the net zeta potential of the sample, which should be calculated using the relationship,

$$\zeta_{Sample} = 2\zeta_{total} - \zeta_{PMMA} \quad (3.2)$$

Figures 3.10-3.12 summarize the zeta potential measurements. The results shown in Figures 3.10 and 3.11 are the average of three runs and the error bars show the standard deviations. The net zeta potential of the membrane calculated according to Equation (3.2) is shown in Figure 3.12 where the iso-electric point (IEP) could be determined to be about pH 8. This result was in good agreement with other study (Knutsen *et al.*, 2006). Knutsen *et al.* (2006) measured the zeta potential of the Anodisc membrane in 10 millimolar KCl and showed that the IEP of both the 0.2 and 0.02  $\mu\text{m}$  membranes was at pH 8. These results were also similar to those reported in the literature for  $\text{Al}_2\text{O}_3$  particles which had an IEP of pH 9 as expected since the Anodisc membranes were made of anodized aluminum (Moosemiller *et al.*, 1989).



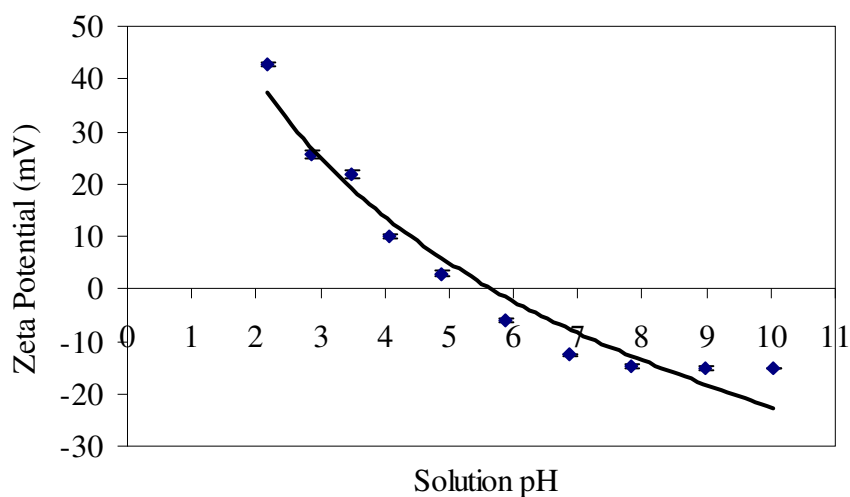


**Figure 3.10** Total zeta potential between PMMA plate and membrane ( $\zeta_{\text{total}}$ ).

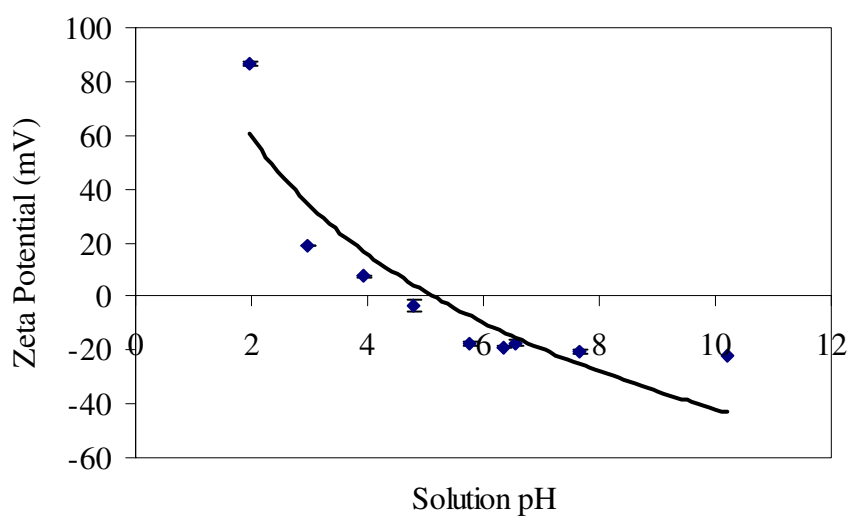


**Figure 3.11** Zeta potential of the PMMA plate ( $\zeta_{\text{PMMA}}$ ).

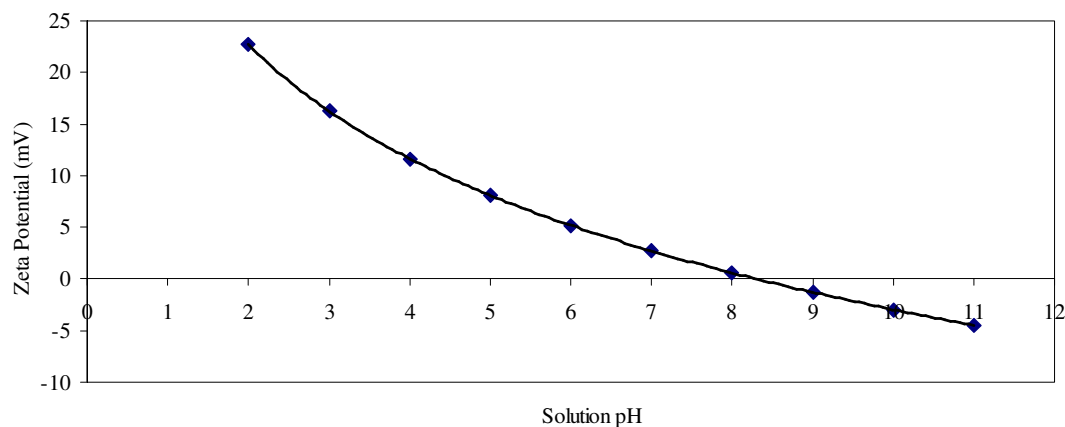


**Figure 3.12** The net zeta potential of the membrane ( $\zeta_{\text{Sample}}$ ).

### 3.3.5 Image analysis

Real color images with high resolutions were captured through a microscope by a digital CCD camera (Qimaging Micropublisher, Canada). The images snapped during the filtration were stored directly into a computer in real time and were further analyzed using image analysis software (Image-pro plus, MediaCybernetics). The area covered by the deposited particles, defined as membrane coverage, was calculated in the following manner.

Figure 3.13 shows the image conversion process. All the colored images from the experiments were first converted into gray-scale images having intensity values of 0–255 (0 for black and 255 for white). Since the pores on the membrane surface showed up as black dots on the DOTM images, the open filter with 2x2 pixels square was applied before converting the gray-scale images to binary images. In images with dark objects on a bright background, the opening filter removed small dark spots and smoothed the object contours. These gray-scale images were then converted to binary images by thresholding, *i.e.*, partitioning the images into only black and white pixels at an arbitrary threshold value using the image analysis software.

In order to determine a threshold value, it was necessary to compare the converted binary image to the original. This was because the microscope employed in the DOTM setup had to be manually focused before each image was taken, thereby altering the contrast and brightness for each of the images. The converted black and white images were used to determine the fractional coverage by particles at a given time through individual pixel enumeration (Kang *et al.*, 2004). Using this method, the coverage on the second fouling layer could also be analyzed.

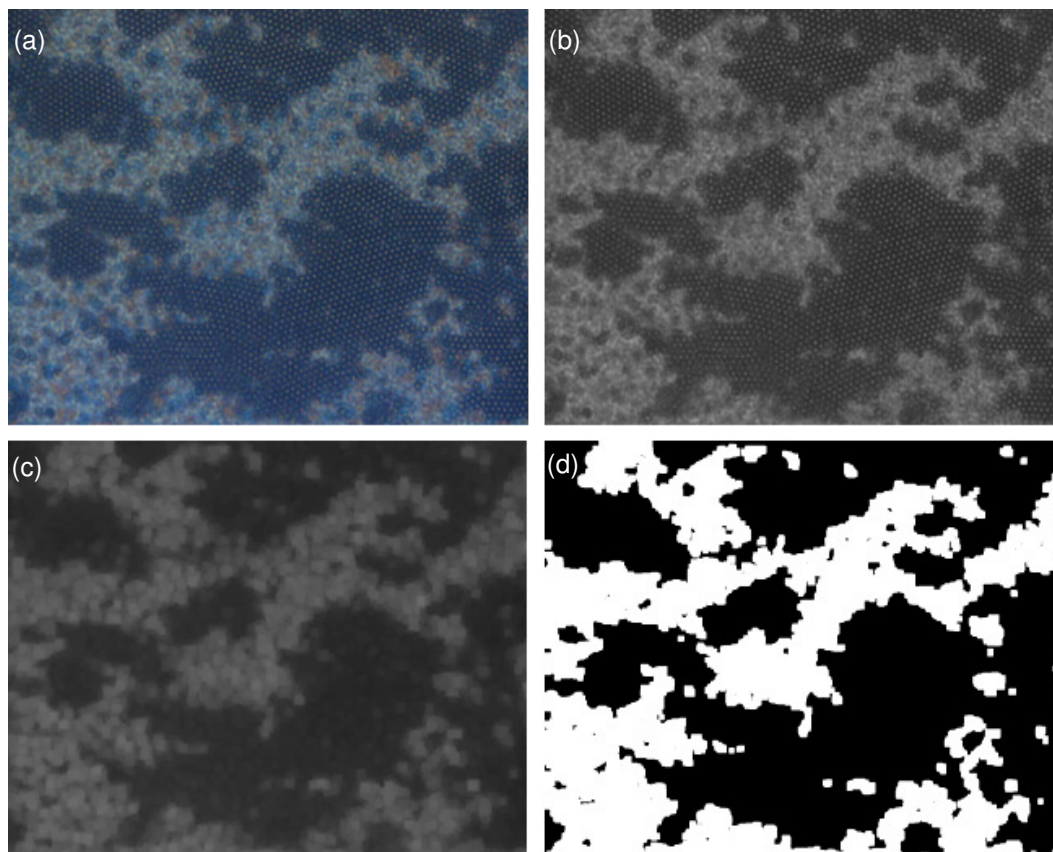


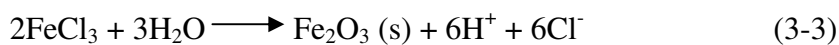
**Figure 3.13** Determination of fractional surface coverage. Raw images (a) obtained from direct microscopic observation were converted into gray-scale (b) and then applied with open filter to cut out the noise (c). Filtered images were then converted into black and white images (d) by choosing an intermediate gray-scale threshold.

### 3.4 Hematite particle preparation and flocculation experiments

Hematite ( $\alpha$ -Fe<sub>2</sub>O<sub>3</sub>) particles were flocculated and used as flocculated feeds for filtration. Hematite particles were prepared by the hydrolysis of ferric chloride (FeCl<sub>3</sub>) at 100 °C and then flocculated in potassium chloride (KCl) solutions at different pH values and shear rates. All the chemicals used were AR grade. All the salt solutions and particle suspensions were dispersed in MilliQ<sup>®</sup> water (<18 MΩ/cm). The mixing was provided by an orbital shaker.

#### 3.4.1 Preparation of hematite particles

Hematite flocs were selected as model polydisperse suspensions to simulate the membrane fouling in the real situation. Before making a hematite floc suspension, hematite ( $\alpha$ -Fe<sub>2</sub>O<sub>3</sub>) particles with a uniform shape and narrow particle size distribution were first prepared by hydrolysis of anhydrous ferric chloride (FeCl<sub>3</sub>). This process was first described by Matijevic *et al.* (1978). The size and morphology were functions of temperature, aging time and quantity of HCl added into the liquor (Petteys *et al.*, 1998). The hydrolysis procedure followed the formula,



To make 500 ml of hematite stock solution, 485 ml of hydrochloric acid (HCl) from a stock of 500 ml with a concentration of 3.75 mM was heated to 100 °C. 2.46 g of FeCl<sub>3</sub> solution was dissolved in the rest of 15 ml of 3.75 mM HCl at room temperature (~25 °C) and then filtered through 0.45 µm syringe filters. The mixed liquor was then added into the hot HCl solution. The mixture was stirred vigorously using a magnetic bar for 15 minutes. When nucleation occurred, the solution appeared dark brown. The solution was then capped loosely and put in a pre-heated oven at 100 °C for 24 hours (Lee, 2005).

The suspension turned red and opaque after 24 hours. It was then removed from oven and cooled down to the room temperature. 4 g of potassium chloride (KCl)

was added into the suspension and then stirred for 30 minutes to separate the hematite particles from residual acids. The washing process was performed to make the solution free from chloride. The suspension was centrifuged for 15 minutes at 6,000 rpm and the supernatant was discarded and the precipitated particles were re-dispersed in MilliQ<sup>®</sup> water. The hematite suspension was treated in an ultrasonic bath to prevent any aggregation of particles. The hematite particle size was measured using the Mastersizer to be in the order of 100 nm which is consistent with the literature (Penners *et al.*, 1986; Waite *et al.*, 1999). The hematite particle shape was approximately spherical as shown in Figure 3.14. The original hematite particle size made by this method was around 30 nm in this study.

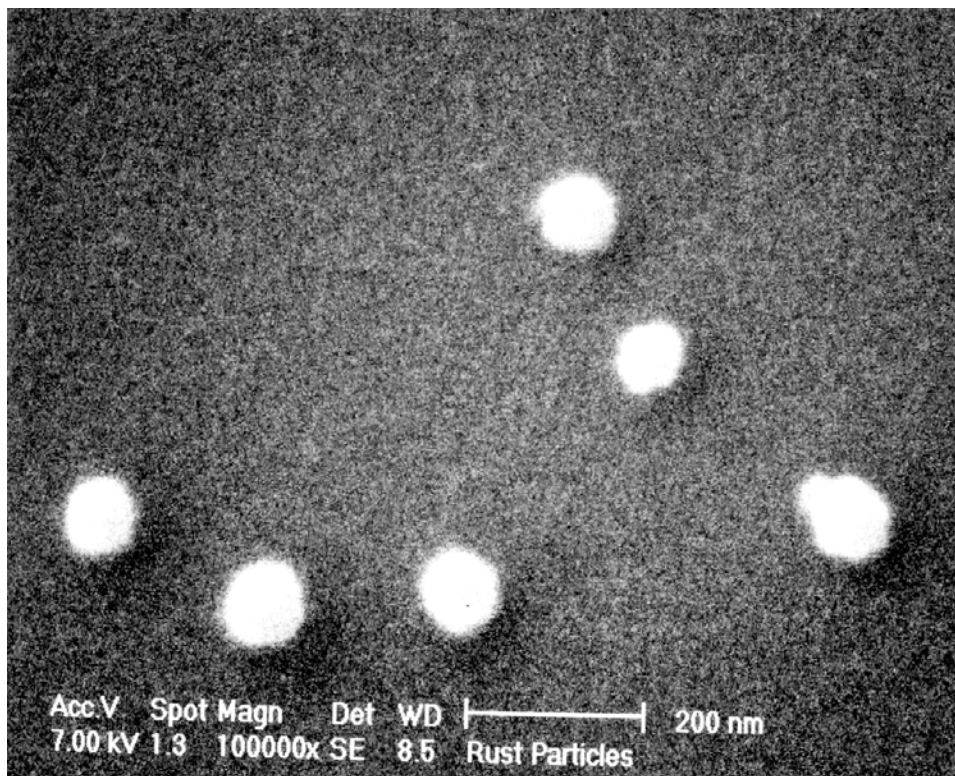


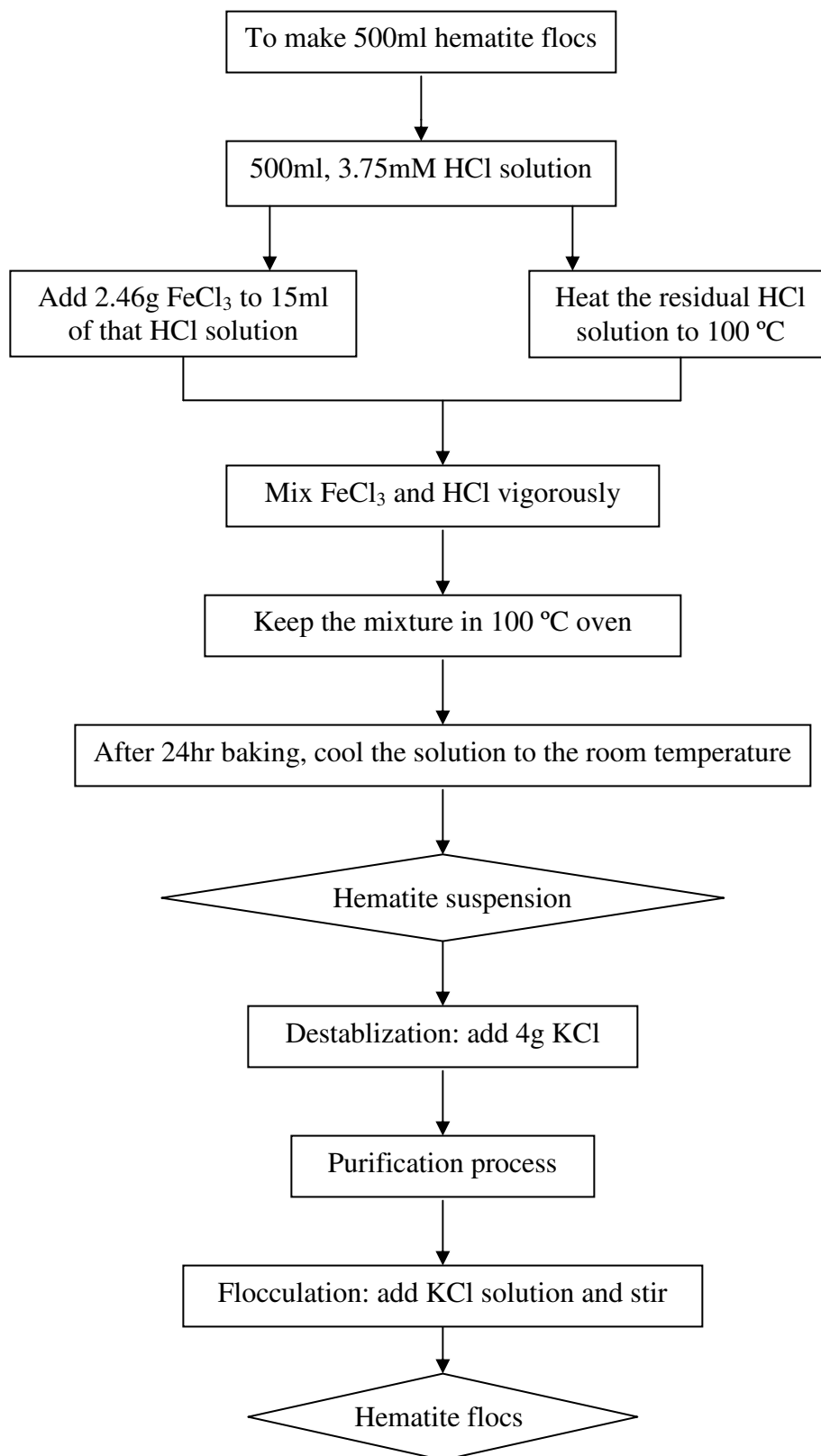
**Figure 3.14** Scanning electron micrograph of hematite particles (adapted from (Petteys *et al.*, 1998).

The centrifuge and ultrasonic processes were repeated five times before the final product was stored in a refrigerator (~4 °C) at a pH of 4 to prevent spontaneous aggregation. 0.1 molar of HCl and NaOH solutions were used to adjust the pH of the solutions.

### 3.4.2 Flocculation for hematite flocs

Hematite flocs were made by the flocculation of hematite particles (Lee, 2005) with salt solution, KCl used as the flocculant. To conduct flocculation, 100 ml of KCl solutions with different concentrations (50-200 mM) were prepared in conical bottles and pH values were adjusted to the desired values. 100 ml of diluted hematite suspension was treated in an ultrasonic bath for 15 minutes before the pH was adjusted to be the same as that of the KCl solution. The hematite suspension was added into the salt solution slowly and a shear force was applied using a shaker with orbital motions at a pre-set speed. The preparation of hematite particles and the flocculation process are summarized in the flowchart shown in Figure. 3.15.

Floc size evolution was monitored using the Malvern Mastersizer 2000 every 10 or 30 minutes (depending on the floc growth rate) until the flocs stopped growing. In the case where the flocs were still growing, the shaking was stopped to terminate the flocculation process when the floc size reached the desired value. Floc size measurement was made again 15 minutes later after the cessation of shear force to make sure that no spontaneous aggregation occurred. The flocculated floc size ranged from 5 up to 80  $\mu\text{m}$ . The post-calculated fractal dimensions were in the range of 1.80 to 2.53 which showed a significant difference in the floc structure. The flocculation results are reported in Chapter 6.

**Figure 3.15 Hematite floc preparation flowchart.**



## 3.5 Filtration experiments

### 3.5.1 Experimental setup

A typical crossflow microfiltration system was set up in laboratory including the DOTM technique integrated into the filtration line. Figure 3.1 shows the crossflow microfiltration rigs used in this project including the DOTM facilities.

The feed solution stored in a reservoir was pumped by a gear pump (Cole-Parmer Instrument) into the filtration line and through the membrane module which was positioned on the working stage of a microscope. The feed solution was then circulated in the pipeline and recycled back to the feed tank. Constant flux stepping was achieved by a peristaltic pump (MasterFlex, Cole-Parmer Instrument) in the permeate line. The permeate liquid was collected in a container on an electronic balance. The mass weight was recorded by a lab PC with an attached timer and transformed into permeate flux according to the time interval and membrane area. The operating pressure was controlled by a pressure gauge fixed in the pipeline down stream of the feed side outlet of the module. Three pressure transducers in the up- and down-stream of the membrane module and permeate side were used to collect the pressure data. The pressure data P1, P2 and P3 were recorded separately in the PC and used to calculate the transmembrane pressure (TMP) using the equation:  $TMP = (P1+P2)/2-P3$ . An electronic flow meter was embedded in the outlet of the pipeline to record the flow rate. All the electrical signals were fed to an A/D data acquisition board connected to the PC for recording and the parameters were displayed in separate graphs using the software of LabView.

### 3.5.2 Experimental protocol

The critical flux of the filtration of particles was defined according to the critical flux concept during the flux stepping filtration test. All the tests were conducted in constant flux mode. The prepared membrane was first inserted between the membrane modules. The two halves of the module were then screwed together. The



whole module with the membrane inside was fitted in the filtration pipeline and mounted on the working stage under the objective. MilliQ<sup>®</sup> water from the feed tank was pumped slowly into the system first. After all the air and bubbles were expelled, the flow rate was adjusted to the desired value. The crossflow was allowed to stabilize for 10 minutes before the concentrated particle solution was spiked into the feed tank. The feed solution was stirred by a magnetic bar to keep the suspension uniform and limit particle aggregation. Data logging was activated to record all the parameters and the observed images were captured simultaneously. The observation focus had to be adjusted all the time in order to get clear images. The average crossflow velocity (computed by dividing the crossflow discharge by the flow area) ranged from 0.05 to 0.3 m/s. The corresponding Reynolds number was 150~900, and hence the flow regime was laminar.

The protocol for critical flux determination involved operations with a series of flux steps. A typical test started from a low flux. If there was no particle deposition or fouling layer on membrane surface during a 15-minute step, the operating flux was regarded as below the critical flux under this situation, and the flux was further increased to a higher step initially with an increment of 15 l/m<sup>2</sup>h. The test continued until 2/3 of the observation membrane area was covered by the foulant during any 15-minute step. This operating flux was then regarded as above the critical flux. The reported critical flux was an average value of the two neighboring fluxes where the fouling transient happened. Due to the non-uniformity of the deposition on the membrane, the experiments were repeated at least three times with an even smaller flux increasing step to verify the critical flux value. The smallest increment in flux which was achievable by the peristaltic pump on the permeate side was 1.5 l/m<sup>2</sup>h. The error bar on data sheets showed the standard deviation of three experiments.

The filtration system was flushed by a 4 g/l detergent solution (Tergazyme, Alconox, U.S.A.) at 40 °C for at least 1 hour. The detergent solution was then drained out, and MilliQ<sup>®</sup> water was pumped in to wash the system again several times. Sodium azide (NaN<sub>3</sub>) solution at a concentration of 2 g/l was also used to

remove microorganisms possibly stained on the wall of the system. At the end, the system was washed thoroughly using MilliQ<sup>®</sup> water.

### 3.6 Electromagnetic field (EMF)

GrahamTek is a multi-nation corporation specializing in development and manufacturing technologies in desalination and filtration for water treatment industry. GrahamTek has developed novel technologies, including an EMF device and a flow distributor that may produce micro-bubbles that appear to show significant effects on reducing fouling in spiral-wound RO modules. The reasons for the beneficial effects are not well established yet. The author was involved in this project initiated by GrahamTek Singapore to investigate the effects of an EMF device on fouling reduction in a model flat-sheet membrane system due to the complex geometry of the spiral-wound RO modules. The DOTM technique was combined with the EMF device to observe particle fouling in electromagnetic fields during flat sheet crossflow microfiltration.

An electromagnetic field (EMF) is present when an electrical current flows through a wire coil (Figure 3.16). The EMF device of GrahamTek used a three-phase AC current. The magnetic field produced was alternating with the AC current. It could be applied either upstream of the membrane module or around the spiral-wound RO module (this is the usual arrangement). It was reported that membrane fouling could be significantly reduced with applied EMF compared to the situation without EMF.

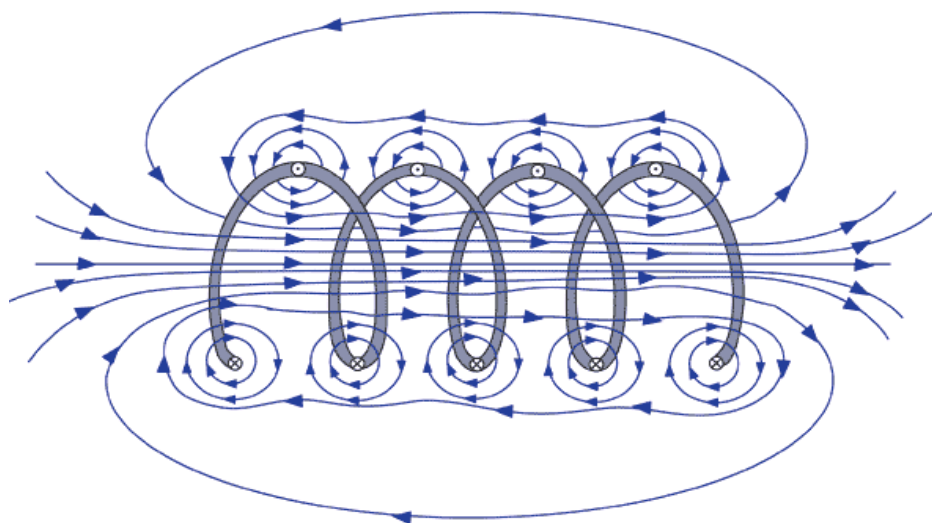


**Figure 3.16** Schematic of the electromagnetic field produced by an electric current flowing through a coil (adopted from internet resources: [www.ndt-ed.org/EducationResources/CommunityCollege/MagParticle/Physics/CoilField.htm](http://www.ndt-ed.org/EducationResources/CommunityCollege/MagParticle/Physics/CoilField.htm) ).

The tests on the effect of EMF were conducted with two EMF devices, the EMF ‘cell winding’ and the EMF ‘upstream’. The EMF devices used in this study were custom-made and provided by the GrahamTek. The EMF ‘cell winding’ was a copper coil around the membrane cell and produced the electromagnetic field right above the membrane surface. The EMF ‘upstream’ was a PVC tube allowing fluid flow through with a copper coil around it. The frequency tested in this study was fixed at 60 Hz. Due to the different configurations, they are described separately in the following sections. Most of the tests were with the EMF cell winding. The results ‘with EMF’ denotes the experiments using the cell winding if not otherwise specified.

### 3.6.1 EMF cell winding

Figure 3.17 shows the picture of the EMF device provided by the GrahamTek, including the power box and the cell winding. The winding was a specially designed and fabricated coil using copper wires. The winding was fitted into the microscope used in DOTM and the membrane cell was inserted into the winding.

The hole in the middle of the winding provided a viewing window allowing observation of membrane surface. The feed solutions experienced the electromagnetic field when passing through the membrane cell. Pressurized air was passed over the cell in order to remove the heat produced by the EMF device. In order to avoid the effect of the heat produced on the filtration results, the steel membrane support used in the previous practice was replaced by a non-conductive plastic membrane support.



**Figure 3.17** Picture of EMF cell winding working with DOTM.

### 3.6.2 EMF upstream

The EMF upstream device was used to find out the evidence of particle aggregation during membrane filtration. Due to the power input to the EMF upstream tube, the feed tended to heat up. To assess this, the feed solution was circulated through the upstream tube and the temperature changes with time were monitored. It was found that the temperature of the feed solution increased from 25 to 40 °C within 3 hours. Yeast cells used in this task would tend to ferment at such a high temperature. It was necessary to keep the temperature constant in order to eliminate this effect and to control the filtration temperature. An independent circulating line was integrated

to the original filtration system to control filtration temperature, as shown in Figure 3.18. The circulating line on the left in Figure 3.18 was used to circulate the feed solution through the EMF upstream tube at a higher flow rate (3 l/min). A water bath with a cooling coil was used to keep the feed temperature constant at 25 °C. The original crossflow filtration loop was run at the usual flow rate (0.85 l/min).

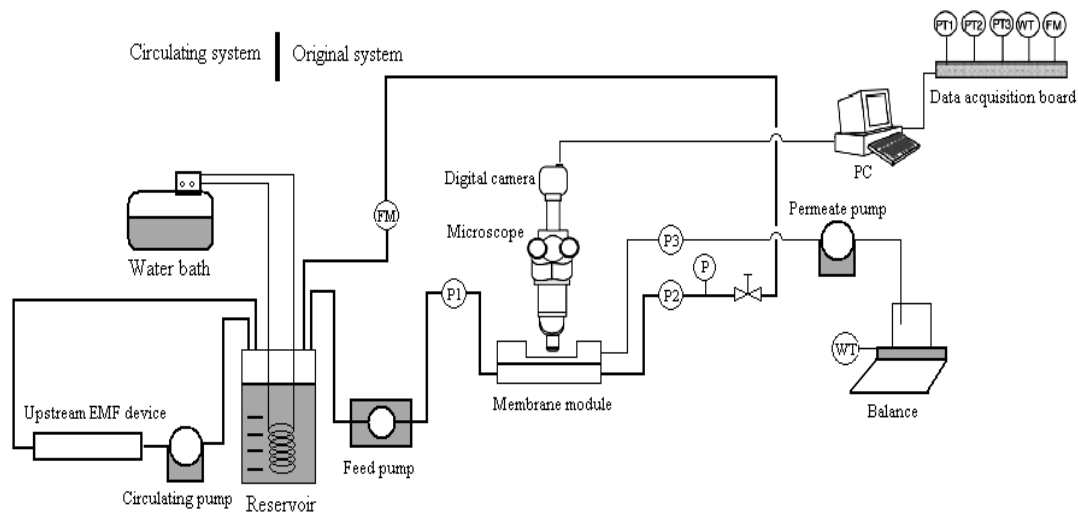


**Figure 3.18 Integrated DOTM system with a circulating line.**

## **Chapter 4 Investigations of factors influencing filtration behavior of single-sized particles**

Membrane fouling in crossflow microfiltration (CFMF) is a major problem that limits the filtration performance in various applications. The fouling process itself is a complicated one. In this chapter, parameters that control the filtration performance were investigated using single-sized latex particles as a precursor to the investigation of mixtures and irregular-shaped flocs. The critical fluxes under various conditions were measured by the DOTM technique. The materials and methodologies used in this study were introduced in Chapter 3. As reviewed in Chapter 2, there are numerous factors influencing the permeate flux in microfiltration. This chapter mainly focuses on investigating the influence of the following factors on the filtration outcome:

- Crossflow velocity (CFV);
- Feed concentration;
- Membrane and particle surface charge;
- Solution ionic strength;
- Particle size;
- Velocity distribution (flow channel height).

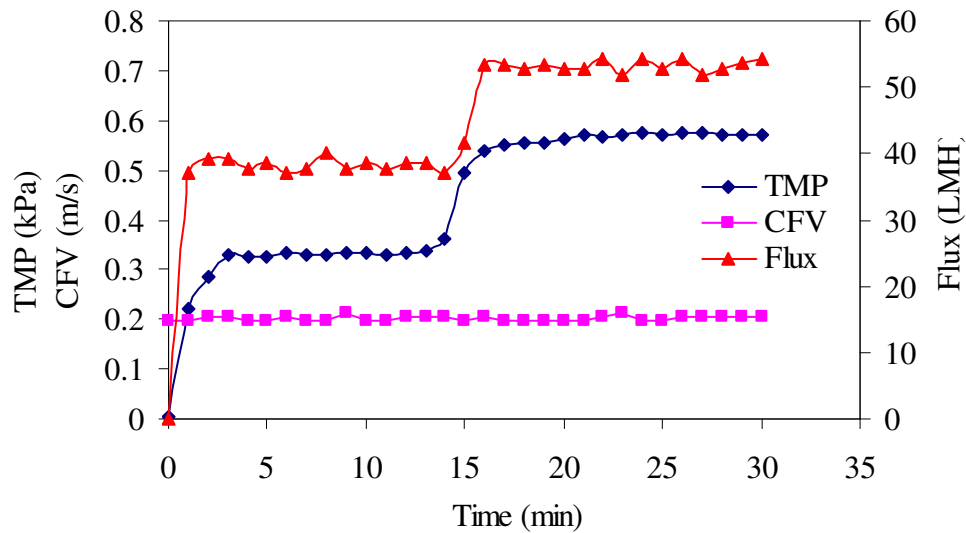
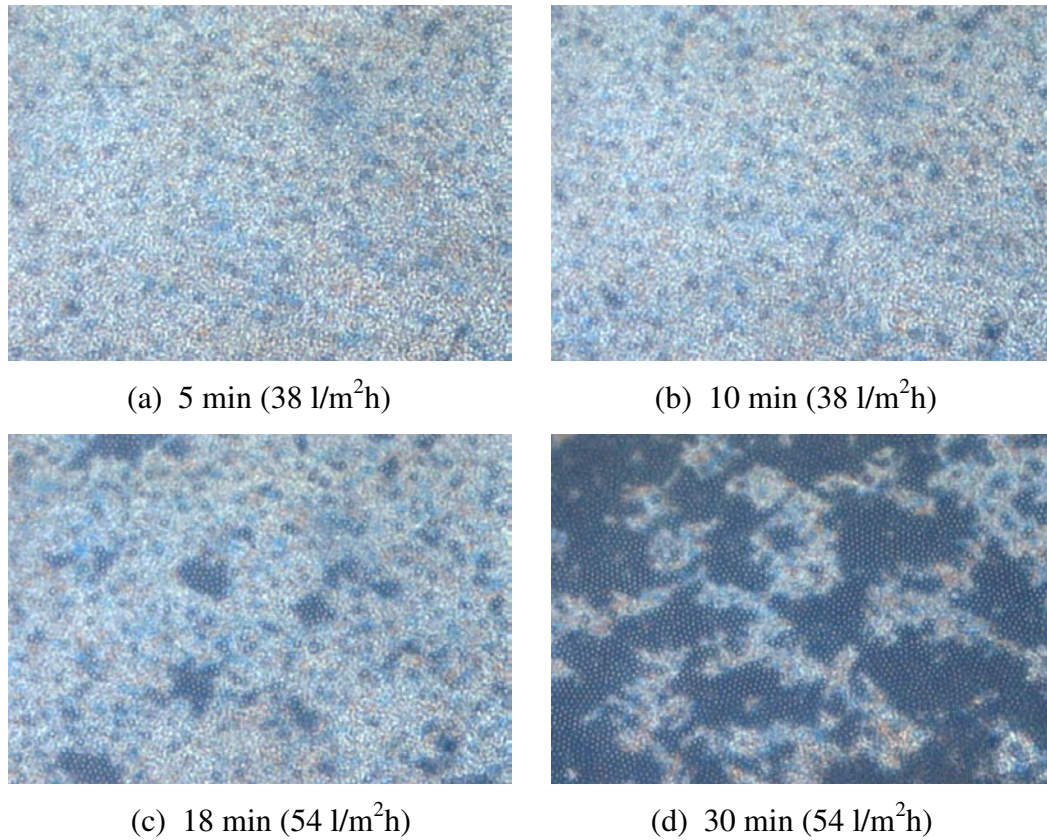
Although there are various works reported in the literature on the fouling mechanisms, most of the studies were conducted in constant pressure operating mode and some results were also not conclusive. Here, the author used instead the concept of critical flux in constant flux mode to study the microfiltration fouling mechanisms. In addition, some results on single-sized particles in this chapter would be used to compare with the data on the mixed feeds presented in Chapter 5. The images obtained by the DOTM were analyzed using image analysis software.

The calculated coverage was integrated into a mass balance model in Chapter 7 as an alternative approach to extracting critical flux values.

#### 4.1 Critical flux measurement of single-sized particles

The critical fluxes of 3.0, 5.0 and 10.0  $\mu\text{m}$  latex particles were determined at various concentrations from 0.01 to 0.05 % vol. and various crossflow velocities using the DOTM protocol described in Section 3.5.2. Most of the filtrations were performed at a CFV of 0.2 m/s. Two membrane cells with different feed flow channel heights (1 and 2 mm) were used to study the influence of the velocity distribution on critical flux. Figure 4.1 shows the typical images of particle deposition of 3.0  $\mu\text{m}$  latex (0.05 % vol.) during a test. The images in Figures 4.1 (a) and (b) were captured at the 5<sup>th</sup> and 10<sup>th</sup> minute respectively during the filtration at a flux of 38  $\text{l/m}^2\text{h}$ . During this period, the particles deposited on the membrane surface in a transient manner at an imperceptible rate. Hence, the flux was judged to be below the critical flux in this case. After 15 minutes without significant fouling on the membrane, the imposed flux was increased to 54  $\text{l/m}^2\text{h}$ . Only 3 minutes after the increase, particles begun to deposit as seen in Figure 4.1 (c). The particles were driven to the membrane surface due to the permeate convection and accumulated individually and in clusters on different parts of the membrane. The preferential particle deposition was probably due to the variation in the local fluxes because of the slight heterogeneity in the membrane pore density (Li *et al.*, 1998). At the end of the 2<sup>nd</sup> step (30 minutes), the membrane area was almost totally covered by the deposited particles (Figure 4.1 (d)). The operating conditions were shown in Figure 4.1 (e). The TMP stayed relatively constant in the 1<sup>st</sup> step ( $J = 38 \text{ l/m}^2\text{h}$ ) but began to increase slowly in the 2<sup>nd</sup> step ( $J = 54 \text{ l/m}^2\text{h}$ ) which was consistent with the observations of the images in Figure 4.1 (a)-(d).





(e) Operating conditions

**Figure 4.1** DOTM images of particle deposition during the filtration of 3.0 μm latex (0.05 % vol.) at CFV = 0.2 m/s. (a) and (b) were taken under an imposed flux of 38 l/m<sup>2</sup>h; while (c) and (d) were at a higher flux of 54 l/m<sup>2</sup>h; (e) shows the operating conditions.



A test across a wide range of flux steps (from a very low constant flux until above the critical flux) with a large increment was conducted to determine an initial critical flux value. The flux stepping test was then refined to only two or three steps below and above this rough value respectively in case the negligible deposited particles would affect the incoming deposition. The test for each critical flux value was repeated at least three times to validate the reproducibility. The critical fluxes of the 5.0 and 10.0  $\mu\text{m}$  particles were measured in the same manner.

## 4.2 Influence of crossflow velocity (CFV)

Experiments were conducted to investigate the influence of crossflow velocity on critical flux at a particle concentration of 0.05 % vol. and at the membrane iso-electric point (pH 8). Figure 4.2 shows that critical flux increased with crossflow velocity. The Reynolds numbers varied from 100 to 600 within the crossflow velocity range of 0.05 to 0.3 m/s. Hence, the flow was in the laminar regime. As discussed in Section 2.2.2 in Chapter 2, crossflow microfiltration could be enhanced by the shear stress produced by the tangential flow across the membrane surface. The CFV distribution was a parabolic approximation in a laminar flow (Figure 4.3). The CFV reported in this study was calculated by dividing the flow rate by the cross section area for flow. Therefore, the reported CFV was an average velocity instead of the local one.

When fouling occurs, a cake layer builds up on the membrane surface. This cake layer takes up some space in the flow channel and reduces the effective channel height. For a flow channel with a height  $H$  and width  $w$ , a volumetric flow rate of  $Q$  has a CFV ( $U$ ) of,

$$U = \frac{Q}{H \times w} \quad (4-1)$$

Shear rate in a thin channel,  $\gamma_o$  will be,

$$\gamma_o = \frac{6U}{H} = \frac{6Q}{H^2 w} \quad (4-2)$$

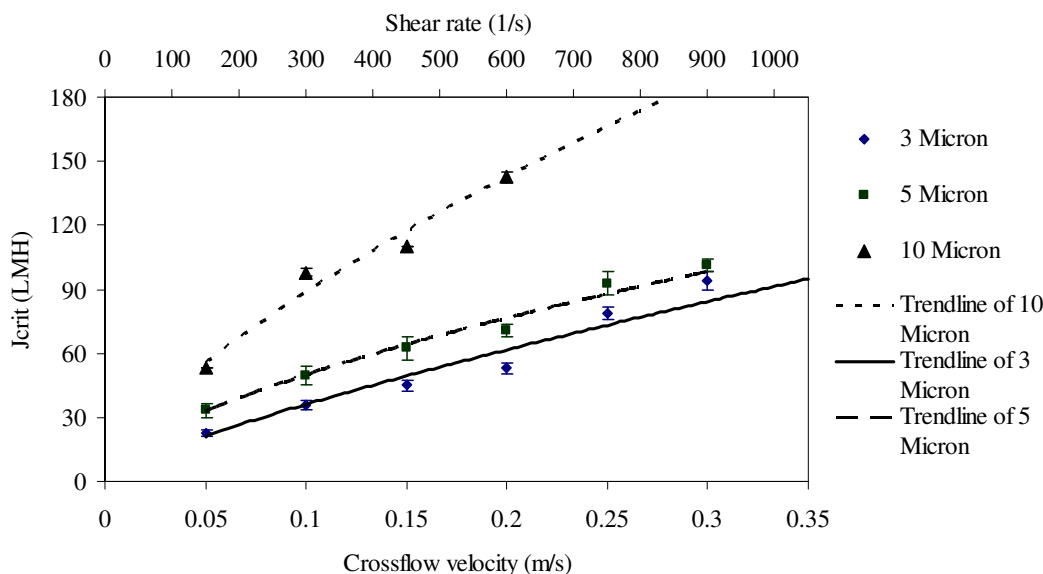


**Figure 4.2 Critical flux vs. crossflow velocity during filtration of latex particles at a concentration 0.05 % vol. and membrane iso-electric point pH 8.**

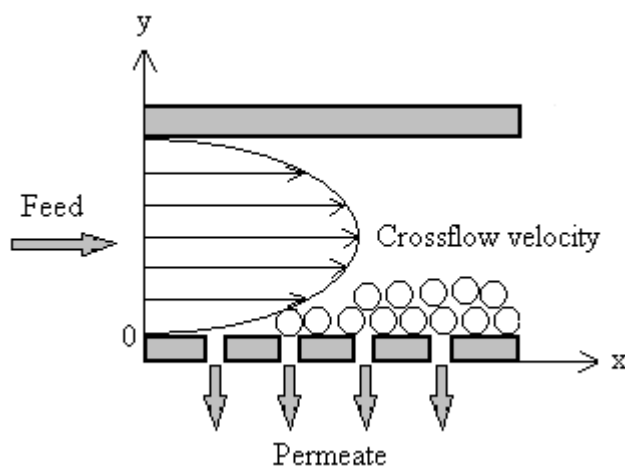
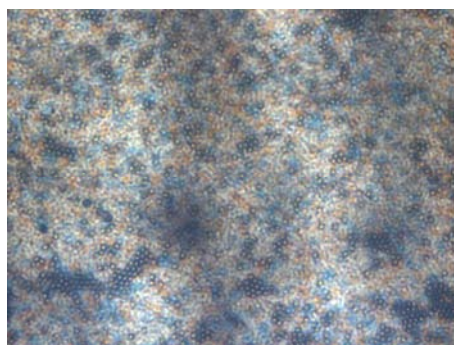


**Figure 4.3 Schematic of crossflow velocity distribution in the flow channel.**

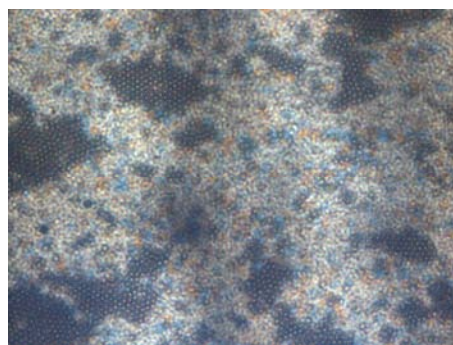
Therefore, as the channel height,  $H$  decreases due to the cake accumulation the surface shear rate increases rapidly (a 10 % increase in  $H$  leads to more than 20 % increase in  $\gamma_o$  for a fixed flow rate  $Q$ ).

The subsequent particles after a cake formation could be prevented from depositing by the even higher shear stress, and thus membrane fouling might not be a continuous process in the flow channel in crossflow microfiltration. When the rate of the deposition is equal to the rate of the re-entrainment, an equilibrium state or a quasi-steady state could be achieved. This is one of the potential competitive advantages of crossflow microfiltration compared with dead-end microfiltration.

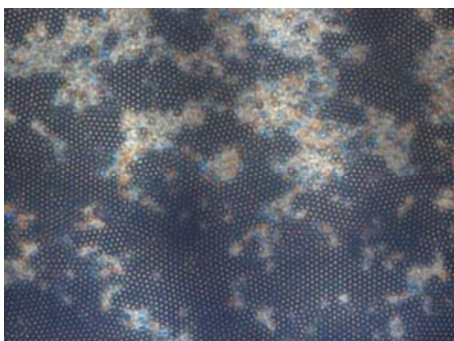
Figure 4.4 shows the typical experimental results during the filtration of 3.0  $\mu\text{m}$  latex using the 1 mm channel height membrane cell. The operating conditions are given in Figure 4.4 (i). The data shows that higher CFV could cause the removal of deposited particles and prevent fouling. The 1<sup>st</sup> flux step was operated at a flux of 30  $\text{l/m}^2\text{h}$  for 15 minutes which was below the critical flux. After 15 minutes, most of the membrane area was still exposed as shown in Figure 4.4 (a). The flux of 30  $\text{l/m}^2\text{h}$  was thus lower than the critical flux. After only 3 minutes when the flux was increased to 37  $\text{l/m}^2\text{h}$ , about 1/3 of the area was covered by the particles (Figure 4.4 (b)). After 3 more minutes, the observation area was almost covered by a mono layer of the particles (Figure 4.4 (c)). The total coverage of the area occurred at the 24<sup>th</sup> minute of the filtration (Figure 4.4 (d)). The CFV was then further increased to 0.36 m/s with the other conditions unchanged. After 3 minutes when CFV was increased, the coverage did not change much although the fouling layer could be observed to start moving on the membrane surface (Figure 4.4 (e)). The lag in the particle removal was probably due to the fact that the removal started from the membrane area near the channel inlet. Some of the deposited particles were re-entrained back to the bulk suspension at the higher CFV after 6 minutes (Figure 4.4 (f)). At the 30<sup>th</sup> minute, the flux was stopped and decreased to zero. Within 3 minutes, increasing numbers of particles were re-entrained back to the bulk (Figure 4.4 (g)). After 4 minutes, most of the area was uncovered (Figure 4.4 (h)).



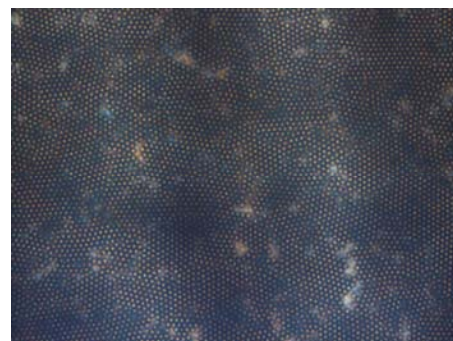
(a) 15<sup>th</sup> min ( $30 \text{ l/m}^2\text{h} < J_{crit}$ )



(b) 18<sup>th</sup> min ( $37 \text{ l/m}^2\text{h} > J_{crit}$ )



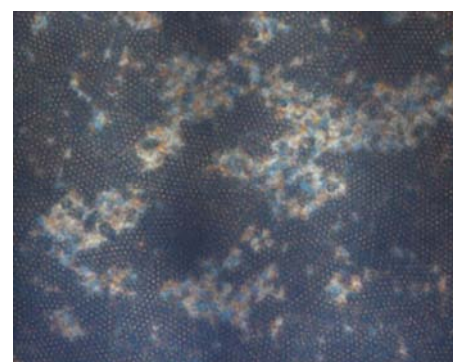
(c) 21<sup>st</sup> min ( $37 \text{ l/m}^2\text{h}$ )



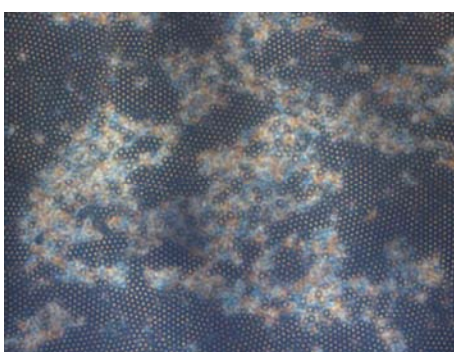
(d) 24<sup>th</sup> min ( $37 \text{ l/m}^2\text{h}$ , CVF increased)



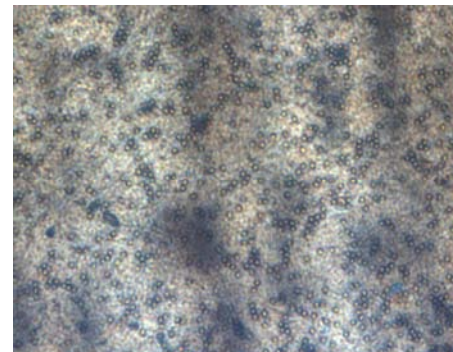
(e) 27<sup>th</sup> min ( $37 \text{ l/m}^2\text{h}$ , cake flowing)



(f) 30<sup>th</sup> min ( $37 \text{ l/m}^2\text{h}$ , cake removed)

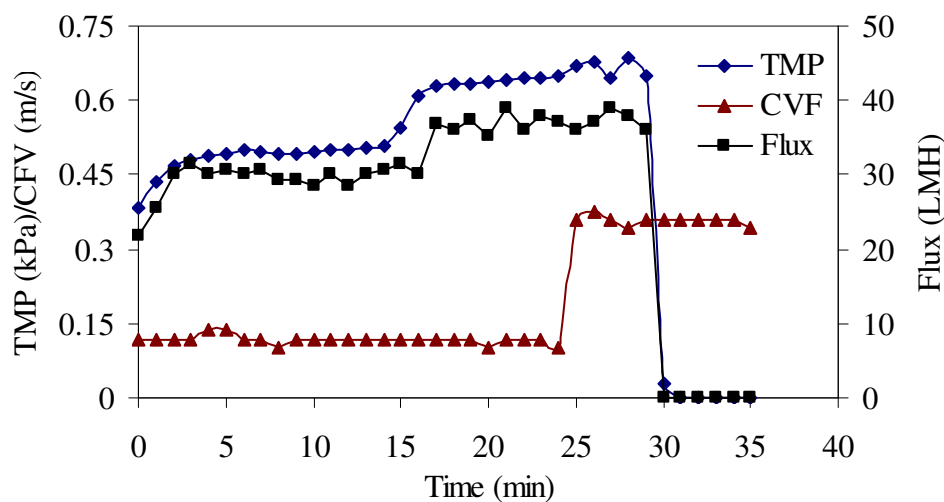


(g) 33<sup>rd</sup> min ( $0 \text{ l/m}^2\text{h}$ )



(h) 34<sup>th</sup> min ( $0 \text{ l/m}^2\text{h}$ , recovered)

(Figure 4.4 to be continued)



(i) TMP and flux profiles

**Figure 4.4** Particles removal during the filtration of 3.0  $\mu\text{m}$  latex particles at concentration 0.05 % vol. and pH 8.

In Chapter 2, theoretical models for crossflow microfiltration were reviewed. According to Equations (2-15), (2-18) and (2-21), permeate flux increases with local shear rate which has a relationship of  $\gamma_o = \frac{6U}{H}$  (Equation (4-2)) with CFV ( $U$ ).

Hence the permeate flux has a power-law relationship with the CFV *i.e.*  $J \propto U^n$ , with  $n = 1/3$  in the laminar flow concentration polarization model based on Brownian diffusion,  $n = 1.0$  in the shear-induced diffusion model and  $n = 2.0$  in the inertial lift model. The relationship between critical flux and crossflow velocity depends on the nature of the back transport. Belfort *et al.* (1994) provided a comprehensive review of the behavior of suspensions and macromolecular solutions in crossflow microfiltration. They proposed three major back transport mechanisms applying to different particle sizes. Table 4.1 shows the particle size ranges applicable to the according dominant mechanisms.

**Table 4.1 Back transport mechanisms for different particle size ranges**

| Back transport         | Brownian diffusion | Shear-induced diffusion | Inertial lift     |
|------------------------|--------------------|-------------------------|-------------------|
| Particle size          | <0.5 $\mu\text{m}$ | 0.5-30 $\mu\text{m}$    | >30 $\mu\text{m}$ |
| Velocity exponent, $n$ | 0.33               | 1.0                     | 2.0               |

The shear-induced diffusion model ( $n = 1.0$ ) was more applicable in this study where 3.0, 5.0 and 10.0  $\mu\text{m}$  latex particles were used. Figure 4.5 shows a log-log plot of critical flux vs. crossflow velocity and shows the slopes of 0.33, 1.0 and 2.0. Clearly, the DOTM data ( $n = 0.77$ ) were much agreeable with the shear-induced back transport mechanism where  $n = 1.0$ .

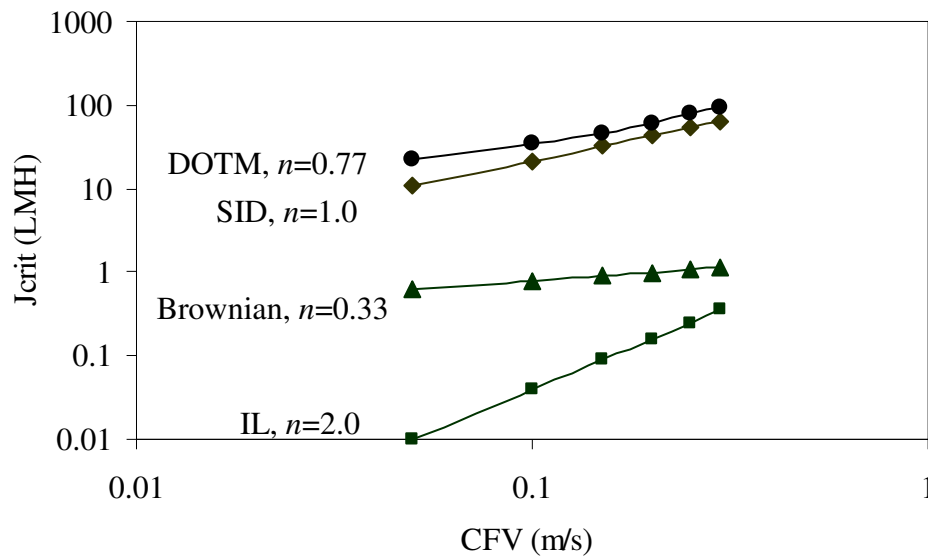


**Figure 4.5  $J_{crit}$  vs. CFV in CFMF according to the back transport mechanisms: Brownian diffusion (Brownian), Shear-induced diffusion (SID) and Inertial lift (IL). Conditions:  $L = 0.11$  m,  $\phi_b = 0.0005$ ,  $\phi_w = 0.6$ ,  $r = 1.5$   $\mu\text{m}$ , Boltzmann's constant  $K = 1.38\text{e-}23$  J/molK,  $T = 293$  K,  $\mu = 0.001$  kg/m, and  $\rho_o = 1000$  kg/m<sup>3</sup>.**

However, on closer analysis, the data correlated to,

$$J_{crit} \propto U^{0.62-0.77} \quad (4-3)$$



This was similar to the work done by Baker *et al.* (1985) using a TiO<sub>2</sub> particulate suspension, where the flux was proportional to the CFV to the power of 0.6. In a recent review, Bacchin *et al.* (2006) noted that there was a relatively wide range of velocity exponents observed in many studies on critical flux.

The model particles used in this study were latex beads with highly uniform particles sizes of 3.0, 5.0 and 10.0 µm. These particle sizes were typical for microfiltration studies (0.02-10 µm), and according to Table 4.1. The dominant back transport mechanism should be the shear-induced diffusion for 0.5-30 µm particles.

### 4.3 Influence of feed concentration

According to the discussions on the effect of feed concentration in Section 2.4.3, Chapter 2, it was anticipated that critical flux declined with the logarithm of particle concentrations. The Brownian diffusion model (Equation (2-15)) and the SID model (Equation (2-18)) showed critical flux and feed concentration has a relationship,

$$J_{Crit} \propto \ln\left(\frac{\phi_w}{\phi_b}\right) \quad (4-4)$$

Although the factor of particle concentration is not shown in the inertial lift model (Equation (2-21)), the critical flux is inversely proportional to the feed viscosity ( $\mu$ ). The viscosity of solutions is believed to be a function of concentration, and hence the feed concentration influences critical flux indirectly through the feed viscosity.

The influence of the particle concentration was tested using single-sized latex particles and washed baker's yeast with a narrow particle size distribution of 5 µm from dilute to concentrated suspensions. A high concentration of the feed solution

impaired the filtration rate since it increased the probability of particle deposition on membrane surface.

Figure 4.6 shows that the critical fluxes decreased with increasing feed concentrations for 3.0, 5.0 and 10.0  $\mu\text{m}$  latex particles respectively. From the three curves in Figure 4.6 it could be seen that the critical flux decreased rapidly first at relatively lower concentrations and gradually reached a steady plateau when the concentration was increased. The critical flux appeared to be proportional to the logarithm of the latex concentration.

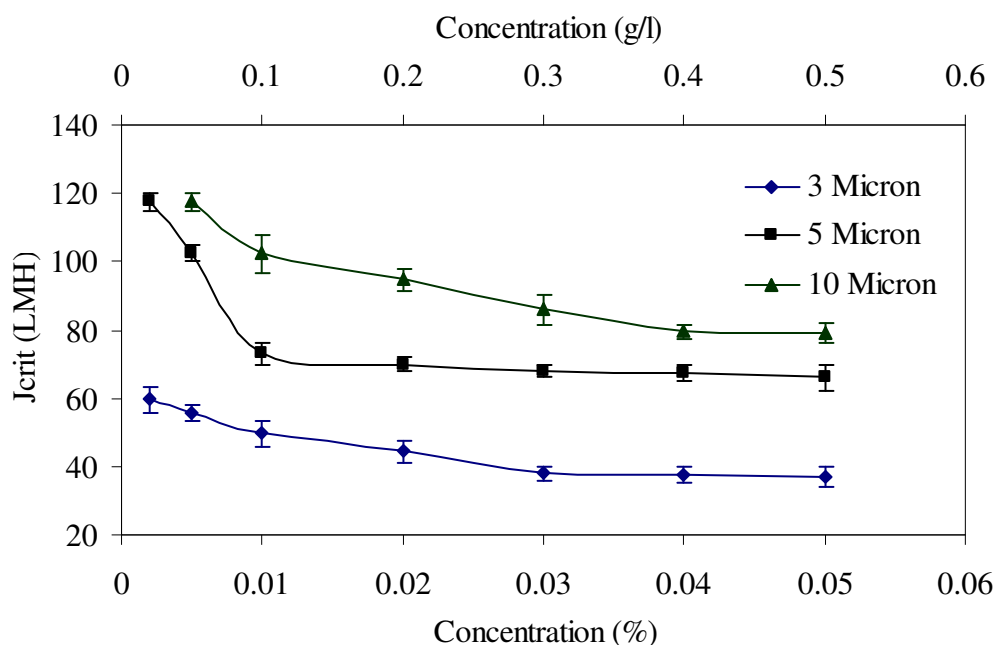


**Figure 4.6 Critical flux vs. latex particle concentration at CFV 0.2 m/s.**

According to Figure 4.7 which shows  $J_{crit}$  vs.  $\log(C)$ , the critical flux appeared to be proportional to the logarithm of the latex concentration as shown in Equation (4-4). This could be explained by the maximum random packing volume fraction which has a value of 0.6. For non-adhesive monodisperse of rigid spheres, there is a maximum random packing volume fraction in the boundary layer. Once the volume fraction accumulates to this maximum value ( $\phi_w \approx 0.6$ ), increasing feed



concentration will no longer have a significant effect on the permeate flux. Eckstein *et al.* (1977) also determined the self-diffusion coefficients ( $D_s$ ) experimentally using spherical and disk-like particles under different concentrations. They found that the diffusion coefficients increased with concentration at low concentration ( $0 < \phi < 0.2$ ). At relatively high concentrations ( $0.2 < \phi < 0.5$ ), the diffusion coefficients were independent of particle concentration (refer to Section 2.3.5, Chapter 2). In this study, the latex particles which were non-adhesive, rigid and spherical as well as with a narrow particle size distribution, were used as the testing model particles. Therefore, the above explanation applies in this case. Another explanation can be used for the steady plateau in Figure 4.6 due to the nature of the logarithm function,  $y = \log(x)$ . The values  $y$  decrease rapidly first and reach a plateau as  $x$  increases.

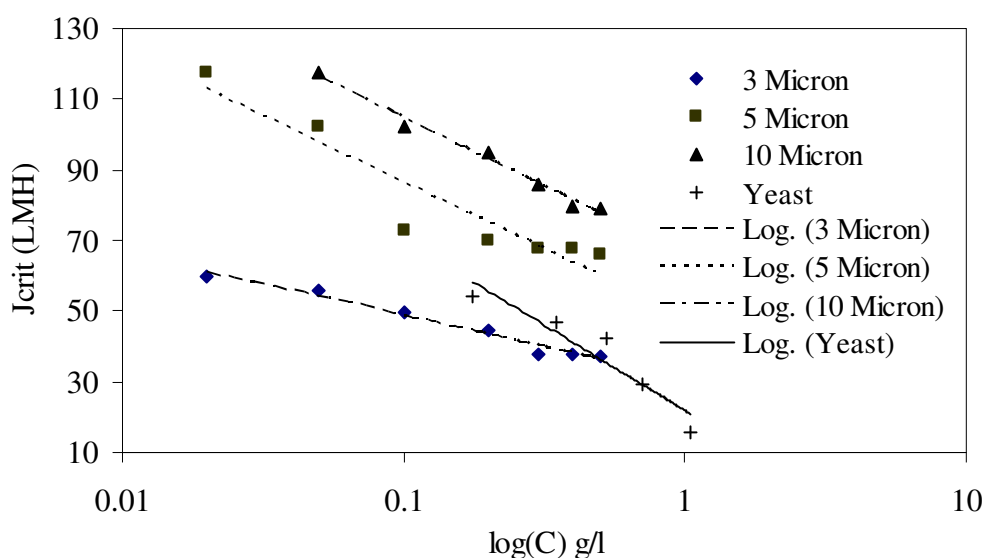


**Figure 4.7 Critical flux vs. log(particle concentration) in filtration of latex and yeast at CFV 0.2 m/s.**

The concentration range tested in this study was low (0.01-0.5 g/l). However, it would be useful to conduct some experiments on suspensions with extremely low concentrations as they are often encountered in water/wastewater treatment.

It was interesting that the critical fluxes of washed yeast decreased with the solution concentration and did not reach a steady state as shown in Figure 4.8. This could be due to the different properties of yeast cells from latex particles. Yeast was a growth form of microorganisms. Yeast cells were not perfectly spherical, and they were more compressible without smooth surface compared with latex particles. The adsorption of the yeast particles had to be considered. Therefore, the explanation of the maximum random packing volume fraction was not valid for such a situation as the conventional filtration theories were based on spherical, non-compressible particles. The purpose of washing yeasts was to remove the extracellular poly substance (EPS) around the yeast cell surface. Images shown in Figure 4.9 are examples during a typical filtration of 0.525 g/l washed yeasts. The deposited yeast particles scattered on the membrane surface.

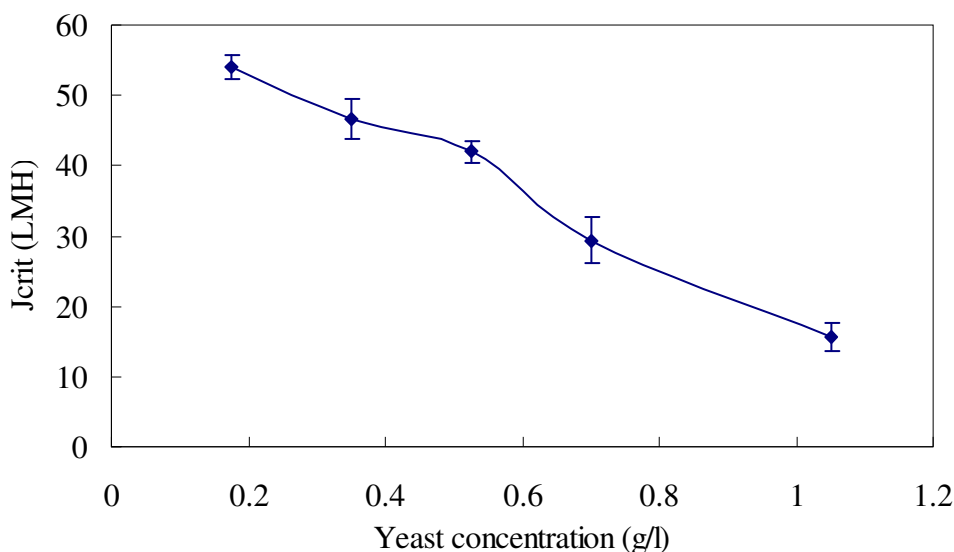


**Figure 4.8** Critical flux vs. yeast particle concentration at CFV 0.2 m/s.

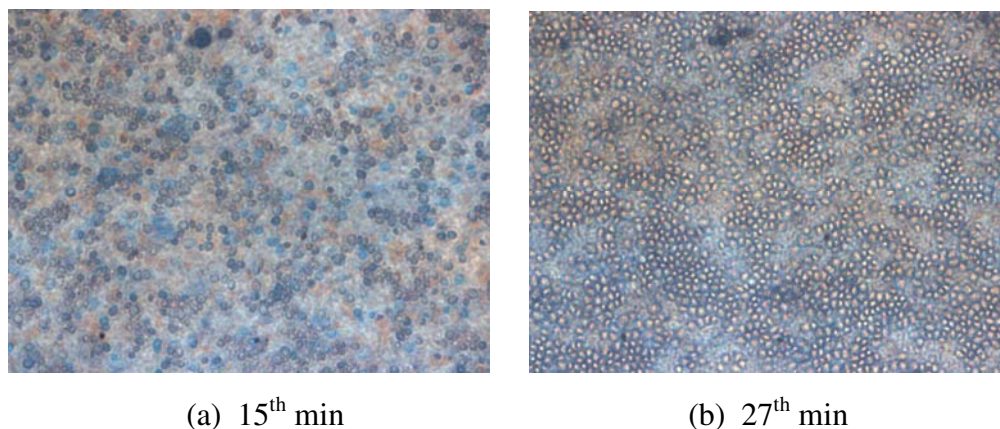


**Figure 4.9** Images captured during filtration of washed yeast at concentration 0.525 g/l and CFV 0.2 m/s. (a) operated at 45 l/m<sup>2</sup>h and (b) operated at 60 l/m<sup>2</sup>h.

#### 4.4 Influence of surface charge (pH)

The surface charge of particles and membranes can be changed by adjusting the solution pH or introducing an electrolyte in the filtration processes. The adjustment of pH and ionic strength of feed solutions are often performed as a pretreatment practice to protect membranes or enhance filtration rate. However, this factor is not integrated into many mathematical models, such as the shear-induced diffusion model. Some references to the influence of pH and ionic strength can be found in the literature (Bacchin *et al.*, 1996; Huisman *et al.*, 1999). However, most of the experiments were conducted in constant pressure mode and the results were explained in terms of the permeability of the structural cake formed from the very beginning of the filtration. In constant flux operations, there will be no cake formed on the membrane below critical flux. In such a situation, pH and ionic strength must exert their influence on the filtration during the transient particle deposition, and hence the electrostatic force has an effect only when the particles are close enough to the membrane. The influence of particle and membrane surface charge on critical flux was studied in this (in terms of pH) and the subsequent (in terms of ionic

strength) sections. This section was aimed to investigate the interactions (adsorption and deposition) between particle and particle as well as particle and membrane.

When a concentrated particle solution is re-dispersed into feed, particle surface charge can be changed accordingly with the suspension pH. The same thing occurs to the membrane surface once it contacts the feed flow. Thus, the repulsion or attraction between particle and membrane can be assessed by measuring the zeta potential of both the particle and the membrane in well defined pH solutions. The zeta potentials of both the particles (latex and yeast) and the membrane were measured and the results were reported in Chapter 3. The results showed that the iso-electric point (IEP) of the membrane was about pH 8 (Figure 3.12). The IEP of the latex particles was around pH 3 (Figure 3.8), and the washed yeast was negatively charged over the range of the tested pH values (pH 2 to 9) (Figure 3.9).

When crossflow filtration occurs, the particles in the feed suspension will be dragged towards the membrane surface by the convective forces due to the permeate flux imposed on the particles. Hydrodynamic 'back transport', such as the shear-induced diffusion, has an opposite effect. As the particle approaches the membrane, electrostatic interaction can occur. Repulsion would exist between particles and membranes with the same charge, and attraction would occur with opposite charges. Higher zeta potentials increase inter-particle repulsion and thus cause less particle deposition as the electrostatic forces are proportional to zeta potential and particle size ( $F_e \propto \xi \times r$ ) (McDonogh *et al.*, 1989). After fouling begins, more particles are transported towards the membrane and form a cake layer on the spot. At this point, the surface charge between particles themselves can exert an influence on the filtration resistance caused by the cake layer. The cake resistance is dependent on the thickness of the electrical double layer on the particles. The double layer is thicker at higher zeta potential (Figure 2.8) since the

double-layer repulsion force is proportional to the square of zeta potential. This causes the particles to avoid contact with each other. The larger distance between the particles in the cake layer leads to a high porosity cake. Therefore, the cake resistance is much lower due to the space between the particles in the cake layer.

The critical fluxes of latex particles and washed yeasts at various pH values are shown in Figures 4.10 and 4.11 respectively. It could be seen from Figure 4.10 that the changes in pH of the feed did not have a significant effect on the critical fluxes of 5.0 and 10.0  $\mu\text{m}$  latex particles. The critical fluxes of the 5.0  $\mu\text{m}$  latex were all around 70  $\text{l/m}^2\text{h}$ . The critical fluxes of 10.0  $\mu\text{m}$  latex varied from 100 to 110  $\text{l/m}^2\text{h}$ . However, it was interesting to find that the critical fluxes of 3.0  $\mu\text{m}$  latex started from a lower point at low pH values and then reached a plateau as the pH increased. This was due to the smaller size of the 3.0  $\mu\text{m}$  latex. The interaction forces between the particles and membrane played a more important role for small particles. The double layer force was negligible for bigger particles compared with the convective drag forces and the hydrodynamic back transport forces.

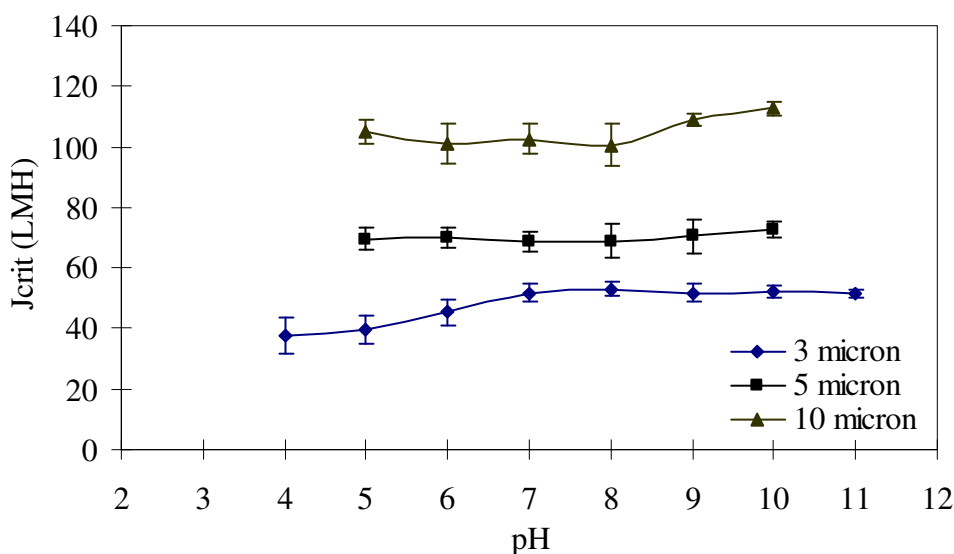


**Figure 4.10** Critical flux vs. solution pH in filtration of latex at CFV 0.2 m/s.

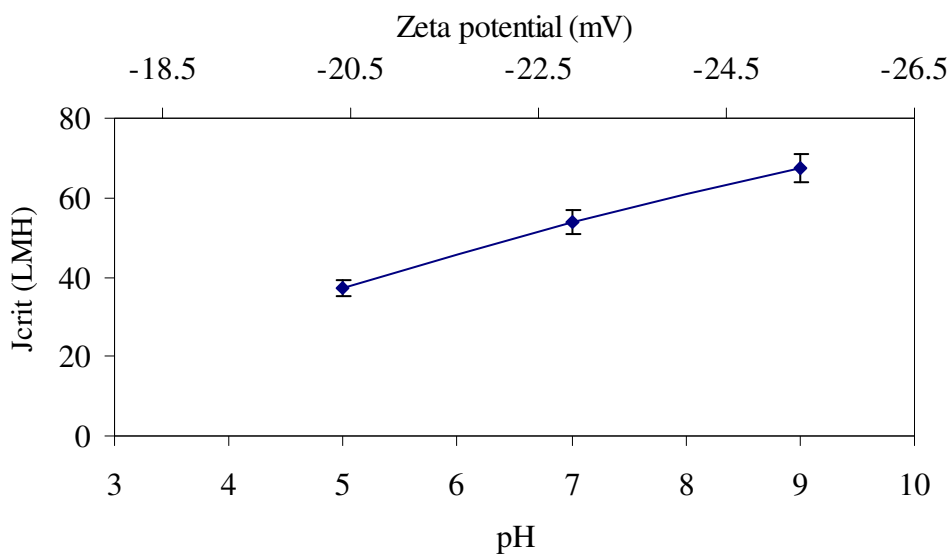


**Figure 4.11** Critical flux vs. solution pH in filtration of yeast at CFV 0.2 m/s.

The interactions between the 3.0  $\mu\text{m}$  latex particles and the membrane at lower pH values could lead to the particle deposition at the startup when the latex was positively charged and the membrane was negative. Figure 4.12 shows 3.0  $\mu\text{m}$  latex particles attached to the membrane at zero flux at pH 5. Once attached, it was difficult to remove the particles by increasing the crossflow. This behavior was not observed with 5.0 and 10.0  $\mu\text{m}$  latex particles, or with yeast cells.

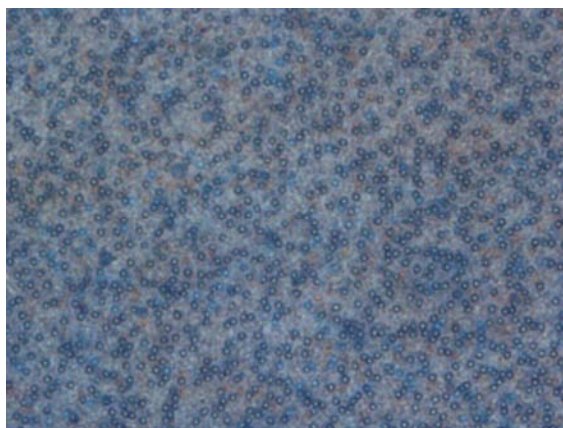


**Figure 4.12** 3.0  $\mu\text{m}$  latex particles attached to the membrane before filtration had started when flux was zero at pH 5.

The particle size distribution was measured using the Mastersizer (Malvern, UK) to detect any particle aggregation in high pH suspensions. The results showed that the particle size distributions were not changed after circulation in the filtration system. In fact, in order to prevent the self-aggregation of latex particles, the feed suspensions were vigorously stirred while running the experiments.

Shown in Figure 4.11 are the critical fluxes of 5.0  $\mu\text{m}$  washed yeast cells at different pH values. The tests were conducted within a limited pH range since the yeast cells could be destroyed at extreme pH values. The yeast cells were negatively charged in the suspensions. They had a high zeta potential of -25 mV at the tested pH values (refer to Figure 3.9). It could be seen that the critical fluxes of the yeasts increased with solution pH. The yeast cells were more susceptible to pH changes than the latex particles. The reason for this was probably because that the yeast cells had a higher absolute zeta potential (Figure 3.9) than the latex particles (Figure 3.8). A conclusion could be drawn that small particulates with high absolute zeta potential were more sensitive to the changes in pH values.

## 4.5 Influence of ionic strength

The critical fluxes of particle suspensions in electrolytes were measured in this study. The solution ionic strength exerted an influence on both particle-particle and particle-membrane interactions by suppressing electrical double layer and reducing electro-kinetic effects. To prevent any particle aggregation, vigorous stirring was applied to the feed suspensions. Figures 4.13 and 4.14 show that the critical fluxes decreased in the presence of NaCl in the feed suspensions. This confirmed the results by Nazzal *et al.* (1994) using 1  $\mu\text{m}$  silica suspensions and  $\alpha$ -alumina membranes. The critical flux decreased rapidly at first when the salt was present in the feed and then reached a stable value regardless of how much salt was introduced.

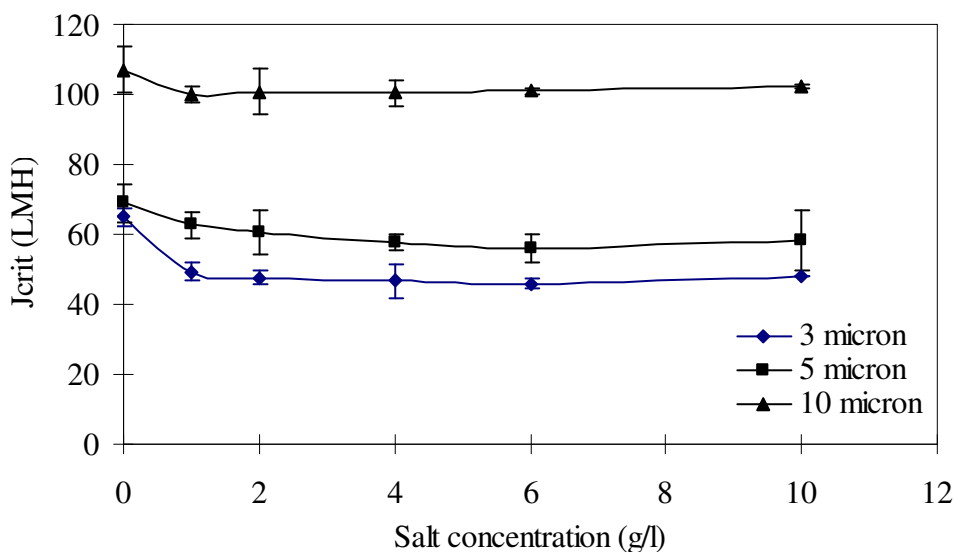


**Figure 4.13 Critical flux vs. ionic strength in the filtration of latex at 0.2 m/s.**

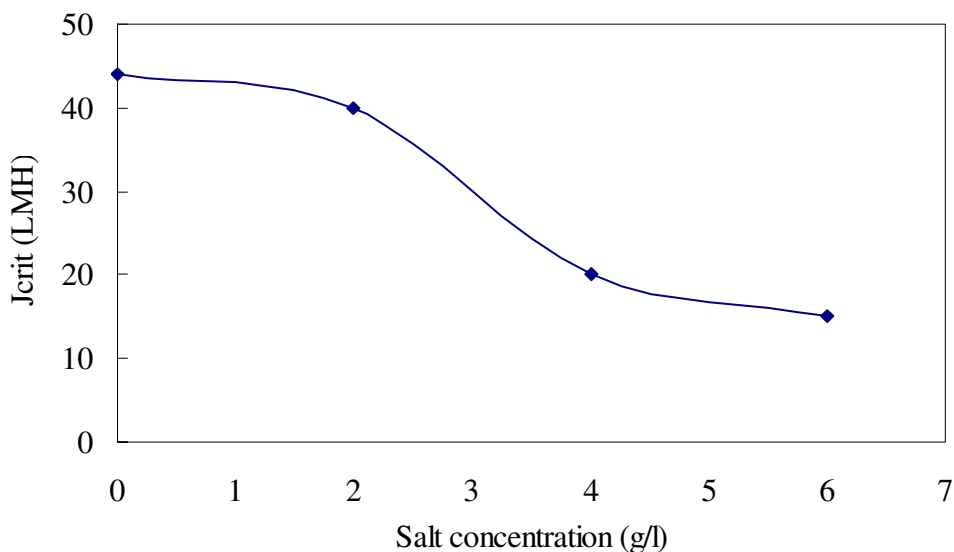


**Figure 4.14 Critical flux vs. ionic strength in the filtration of yeast at 0.1 m/s.**

High ionic strength caused the critical flux to decrease for both latex and yeast particles. However, its effect had different magnitudes, and was more significant for the yeast cells (decreased by 55%) than the 3.0  $\mu\text{m}$  latex particles (decreased by 30%). Thus the permeate flux of yeast was relatively more sensitive to the changes in ionic strength than the latex particles, and this linked to the greater sensitivity of



the yeast flux. Sharma *et al.* (1992) studied the effect of ionic strength on the detachment of colloidal particles from surfaces using 10  $\mu\text{m}$  glass microspheres in 1 molar NaCl. They found that the effect of ionic strength was not as large as pH in their case. Decreasing ionic strength only produced a marginal increase in detachment. This was in agreement with the results of 10.0  $\mu\text{m}$  latex particles in Figure 4.13.

Nazzal and Wiesner (1994) evaluated the effects of pH and ionic strength on the performance of ceramic microfiltration membranes ( $\alpha$ -aluminum, 0.8  $\mu\text{m}$ ). They measured the zeta potentials of alumina and silica in two different ionic strength electrolytes. The IEP of their membranes was at pH 8.3 which is similar to the Anodisc membranes (IEP at pH 8) used in this study. They found that the zeta potentials of the membrane and silica in the two ionic strength electrolytes were similar. They used particle-free electrolyte and silica suspension at the same pH and ionic strength to test the membrane permeability. Even using the particle-free electrolyte only, the membrane permeability decreased at higher ionic strength. The membrane permeability under different salt concentrations was also tested in this study. The results showed little difference (10 %) compared with the MQ water. The electro-kinetic properties of the silica particles played a minor role in the membrane permeability, probably due to the changes in the composition of counter ions that accumulated near the pore wall within the membrane. In other words, ionic strength had no effect on the zeta potentials of particles and membranes. The interactions between particles and membranes were not influenced by ionic strength. This could explain why the permeate flux decreased once the salt was present in the feed and then did not change with the salt concentration. Unlike the latex particles, the yeast cells were more sensitive to the ionic environment. The outer layer of the cells could behave readily according to the changes in the ionic environment.

Singh and Song (2005) investigated the effect of ionic strength colloidal fouling in terms of fouling potential. Similarly, they found that the fouling potentials achieved a plateau with the increasing of ionic strength meaning that the permeate flux decline was independent of ionic strength at relatively high salt concentrations. They ruled out the possibility of particle coagulation. Unfortunately, they did not provide an explanation for that phenomenon.

Chang *et al.* (1995) studied the effect of electrolyte concentration on the quasi-steady state permeate flux. The permeate flux declined slowly at relatively high electrolyte concentrations.

## 4.6 Influence of particle size

It is well accepted that the size or size distribution of particulates to be filtered has a significant influence on filtration performance. Colloidal particles can block or penetrate MF filters resulting in frequent membrane replacement or low quality in permeate. Pretreatments such as flocculation *etc.* are often required to aggregate colloids as large flocs are preferred in filtration and separation processes. In practice, the suspensions to be treated in MF normally consist of particles with various species and different particle sizes instead of a uniform value. The selection of membrane filters depends heavily on the smallest particles in order to remove all of the suspended solids. In this section, the influence of uniform particle sizes of monodisperse latex suspensions was discussed. The effect of particle size distribution was discussed in the subsequent two chapters.

In this study, 3.0, 5.0 and 10.0  $\mu\text{m}$  latex particles were used to test the critical flux as a function of particle size. It could be seen clearly from Figure 4.15 that the critical flux increased with the latex particle size. The 10.0  $\mu\text{m}$  latex particles

always gave higher critical fluxes. According to Figure 2.9 in Chapter 2, the Brownian diffusion model (Equation (2-15)) predicted that the permeate flux decreased with the particle size for small particles less than about  $0.5\ \mu\text{m}$  as shown in Table 4.1. Although the shear-induced diffusion and the inertial lift models (Equations (2-18) and (2-21)) both predicted that the bigger particles produced higher permeate flux, the degree was different. The influence of particle size was more sensitive for particles larger than  $30\ \mu\text{m}$  than for particles in the range of  $0.5$  to  $30\ \mu\text{m}$ .

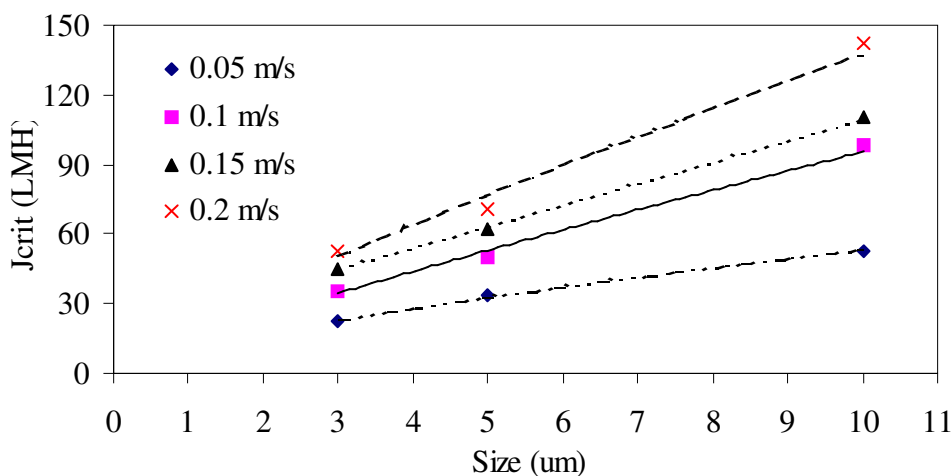


**Figure 4.15**  $J_{crit}$  vs. size of latex particles at pH 8, CFV 0.2 m/s and concentration 0.05 % vol..

Based on the measured relative magnitudes of  $J_{crit}$ , the relationship  $J_{crit} \propto a^m$  (Equation (5-1)  $J_{crit} = AU^n a^m$ ) gave an exponent  $m$  in the range 0.7 to 0.8. This exponent was significantly lower than the value of 3.0 required for the inertial lift model and closer to that of 1.33 predicted by the shear-induced diffusion model. Hence, the current results supported the notion that the back transport was mainly due to the shear-induced diffusion. The deviation in the exponent  $m$  implied that the back transport could be a combination of two or more mechanisms.

## 4.7 Influence of flow channel height

As discussed in Section 4.2, the permeate flux in crossflow MF is correlated with the shear rate across the membrane surface. This shear rate can be calculated by the expression  $\gamma_o = \frac{6U}{H}$ . It can be seen that the shear rate is a function of channel height ( $H$ , m) and crossflow velocity ( $U$ , m/s). Based on these considerations, it is worth studying the effect of feed channel geometry on critical flux. In this thesis, most of the experimental results were obtained using a membrane cell with a feed flow channel height of 2 mm. For comparison, a membrane cell with a feed flow channel height of 1 mm was tested. In this section, the two membrane cells with different feed channel heights (1 and 2 mm) were used to study the effect of feed channel height on critical flux.

Table 4.2 shows the results of critical fluxes using the two membrane cells. The critical fluxes of single-sized latex particles were obtained using the membrane cell with 1 mm channel height. These results were compared with those mentioned in Section 4.2. In Table 4.2, the average shear stress produced by the tangential flow was calculated using the expression  $\gamma_o = \frac{6U}{H}$ . Thus the shear rate in the case using 1 mm channel under 0.1 m/s was the same as that using 2 mm channel under 0.2 m/s. From this table, it could be seen that although the shear rates using the two membrane cells were the same, the critical fluxes defined by the DOTM were different. When the CFV/shear rate was doubled using the 1 mm membrane cell, the critical fluxes of the single-sized particles were more than doubled, while it was less than doubled for the 2 mm cell.

**Table 4.2 Critical flux measurements under different CFVs using two membrane cells with different flow channel heights at concentration 0.05 %**

| Particle size<br>( $\mu\text{m}$ ) | Channel height<br>(mm) | CFV<br>(m/s) | Shear rate<br>$\gamma$ ( $\text{s}^{-1}$ ) | $J_{crit}$<br>( $\text{l/m}^2\text{h}$ ) | $J_{crit}/\gamma$ |
|------------------------------------|------------------------|--------------|--|--|-------------------|
| <b>3.0</b>                         | 1.0                    | 0.1          | 600  | 32                                       | 0.05              |
|                                    |                        | 0.2          | 1200                                       | 75                                       | 0.06              |
|                                    | 2.0                    | 0.1          | 300  | 35                                       | 0.12              |
|                                    |                        | 0.2          | 600  | 50                                       | 0.08              |
| <b>5.0</b>                         | 1.0                    | 0.1          | 600  | 42                                       | 0.07              |
|                                    |                        | 0.2          | 1200                                       | 105                                      | 0.09              |
|                                    | 2.0                    | 0.1          | 300  | 50                                       | 0.17              |
|                                    |                        | 0.2          | 600  | 70                                       | 0.12              |
| <b>10.0</b>                        | 1.0                    | 0.1          | 600  | 110                                      | 0.18              |
|                                    |                        | 0.2          | 1200                                       | 190                                      | 0.16              |
|                                    | 2.0                    | 0.1          | 300  | 98                                       | 0.33              |
|                                    |                        | 0.2          | 600  | 142                                      | 0.24              |

According to the mathematical theories (for example, SID), the critical fluxes should be the same regardless of the flow channel height as long as the shear rate is constant. In the shear-induced diffusion model which is often used to predict the permeate flux in CFMF, the critical flux varies linearly with the shear rate (Belfort *et al.*, 1994). However, such a phenomenon did not occur to the two membrane cells in this study. There were two possibilities to explain this. First, the shear-induced diffusivity was an empirical coefficient derived from the experiment tests using large particles (500 and 1600  $\mu\text{m}$ ) in high particle concentrations in linear shear flows at low Reynolds numbers. These were not the conditions in this study. Second, the way of calculating the shear rate was over-simplified. The average values of CFV were used to represent the flow conditions in the feed channel. Actually there was a velocity gradient along the channel height. The real local shear rate had to be calculated by the laminar flow profile. The complicated flow made the precise

predictions difficult and therefore led to the differences between the experimental results and theoretical predictions.

The local crossflow velocities shown in Figure 4.16 were calculated according to the relationship (Massey, 1989):

$$u(y) = 3U_o y(2H_o - y) / 2H_o^2 \quad (4-5)$$

where  $u(y)$  is the local velocity along the flow channel height,  $U_o$  is the maximum crossflow velocity,  $H_o$  is half channel height and  $y$  is the distance from the channel wall.

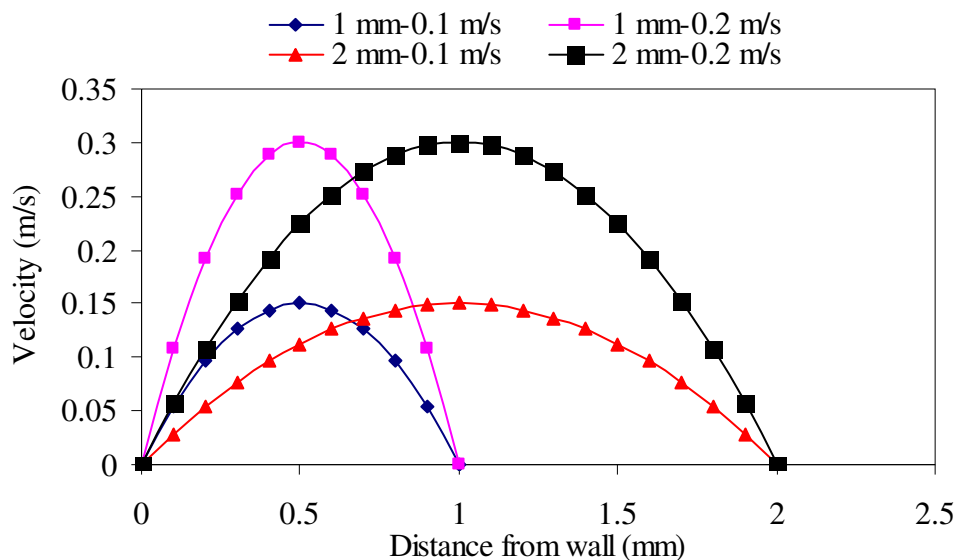


**Figure 4.16 Crossflow velocity distribution in the flow channel.**

The flow velocity distributions along the 1 and 2 mm flow channels at a CFV of 0.1 and 0.2 m/s respectively are shown in Figure 4.16. It could be seen that the use of the average CFV in the mathematical models was over-simplified. Further

corrections on this issue should be done. The investigation of the flow conditions in the flow channel was out side the scope of this study due to the time constraint.

The last column in Table 4.2 shows the normalized critical fluxes divided by the shear rate. It was noticed that for each particle size, each flow channel had the similar normalized critical fluxes at different CFVs. Table 4.3 shows the normalized critical fluxes of the shear rate and channel height for the latex particles. It could be seen that the normalized critical flux was doubled when the particle size was increased from 5.0  $\mu\text{m}$  to 10.0  $\mu\text{m}$ . The normalized critical fluxes were good universal guidance for the operating practice.

**Table 4.3 Normalized critical fluxes for the latex particles**

| Size                    | 3.0             | 5.0             | 10.0            |
|-------------------------|-----------------|-----------------|-----------------|
| $J_{crit}/\gamma_o * H$ | $0.06 \pm 0.01$ | $0.08 \pm 0.01$ | $0.16 \pm 0.02$ |

## 4.8 Summary

The major factors influencing the performance of crossflow microfiltration were investigated using a non-invasive and in situ observation technique (DOTM). The single-sized spherical latex particles with uniform particle sizes (3.0, 5.0 and 10.0  $\mu\text{m}$ ) were used as the model particles to eliminate the complexities of the particle structure and size distribution. The commencement of the particle deposition was observed clearly by the DOTM technique. It was observed that the critical flux increased with the CFV or shear rate. However, the relationship between the flux and CFV was not linear and the exponent was less than 1.0. The critical flux decreased with the feed particle concentration as the higher particle numbers increased the possibility for particle landing on the membrane surface. The pH and ionic environment of the feed suspensions were well controlled. The changes in pH

had more significant effect on the membrane fouling for the smaller latex particles. Increase in pH increased the critical flux of the washed baker's yeast suspensions. The presence of salt in the suspensions had negative influence on permeate flux due to the thinner electric double layer. The increase in particle size benefited the filtration performance. The larger particles produced higher critical flux. This was the reason why particle aggregation was often practiced to improve the separation process. Two membrane cells with different flow channel heights (1 and 2 mm) were used to study the influence of the cell morphology. The fluid flow condition in the feed channel had a direct influence on the critical flux. The complexity of the fluid conditions in the flow channel should be avoided when study the factors influencing the filtration rate. Two possible reasons why there was difference between the experimental results and model predictions based on the shear-induced diffusion model were proposed. The way of calculating the shear rate was oversimplified and was probably the reason for the observations in this study.



## Chapter 5 Critical flux and particle deposition of bidisperse suspensions during crossflow microfiltration

Crossflow microfiltration (CFMF) is widely used for particulate removal in industries, including clarification of fruit juices in food industry, separation of bacteria in pharmaceutical industry, and cleaning of potable water in water treatment plant *etc.* The build-up of a particle layer on membrane surface, *i.e.* membrane fouling, is a major challenge in these operations. Fortunately, the fouling layer can be controlled at a low level by the tangential flow parallel to the membrane surface in CFMF. Lower pressure and higher flux are possible when the system is operated properly. Membrane fouling occurring during crossflow microfiltration is a complicated process. Well-defined polystyrene latex particles are often used to study the factors influencing the permeate flux in the literature. When operated below critical flux, the permeate flux is often the same as the flux for pure water according to the concept of “critical flux” (Field *et al.*, 1995). However, the permeate flux for microorganism separation is usually lower than that for pure water even below the critical flux. This is due to the complex nature of the microorganism feeds where the microbial cells are able to attach readily to almost any submerged surface. Deposited cells will grow eventually resulting in concentrated solutions and produce extra-cellular polymeric substances (EPS), and then form a bio-film (Bos *et al.*, 1999). The presence of a bio-film is often referred to as bio-fouling. Hence, the study of how the nature of microorganism feeds influences the permeate flux is necessary. Among the parameters, the particle size and distribution are of interest in this study.

The effect of particle size was reviewed in Section 2.4.7, Chapter 2. Experimental results were also presented for mono-sized latex particles in Section 4.6 in Chapter 4. However, in the real situation, the particle suspensions often contain different-sized particulates and even different species. This particle size distribution will make the fouling process even more complicated. Unfortunately, most fouling mechanism studies were focused on the idealized situation where only particles with uniform size were present in the suspensions. A study using bidisperse

suspensions to investigate the fouling mechanisms should be useful as a transition from the idealized situation to the more realistic situations.

The definition of critical flux implied that at the critical value the convective drag forces on the particles towards the membrane (caused by the permeate flux) would balance the back transport forces (caused by the tangential crossflow) away from the membrane. Neglecting electrostatic interactions, the back transport mechanism could be inertial lift (Drew *et al.*, 1991) or shear-induced diffusion (Zydney *et al.*, 1986). Both of these mechanisms predicted a critical flux relationship of the form,

$$J_{critical} = AU^n a^m \quad (5-1)$$

where  $U$  is the crossflow velocity and  $a$  is the particle radius. The exponent  $m$  is 3 for the inertial lift and 1.33 for the shear-induced diffusion.

According to Equation (5-1) for particles in the micron-size range, the critical flux is predicted to increase with particle size (Figure 2.9), and this trend was clearly observed by Kwon *et al.* (2000) and Li *et al.* (2000), and the magnitude and trend favored the shear-induced diffusion mechanism (Li *et al.*, 2000). In Chapter 4, the influence of the crossflow velocity was discussed (Section 4.2). The exponent,  $n$  was measured to be 0.62 to 0.77 which was comparable with the shear-induced diffusion (SID) model ( $n = 1.0$ ). Figure 4.5 also showed that the results were in good agreement with the SID model.

In practical applications, the value of critical flux is often determined by monitoring the transmembrane pressure (TMP) in a flux stepping test (Li *et al.*, 1998). As the flux is stepped upwards, a flux is reached where a cake begins to form and TMP starts to steadily increase. This flux is then defined as the critical flux. However, the critical flux value obtained in this manner is usually higher than the actual value unless sufficient time is allowed for the deposition to accumulate and cause a detectable increase in pressure (Li *et al.*, 1998). This may be due to either the low

sensitivity of the pressure transducers to minor pressure changes or the low specific resistance provided by the foulants.

Another approach to identifying critical flux is to utilize optical instruments to view the particle deposition on a membrane. With well-controlled crossflow hydrodynamics, it is possible to see the membrane shifting from no particle deposition to cake formation as the flux transits across the “critical flux”. The observation approach also provides direct insights of fouling mechanisms.

In real systems, the feed suspensions are likely to be mixtures of sizes. For a mixture, the cake formed in crossflow should preferentially contain smaller particles, as these particles have a lower critical flux. This observation was achieved previously (Li *et al.*, 1998). However, the effect of mixture composition on critical flux received little attention. One report by Madaeni (1997b) using latex particles of 1.0 and 0.1  $\mu\text{m}$  size and their mixture (50/50 in composition) gave critical fluxes of 120, 105 and 88  $\text{l/m}^2\text{h}$  respectively, *i.e.* the mixture gave the lowest critical flux. The reported critical fluxes were obtained by flux stepping and TMP measurements. There might be some interactions between the particles and the membrane pores since the pore size (0.22  $\mu\text{m}$ ) was larger than the smaller particles such that the smaller particles could block or penetrate through the membrane. The membrane pore blockage would lead to a lower critical flux.

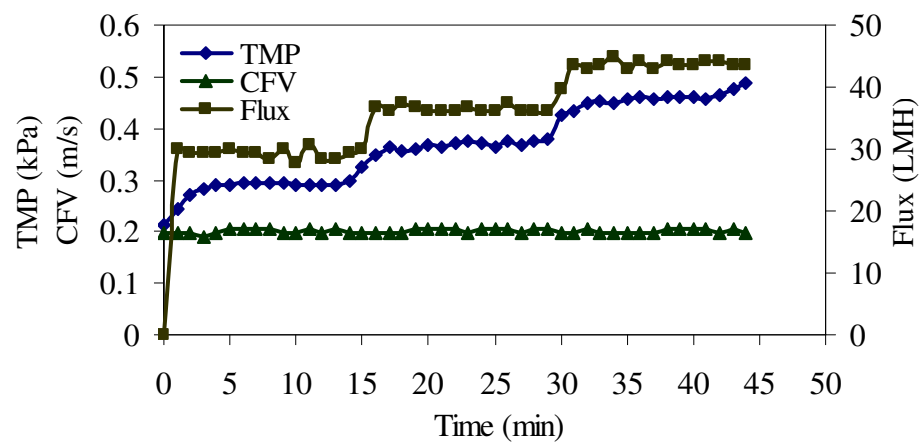
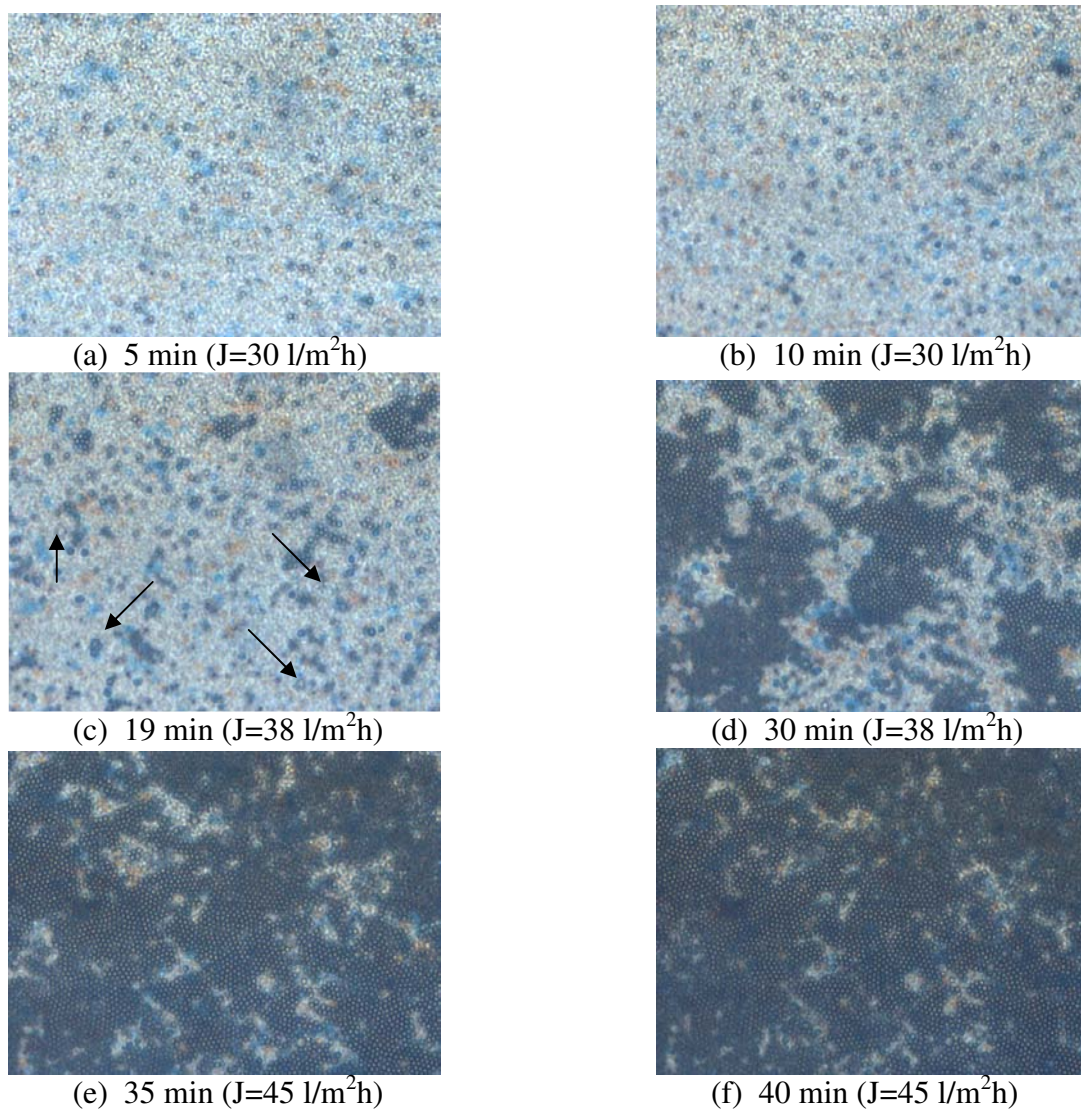
In this study, the non-invasive, in situ, direct observation through membrane technique, rather than TMP monitoring, was used to investigate the changes in the critical fluxes of idealized bidisperse suspensions with different compositions of particle sizes and concentrations. The critical fluxes of single-sized latex particles (3.0, 5.0 and 10.0  $\mu\text{m}$ ) and their mixed suspensions (3.0+5.0  $\mu\text{m}$ , 5.0+10.0  $\mu\text{m}$  and 3.0+10.0  $\mu\text{m}$ ) were determined using the DOTM. The critical fluxes of the single-sized particles in Chapter 4 were used as a distinct comparison with the results to be reported in this chapter. This is the first reported investigation of bidisperse suspensions of latex beads each with a discrete distribution in CFMF using the DOTM technique.

## 5.1 Critical fluxes of bidisperse latex feeds

In order to compare the filtration behavior between single-sized and mixed latex suspensions, the critical fluxes of both suspensions have to be determined separately. In Chapter 4, the critical fluxes of the single-sized latex particles (3.0, 5.0 and 10.0  $\mu\text{m}$ ) under various conditions were measured. In this section, the critical fluxes of the mixed latex suspensions (3.0+5.0  $\mu\text{m}$ , 5.0+10.0  $\mu\text{m}$  and 3.0+10.0  $\mu\text{m}$ ) were measured by the DOTM and the results were compared with those in Chapter 4.

In an attempt to understand the effects of particle-particle interactions on filtration rate and the fouling mechanisms of mixed feeds, bidisperse suspensions were tested by mixing two single-sized latex particles together at different concentration ratios. The critical fluxes of the bidisperse suspensions were then measured at a crossflow velocity of 0.2 m/s.

Figure 5.1 (a)-(f) shows the evidence that the smaller particles in the mixed suspensions deposited on the membrane during the filtration of a mixture of 3.0 and 5.0  $\mu\text{m}$  latex particles at concentrations of 0.05 and 0.01 % vol. respectively. The operating conditions were recorded in Figure 5.1 (g). It could be seen from Figure 5.1 (a) and (b) that at the permeate flux of 30  $\text{l/m}^2\text{h}$ , no significant deposition of particles on the membrane surface was observed. After the imposed flux was increased to 38  $\text{l/m}^2\text{h}$  from the 15<sup>th</sup> minute, the smaller particles in the mixed suspension started to deposit on the membrane at a moderate rate (Figure 5.1 (c) and (d)). The fouling pattern was not much different from the fouling by the single-sized particles. Some larger particles were spotted on the membrane surface during the occurrence of fouling (refer to the arrows in Figure 5.1 (c)). However, the larger particles deposited on the membrane were negligible compared with the huge amount of the smaller particles and often were re-entrained back to the bulk. The membrane was totally covered by a mono layer of the smaller particles after 40 minutes (Figure 5.1 (f)) after the flux was increased further up to 45  $\text{l/m}^2\text{h}$ . The TMP history in Figure 5.1 (g) showed a transient variation consistent with the observations in the images.



(g) Operating conditions

**Figure 5.1** DOTM images of particle deposition during filtration of 3.0 and 5.0  $\mu\text{m}$  latex particles (0.05 and 0.01 % vol. respectively) at CFV = 0.2 m/s.



Figure 5.2 shows the critical fluxes of 3.0 and 5.0  $\mu\text{m}$  latex particles at a crossflow velocity of 0.2 m/s where the concentrations of 3.0  $\mu\text{m}$  latex were fixed at 0.02 and 0.05 % vol. respectively and the concentrations of 5.0  $\mu\text{m}$  latex particles were changed from 0.01 to 0.05 % vol. The critical fluxes of the individual components from 0.01 to 0.05 % vol. were also shown.

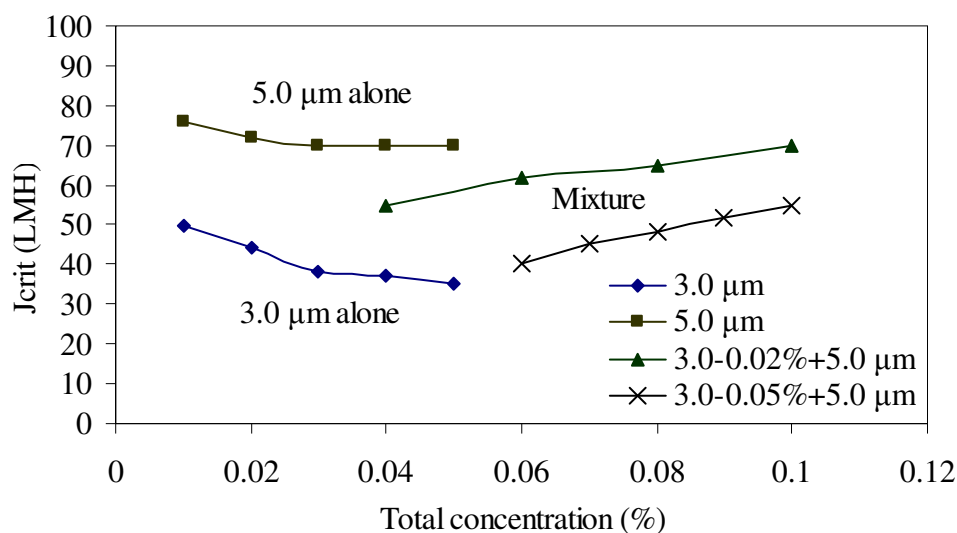


**Figure 5.2 Critical flux of single and mixed feeds of 3.0 (0.05% vol.) and 5.0  $\mu\text{m}$  latex particles at CFV = 0.2 m/s.**

The first important observation here was that only the smaller particles in the bidisperse suspensions were found to deposit on the membrane surface when the imposed flux was higher than the critical flux of the bidisperse suspensions, and the first fouling layer on the membrane only consisted of the smaller particles (Figure 5.1). Unfortunately, it was not known whether the larger particles deposited in the subsequent fouling layers or not due to the technical limitations of the DOTM technique described in Chapter 3. However, one could ascertain that when the larger particles deposited, it would be at a flux greater than the critical flux of the smaller particles. The mixture data in Figure 5.2 were effectively the critical fluxes of the smaller particles at a constant concentration in the presence of increasing concentrations of the larger particles. In Figure 5.2, the concentration vs. critical flux curves of single-sized latex particles showed a decreasing trend. The reason was discussed in Section 4.3 in Chapter 4. However, the curves of bidisperse latex

suspensions showed a contrary trend. The critical fluxes of the mixed feeds increased with the concentration of the larger latex particles present in the mixtures although the total concentrations were increased. The larger particles overcame the concentration effect and increased the critical flux. For the same total concentration, the critical flux was higher if there were more of the larger particles and less of the smaller particles in the mixed suspensions.

Additional tests on the critical fluxes of the bidisperse suspensions of 5.0 +10.0  $\mu\text{m}$  and 3.0 +10.0  $\mu\text{m}$  latex particles were also conducted (shown in Figures 5.3 and 5.4). Similar phenomena on mixtures of 5.0+10.0  $\mu\text{m}$  and 3.0+10.0  $\mu\text{m}$  latex particles occurred as described above in the experiments. Only the smaller latex particles in the bidisperse suspension deposited on the membrane until the entire membrane surface was covered by the smaller particles. Then the experiment had to be stopped after a mono cake layer was formed.

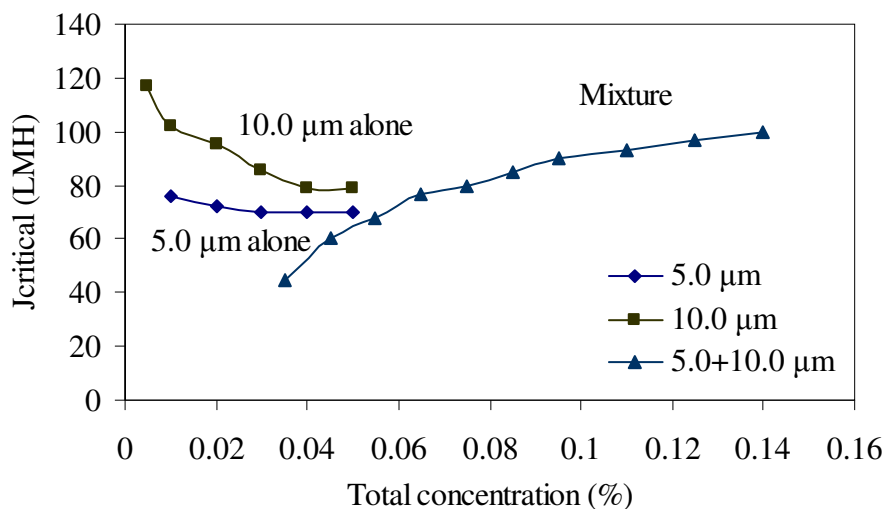


**Figure 5.3 Critical flux of bidisperse feed of 5.0 (0.025 % vol.) and 10.0  $\mu\text{m}$  latex particles at CFV = 0.2 m/s.**

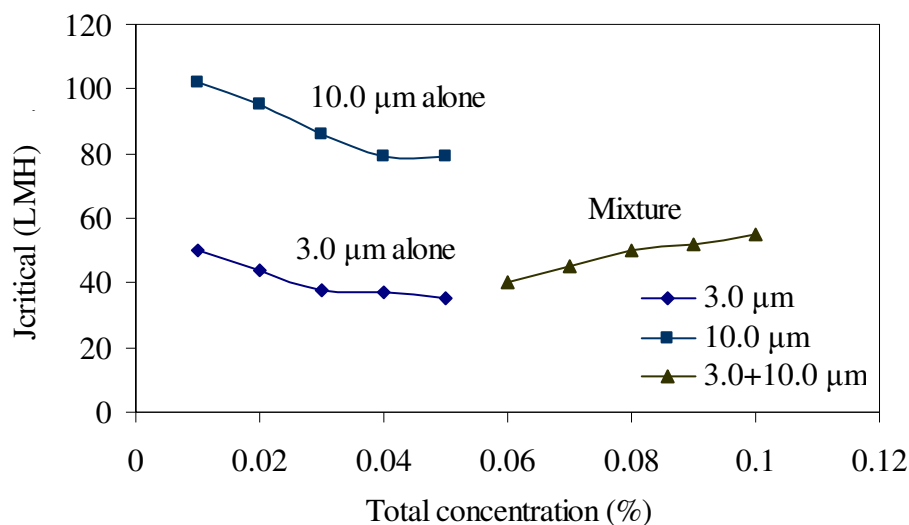


**Figure 5.4** Critical flux of bidisperse feed of 3.0 (0.05 % vol.) and 10.0  $\mu\text{m}$  latex particles at  $\text{CFV} = 0.2 \text{ m/s}$ .

Figure 5.5 summarizes the percentage of critical flux improvement brought about by the addition of the larger particles into the systems. It could be seen that the critical flux increased with the concentrations of the larger particles and the improvement could be as high as about 120 % when the larger particles were added, even though the absolute concentration was also increased at the same time.

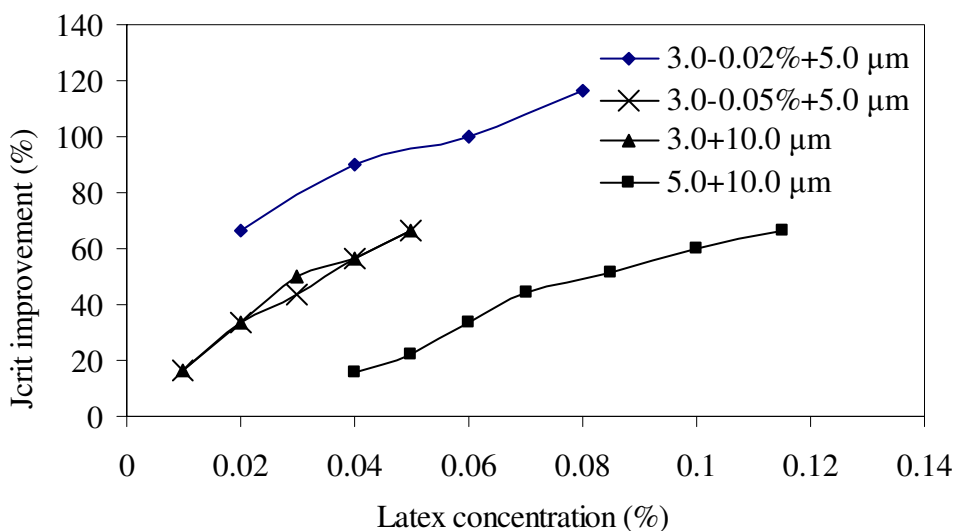


**Figure 5.5** Critical flux improvement by the addition of big particles during the filtration of the mixed latex particles at  $\text{CFV} = 0.2 \text{ m/s}$ .



Table 5.1 summarizes the experimental results of the critical fluxes measured in the tests. The results illustrated the fact surprisingly that the critical fluxes of the bidisperse suspensions were higher than the individual single-sized particles even though the bidisperse suspensions were at a higher concentration. Thus the presence of the larger particles increased the critical flux of the smaller (compare for 3.0  $\mu\text{m}$  at 0.05 % alone at a critical flux of 37  $\text{l/m}^2\text{h}$  and in the presence of 5.0  $\mu\text{m}$  at 0.05 % a critical flux of 55  $\text{l/m}^2\text{h}$ ). Similarly, the presence of the smaller particles could increase the critical flux of the larger (compare 10.0  $\mu\text{m}$  at 0.05 % alone with a critical flux of 77  $\text{l/m}^2\text{h}$  and in the mixture with 5.0  $\mu\text{m}$  particles a critical flux of > 90  $\text{l/m}^2\text{h}$  in Figure 5.3 [only 5.0  $\mu\text{m}$  particles were observed above this flux]). In other words, the interactions between the smaller and larger particles increased the critical fluxes. Furthermore, the critical fluxes of the mixed suspensions increased with increasing concentrations of the larger particles, the trend of which was in stark contrast with the behavior of a single particle size.

**Table 5.1 Critical fluxes of latex particles suspensions**

**Unit:  $J$ -  $\text{l/m}^2\text{h}$**

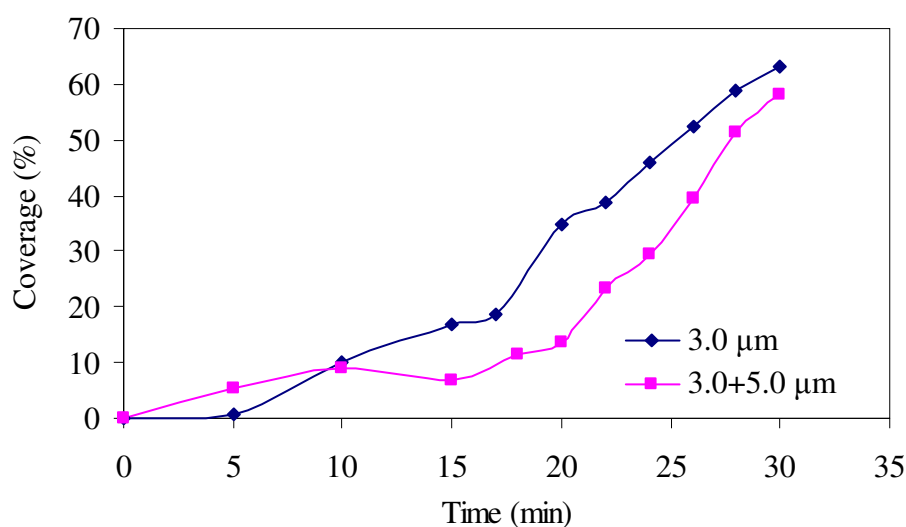
| CFV 0.2 m/s     | 3.0 $\mu\text{m}$     | 5.0 $\mu\text{m}$     | 10.0 $\mu\text{m}$    | 3.0+5.0 $\mu\text{m}^*$ | 5.0+10.0 $\mu\text{m}^*$ | 3.0+10.0 $\mu\text{m}^*$ |
|-----------------|-----------------------|-----------------------|-----------------------|-------------------------|--------------------------|--------------------------|
| Concentration % | $J_{\text{critical}}$ | $J_{\text{critical}}$ | $J_{\text{critical}}$ | $J_{\text{critical}}$   | $J_{\text{critical}}$    | $J_{\text{critical}}$    |
| 0.01            | 50                    | 76                    | 102                   | 40                      | 45                       | 40                       |
| 0.02            | 44                    | 72                    | 95                    | 45                      | 60                       | 45                       |
| 0.03            | 38                    | 70                    | 86                    | 48                      | 68                       | 50                       |
| 0.04            | 37.5                  | 70                    | 77                    | 52                      | 77                       | 52                       |
| 0.05            | 37                    | 70                    | 77                    | 55                      | 80                       | 55                       |

**\*Note:** For the 3.0+5.0  $\mu\text{m}$  suspensions, the concentration of 3.0  $\mu\text{m}$  particles was fixed at 0.05 % vol. and the first column indicates the concentration of the 5.0  $\mu\text{m}$  particles. For the 5.0+10.0  $\mu\text{m}$  suspensions, the concentration of 5.0  $\mu\text{m}$  particles was fixed at 0.025 % vol. and the first column indicates the concentration of the 10.0  $\mu\text{m}$  particles. For the 3.0+10.0  $\mu\text{m}$  suspensions, the concentration of 3.0  $\mu\text{m}$  particles was fixed at 0.05 % vol. and the first column indicates the concentration of the 10.0  $\mu\text{m}$  particles.

## 5.2 Evidence from image analysis for the improved critical flux

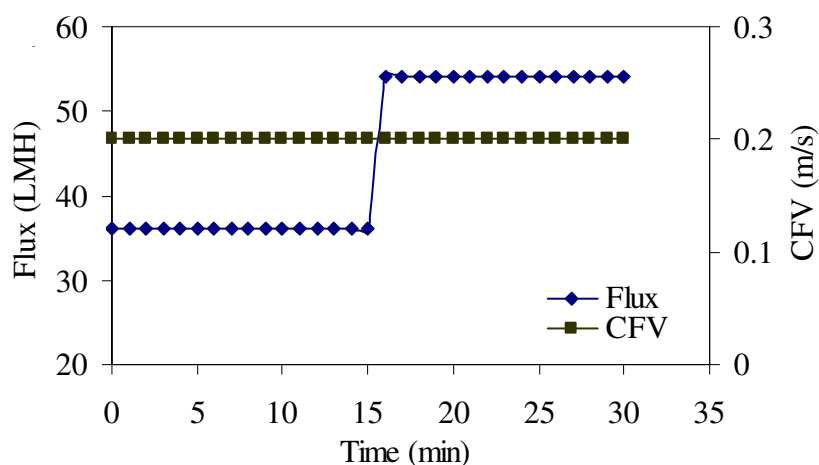
In order to confirm the results presented above and obtain more insights from the results, the analysis on the DOTM images was performed as described in Chapter 3.

Figure 5.6 (a) shows the extent of membrane coverage by the deposited particles during the filtration of 3.0  $\mu\text{m}$  latex at a concentration of 0.05 % vol. and 3.0 + 5.0  $\mu\text{m}$  both at a concentration of 0.05 % vol. respectively using the image analysis. The operating conditions are shown in Figure 5.6 (b). During the 1<sup>st</sup> flux step (before the 15<sup>th</sup> minute), the permeate fluxes (36 l/m<sup>2</sup>h) were below or close to the critical flux for both cases as illustrated by the fact that the coverage was low (below 20 %). After the flux was increased to about 54 l/m<sup>2</sup>h, the smaller particles began to deposit on the membrane and the rate of change in coverage increased significantly. However, it could be clearly seen that the deposition rate of the smaller particles was lower in the presence of the larger particles despite the fact that the concentration of the smaller particles was the same in both cases. This could serve as further evidence that the presence of the larger particles prevented the smaller from landing on the membrane and thus improved the critical flux.



(a)

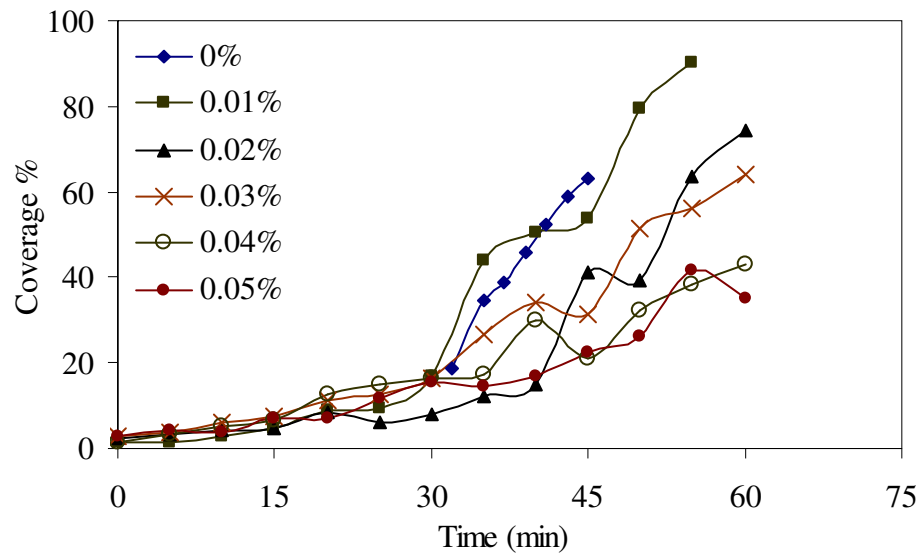
(Figure 5.6 to be continued)



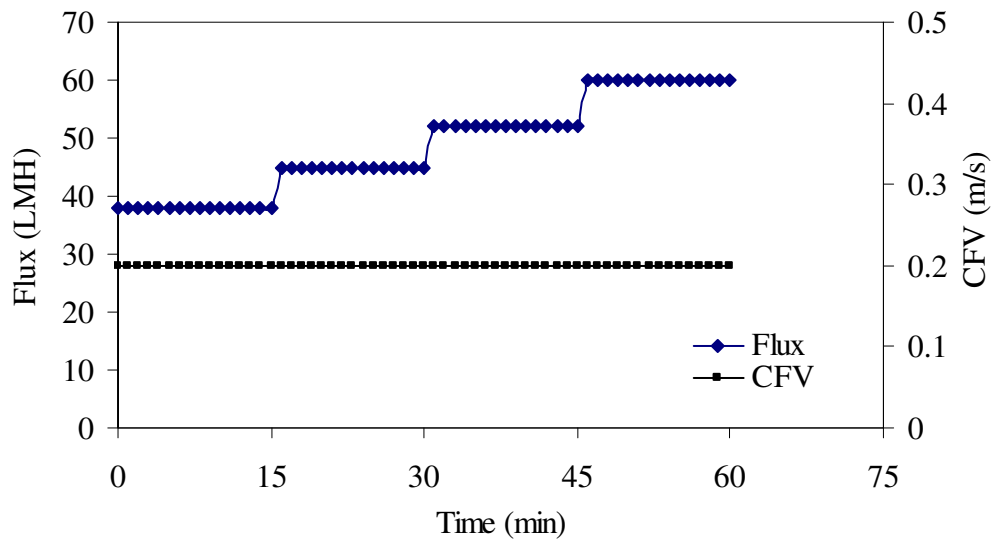
(b)

**Figure 5.6 Comparison of membrane coverage between 3.0  $\mu\text{m}$  only and 3.0 + 5.0  $\mu\text{m}$  mixed system: (a) membrane coverage by image analysis, and (b) operating conditions (latex concentration: 3.0  $\mu\text{m}$  only at 0.05 % vol. and 3.0 + 5.0  $\mu\text{m}$  at 0.05 % vol. respectively).**

The images captured during the filtrations of the mixed feeds of 3.0 and 10.0  $\mu\text{m}$  were also analyzed. Similar trends were found for a range of 10.0  $\mu\text{m}$  latex concentrations, as shown in Figure 5.7. The coverage of the membrane showed the effect of the presence of the larger particles where the addition of the larger particles slowed down the deposition rate. It could be seen that at some points the membrane coverage decreased slightly. This was due to the transient removal of clusters formed on the membrane surface. When above the critical flux, some of the particles landed preferentially on the membrane, possibly due to the local pore size distribution. The later incoming particles tended to accumulate around the deposited particles and formed a cluster. Due to the surface interactions, these particles stayed together on the membrane surface. When the cluster size became large, the clusters could be removed back to the bulk due to the increased back diffusion. However, overall, the membrane coverage increased with time for all the mixtures, and the greater the concentration of the larger particles, the slower the coverage.



(a)



(b)

**Figure 5.7 Comparison of membrane coverage between 3.0  $\mu\text{m}$  only and 3.0 + 10.0  $\mu\text{m}$  mixed system: (a) membrane coverage by image analysis, and (b) operating conditions (3.0  $\mu\text{m}$  latex particles concentration was fixed at 0.05 % vol.).**

The shape of the cake coverage curve was of interest, and tended to have a sigmoid shape. Thus, in Figure 5.6 (a), the coverage appeared to be accelerating from 15 to 25 minutes and then slowed down when the coverage exceeded 50 %. The period of

acceleration could be explained by the fact that as the membrane became covered by the smaller particles, the local flux increased in the region uncovered causing a more rapid deposition. The eventual slowing down in the rate of coverage might be due to the probability that a particle would need to pass across an uncovered region of membrane to increase the coverage (this probability is 100 % for an uncovered membrane and 0 % for a completely covered membrane). The combined effects of local increase in flux and decrease in probability of deposition eventually produced a sigmoid profile. The features of coverage kinetics will be further discussed in Chapter 7.

### 5.3 Discussion

The most important finding in this study is that the filtration of single-sized smaller particles could be enhanced by adding larger particles into the feed suspensions, as demonstrated by the fact that the presence of larger particles led to remarkable increases in the critical fluxes. Considering the role of larger particles in the crossflow filtration of the mixtures, it is important to distinguish between the conditions where cake layers are formed (supra-critical flux) and the conditions where the deposits are incipient, as in critical flux determination. Thus where cakes are found, typically by operating at a constant pressure with modest crossflow, the combined cake resistance could be increased by the mixture composition. This has been reported by Madaeni *et al.* (1996) in microfiltration and again by Madaeni (1998) in ultrafiltration. In their experiments, gold sols (50 nm) and latex particles (1  $\mu\text{m}$ ) were mixed together. The results showed that the presence of the latex particles impaired the filtration of the gold sols, and increased the resistance because of the different structures of the cake layers formed on or in the membrane based on their transmission electron microscopy (TEM) images. In those experiments, cake layers were deliberately formed at raised pressures and above critical fluxes in a stirred cell.

The beneficial effects of larger particles on the membrane filtration of smaller species were reported for conditions where there was a concentration polarization of

the smaller species (Bixler *et al.*, 1970; Fane, 1984). The effect of the larger particles was attributed to the additional surface shear and boundary layer disturbance which increased the back transport of the smaller species.

The results in this study related to the “pre-polarization” condition implied by the critical flux. To our knowledge, the only similar experimental studies on the critical flux of suspensions are those reported by Madaeni (1997a; 1997b) who investigated latex suspensions of 0.1 and 1.0  $\mu\text{m}$  and their mixtures (50% each) in crossflow microfiltration, and measured the critical fluxes at the same concentration (0.2 g/l). The critical flux for the mixture was found to be lower than the individual components. SEM images showed that the smaller particles were dominant in the cake layer which is consistent with our observations. Unfortunately, the critical fluxes of 0.1  $\mu\text{m}$  latex at 0.1 g/l or the mixture at 0.4 g/l were not measured which would make the results comparable to the current study. In another study (Madaeni, 1997a), Madaeni performed further measurements of the critical fluxes of latex suspensions of 0.1 and 1.0  $\mu\text{m}$  and their mixtures at various operating conditions. The results showed that the critical fluxes of the mixtures were always lower than those for the individual single-sized particles. The reason suggested was attributed to the change in the packing density of the flowing cake layer due to the concentration polarization near to the membrane surface. However, once a polarized layer reached its maximum concentration the operation was above the critical flux, by definition. The opposite trends from this study compared with Madaeni (1997a; 1997b) might also be due to the size differences. For fine particles ( $\sim 0.1 \mu\text{m}$ ), the filtration mechanism was through the Brownian back-diffusion away from the membrane, and the particle surface charge could have significant effects on the critical flux. For larger particles ( $\sim 1 \mu\text{m}$ ), the back-transport mechanism was most probably the shear-induced diffusion which convected the particles away from the membrane by particle-particle interactions, such that the critical flux was largely independent of the particle surface charge (Kwon *et al.*, 2000).

The reasons for the increased critical fluxes of the mixtures observed in this study cannot be revealed experimentally at present, but several possible explanations can

be raised. Firstly, if the addition of larger particles caused aggregation of the small and large particles, the concentration of the small particles would drop and the size of the larger particles would increase. Both effects would increase the observed critical flux. However, this was unlikely to occur as the latex particles were “stable” suspensions under the condition of the experiments. Also the individual particle (3.0, 5.0 and 10.0  $\mu\text{m}$ ) was “well-behaved” in the critical flux tests, indicating no self-aggregation.

The second possible explanation relates to the scouring effect of large particles observed in other studies (Bixler *et al.*, 1970; Fane, 1984), and this could have a role. To test this hypothesis, a cake of 5.0  $\mu\text{m}$  as small particles was formed at a flux of 60  $\text{l/m}^2\text{h}$  (above the critical flux of 40  $\text{l/m}^2\text{h}$ ). Then 10.0  $\mu\text{m}$  as large particles were added at a concentration of 0.05 %. No cake removal was observed which suggested that the scouring effect due to the big particles was negligible.

The third possible explanation is that the addition of the larger particles influenced the shear-induced diffusivity. The original data on the shear-induced diffusivity  $D_s$  (Eckstein *et al.*, 1977) for dilute suspensions,  $0 < \phi < 0.2$ , has the form,

$$D_s = 0.1\phi(a^2\gamma_0) \quad (5-2)$$

where  $\phi$  is concentration and  $\gamma_0$  is shear rate. Equation (5-2) is an empirical relationship derived from large particles (500  $\mu\text{m}$ ) at relatively high concentrations (>5 % vol.), but at relatively low shear rates (<10  $\text{s}^{-1}$ ).

Zydney and Colton (1986) incorporated Equation (5-2) into the L  v  que solution of the Film Model and obtained a relationship of the form,

$$J = k\left(\frac{a^4}{L}\right)^{1/3}\gamma_o \ln\left(\frac{\phi_w}{\phi_b}\right) \quad (5-3)$$

where  $k$  is a constant,  $\phi_w$  and  $\phi_b$  are the particle volume fractions at the wall and bulk. It was shown by Li *et al.* (2000) that this form of equation could correlate much of their critical flux data for monodisperse latex suspensions with  $k = 0.0595$  at the wall concentration  $\phi_w = 0.2$ . Our results implied that the concentration of the larger particles should be incorporated into equation (5.2) for  $D_s$ .

In a recent work by Kromkamp *et al.* (2005; 2006; 2002), the shear-induced diffusions in bi- and poly-disperse suspensions were investigated using computer simulations. It was found that the shear-induced diffusivity of the smaller particles was higher for the bidisperse suspensions than for the monodisperse suspensions. Their simulations showed that the shear-induced diffusivity was dependent on the particle composition as the diffusivity was greater for a bidisperse suspension with more large particles. This complied with the experimental results in this work that the critical fluxes of the mixed latex were increased with the concentration of the larger latex particles. They also conducted experiments on bidisperse latex suspensions using a confocal scanning laser microscope. It was found that the fouling load on the membrane surface was low with large particles in the suspension. Overall, the shear-induced diffusivity was determined by the larger particles in the bidisperse suspensions and was higher than in the respective monodisperse suspensions. According to the simulation, the smaller particles obtained an enhanced shear-induced diffusivity similar to the larger particles. This was not our observation in all cases.

Shauly *et al.* (1998) incorporated the particle size distribution into a shear-induced model. They described a phenomenological model of the shear-induced diffusivity for a polydisperse suspension with discrete particle sizes. The diffusion coefficient for the  $i$ th species was of the form,

$$D_{s,i} = k \gamma \bar{a} a_i \phi \phi_i \quad (5-4)$$



where  $k$  was a dimensionless constant,  $\bar{a}$  was average particle size,  $a_i$  was particle size of species  $i$  and  $\phi$  was volume fraction. This relationship also supported our observations qualitatively.

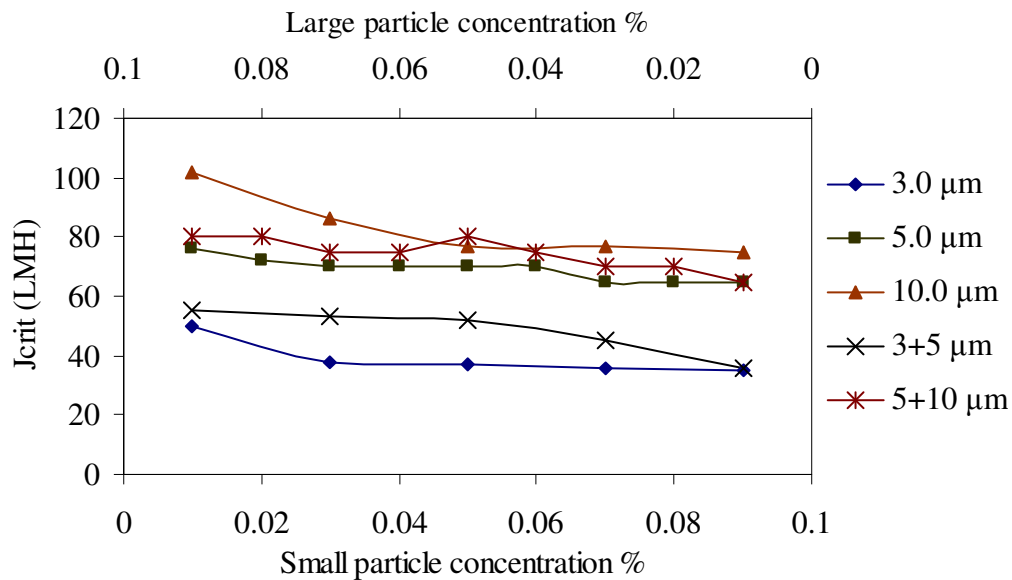
Overall, the applications of the shear-induced diffusion to membrane filtration showed some success (Belfort *et al.*, 1994; Li *et al.*, 2000; Zydney *et al.*, 1986), but has not been accurately predictive. The difficulty was in defining the concentration  $\phi$  since the zone of importance was in the near-membrane region where particles accumulated. It could be postulated that the introduction of larger particles into the suspension of smaller particles increased momentum transfer by particle-particle collisions and this augmented the shear-induced diffusion coefficient of bulk components. Thus, the mechanism of critical flux enhancement appeared to be due to the augmentation of the shear-induced diffusivity.

The experiments in the current study using ideal model latex particles were in essence similar to flocculating a proportion of small particles in advance. It was in fact consistent with the industrial practice whereby the colloidal particles are commonly pre-flocculated prior to microfiltration. According to the relevant observations (Li *et al.*, 1998), the filtration rate was dominated only by smaller particles, since only smaller ones were deposited on the membrane surface during the filtration due to the depolarization (Belfort *et al.*, 1994) and the classification (Baker *et al.*, 1985) mechanisms of the smaller particles. Hence, the deposition behavior for the bidisperse feed recorded in this study reflected the same trend. Although the physical reasons need to be further explored, it was possible that the larger particles were dominant in the transport behavior because of their larger back-diffusion coefficients as well as their ability of disturbing the boundary layer and thereby benefited the back-transport of the smaller particles.

## 5.4 Effect of the relative composition of larger particles in mixed latex feeds

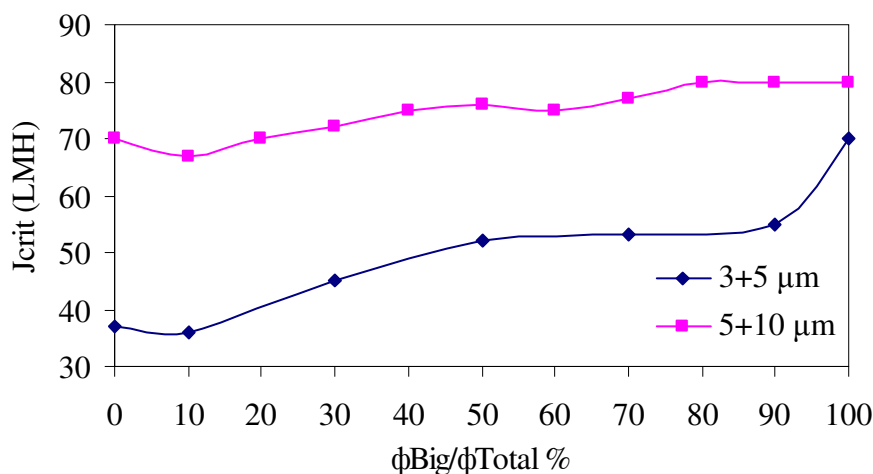
It was found that during the filtration of bidisperse latex suspensions, the smaller particles landed on the membrane surface first when fouling occurred as reported in Section 5.1. The presence of larger latex particles in the mixtures enhanced the critical fluxes even though their concentrations increased in the mixed feeds. Although the total concentrations were higher due to the introduction of the larger particles, the critical fluxes of the bidisperse suspensions were still higher compared with the monodisperse latex suspensions which had the same concentrations of the smaller particles. Also, as discussed in Section 4.3, Chapter 4, the concentration of feed suspensions had an influence on the critical fluxes of particle suspensions due to the higher possibility of particles depositing on the membrane in highly concentrated suspensions. In order to eliminate the influence of the increased total concentration, bidisperse latex suspensions with the same total concentration but various composition ratios were prepared to investigate the fouling mechanisms.

Figure 5.8 shows the critical flux measurements of mixed latex particles 3+5 and 5+10  $\mu\text{m}$  at a total concentration of 0.1 % vol. but different ratios. The critical fluxes reported in Chapter 4 of single-sized latex particles are also plotted in Figure 5.8 for a comparison. In Figure 5.8, the lower axis represents the small particle composition in the mixtures. This axis is applicable to all the data points. The upper axis represents the large particle composition in the mixtures and the values are plotted in reverse order. Note that the upper axis is applicable to both the 3+5 and 5+10  $\mu\text{m}$  mixed data points. All the experiments were operated at a CFV of 0.2 m/s. Although the total concentrations were not changed, the critical fluxes of mixed latex particles 3+5 and 5+10  $\mu\text{m}$  still decreased as the composition of the smaller latex particles was increased while the composition of the larger latex particles was decreased at the same time. In another words, the enhancement in the critical flux caused by the addition of the larger latex particles was reduced as the concentration of the larger particles in the mixtures decreased.



**Figure 5.8 Critical fluxes of mixed latex particles 3+5 and 5+10 μm at various composition ratios but a fixed total concentration 0.1 % vol. at CFV 0.2 m/s.**

The benefits due to the presence of the larger particles could be seen clearly from Figure 5.9. As the composition ratios of the larger particles increased in the mixed feeds, the critical fluxes of the mixtures were improved. This additional evidence showed that the critical flux could be enhanced by introducing the larger particles to increase the particle-particle interactions regardless of the effect of increasing the total concentration. It should be noted that over the mixture range the predominant particles depositing were the smaller ones, so the critical fluxes were those of the smaller particles in the presence of the larger particles. The data points at  $\phi_{Big}/\phi_{Total} = 0$  and 100 % were showing the critical fluxes of the mono-suspensions of the small and big particles respectively. In the mixed systems shown in Figure 5.9, the ratio of the two sizes was almost doubled ( $d_{large}/d_{small} \approx 2$ ). In the system of 5+10 μm, the critical flux gradually reached a stable value similar to the situation when there were only large particles in the suspensions, which means the smaller particles obtained similar shear-induced diffusivities as the larger particles. This was in agreement with the computer simulations by Kromkamp (2006) mentioned above. However, in the mixed suspensions of 3+5 μm, the critical fluxes were significantly lower than when there were only 5 μm particles. Therefore in this case, the size of the smaller particles in the polydisperse suspension was determinant of critical flux.



**Figure 5.9 Increase in the critical fluxes of mixed latex particles 3+5 and 5+10  $\mu\text{m}$  as the composition ratio of the bigger particles increased.**

## 5.5 Factors influencing the critical fluxes of bidisperse latex feeds

Factors such as pH, crossflow velocity and channel height that might influence the interactions between the smaller and larger particles and in turn affect the critical flux were studied in this section.

### 5.5.1 Influence of CFV on critical flux of bidisperse latex feeds

The critical fluxes of mixed latex suspensions of 3.0 and 5.0  $\mu\text{m}$  particles at different crossflow velocities (CFVs) were measured using the DOTM technique. The mixed suspensions were dispersed in the well controlled solutions at pH 8 (membrane iso-electric point) without any salt. Figure 5.10 shows the critical fluxes of single-sized latex particles 3.0 and 5.0  $\mu\text{m}$  as well as of mixed particles 3.0+5.0  $\mu\text{m}$  at concentration 0.025% each and 0.05% each respectively. The overall trend was that the critical fluxes of the mixed suspensions increased with the CFV as the single-sized latex particles. The critical fluxes of the mixed feeds 3.0+5.0  $\mu\text{m}$  at concentration 0.05% each were higher than those fluxes of the single-sized 3.0  $\mu\text{m}$  particles due to the addition of the larger particles even when the total concentration was doubled. The critical fluxes of the mixed feeds 3.0+5.0  $\mu\text{m}$  at concentration 0.025% each were even higher at different CFVs which were similar to the critical

fluxes of the single-sized 5.0  $\mu\text{m}$  latex with the same total concentration. However, the benefit of the addition of larger particles seemed to vanish at higher CFVs. Except for the critical flux of the single-sized 5.0  $\mu\text{m}$  latex, the critical fluxes of the other three suspensions were almost the same when the CFV was 0.3 m/s. This implied that the shear-induced diffusion might not be the only mechanism at work. For example, the inertial lift (Section 2.3.6) is independent on particle interactions but becomes predominant at higher CFV for larger particles.

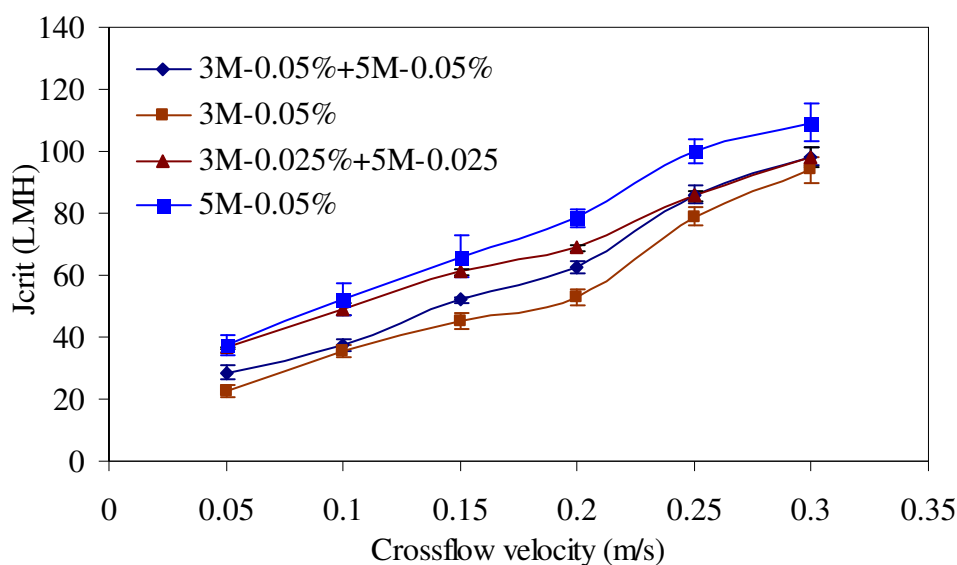


**Figure 5.10** Critical fluxes of 3.0+5.0  $\mu\text{m}$  mixed latex feeds at various CFVs.

### 5.5.2 Influence of pH on critical flux of bidisperse latex feeds

As discussed in Chapter 2, the permeate flux and membrane fouling are functions of surface charge of both particles and membrane in MF. The magnitude of the surface charge is called zeta potential ( $\zeta$ , mV). Change of the zeta potential can be achieved by adjusting the pH value of the solutions. The influence of pH on the critical flux of mixed latex suspensions was investigated by controlling the pH of the feeds.

The critical fluxes of mixed latex feeds of 3.0+5.0  $\mu\text{m}$  at concentration 0.05 % vol. each under different pH values are shown in Figure 5.11. The results on the influence of surface charge (pH) were discussed in Section 4.4 in Chapter 4. As

shown in Chapter 4, the surface charge had a significant effect on critical fluxes of single-sized latex particles only when the particle size was  $\leq 3.0 \mu\text{m}$ . The electrical double layer interactions applied negligible effects on the larger particles. Since only the smaller particles deposited on the membrane surface, the critical fluxes of the mixed suspension of 3.0 and 5.0  $\mu\text{m}$  latex particles showed a similar trend *i.e.* the critical flux increased with the solution pH but at a level about 10 % higher. Some interactions between the smaller and the larger particles were expected and as a result would have an influence on the critical flux of the mixed suspensions.

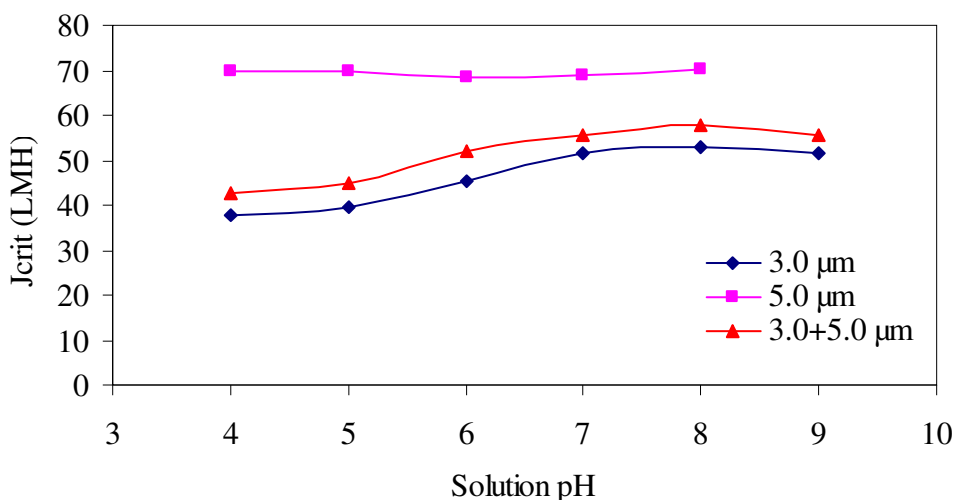


**Figure 5.11 Critical fluxes of 3.0+5.0  $\mu\text{m}$  mixed latex feeds vs. pH.**

### 5.5.3 Influence of channel height on critical flux of bidisperse latex feeds

In CFMF, the control of concentration polarization and cake formation are usually accomplished by either increasing tangential shear at the membrane surface or producing secondary flows. In practice, increased tangential shear is only achievable at additional costs and more energy usage. Therefore, using thin feed flow channels to promote more shear stress near the membrane surface should be more practical and feasible. A 1 mm channel cell was used in this section and was compared with the 2 mm cell to study the effect of the channel height on the critical fluxes of bidisperse latex feeds due to the different ways the crossflow was distributed in the channel. The initial purpose of doing this was to confine the

mixed latex particles within an even smaller flow channel and therefore enhance the improvement in critical flux caused by the addition of the larger particles considering that this improvement could be achieved by some augmentation in the interactions (SID) between the small and large particles. This section was focused on the effect of crossflow velocity distributed in two feed flow channels with different channel heights.

The effect of channel geometry was reported previously in the literature. Levy and Earle (1994) conducted a study on the effect of channel height on crossflow ultrafiltration using particle free protein solutes. It was found that a flow channel with larger height gave a higher permeate flux than a channel with a small height at the same wall shear rate. Unfortunately, they did not mention the reason in the paper. Hoek *et al.* (2002) also studied the influence of crossflow membrane filter geometry and shear rate on colloidal fouling in reverse osmosis separation. They found contrary results that decreasing channel height led to thinner concentration polarization layer and colloidal fouling layer at the same shear rate. However, in the same feed channel, a larger shear rate did not produce greater permeate flux. Their results showed that the crossflow shear rate and the feed channel height interacted to influence the filtration performance.

Table 5.2 shows the results of the critical fluxes of three mixed latex suspensions using the 1 and 2 mm channel cells at a CFV of 0.1 and 0.2 m/s respectively. The first four columns are showing the experimental conditions. In the fifth column are the critical fluxes of the smaller particles in bidisperse suspensions followed by the critical fluxes of monodisperse suspensions which consisted only of the small particles with the same concentrations. The last column shows the increased critical flux in percentage. The critical fluxes of the single-sized latex particles (3.0, 5.0 and 10.0  $\mu\text{m}$ ) in the two flow channels are listed in Table 4.2 in Chapter 4 for a comparison.

**Table 5.2 Critical flux measurements under different CFVs using two membrane cells with different flow channel heights at a latex particle concentration of 0.05 % each**

| Mixture<br>( $\mu\text{m}$ ) | Channel<br>(mm) | CFV<br>(m/s) | Shear<br>( $\text{s}^{-1}$ ) | $J_{crit}$<br>( $\text{l/m}^2\text{h}$ ) | $J_{crit}$<br>of small | Increase<br>% |
|------------------------------|-----------------|--------------|------------------------------|--|------------------------|---------------|
| <b>3.0+5.0</b>               | 1.0             | 0.1          | 600                          | 38                                       | 32                     | 19            |
|                              |                 | 0.2          | 1200                         | 80                                       | 75                     | 7             |
|                              | 2.0             | 0.1          | 300                          | 38                                       | 35                     | 9             |
|                              |                 | 0.2          | 600                          | 60                                       | 50                     | 20            |
| <b>3.0+10.0</b>              | 1.0             | 0.1          | 600                          | 40                                       | 32                     | 25            |
|                              |                 | 0.2          | 1200                         | 55                                       | 75                     | -36           |
|                              | 2.0             | 0.1          | 300                          | 40                                       | 35                     | 14            |
|                              |                 | 0.2          | 600                          | 60                                       | 50                     | 20            |
| <b>5.0+10.0</b>              | 1.0             | 0.1          | 600                          | 45                                       | 42                     | 7             |
|                              |                 | 0.2          | 1200                         | 60                                       | 105                    | -75           |
|                              | 2.0             | 0.1          | 300                          | 55                                       | 50                     | 10            |
|                              |                 | 0.2          | 600                          | 80                                       | 70                     | 14            |

The critical flux was expected to be similar at the same shear rate according to the shear-induced diffusion model. However, in the two channels at the same shear rate, the critical fluxes were much higher when using the 2 mm channel (at a CFV of 0.2 m/s with shear rate  $600 \text{ s}^{-1}$ ) than when using 1 mm channel (at a CFV of 0.1 m/s with shear rate  $600 \text{ s}^{-1}$ ) for both mono- and bidisperse suspensions. Overall, the trends could be summarized as follows:

- (i) For both channel heights,  $J_{crit(mix)}$  and  $J_{crit(small \text{ only})}$  increased with CFV and shear;
- (ii) At the same shear rate ( $600 \text{ s}^{-1}$ ) the larger channel height gave higher values of  $J_{crit(mix)}$  and  $J_{crit(small \text{ only})}$ ;



- (iii) For both channel heights larger particles enhanced  $J_{crit(mix)}$  at the lower shear rates of 300 and 600  $s^{-1}$ ;
- (iv) At the highest shear rate (1200  $s^{-1}$ , only in the thinner channel) the effect of larger particles was either small or negative.

Point (iv) is the most unexpected and suggests that the benefit of larger particles was lost at the highest shear rate. This was in line with the effect reported earlier for crossflow velocity in Figure 5.10 where the single and mixed data merged at the highest CFV. The mechanism whereby the large particles had a negative effect at high shear was not obvious, but it could be due to the instabilities occurring at high shear being dampened by the presence of the additional larger particles. More study is required to elucidate the interplay of shear rate, channel height and particle mixture and concentration.

## 5.6 Summary

In this chapter, the critical fluxes of 3.0, 5.0 and 10.0  $\mu m$  latex particles and their bidisperse mixtures (3.0+5.0  $\mu m$ , 3.0+10.0  $\mu m$  and 5.0+10.0  $\mu m$ ) with different compositions under various conditions were determined visually by the DOTM technique in a 2 mm flow channel. The smaller particles determined the filtration rate as they were the only species deposited on the membrane surface. Significant increases in critical flux were recorded by the addition of the larger particles into the feed suspensions. The percentage improvement in the critical flux increased with the concentration of the larger particles added. Image analysis of the coverage on the DOTM images under the same operating conditions also showed that the deposition rate was slower in the mixed system than in the single-sized feed. Several possibilities were proposed to account for the enhancement in critical flux. It was postulated that the enhancement of critical flux was due to the augmentation of the shear-induced diffusivity caused by the momentum transferred from the larger particles.

Factors such as pH and CFV that might influence the critical fluxes of bidisperse latex suspensions were also investigated. The bidisperse suspensions showed similar trends to the monodisperse feeds with pH and CFV.

Two membrane cells with different channel heights (1 and 2 mm) were used to enhance the particle interactions in a confined space. It was unexpected that the beneficial effect of the larger particles in the mixed suspensions was lost when using the 1 mm flow channel. In some circumstances, the critical fluxes were lower in the presence of larger particles than for the monodisperse suspensions in the 1 mm channel (negative increased percentage in Table 5.2). The permeate fluxes from different channel geometries were not identical even when the membrane wall shear was the same. The channel geometry was found to have an effect on the filtration rate together with the crossflow velocity. This implied that the shear-induced diffusion was not the only back transport mechanism in operation.

## **Chapter 6 Critical flux and particle deposition of flocculated suspensions during crossflow microfiltration**

The wide applications of microfiltration are often hindered due to the buildup of a cake layer on the membrane surface. This fouling layer can cause decline in permeate flux, low permeate flux, frequent chemical cleaning or frequent membrane replacement and compromised permeate quality. A better understanding of the particle deposition dynamics is necessary in order to improve the design and operation of microfiltration processes. For several decades, the study of the membrane fouling mechanisms during crossflow microfiltration has been intensely carried out since the crossflow configuration has a potential advantage of low fouling. Particle deposition has been observed by many advanced techniques experimentally, and at the same time, the permeate flux has been predicted by several back-transport mechanisms theoretically. However, almost all the studies on this topic use or assume rigid and spherical particles with a single size.

The previous two chapters started with mono-sized latex particles (Chapter 4) and moved on to bidisperse mixtures (Chapter 5), showing that critical fluxes increased in mixed systems. This chapter steps further to the real systems by studying the critical fluxes of flocculated solids. These types of solids can be found in crossflow membrane filtration of flocculated raw water or used water or in MBRs. Flocculated solids in suspensions are usually large “particles” of irregular shapes and with a size distribution (polydispersed). They typically compose an arrangement of primary particles to form a body with interior structure, characterized by the fractal dimension (refer to Section 6.2 below). The aim of this chapter is to establish the effect of floc properties on critical flux in crossflow membrane filtration.

The effects of the particle size and distribution (characterized as polydispersity) and particle structure (characterized as fractal dimension) on the critical flux were studied in this chapter using the ‘in-house’ hematite suspensions. The initial hematite ( $\alpha\text{-Fe}_2\text{O}_3$ ) particles were prepared by hydrolysis of anhydrous ferric chloride ( $\text{FeCl}_3$ ). The preparation process was introduced in Section 3.4, Chapter 3.

The hematite particles were then flocculated in potassium chloride solutions under various conditions. Hematite flocs with different particle sizes and distributions as well as fractal dimensions were achieved by flocculation. The critical fluxes of hematite flocs were measured using the DOTM technique and reported along with observation of the motion of hematite flocs during the filtration.

## 6.1 Polydispersity of suspensions in membrane separation

Membrane fouling is a complicated process. The fouling mechanism is a function of many factors, such as feed properties, membrane morphologies and operating conditions. Among them, the particle size distribution is a major parameter since it not only determines dynamics of the particles deposition, but also exerts an influence on the cake properties. Most of the particles to be separated in MF fall into the 0.5 to 30  $\mu\text{m}$  size where shear-induced diffusion is the dominant back transport mechanism (Belfort *et al.*, 1994). As reviewed in Chapter 2, shear-induced diffusion is the particle back transport mechanism in shear flow caused by particle-particle interactions. The diffusion is largely determined by the particles size. Smaller particles have lower back transport diffusivity, and hence more easily deposit on the membrane surface. They are also more susceptible to the ionic environment as shown in Chapter 4. The electrical forces can retain the smaller particles on the membrane surface forming a cake layer. The cake layer formed by smaller particles has narrower pathways (lower void fractions,  $\varepsilon_c$ ) giving high resistance and therefore causes greater increase in TMP. In most fouling studies, the feed solutions are often ideally regarded as monodisperse suspensions. In conventional filtration theory, the factor of particle size is simply expressed as the average particle diameter. However, polydisperse suspensions are often encountered in normal practice. Suspensions to be treated are inevitably polydisperse due to the complexity of the raw water. Moreover, there are often different species of particulates in the suspensions. A full understanding of the membrane fouling mechanism is not possible unless the effect of polydispersity has been incorporated. It was expected that a study using a model polydisperse suspension would provide a better understanding on the fouling mechanisms.

The properties of cake formed by separating polydisperse suspensions were studied experimentally and it was found that the particle size in the particle layer was smaller than in the bulk suspensions (Baker *et al.*, 1985; Chellam *et al.*, 1998; Li *et al.*, 1998; Ould-Dris *et al.*, 2000). Mackley and Sherman (1992) used a direct observation technique to study the cake growth in crossflow microfiltration using particles with a particle size of 125-180  $\mu\text{m}$ . The findings that thinner cake layers formed at a higher crossflow velocity but gave lower permeate flux suggested that the cake layer consisted of the smaller particles. Li *et al.* (1998) used the same observation technique (DOTM) as used in the current work to study the deposition of narrowly distributed latex particles. They found that the particle distribution of the deposited particles was smaller at the higher crossflow velocity. Ould-Dris firstly attempted to modify the shear-induced diffusion model to incorporate the effect of polydispersity using the mean diameter of the particles (2000). Kramadhati *et al.* (2002) evaluated the shear-induced diffusion model for the microfiltration of polydisperse suspensions. Their calculations showed that the deposited particle layer was made of the smaller particles only. Recently, Kromkamp *et al.* (2006) performed computer simulations to study the dynamics of particle deposition in crossflow microfiltration based on the shear-induced diffusion model. The shear-induced diffusivity of the small particles was increased in the presence of the large particles in the bidisperse suspensions compared with the monodisperse suspensions. Their experiments also showed that the deposition load was decreased as the large particle composition was increased (Kromkamp *et al.*, 2002).

## 6.2 Fractal concept in membrane separation

As shown in Chapter 2, the conventional theoretical flux predictions are based on the assumption that the particulates to be separated are solid, spherical and have a uniform particle size. Particle size and density are believed to influence the settling velocity and flocculation rate in the conventional separation processes. Recently, the fractal structure of aggregated flocs was found to influence the separation processes, such as settling (Johnson *et al.*, 1996) and filtration (Redman *et al.*, 2001). For example, in the sedimentation process, the characteristics of aggregates

such as mass, density, volume and porosity were determined by the fractal structure, and the particle collision frequency as well as the settling velocities was also influenced by the fractal dimension. Johnson *et al.* (1996) showed that settling velocities of porous aggregates were on average 4-8.3 times higher than the impermeable spheres. Apart from the effect of particle size on the settling velocities, fractal dimension also had a significant impact on that. They found that the drag coefficients on the porous aggregates ( $d_F < 3.0$ ) were lower than solid particles ( $d_F = 3.0$ ) in the fluid flow. The effect of getting particles porous was equivalent to decreasing crossflow velocity.

The permeability of fluid through a layer of particles was often estimated using the Carman-Kozeny equation, Darcy's law and Brinkman's equation (Chellam *et al.*, 1993). The models showed that porous flocs had a high permeability and experienced less drag force than solid particles with the same particle size, *i.e.* the lower the fractal dimension, the higher permeability and the lower the drag force.

Recent research (Guan *et al.*, 2001) showed that the fractal structure of sludge had an influence on the specific resistance in the sludge dewatering process. According to the Carman-Kozeny equation (Equation (2-8)), the specific resistance of the cake layer formed by uniform spherical particles had the form,

$$\alpha_c = \frac{36K(1-\varepsilon_c)}{\rho d^2 \varepsilon_c^3} \quad (6-1)$$

The specific resistance is determined by the particle size ( $d$ ) and the void fraction of the cake layer ( $\varepsilon_c$ ). Therefore, for the filtration of non-compressible, non-aggregated spherical particles, there are the relationships,

$$\alpha_c \propto \frac{1}{d^2} \quad (6-2)$$

and,

$$\alpha_c \propto \frac{1-\varepsilon_c}{\varepsilon_c^3} \quad (6-3)$$

It shows that the cake resistance is strongly dependent on the particles size and cake porosity. Relationships (6-2) and (6-3) are valid only when  $\varepsilon_c$  is the void fraction of a randomly packed cake and has a value about 0.4. The aggregates of solid primary particles have structural characteristics. It was proposed that the porosity of flocs is dependent on both particle size and fractal structure (Guan *et al.*, 2001),

$$\varepsilon_{floc} = 1 - \rho = 1 - \left( \frac{d_{floc}}{d_{particle}} \right)^{d_F - 3} \quad (6-4)$$

Therefore, a relationship between specific resistance and fractal dimension,

$$\alpha_c \propto \frac{1}{\left( \frac{d_{floc}}{d_{particle}} \right)^{3-d_F} \times \left[ 1 - \frac{1}{\left( \frac{d_{floc}}{d_{particle}} \right)^{3-d_F}} \right]^3} \quad (6-5)$$

The relationship between filtration behaviour and fractal dimension shown in Equation (6-5) indicates that the conventional filtration theories have to be re-evaluated to include the effect of the fractal structures of the aggregates. As for the porous, compressible cakes in filtration, the situation is even more complicated (Equation (2-10)). More recently, the effect of floc size and structure on specific cake resistance and compressibility in dead-end microfiltration was studied (Lee *et al.*, 2003). The results showed that the cake resistance by fractal flocs was a function of floc mean size and fractal dimension. The resistance by the fractal aggregates was lower than by the non-aggregated particles of the same size, and the fractal structures of the aggregates had more significant effect on the smaller flocs.

### 6.3 Flocculation of hematite particles

The aggregation of particle flocs depends on the physiochemical conditions of suspensions. The important factors influencing the particle aggregation include

coagulant dosage, particle concentration, shear intensity, salt concentration and solution pH *etc.* These factors affect not only particle size distribution, but also floc structure. The purpose of flocculation experiments using hematite particles was to establish protocols for ‘model’ floc preparation to be used in the subsequent filtration experiments. The hydrolysis of hematite particles was a very complicated process. It involved many chemical reaction mechanisms. Therefore, the reproducibility of the tests was not expected high. A large amount of hematite suspensions had to be prepared beforehand for filtration tests to keep the conditions constant. The methods of the measurements of particle size distribution and fractal dimension were detailed in Chapter 3. The floc size ( $d(v, 0.5)$ ) reported here was the mean size equivalent to the spherical particles which had the same volume. The numbers shown beside the result curves were the fractal dimensions of the flocs.

### 6.3.1 Effect of hematite concentration

The effect of hematite particle concentration on flocculation rate was studied under the same conditions ( $[KCl] = 100$  mM, pH 8.0, Shear rate 150 rpm). The results are shown in Figure 6.1. The numbers shown in Figures 6.1-6.4 were the measured fractal dimension values.

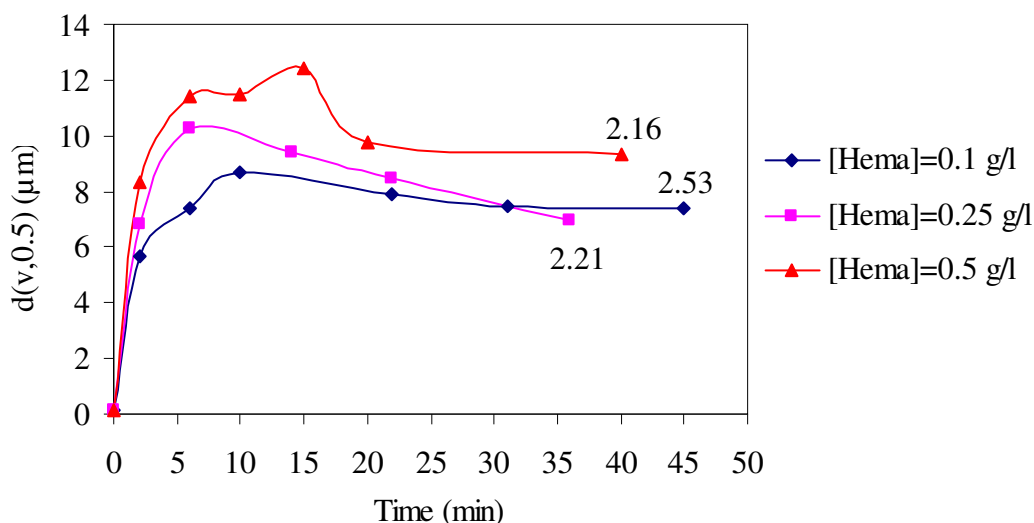


**Figure 6.1** Size evolution with different concentration of hematite particles ( $[KCl] = 100$  mM, pH 8.0, Shear rate 150 rpm).



We could see that the flocculation rate was faster at higher hematite particles concentration, as expected from Equations (2-22) and (2-23). Large flocs were obtained at the higher hematite concentration. The fractal dimension was higher when the hematite concentration was low. A decline in floc sizes was observed at the later stage of flocculation. This might be due to the high shear forces applied (refer to Section 6.3.4). Rearrangements of the flocs induced by the differential fluid velocity resulted in more compact flocs ( $d_F > 2.1$ ).

### 6.3.2 Effect of ionic strength

As shown above in Figure 6.2, the effect of ionic strength was tested under four different salt (KCl) solution concentrations. The results showed that the flocculation rate was faster at the higher KCl concentration. This was consistent with suppression of the double-layer as ionic content increased. The flocs formed in higher salt concentration were larger and the fractal dimensions were lower. In effect, rapid flocculation led to larger and more open floc structures.

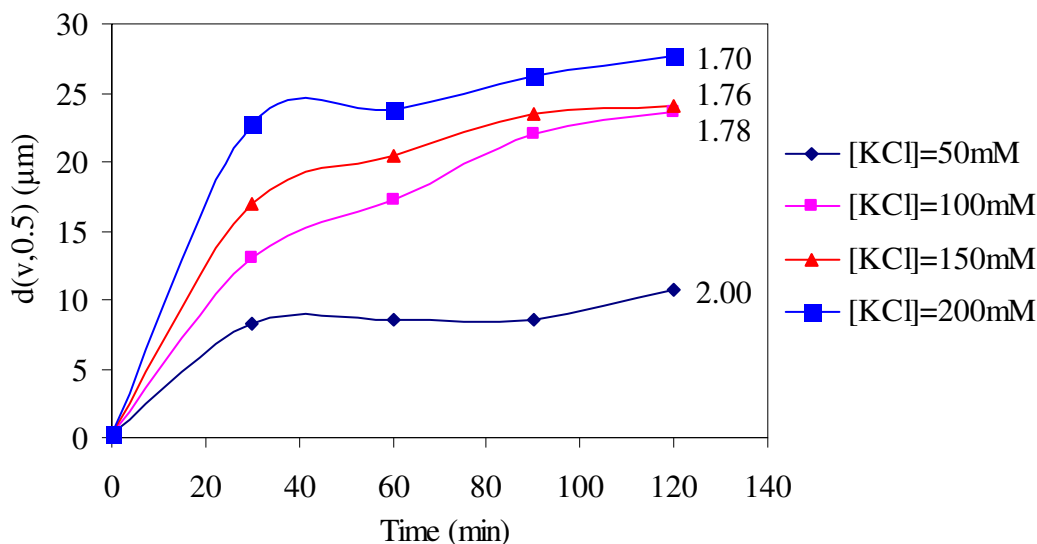


**Figure 6.2** Size evolution with different concentration of KCl ([Hema] = 1 g/l, pH 8.0, Shear rate 150 rpm).

### 6.3.3 Effect of pH

Solution pH was critical for the aggregation of hematite particles. According to the literature (Lee, 2005), hematite particles had weak charges around the neutral pH value, but strong charges at extreme pH values. For example, the zeta potentials of the hematite particles were  $\pm 25$  mV at pH 3 and 11 respectively. Flocculation of hematite particles was more difficult with strong surface charges due to the high electrical repulsive forces. Therefore, the surface charge of the hematite particles had to be neutralized to a low level (around  $\pm 10$  mV) in order to aggregate particles. Particle aggregation was found to be initiated at the pH values 7~9 even before the shear stress was applied.

Figure 6.3 shows that the floc size increased with the pH values. The fractal dimension decreased with increasing the pH values in the range 6.0 to 9.0. In the case of pH = 8.0 and 9.0, although there were big differences in the floc size, the fractal dimensions were similar.

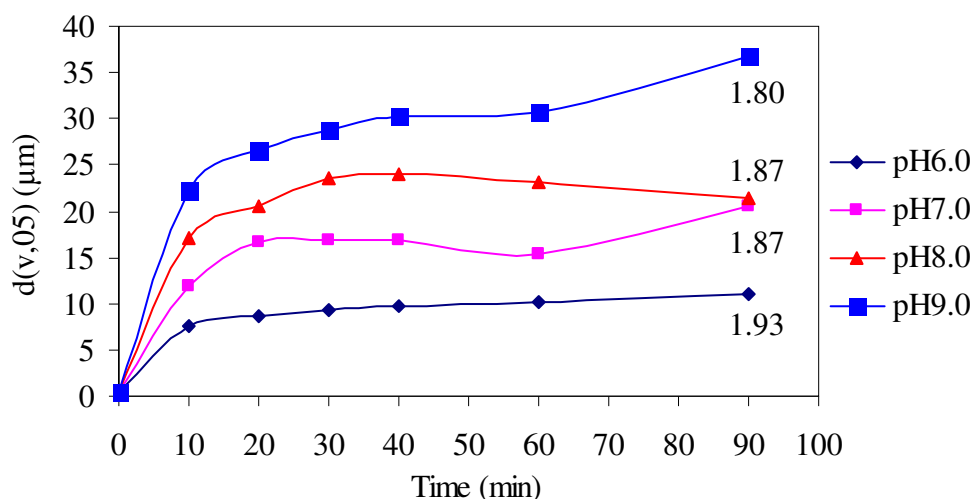


**Figure 6.3** Size evolution with different pH ([KCl] = 150mM, [Hema] = 0.84 g/l, Shear rate 150 rpm).

### 6.3.4 Effect of shear rate

Four different stirring speeds were applied to study the effect of the shear rate. The results are shown in Figure 6.4.

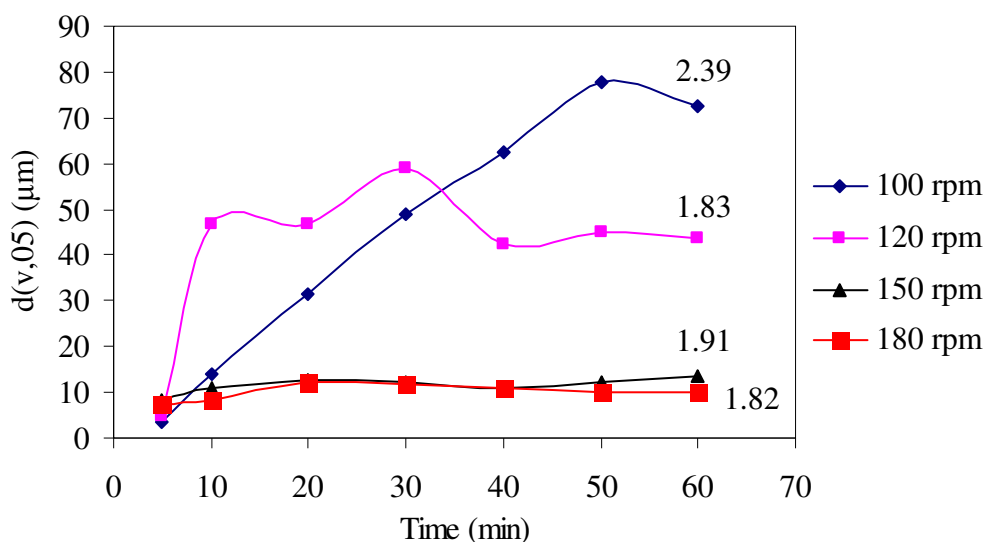


**Figure 6.4** Size evolution with different shear rate ( $[\text{KCl}] = 50\text{mM}$ ,  $[\text{Hema}] = 0.5\text{ g/l}$ ,  $\text{pH} = 8.0$ ).

At a low shear rate (100 rpm), the floc size continued to increase gradually with time and reached its maximum value after almost one hour. At a higher shear rate (120 rpm), however, the hematite flocs achieved the stable size rapidly within 10 minutes compared with the flocculation at the lower shear rate (100 rpm). High shear rate was assumed to produce large flocs as it increased the possibility of particle interactions. However, after 30 minutes of flocculation, the floc size at the higher shear rate (120 rpm) stopped increasing and decreased a little, and then reached a plateau smaller than that at the lower rate (100 rpm). It seemed that the hematite flocs were restructured at the higher shear rate. This beneficial effect of the shear rate was not infinite. Two higher shear rates (150 and 180 rpm) were tested and the floc sizes at these shear rates were almost the same and did not change too much during the flocculation. The stabilized sizes were smaller than formed at the lower shear rates (100 and 120 rpm). This was probably because the flocs were

broken up by the great high shear. Some self-aggregation of particles was observed at 80 rpm. When the shaker providing orbital motion was set at 80 rpm, the solution (200 ml) in the sample bottle was observed to be almost stagnant. Hence, the lowest shear rate studied was 100 rpm due to inhomogeneous shaking below that. The fractal dimension achieved the highest value at a low shear rate (100 rpm). When the external shear forces were imposed, breakage and rearrangement of the flocs occurred due to the fluid velocity gradient. At higher shear rates (150 and 180 rpm) the floc sizes were similar, but the flocs were more compact at 150 rpm.

### **6.3.5 Conclusions on particle flocculation**

Apart from the effect of time on the floc growth, the experimental results above showed how physicochemical flocculating conditions affected the floc size and structure. The flocculation rate was enhanced at high hematite concentration, high KCl concentration and high pH value. A high shear rate had a negative effect on the floc size due to floc breakage and rearrangement. The fractal dimension reflected the floc structure. Although the floc size might be similar in some cases at different flocculating conditions, the critical flux was expected to be different due to the different floc structures (fractal dimension) in crossflow fluid. The results of the fractal measurements showed that the fractal dimension was lower at higher flocculation rate, which meant that the flocs formed at high rates were less compact.

## **6.4 Critical/Sustainable fluxes of hematite flocs**

According to the findings in Chapter 5 that the smaller particles in bidisperse suspensions would first deposit on the membrane surface, the membrane fouling caused by the particles in a polydisperse suspension should exhibit a similar pattern that the critical flux could be enhanced by the larger species. The species with different sizes in a polydisperse suspension would compete to reach and deposit on the membrane surface. Above the critical flux, the class of the particles with the smallest particle size was expected to deposit first on the membrane surface. Assuming feed recycle (rather than once-through), after all the particles in the first

class (consisting of the smallest particles in the distribution) have deposited, the second class of particles with slightly larger particle size should deposit around or on the existed layer consisting of only the particles in the first class. The subsequent fouling on top of the first fouling layer would not contribute so much to the total resistance due to the lower specific resistance of the larger particles. Therefore, the permeate flux would stop decreasing in constant pressure operation or the transmembrane pressure would stop increasing in constant flux operation. For the once-through process, the kinetics would differ from a continuous supply of the smaller particles in the distribution. The net flux of each size would depend on its critical flux and the imposed operating flux. However, the smaller particles in the suspensions determine the filtration performance. In an attempt to take the polydispersity into account, Dharmappa *et al.* (1992) found that the concentration of the larger species in the fouling layer increased first for a short period and then decreased substantially. The concentration of the smaller species in the fouling layer continued to increase. Figure 6.5 shows the schematic of the membrane fouling caused by polydisperse suspensions as described above. This was based on an assumption that the interactions between particles were neglected.

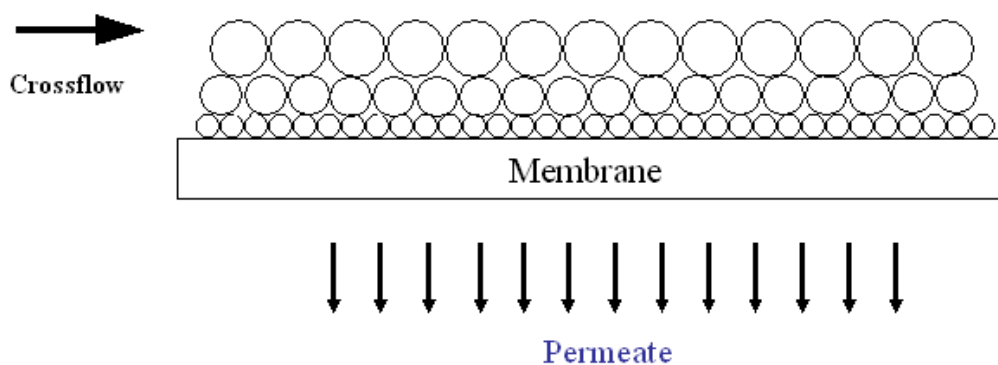


**Figure 6.5 Schematic of membrane fouling by polydisperse suspensions.**

However, usually there are strong connections between the particles in polydisperse suspensions. This is especially for the polydisperse suspensions containing different species. For example, small organic matters (proteins) could be absorbed onto larger inorganic particles (hematite) (Thiruvengkatachari *et al.*, 2002). Figure 6.6 shows the schematic of fouling development by polydisperse suspensions. The

smaller particles will be scattered on membrane in 1<sup>st</sup> stage. As deposition continues, more particles (either small or large) will accumulate around the deposited particles and form big clusters on the membrane surface in 2<sup>nd</sup> stage. When the clusters grow big enough, they can be swept away and back to the bulk solution due to the higher back transport velocity. It is possible that parts of the membrane return back to the state before 1<sup>st</sup> stage, and the cycle will repeat. This is likely to be a partial phenomenon across the surface. However, in this scenario, the system could be operated at a sustainable flux or even a super-critical flux for a long term. A similar fouling pattern to that shown in Figure 6.6 is expected for hematite flocs. Moreover, the amorphous flocculated flocs could bridge each other on the membrane to form a more porous cake layer.

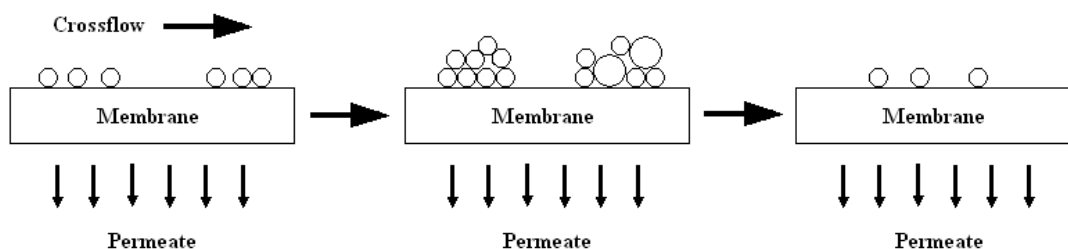


**Figure 6.6 Schematic of fouling development by polydisperse suspensions.**

Membrane fouling caused by the hematite flocs in polydisperse suspensions was observed under various conditions. The critical fluxes of the model flocculated hematite suspensions with various mean sizes and fractal structures were measured using the same protocol as the latex particles. However, due to the fragility of the flocculated flocs and high shear forces caused by the feed pump, flocs could re-structure during the filtration process. To minimize the effects, the CFVs were controlled less than 0.15 m/s and the critical flux measurements were finished within two flux steps. After each run, the feed solution and the membrane were not reused. The measurements were repeated three times to reproduce the results.

Figure 6.7 is an example showing the filtration procedure of the hematite flocs at a CFV of 0.1 m/s. The flocs deposited on the membrane surface were much smaller than the measured mean size ( $d(v, 0.5) = 9.6 \mu\text{m}$  in this case). The phenomenon that



the smaller flocs preferentially deposited on the membrane was in accordance with the findings from the mixed latex particles in Chapter 5. The smaller flocs started depositing on the membrane surface as an ‘individual floc’ (Figure 6.7 (a)). The subsequent flocs deposited around the existing foulants and grew into a larger floc (Figure 6.7 (c), (d) and (e)). As the flocs accumulated, the aggregated larger ‘individual flocs’ were removed back into the bulk due to the higher shear (Figure 6.7 (f)) as predicted by the back diffusion mechanisms that back transport was stronger for larger particles in the shear flow. Under these circumstances, the membrane surface was recovered and available again for filtration.

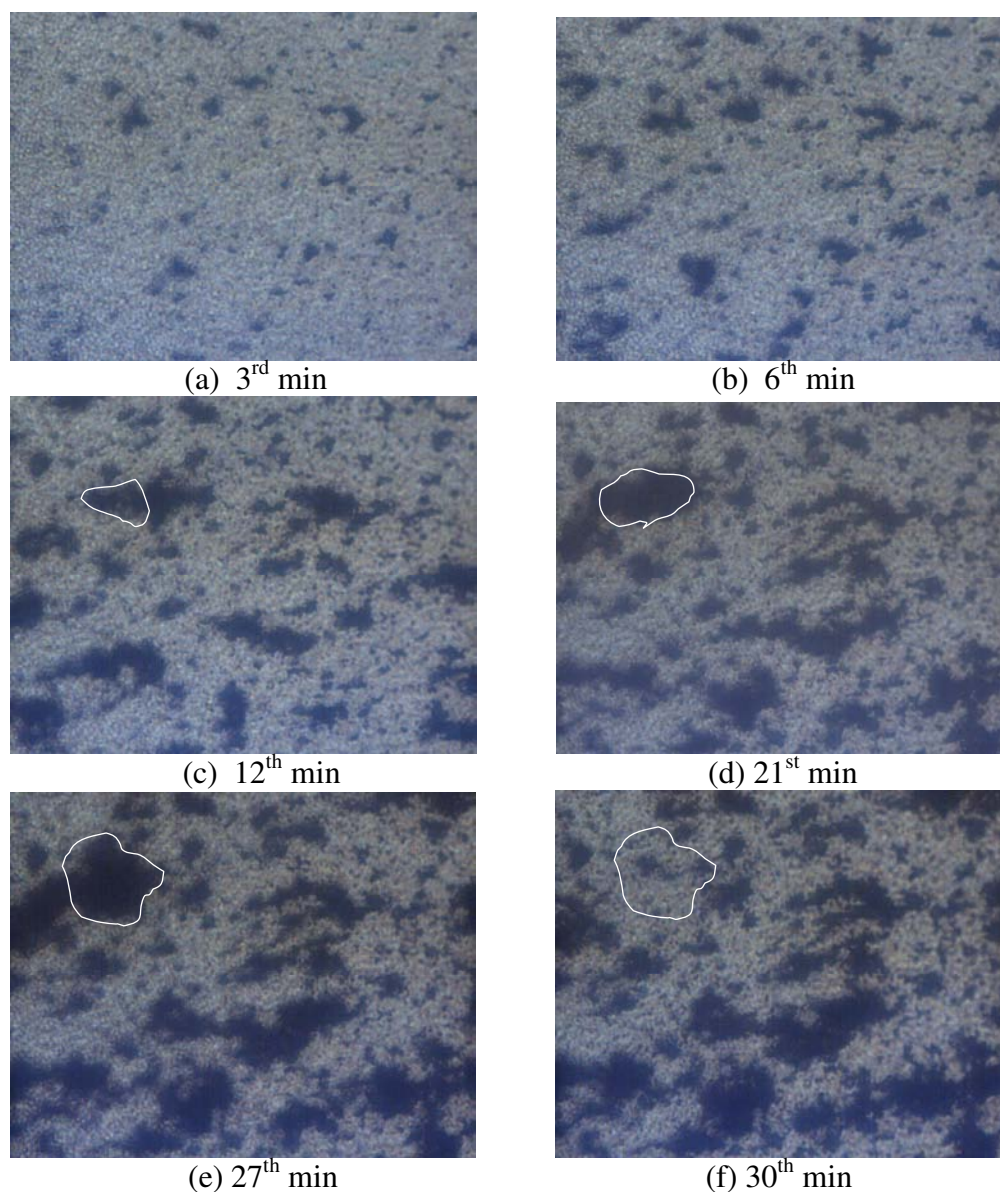


**Figure 6.7** DOTM images during filtration of flocculated hematite flocs ( $d(v, 0.5) = 9.6 \mu\text{m}$ ), CFV 0.1 m/s, floc concentration 0.2 g/l.

Even if there was a layer of flocs on the membrane surface at the moment before the large chunks were removed, the resistance caused by the cake would not be high due to the high permeability of the flocs (Lee, 2005). By repeating this cycle, the system could be operated sustainably at a somewhat higher flux than critical flux without heavy fouling on the membrane surface. Unlike the model spherical particles, flocs rolling on the membrane surface when operated near the critical flux (Li *et al.*, 1998) were not observed during the filtrations. This was probably due to the non-spherical nature and the roughness of the floc surface, and also the ration of particle diameter and membrane pore would affect particle rolling on the membrane surface. The ‘cotton-like’ properties made the flocculated flocs attached firmly to the membrane surface and to each other as well.

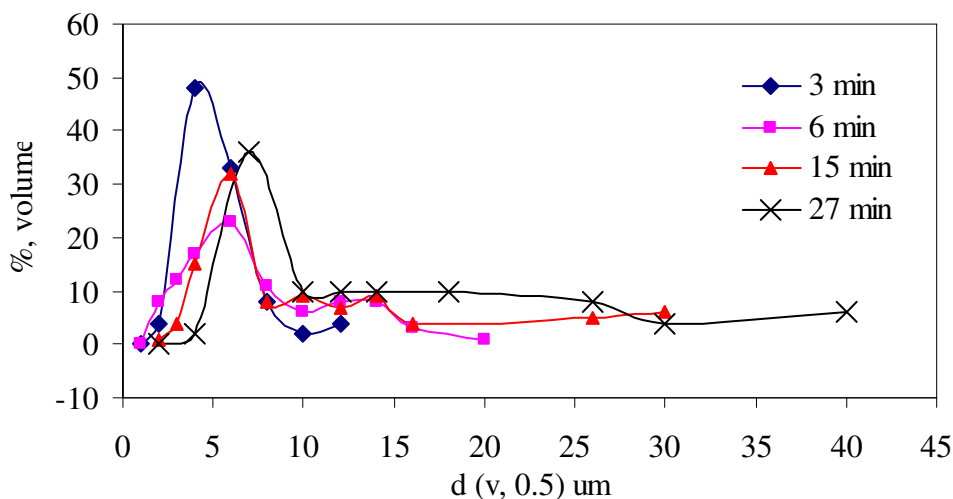


**Figure 6.8 Particle size distribution evolution of the deposited flocs on the membrane shown in Figure 6.7.**

The DOTM images in Figure 6.7 were analyzed using image analysis. Figure 6.8 shows the particle size distribution evolution on the membrane surface during the filtration. Due to the amorphous shape of the deposition, the covered area was analyzed only. The particle size reported in Figure 6.8 was the mean size equivalent to the spherical particles with the same area. According to the particle size measurements of the deposited flocs on the membrane surface, the particles in the cake layer preferentially consisted of the smaller flocs. This was in good agreement



with the findings on mixed latex bidisperse solutions as the smaller species always deposited first on the membrane surface under the controlled flux operation. As the filtration continued, the particle size distribution on the membrane moved towards larger since the smaller flocs tended to attach to each other due to the amorphous shape and the rough surface.

## 6.5 Membrane fouling by hematite polydisperse suspensions

The critical fluxes of flocculated suspensions were measured in this section. The experimental protocols were described in detail in Section 3.5.2. Figure 6.9 shows the critical fluxes of the different sized hematite flocs at various CFVs. Generally, the critical flux increased with the floc size, as observed in Chapter 4 for the mono-sized latex particles. However, the curves for the 22.4  $\mu\text{m}$  and 23.8  $\mu\text{m}$  flocs were of interest. The critical fluxes decreased while the floc size increased. This was probably due to the porous structure of the flocs they obtained during the flocculation process. The larger flocs had a more porous structure ( $d_F = 1.85$ ) and the smaller flocs had a more compact structure ( $d_F = 2.13$ ) according to Figure 6.9.

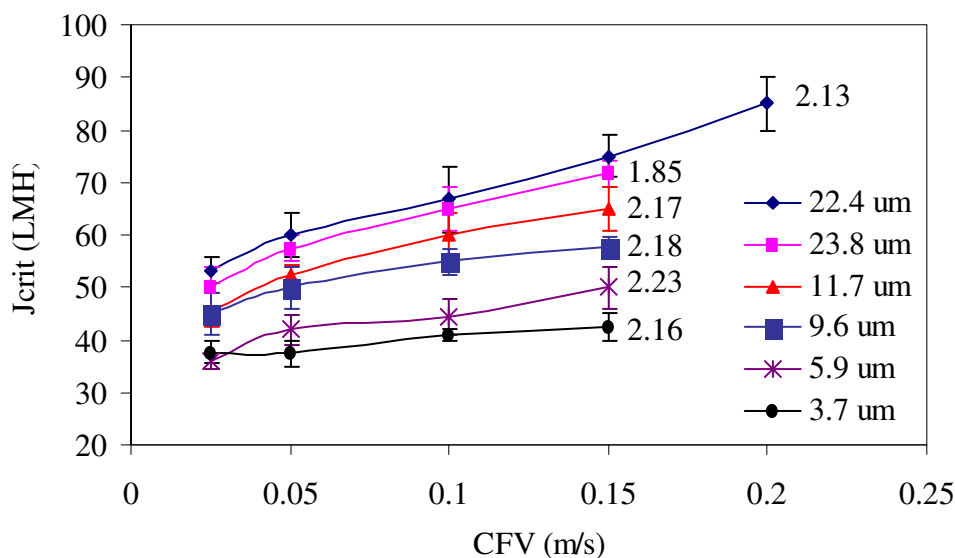
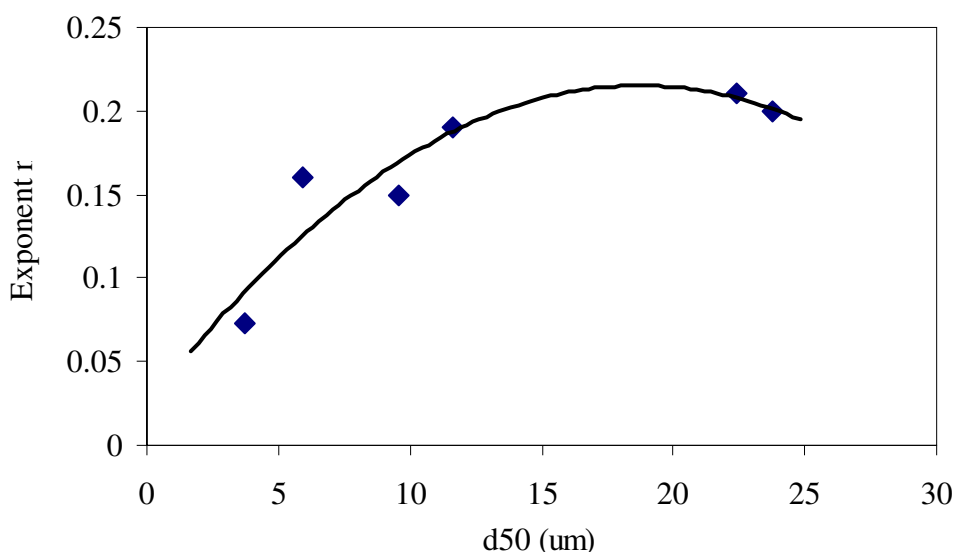


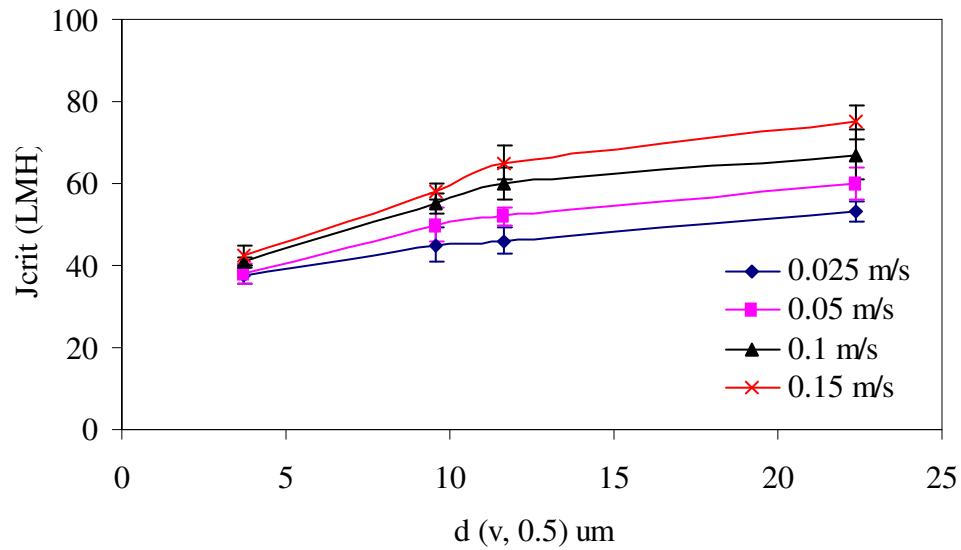
Figure 6.9 Critical fluxes of hematite flocs under different CFVs.

The overall trend was that the critical fluxes increased with the CFVs, however the dependence on the CFV was lower compared with the solid spherical latex particles. Figure 6.10 shows the exponents,  $n$  for the CFV with the particle size. The exponents had a wide range from 0.07~0.2 and were much lower than 0.62~0.77 for the latex particles. This trend was more significant for the smaller flocs. It was likely that the influence of the CFV was less effective due to the porous intra-floc structure. More fluid would pass through the flocs, and therefore the drag forces on the flocs were decreased as found that the drag coefficient of porous particles was lower than solid particles in sedimentation (Johnson *et al.*, 1996).



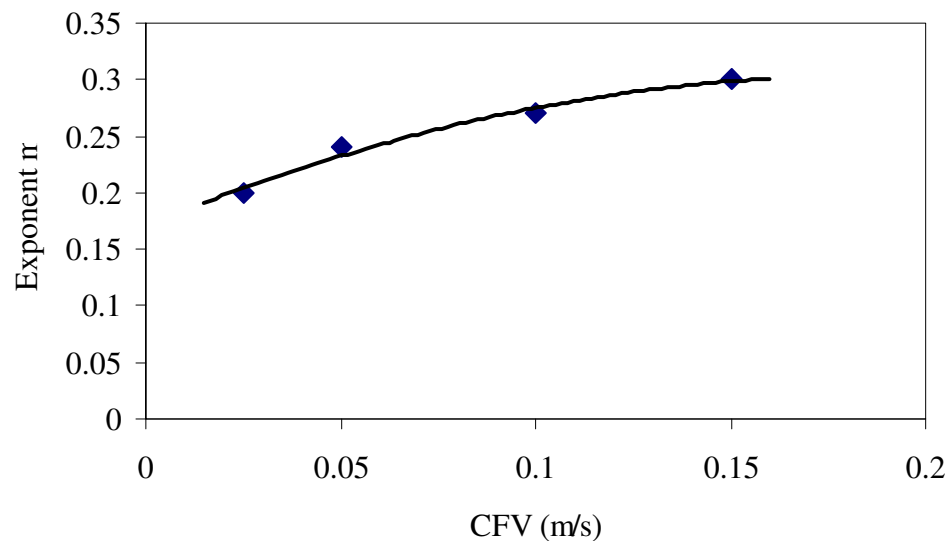
**Figure 6.10** CFV exponents,  $n$  for the hematite flocs.

Figure 6.11 shows the critical fluxes of different sizes of hematite flocs with similar fractal structures ( $d_F = 2.13 \sim 2.18$ ). The critical flux increased with the floc size overall. According to the findings on the mixed latex suspensions, the critical flux was only determined by the smallest particles in the suspensions and it could be enhanced due to the presence of the larger particles. Although only the smaller flocs were supposed to deposit on the membrane surface, in the polydisperse suspensions, a high mean particle size meant there was a high proportion of larger flocs in the suspensions. The high proportion of the larger flocs would enhance the critical fluxes by the same principals as in the bidisperse latex systems.



**Figure 6.11** Critical fluxes for different sizes of the hematite flocs.

The exponents on particle size ( $m$ ) are shown in Figure 6.12. The exponents were around 0.25 which was much lower than 1.33 for the conventional filtration theories (SID). The mean floc size probably could not be representative of the whole polydisperse suspensions.



**Figure 6.12** Particle size exponents,  $m$  for the hematite flocs.

## 6.6 Membrane fouling by fractal hematite flocs

Recent studies showed that the particle fractal structure had an influence on performance (Guan *et al.*, 2001; Lee *et al.*, 2003; Waite *et al.*, 1999). However, there is no report so far on the influence of fractal structure on the particle deposition during crossflow filtration. The relationships between specific cake resistance and fractal dimension during dead-end filtration were studied. In this study, the deposition of particles with different fractal structures on the membrane surface during crossflow microfiltration was observed using the in-situ DOTM technique.

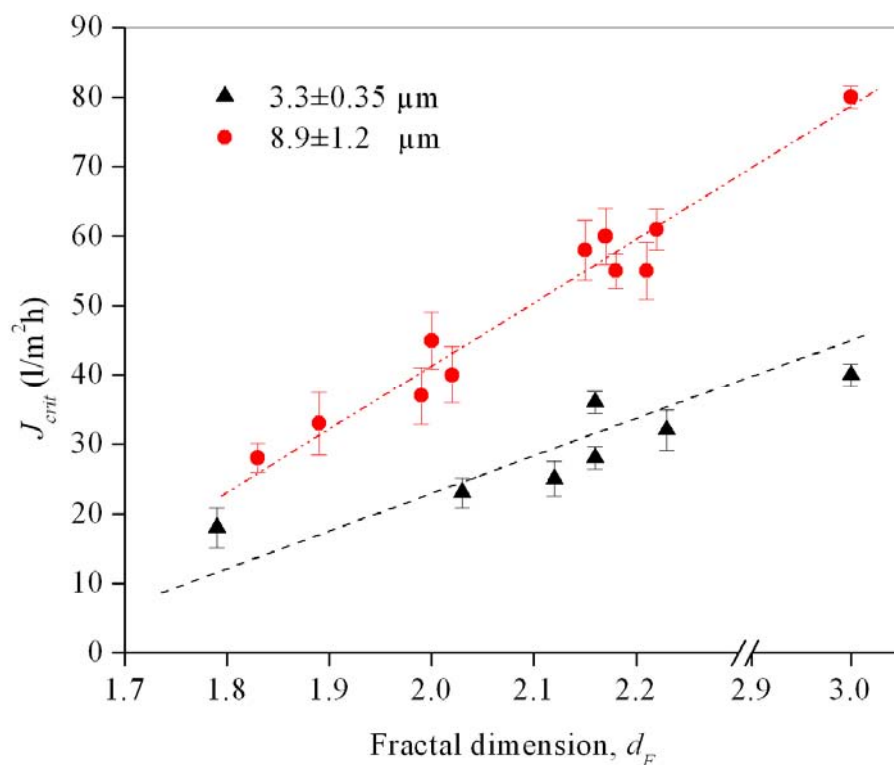


**Figure 6.13** Critical fluxes of hematite flocs with different fractal dimensions but similar mean particle size at CFV 0.1 m/s (data points at  $d_F = 3.0$  are extrapolated from the latex results).

The critical fluxes of two series of model hematite polydisperse solutions were measured and the results are shown in Figure 6.13. Each series had a similar particle mean size ( $3.3 \pm 0.35$  or  $8.9 \pm 1.2 \mu m$ ) but different fractal dimensions (1.79 ~ 2.23). All the experiments were conducted at a CFV of 0.1 m/s and a particle

concentration of 0.2 g/l. Two data points when  $d_F = 3.0$  (solid particles) with similar particle sizes and experimental conditions were extrapolated from the previous latex results according to Figure 4.2. It could be clearly seen that the critical flux increased with the fractal dimension for both series of hematite solutions although each solution had similar particle sizes respectively. Higher critical fluxes were obtained by the larger flocs as expected. However, the difference became smaller as the fractal dimension decreased.

The fractal dimension had a significant effect on the larger particles since it could be seen from Figure 6.13 that the critical flux increased faster than for the smaller particles. For the compact flocs ( $d_F > 2.0$ ), the critical flux increased with particle size. This was in accordance with the back transport theories for solid spheres. For the more porous flocs ( $d_F < 2.0$ ), the particle size had less significance on the critical flux. This could be explained by comparing the permeability of the porous flocs to the fluid. As the fractal dimension decreased, the flocs became more porous and their permeability to the flow increased, and therefore the drag forces caused by the tangential flow decreased (Figure 2.10) (Chellam *et al.*, 1993). The back transport diffusion or the inertial lift was compromised by the open porous structure. Johnson *et al.* (1996) also found that the porous aggregated particles had higher settling velocities in the sedimentation process.

The influence of fractal dimension on dead-end filtration was reported in the literature (Lee, 2005; Lee *et al.*, 2003). However, the effect of fractal geometry on critical fluxes in crossflow operations was different from that on dead-end cake filtration. For example, Lee (2005) studied the specific resistance of cakes formed by highly permeable hematite flocs in dead-end microfiltration. In this case, Lee found that filtration performance was less dependent on the fractal dimension due to the fact that the specific cake resistance by the larger flocs ( $\sim 40 \mu\text{m}$ ) did not change much with the fractal structure. However, the filtration rate was better for the smaller flocs ( $\sim 15 \mu\text{m}$ ) with lower fractal dimensions. This was explained by the inter-floc permeability and intra-floc porosity. The high inter-floc permeability did not improve the filtration performance since the intra-floc porosity was high enough

provided by the larger flocs. Therefore, the fractal dimension had a significant influence on the smaller flocs with lower intra-floc porosity in terms of specific cake resistance. In this study, the particle back transport diffusion was the main mechanism. The drag forces on the particles caused by the shear flow were crucial for the transient of particle deposition on the membrane surface. The properties of the cake made of the highly permeable flocs were not the concern in this study.

The fractal dimensions of the hematite flocs in this study were in a range of 1.7-2.3. Most of the porous particles encountered in separation processes are in this range (Lee, 2005). The results obtained from the model flocculated hematite suspensions could be representative of the real feeds. A linear trend line was drawn for each set of the data in Figure 6.13. It was noticed that the critical fluxes of solid latex particles extrapolated from previous results in Chapter 4 complied with the trend qualitatively. It was believed that the critical fluxes of aggregated particles were influenced by the fractal structures and increased with the fractal dimensions. In conclusion, not only the filtration was determined by particle size, the critical fluxes of flocculated feeds depended significantly on the fractal structure of the flocs as well as shown in Figure 6.13. The conventional filtration theories, such as Carman-Kozeny equation and SID model, assuming uniform solid particles need to be further modified in order to provide satisfactory predictions for the real situations.

## 6.7 Summary

Although most of the filtration models were developed assuming single particle size, the influence of the flocculated particle on the filtration had attracted some attention. The studies on the effect of particle size distribution in the literature were reviewed in this chapter. A concept of geometry, fractal dimension ( $d_F$ ) was introduced into the separation processes, and how this parameter affected filtration performance was explained. To our knowledge, there is no reported study on floc properties on the critical flux of the flocs in crossflow membrane filtration.

Protocols for preparing a variety of hematite polydisperse suspensions with different particle size distributions and fractal dimensions were presented. The factors influencing the flocculation of hematite particles were investigated and model flocculated flocs with various size distributions (5~80  $\mu\text{m}$ ) and fractal dimensions (1.7~2.5) were obtained for the crossflow microfiltration tests.

The critical fluxes of hematite polydisperse suspensions were determined using the DOTM technique. The deposition mechanisms of flocculated particles were observed. The behaviour of the flocs depositing on the membrane surface was found to be very different from the rigid spherical particles studied previously. Long-term operation at a sustainable flux could be possible for the flocculation-filtration system due to the broader particle size distribution as well as porous structure and the tendency for re-entrainment. A good practice in the filtration of flocculated feeds was to reduce the proportion of smaller particles as much as possible.

The dominating factors, crossflow velocity, particle size and fractal structure were investigated during the crossflow microfiltration of flocculated polydisperse suspensions. The critical fluxes increased with the crossflow velocity and particle mean size as predicted by the back diffusion mechanisms. However, the degree of their effects differed from the model spheres due to the particle size distribution and porous structure. The CFV exponents ( $n$ ) extracted from the hematite (0.07~0.2) were much lower than from the latex (0.62~0.77). The size exponent ( $m$ ) obtained from the hematite (~0.25) was also much lower than from the latex (~0.8). The critical fluxes for the porous flocs were proved to increase with fractal dimension. Fractal dimension was more influential on larger flocs as the critical fluxes increased greatly at higher fractal dimensions.

The results shown here indicated that permeate flux predictions using conventional critical flux theories would not be suitable for flocculated feeds unless the particle size distribution and the fractal structure could be accountable in the models.

## **Chapter 7 Determination of critical flux by mass balance technique combined with DOTM**

### **7.1 Comparison of critical flux measurement techniques**

The concept of critical flux has been widely applied to the study of membrane fouling by many membrane researchers since it was first proposed by Field *et al.* (1995). As discussed in Chapter 2, TMP monitoring, mass balance and direct observation are the major techniques that were commonly used to determine the critical flux value in crossflow microfiltration. Chapters 4, 5 and 6 provided a qualitative understanding of membrane fouling mechanisms which could be influenced by feed properties (concentration, size, pH and ionic strength) and hydrodynamic conditions (flux, CFV and channel height) using the observation technique of DOTM. In those chapters, the flux stepping and the DOTM technique were used to obtain the critical fluxes. It was recognized that this approach might be somehow subjective, although an individual observation could probably identify the critical flux within  $\pm 5 \text{ l/m}^2\text{h}$ .

The objective of this chapter is to compare the critical flux measurements and develop a more quantitative method by analyzing the images of the DOTM combining with mass balance calculation to determine the critical flux of particle suspensions in crossflow microfiltration.

#### **7.1.1 Transmembrane pressure (TMP) monitoring**

Among the techniques available to determine the critical flux, TMP monitoring is the most popular method since it can be done simply by conducting a flux stepping test and monitoring the TMP increase. In this case, the critical flux is defined as the highest flux that causes no steady increase in TMP. The flux is controlled constant for a defined duration, and then increased with a certain increment until the critical flux is reached. This can be achieved by a pump in the permeate line and thus the



pressure only in permeate line changes (actually decreases) with the flux increment. When the operating flux is below the critical flux, the TMP is constant since no fouling occurs. When the critical value is exceeded, the particles deposit and steadily form a cake layer on the membrane surface and the resistance provided by this cake layer causes the increase in TMP. Considering the effect of the increment between the steps, the average of the highest flux without TMP increasing and the lowest flux with TMP increasing is often regarded as the critical flux. A graph of the rate of TMP increase ( $dTMP/dt$ ) vs. operating flux can be plotted to determine the critical flux. However, strictly speaking, the critical flux is defined as the point that particles start depositing on the membrane surface. Therefore the critical flux determined by TMP monitoring could be higher than the defined value. This discrepancy could be made worse by the low sensitivity of the pressure transducers and/or the low specific resistance provided by the foulants unless sufficient time is given to allow the accumulation of the particle deposition and a change in TMP is detectable by the pressure transducers. Unfortunately, the flux stepping test is normally practiced for 10 to 30 minutes during each constant flux step. There is not a standard protocol for the flux step duration. For some foulants, with a very low specific resistance, a longer duration is necessary before the formed cake layer induces any TMP increase that can be detected by the pressure transducers. Hence the critical flux determined by the TMP monitoring is a function of the operating duration. This is especially important for membrane bio-reactor (MBR) operations. The startup flux value at the beginning of the flux stepping test also has an effect on flux-TMP profiles. If the startup flux is too high and near the critical flux, incipient fouling occurs. The deposited particles will have an influence on the subsequent fouling. Therefore, it is suggested to start up from a relatively low permeate flux.

Chen *et al.* (1997) studied the flux-TMP profiles of colloidal silica in CFMF. The flux stepping tests were performed 30 minutes for each step. The flux was increased first and then decreased in the same manner. The TMPs for the decreasing flux steps did not follow the ones for the increasing flux step even when there was no TMP increasing for any step. The decreasing flux steps required higher TMPs for the same flux during the increasing flux steps, implying that particles deposition

occurred during the increasing flux steps even though there was no detectable TMP increase. They also studied the startup protocol and found that the TMP was much lower if the imposed flux was stepped up gradually from a low value than if the constant flux was applied directly up to the highest value. They proposed that this could be due to the different conditions in the boundary and cake layers formed under the two scenarios.

Similarly, Wu *et al.* (1999) conducted flux stepping up and down experiments with the help of sensitive TMP measurements to trace membrane fouling. They ran a constant flux  $J_1$  for 5 minutes as step 1 and recorded the corresponding TMP as  $TMP_1$ . Then the flux was stepped up to a higher value for 5 minutes again. After that, the flux was stepped down to the previous value. The TMP for this step was recorded as  $TMP_1'$ . The difference between  $TMP_1$  and  $TMP_1'$  was referred as “deviation”. If the deviation in TMP was zero, it was presumed no fouling occurred on the membrane surface and the flux would be further stepped up and down in the same way until the deviation was no longer zero. The extra resistance due to either adsorption or deposition required increase in the TMP to keep the previous flux constant.

### 7.1.2 Direct observation

In the literature, non-invasive, in situ techniques were developed to study fouling phenomena and measure the critical fluxes for all kinds of suspensions under various conditions (Altmann *et al.*, 1997; Hughes *et al.*, 2006; Li *et al.*, 1998; Mairal *et al.*, 2000; Mc Donogh *et al.*, 1995; Mores *et al.*, 2001). These techniques, especially the visual observation techniques provided insights and information on the interactions between particles and membrane surface, the cake thickness, the fouling pattern and so on. A flux value is definitely above the critical flux if significant and continuous deposition is observed on the membrane surface. In this case, the critical flux is defined as the highest flux that causes no or negligible fouling on the membrane under the operating conditions. The critical fluxes determined by the direct observation techniques tend to be lower than those by the

TMP monitoring method. Two review papers available in the literature provide a good summary on the non-invasive, in situ techniques for membrane fouling studies (Chen *et al.*, 2004a; Chen *et al.*, 2004b).

### 7.1.3 Mass balance

Apart from the above mentioned methods of determining critical flux, another way to measure the critical flux for separation of particles from suspensions is to monitor the changes in solute or particle concentration. When fouling occurs, particles will deposit on the membrane and be lost from the filtration system. For feed and permeate recycle, the decrease in the concentration in the feed reservoir can be monitored over time. Alternatively, one can calculate the mass of cake deposited per unit area of membrane ( $\omega$ ) using Equation (2-9) in Chapter 2. The specific cake resistance of the foulant needs to be measured beforehand. The cake resistance in Equation (2-9) can also be calculated using the Darcy's law (one of Equations (2-1) to (2-5)). This method has the same limitation as the TMP monitoring technique. It depends on the sensitivity of the pressure transducers and the specific resistance that the fouling cake provides. In addition, the compressibility of the cake could complicate the situation. Once the mass on the membrane surface is determined, the particle deposition rate (kg/s) at different operating fluxes can be plotted as a function of permeate flux. The critical flux is then the flux at which the particle deposition rate is zero. Technically, it is the intercept of the deposition rate vs. permeate flux curve extrapolated on the x-axis. The mass balance technique is a more sensitive method for determining the critical flux because it is based on the commencement of particle deposition. However, it can be limited if particles are lost due to adsorption in the piping system.

Kwon and Vigneswaran (1998) measured the critical fluxes of three different sizes of latex particles (0.46, 3.2 and 11.9  $\mu\text{m}$ ) using both TMP monitoring and mass balance methods. They monitored the feed concentration in terms of turbidity while the flux stepping tests were conducted. The TMP increase was sensitive to the particle deposition caused by small particles of 0.46  $\mu\text{m}$  latex due to the high

specific resistance. The cake layer formed by the medium sized particles of 3.2  $\mu\text{m}$  latex did not incur significant increase in TMP. For particles of 11.9  $\mu\text{m}$  latex, the TMP did not increase at all although severe fouling occurred on the membrane surface. Compared with TMP monitoring, the mass balance approach corresponded well with the particle deposition for all sizes of latex particles. This was especially true for the larger particles since only a small amount of deposited particles would cause a significant decrease in the feed concentration. The results showed that the critical fluxes defined by mass balance were usually lower but more precise than those defined by TMP monitoring. In a later paper (Kwon *et al.*, 2000), they involved more sizes of latex particles and calibrated the feed concentration at zero permeated flux considering the possibility of particle adsorption on the system walls. The constant fluxes were stepped up continuously with a cleaning process after each step to remove the deposited particles during the previous step. By monitoring the concentration change, the mass deposited on the membrane surface was calculated at different flux values. The deposition rate (obtained from logarithmic regression) vs. permeate flux was plotted. The relationship between deposition rate and permeate flux was observed to be linear. The x-intercept of the linear line was taken as the critical flux based on mass balance. It was clearly observed that the difference between the critical fluxes based on TMP increase and mass balance was greater as the particle size increased.

## 7.2 Mass balance combined with observation technique

As stated in the previous chapters (Chapters 4, 5 and 6), all the critical fluxes were measured by the DOTM technique in this study. A light transmission microscope was used to observe the membrane surface while constant flux stepping tests were conducted. Each constant flux step was run for 15 minutes. For a certain permeate flux value, if two-thirds of the observed area was covered by deposited particles, this flux was then regarded as above the critical flux. The 'critical flux' defined by the DOTM was hence the average value of fluxes for no deposition to continuous deposition on the membrane surface. Although the flux-TMP profiles were recorded during the experiments, they did not give reliable information on critical flux

determination due to the large particle sizes used in this study, and therefore the low specific resistance the particles provided. As shown in Chapter 2, the resistance of a formed cake layer caused by the relatively small particles (3.0  $\mu\text{m}$ ) was negligible compared with the membrane resistance. The TMP was effectively constant above the critical flux when a continuous particle deposition could be seen on the membrane surface by the DOTM technique. In order to improve the accuracy of the DOTM technique and find the “real” critical flux, below which there is no particle deposition (as defined the “critical flux” concept), a new method was proposed here whereby the DOTM technique was combined with the image analysis and the mass balance method to determine the critical flux. The approach was to measure the rate of surface coverage at different fluxes and extrapolate the data to find the flux at which the rate of coverage became zero.

‘Rate of coverage’ was examined using cake formation in MF. For example, Mores *et al.* (2001) used another observation technique, called the direct visual observation (DVO) technique to study yeast deposition and removal in microfiltration. A microscope was used to view the particle deposition just above the membrane surface instead of through the membrane as in the DOTM. The images captured by DVO were not clear enough to distinguish the individual particles. However, the fouling area was distinct enough to calculate the coverage of a mono layer. They also proposed a relationship between the permeate flux and coverage fraction,

$$J_f = (1 - \beta_m)J_o + \beta_m J_m = J_o - (J_o - J_m)\beta_m \quad (7-1)$$

They defined  $J_f$  as the overall forward filtration flux and  $J_m$  as the flux through the portion of membrane fouled with a monolayer, and the parameter  $\beta_m$  as the fraction of the membrane surface covered in a mono layer. They found that a complete coverage of a mono layer only reduced the permeate flux by 30 %, indicating that the deposited particles only partially blocked the membrane pores.

Instead of using a visual observation technique, Ho *et al.* (2000) developed another approach to predicting permeate flux. They assumed that the rate of coverage or

blockage was proportional to the convective flow rate of the protein aggregates to the membrane surface.

$$\frac{dA_{open}}{dt} = -\alpha Q_{open} c_b \quad (7-2)$$

where  $\alpha$  was defined as a pore blockage parameter which was equal to the membrane area blocked per unit mass of the protein convected to the membrane surface and  $c_b$  was the bulk concentration. Based on this equation, they further developed a combined pore blockage and cake filtration model for the protein fouling.

Recently, Knutsen *et al.* (2006) used the DVO technique to measure the fraction deposition ( $\theta$ ) which was the fraction of particles convected to the membrane surface by the permeate flow. They also proposed a mass balance equation,

$$\frac{dC_w}{dt} = \theta J c_b \quad (7-3)$$

where  $C_w$  (number of particles/mm<sup>2</sup>) was the area concentration of particle number on the membrane surface and  $c_b$  was the number concentration (particles/volume) in the feed. The area concentration was found to be linear with time at different permeate fluxes. Using this equation, the fraction depositions were calculated at different permeate fluxes. The highest flux with zero fraction deposition ( $\theta = 0$ ) was regarded as the critical flux.

Kang *et al.* (2004) also conducted direct microscopic observation experiments to study the biofouling during crossflow microfiltration. They found that the microbial deposition rate was linear with the permeation velocity. Their coverage curve showed a similar sigmoid shape to that found in this study. Surface coverage increased linearly with time up to 40-60 % and then slowed down when fouling continued. They claimed that this was due to the fact that deposition onto the covered area was not taken into account. However, in the study reported in this

thesis, latex particles always formed a mono layer first before the second layer was built up. Kang *et al.* set up a mass balance based on the observed membrane view between the number concentration and the fraction surface coverage,

$$N = \frac{\theta(t)}{\pi a^2 A_m} \frac{1}{N_0} \quad (7-4)$$

where  $N$  was the normalized bound cell density (number of cells/m<sup>2</sup>).  $\theta$  was the coverage fraction.  $A_m$  was the observation area. And  $N_0$  was the bulk feed cell concentration.

### 7.3 Mass balance equation development

In microfiltration, permeate flux is the only driving force that causes particles to move towards and deposit on membrane surface if the electrical attraction between the particles and the membrane can be neglected. In other words, the particles will deposit on the membrane surface under a net convection ( $J - J_{crit}$ ) if the net permeate flux is positive. The fouling rate is assumed to be proportional to the net convective permeate flux on the particles,

$$\frac{dm}{dt} = \theta c_b (J - J_{crit}) A \quad (7-5)$$

$\theta$ : fraction of particles convected and deposited on the membrane

$m$ : mass of foulant deposited on the membrane, kg

$c_b$ : bulk concentration, kg/m<sup>3</sup>

$J$ : operating flux, m/s

$J_{crit}$ : critical flux, m/s

$A$ : membrane area, m<sup>2</sup>

Equation (7-5) differs from Equation (7-3) (Kang *et al.*, 2004), since it is based on a net flux of particles provided by ( $J - J_{crit}$ ). Equation (7-5) implies that when  $J > J_{crit}$ ,

particles begin to deposit, and a proportion of them ( $\theta$ ) remain in the cake. When  $\theta$  is equal to 1.0 all particles accumulate in the cake; and when  $\theta < 1.0$ , only a portion of the particles convected remain on membrane.

The DOTM technique used in this study could detect the commencement of particle deposition when fouling occurred over a small sample of the membrane. The images captured by the camera provided distinct information of the number of deposited particles and the area of formed cake on the membrane surface at a moment in time. The downloaded images could be further examined and analyzed after the filtration experiments. Model particles (latex beads in this study) with defined shape and known properties (size and density) were used in this study, and hence the fouling layer coverage on the membrane could be reliably converted to the mass of the foulants. Measurement of the fouling mass by this method was believed to be more sensitive and accurate than the feed concentration measurements *i.e.* monitoring concentration change in the feed reservoir. However, the observation method had its own limitations. The membrane fouling over a small observation area was taken to represent the whole membrane area, thus the results largely depended on the selection of the observation area. To be consistent and representative, the microscopic objective was focused on the center of the membrane area during all the filtration experiments. Then Equation (7-5) can be further developed to incorporate the coverage data into the equation.

The volume of a single spherical latex particle with a diameter of  $d$  is,

$$V = \frac{1}{6}\pi d^3 \quad (7-6)$$

A single spherical latex particle has a mass of,

$$m' = \rho V = \frac{1}{6}\rho\pi d^3 \quad (7-7)$$

$\rho$ : particle density (for latex particles,  $1.05 \times 10^3 \text{ kg/m}^3$ )



$d$ : particle diameter (3.0, 5.0 and 10.0  $\mu\text{m}$  used in this study)

Assuming that number of  $n$  particles deposited on the membrane surface, the mass of the deposited particles on the membrane can be expressed,

$$m = nm' = \frac{1}{6} \rho \pi d^3 n \quad (7-8)$$

$n$ : number of particles deposited on the membrane

The deposited mass rate is, according to Equation (7-8),

$$\frac{dm}{dt} = \frac{1}{6} \pi \rho d^3 \frac{dn}{dt} \quad (7-9)$$

The projected area of a single spherical particle with a diameter  $d$  on membrane is,

$$A_{\text{sphere}} = \frac{1}{4} \pi d^2 \quad (7-10)$$

The number of the deposited particles on membrane surface will then be,

$$n = \frac{A_{\text{covered}}}{A_{\text{sphere}}} = \frac{4A_{\text{covered}}}{\pi d^2} \quad (7-11)$$

Since the membrane fouling coverage is defined as,

$$\text{Coverage} = \frac{A_{\text{covered}}}{A_{\text{observation}}} \quad (7-12)$$

$A_{\text{sphere}}$ : cross section area of a sphere ( $\text{m}^2$ )

$A_{\text{covered}}$ : total particle covered area on membrane surface ( $\text{m}^2$ )

$A_{\text{observation}}$ : observation area ( $\text{m}^2$ )

Combining and integrating Equations (7-11) and (7-12) into Equation (7-9),

$$\frac{dm}{dt} = \frac{2}{3} \rho d \frac{dA_{\text{covered}}}{dt} = \frac{2}{3} \rho d \cdot \frac{d\text{Coverage}}{dt} \cdot A_{\text{observation}} \quad (7-13)$$

The mass balance equation (7-5) now becomes,

$$\frac{d\text{Coverage}}{dt} = \frac{3}{2} \frac{c_b}{\rho d} \theta (J - J_{\text{crit}}) \quad (7-14)$$

Based on Equation (7-14), the membrane coverage change rate ( $\frac{d\text{Coverage}}{dt}$ ) can be obtained by analyzing the DOTM images. Input data are  $c_b$ , the particle concentration in the bulk solution, which is known at the beginning of the filtration, and  $J$  which is the constant operating flux. The only unknown is the critical flux,  $J_{\text{crit}}$  which is to be determined. A graph (deposition rate vs. permeate flux) can be plotted then. Figure 7.1 illustrates how to obtain the critical flux by the mass balance equation combined with the DOTM images. To determine  $J_{\text{crit}}$ , the data  $\frac{d\text{Coverage}}{dt}$  vs.  $J$  can be plotted. The intercept on the x-axis is the estimated critical flux when there is no particle deposition on the membrane surface (Figure 7.1).

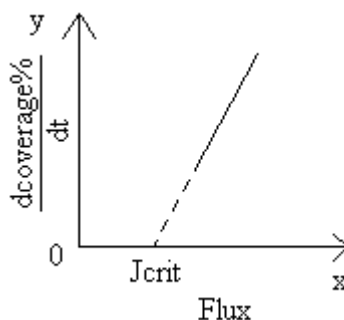


**Figure 7.1 Schematic plot of coverage rate vs. permeate flux.**

When fouling occurs, the particles initially deposit on the clean membrane which provides 100 % of open area for the permeate flux. As the particle deposition continues, the available open area for filtration reduces, and the average permeate flux can no longer be used in the calculations anymore. The local flux has to adjust itself in order to maintain the average constant flux operation, *i.e.* the local flux on the open area has to increase to compensate for the reduction in the fouled area. As expressed in the classical cake filtration model (Ho *et al.*, 2000), the overall permeate flow rate across the fouled membrane could be expressed as the sum of the flow rates over the open and covered membrane area,

$$Q = Q_{open} + Q_{covered} \quad (7-15)$$

$Q$ : the filtration flow rate across the membrane ( $\text{m}^3/\text{s}$ )

$Q_{open}$ : the filtration flow rate across the unfouled membrane ( $\text{m}^3/\text{s}$ )

$Q_{covered}$ : the filtration flow rate across the fouled membrane ( $\text{m}^3/\text{s}$ )

Rewriting Equation (7-15) in terms of permeate flux,

$$JA_{observation} = J_{open}A_{open} + J_{covered}A_{covered} \quad (7-16)$$

and,

$$A_{observation} = A_{open} + A_{covered} \quad (7-17)$$

where  $J$  is the average permeate flux across the observation membrane area ( $A_{observation}$ ),  $J_{open}$  is the permeate flux over the clean membrane area ( $A_{open}$ ) and  $J_{covered}$  is the permeate flux over the mono deposition layer ( $A_{covered}$ ) which is a function of the foulant properties.

Two boundary conditions can be discussed for Equation (7-16). If the specific resistance is high and the cake blocks the covered area totally, there is no flux through the covered membrane area, *i.e.*  $J_{covered} = 0$ , and then the local flux on the

open area ( $J_{open}$ ) is inversely proportional with the open area ( $A_{open}$ ). On the other hand, if the specific resistance of the foulant is low and negligible, and the membrane pore size is uniform, there is only one homogeneous permeate flux across the membrane, *i.e.*  $J = J_{open} = J_{covered}$ . In this case, the fouling rate is absolutely linear with time as shown in Equation (7-14). In between, when the fouling layer is semi-permeable and the fouling resistance cannot be neglected, the relationship between  $J_{open}$  and  $J_{covered}$  is inversely linear. Figure 7.2 shows the relationship between  $J_{open}$  and  $J_{covered}$  when the operating average flux ( $J$ ) is 30 m/s and half of the membrane area is covered according to Equation (7-16). The first and the last points in Figure 7.2 are describing the two boundary conditions discussed above.

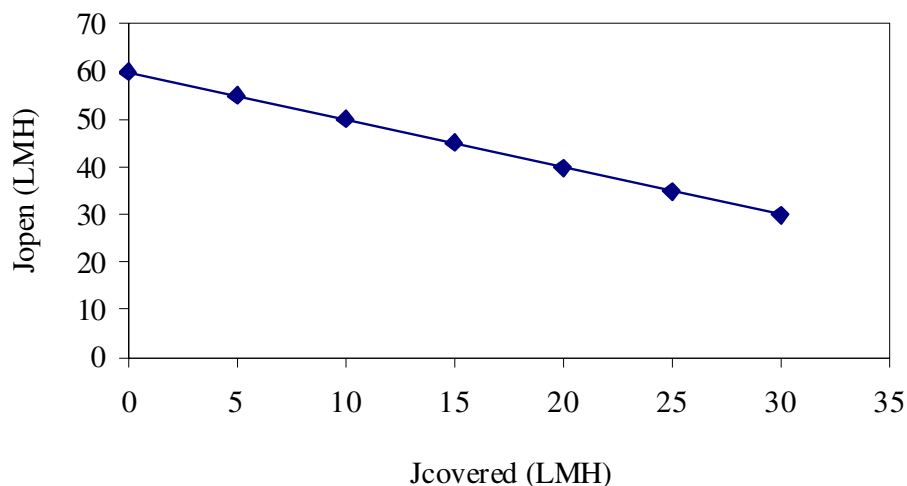


**Figure 7.2**  $J_{covered}$  vs.  $J_{open}$  where  $J = 30 \text{ l/m}^2\text{h}$  and  $A_{open} = A_{covered}$ .

Combined with the mass balance equation, the local fluxes through the open and covered membrane areas can be modified as,

$$\frac{dA_{covered}}{dt} = \frac{3}{2} \frac{c_b}{\rho d} [(J_{open} - J_{crit})A_{open} + (J_{covered} - J'_{crit})A_{covered}] \quad (7-18)$$

for  $\theta = 1.0$ , where  $J_{crit}$  is the critical flux of the new and clean membrane and  $J'_{crit}$  is the critical flux of the fouled membrane covered by a mono particle layer. With a

mono layer of foulants on top of the clean membrane, it is as if a “new” piece of membrane is being used.  $J'_{crit}$  might be an approximation of  $J_{crit}$  depending on the properties of the cake layer formed on the membrane surface.

Equation (7-18) is a dynamic process describing the relationship between  $J_{crit}$  and  $J'_{crit}$  as the membrane fouling continuously occurs. It is based on the assumptions that the filtration rate is no longer homogeneous when particle deposition appears on the membrane surface, and there is still permeate flow through the covered area, *i.e.* the deposited cake layer is partially permeable to the flow. Equation (7-18) shows the relationship of the local fluxes between the permeate flux on the clean membrane and the permeate flux on the fouled membrane as the membrane shifts from no fouling to total coverage.

It is not possible yet to measure the local fluxes during the filtration. However, the extreme conditions can be discussed according to Equation (7-18). When operated at sub-critical flux, there is no particle deposition on the membrane surface. The changing rate of the covered area is hence equal to zero. Only the permeate flux through the clean membrane contributes to the filtration rate. The critical flux is equal to the maximum  $J_{open}$  where there is no particle deposition at all. On the contrary, when the membrane is totally covered by a mono layer of the deposited particles, Equation (7-18) has a simple form (for  $\theta = 1.0$ ),

$$\frac{dA_{covered}}{dt} = \frac{3}{2} \frac{c_b}{\rho d} (J_{covered} - J'_{crit}) A'_{covered} \quad (7-19)$$

where  $A'_{covered}$  is the covered area on the second fouling layer and increases linearly with  $dA_{covered}/dt$  according to Equation (7-19).

## 7.4 Results

In Chapters 4 and 5, the critical fluxes were measured in flux stepping tests using the DOTM technique. The imposed flux steps were increased continuously in one filtration run. Since incipient deposition occurred in reality even below the critical flux, the deposited particles in the previous step could have effects on the incoming particles in the following step. In order to avoid this accumulation effect, some selected experiments were repeated and each flux step was conducted separately with a new piece of membrane each time. Flux steps slightly below and above the critical flux were conducted in two runs for 15 minutes each or until the membrane coverage did not change significantly. However, the available flux step values were very limited. When above the critical flux, the fouling occurred rapidly and total coverage appeared within minutes. The time interval between the captured images was set to one minute or 30 seconds according to the fouling rate.

Figures 7.3 to 7.5 are the examples of the coverage development on the membrane surface in the filtrations of 3.0, 5.0 and 10.0  $\mu\text{m}$  latex particles. The operating conditions are shown in the legends. It was found that during the single flux-step experiment, the coverage curves typically showed a sigmoid shape. This agreed with the results shown in Chapter 5 (Figures 5.6 and 5.7). The incipient portions of the curves, where there were no significant increase in membrane coverage with time, showed some filtration start-up effects, as it took a couple of minutes before the particles were dragged from the bulk to the polarization boundary layer and then started depositing on the membrane surface. It was also possible that the particle deposition occurred on the upstream of the observed area first and then took some time to appear in the observing view. Therefore, the membrane coverage rate was relatively low at the beginning of the filtration. This stage was defined as the start-up of the filtration. Once the particle deposition started, the particles accumulated around the existing particles and the coverage increased sharply with time. This was the second stage of the fouling process. These portions of the coverage curves were shown to be linear as expected during the second stage and there might be particle cluster removal during this period. In the last stage, the fouling seemed to stop

growing when the coverage reached around 80 % proceeded from the second stage. The coverage curve reached a plateau after that. It was difficult for the subsequent particles to fill up the gaps between the deposited particles. This was probably due to the increase of the repulsive interactions since the formed cake was made up of particles with the same surface charge. This will be discussed in the next paragraph.

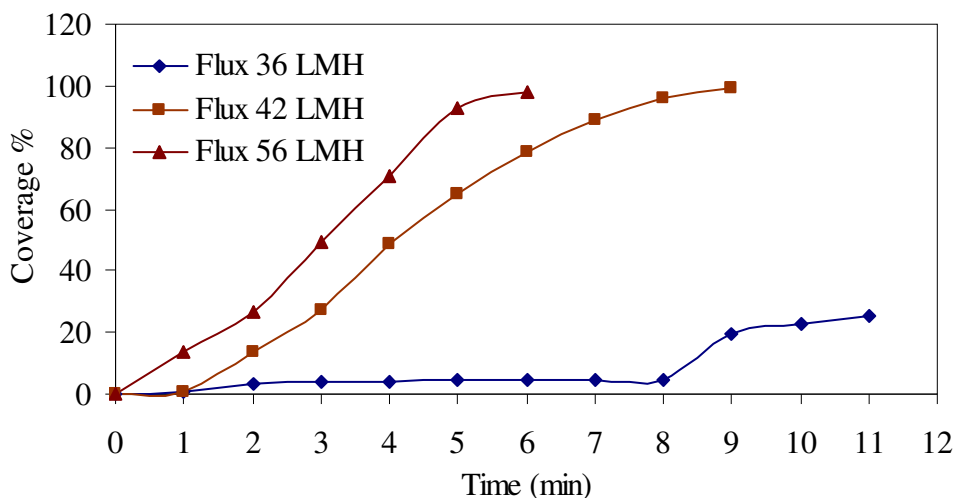


**Figure 7.3** Membrane coverage development in the filtration of 3.0 µm latex at a concentration of 0.05 % vol., pH 8.0 and a CFV of 0.2 m/s.

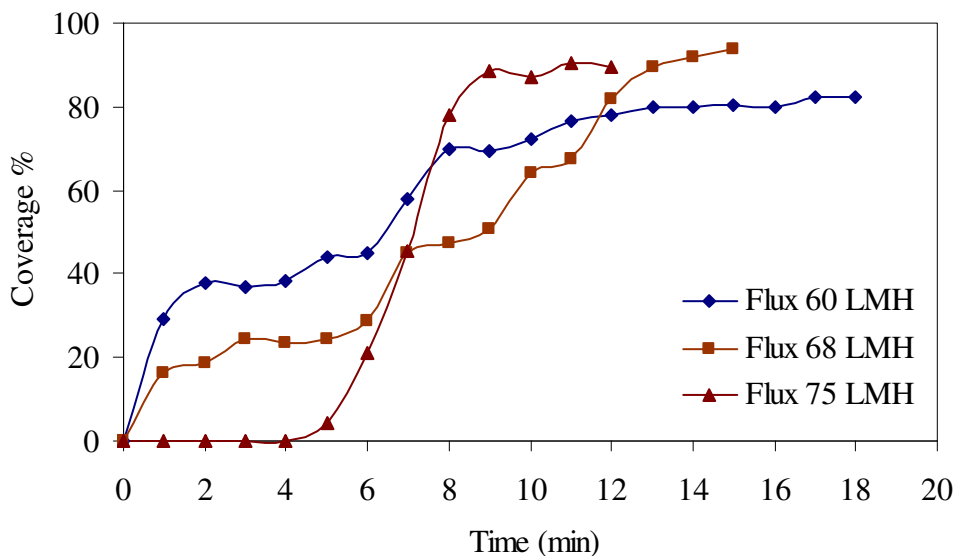


**Figure 7.4** Membrane coverage development in the filtration of 5.0 µm latex at a concentration of 0.05 % vol., pH 8.0 and a CFV of 0.2 m/s.

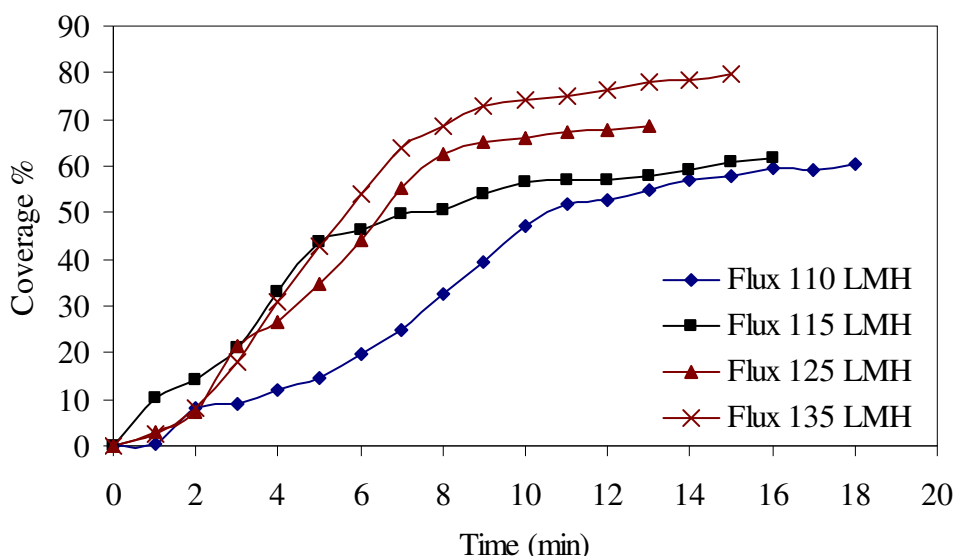


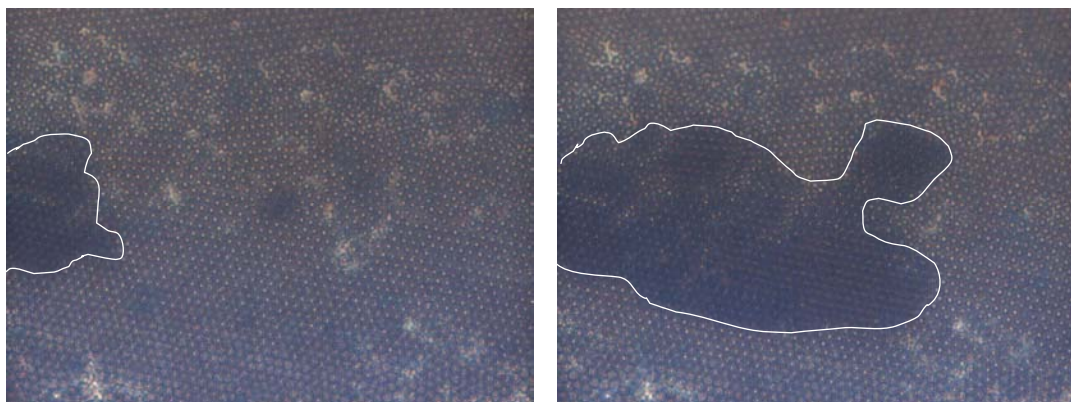
**Figure 7.5** Membrane coverage development in the filtration of 10.0  $\mu\text{m}$  latex at a concentration of 0.05 % vol., pH 8.0 and a CFV of 0.2 m/s.

Decrease in the membrane coverage curve was noticed during the particle deposition (Figure 7.4). The fluctuation was due to the removal of the deposited particles. As the particles accumulated onto the membrane surface, cluster growth would occur due to the filtration pressure. The formed aggregates tended to be removed by the shear flow due to the larger size. This was in accordance to the experimental observations as the removal of a large chunk of the particles was observed. Although there were some variations in the membrane coverage, the overall increasing trends still could be seen from the figures.

A second layer of particles was observed to build up after almost total coverage by the first layer. Figure 7.6 shows an example of a second layer developing on the first layer in the filtration of 5.0  $\mu\text{m}$  latex particles. Although the second layer was blurry in the image, the hue between the first and the second layers was distinguishable. Shown in Figure 7.7 is the image analysis of the results in Figure 7.6. Figure 7.7 (a) shows the membrane coverage for the first layer of the latex particles (images not shown). Figure 7.7 (b) shows the development of the second layer formed on the first layer, and Figure 7.7 (c) is a combination of (a) and (b). The coverage curve for the second layer showed a qualitatively similar pattern to



the first layer. However, the second layer reached a lower ‘plateau’ than the first layer. This might be due to the very different surface presented to the second layer. The first layer occurred on a relatively smooth surface with a surface charge of 0 mV, compared with the particle charge of  $-10$  mV. The second layer came to a surface which was more uneven (made up of a layer of  $5.0\text{ }\mu\text{m}$  particles) and of the same surface charge. In fact, the second layer could have a slightly higher  $J_{crit}$  than a different higher deposition fraction ( $\theta$ ) due to the effect of roughness. It was believed that the fouling would continue in the same way in the following layers.



(a) A second particle layer

(b) 1.5 minutes after (a)

**Figure 7.6** An example of second layer build-up during the filtration of  $5.0\text{ }\mu\text{m}$  (0.05 % vol.) latex suspension at pH 8 and CFV 0.05m/s.

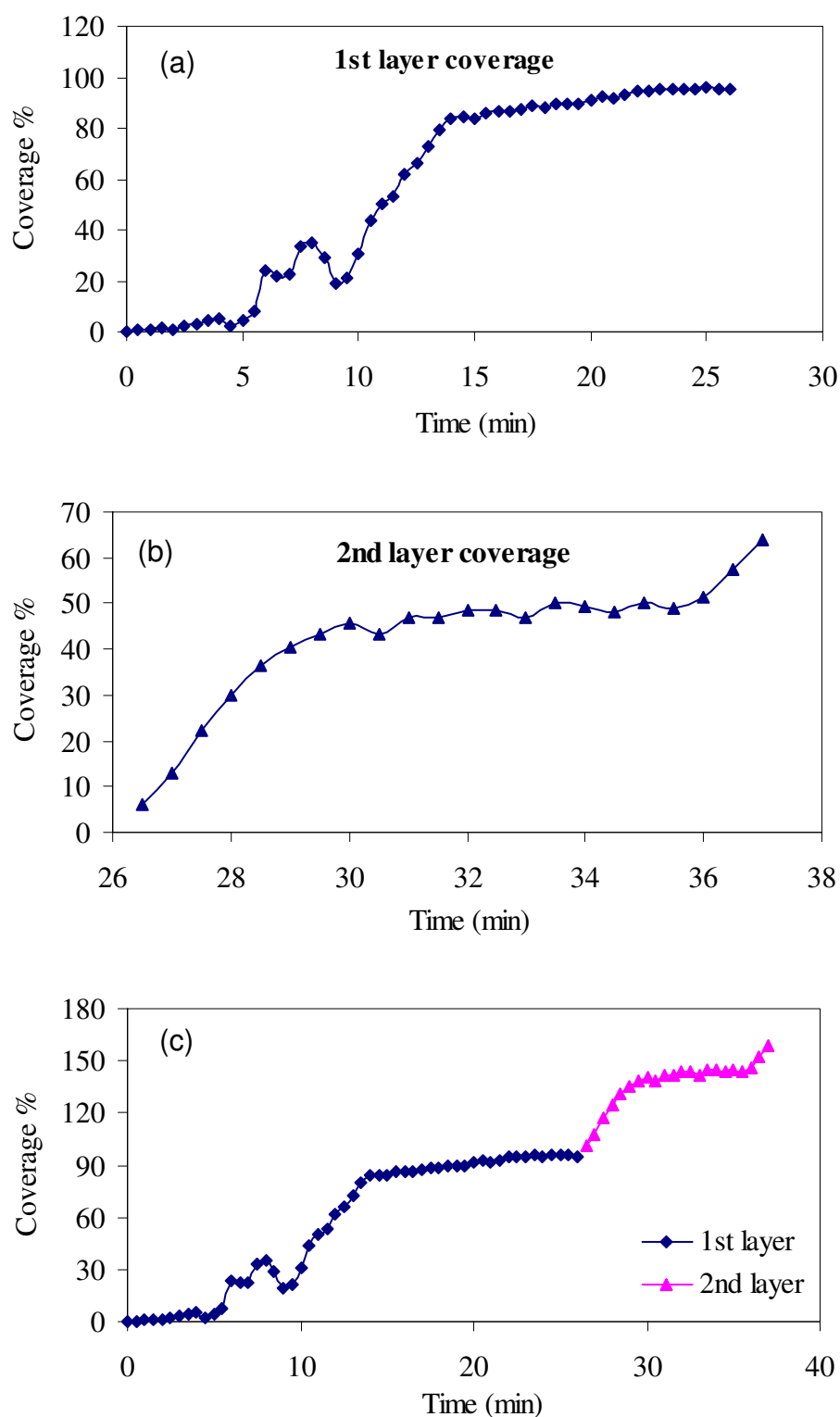


**Figure 7.7** Membrane coverage development in the filtration of 5.0 μm latex at a concentration of 0.05 % vol., pH 8.0 and CFV 0.2 m/s. (a) 1<sup>st</sup> layer coverage, (b) 2<sup>nd</sup> layer coverage and (c) combined coverage.

In order to investigate the deposition rate ( $\frac{d\text{Coverage}}{dt}$ ) based on Equation (7-14), a linear regression was performed on the particle deposition rates obtained from Equations (7-2), (7-3) and (7-4). A linear trend line was drawn for the most linear part of the coverage curves. The gradient of the trend line with the highest R-squared was taken as the average particle deposition rate. The curves of average deposition rate vs. permeate flux for different sizes of latex particles were plotted in Figure 7.8. The equations shown in the legend were the linear regressions for 3.0, 5.0 and 10.0  $\mu\text{m}$  latex particles respectively. The R-squared values were quite high. The intercept on the flux axis with a zero deposition rate was regarded as the critical flux by the mass balance method. This was a flux below which there should be no particle deposition on the membrane. In this case, the critical fluxes were 35, 60 and 71 for 3.0, 5.0 and 10.0  $\mu\text{m}$  latex particles respectively. The larger particles gave higher critical fluxes as expected from the previous work.

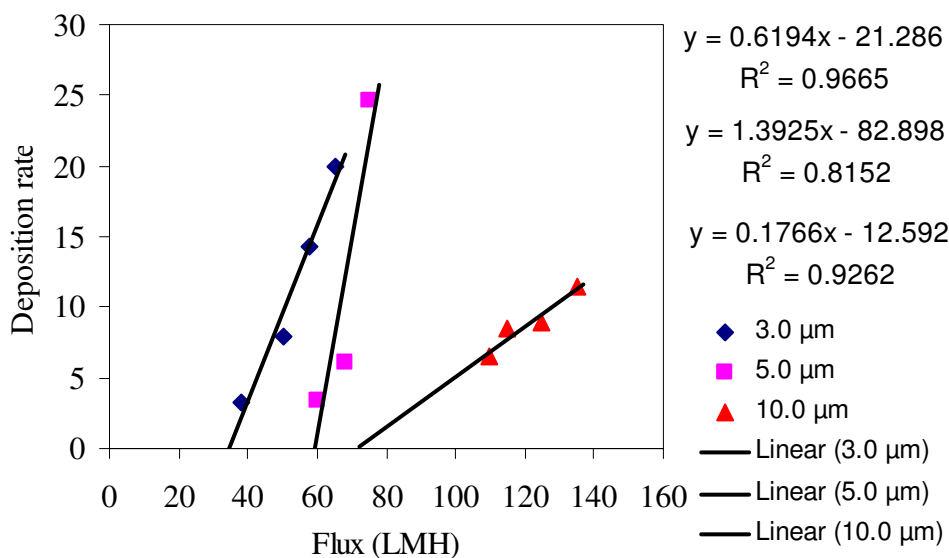


**Figure 7.8 Particle deposition rate vs. permeate flux.**

Using the same mass balance method, the critical fluxes at different crossflow velocities, pH values and feed concentrations were measured. The results are shown in Tables 7.1 to 7.3 and compared with the previous results measured by the DOTM. The critical fluxes based on the mass balance method were always lower than the

DOTM values. The discrepancy appeared greater at the lower values of  $J_{crit}$  where the DOTM method might be less precise. For the larger particles and higher fluxes,  $J_{crit}(\text{mass balance})$  was about 90 % of  $J_{crit}(\text{DOTM})$ . As described in the experimental protocols (Section 3.5.2 in Chapter 3), the critical flux defined by the DOTM was an average value of the neighboring fluxes where the fouling transient happened. The accuracy of the critical flux determined by the DOTM depended on the increment of the neighboring flux steps. There might still be fouling on the membrane slightly below this critical flux. Potentially, the critical flux by the mass balance was more accurate as it came from the extrapolations of the trends from several experiments. In practice, image analysis was more time consuming unless it could be automated.

**Table 7.1 Comparison of  $J_{crit}(\text{DOTM})$  and  $J_{crit}(\text{MB})$  (mass balance) for the filtration of 3.0  $\mu\text{m}$  latex particles (0.05 vol. %) suspension at CFV of 0.2m/s but different pH values**

| pH | $J_{crit}(\text{DOTM})$<br>(l/m <sup>2</sup> h) | $J_{crit}(\text{MB})$<br>(l/m <sup>2</sup> h) | $\frac{J_{crit}(\text{MB})}{J_{crit}(\text{DOTM})}$ |
|----|---|---|---|
| 6  | 45  | 23  | 0.51  |
| 7  | 51  | 40  | 0.78  |
| 8  | 53  | 38  | 0.72  |
| 9  | 52  | 42  | 0.81  |
| 10 | 52  | 47  | 0.90  |

**Table 7.2 Comparison of  $J_{crit}(\text{DOTM})$  and  $J_{crit}(\text{MB})$  (mass balance) for the filtration of 5.0  $\mu\text{m}$  latex particles (0.05 vol. %) suspension at pH 8 but different CFVs**

| CFV<br>(m/s) | $J_{crit}(\text{DOTM})$<br>(l/m <sup>2</sup> h) | $J_{crit}(\text{MB})$<br>(l/m <sup>2</sup> h) | $\frac{J_{crit}(\text{MB})}{J_{crit}(\text{DOTM})}$ | $\frac{J_{crit}(\text{MB})}{\text{CFV}}$ |
|--------------|---|---|---|--|
| 0.05         | 33  | 26  | 0.79  | 520                                      |
| 0.10         | 50  | 40  | 0.80  | 400                                      |
| 0.15         | 62  | 49  | 0.79  | 327                                      |
| 0.20         | 71  | 60  | 0.85  | 300                                      |
| 0.25         | 93  | 87  | 0.94  | 348                                      |

**Table 7.3 Comparison of  $J_{crit}(\text{DOTM})$  and  $J_{crit}(\text{MB})$  (mass balance) for the filtration of 10.0  $\mu\text{m}$  latex suspensions at constant CFV of 0.2m/s, pH 8 but different concentrations**

| <b>Concentration<br/>(% vol.)</b> | <b><math>J_{crit}(\text{DOTM})</math><br/>(<math>\text{l/m}^2\text{h}</math>)</b> | <b><math>J_{crit}(\text{MB})</math><br/>(<math>\text{l/m}^2\text{h}</math>)</b> | <b><math>\frac{J_{crit}(\text{MB})}{J_{crit}(\text{DOTM})}</math></b> |
|-----------------------------------|---|---|---|
| 0.005                             | 118   | 105   | 0.89  |
| 0.01                              | 102   | 96  | 0.94  |
| 0.02                              | 94  | 85  | 0.90  |
| 0.03                              | 86  | 79  | 0.92  |
| 0.04                              | 78  | 70  | 0.90  |
| 0.05                              | 80  | 71  | 0.89  |

The fractional depositions,  $\theta$  of 3.0, 5.0 and 10.0  $\mu\text{m}$  latex particles were calculated under various conditions using Equation (7-14). Figure 7.9 shows the fractional depositions of the 3.0  $\mu\text{m}$  latex particles with a concentration of 0.05 % vol. decreasing with the solution pH values at CFV 0.2 m/s. It could be seen that a higher fraction of the 3.0  $\mu\text{m}$  latex particles deposited on the membrane surface at pH 7.0 when below the membrane iso-electric point (pH 8.0). Almost hundred percent of the particles landed at pH 6. Above pH 8.0, a lower fraction of the latex particles deposited and the solution pH had little effect on the particle deposition. The bottom occurred at the membrane iso-electric point (pH 8.0) where there was no surface charge on the membrane. This was in good agreement with the critical flux measurements of the 3.0  $\mu\text{m}$  latex particles at various pH values in Figure 4.9 or Table 7.1. The fractional depositions decreased with the pH due to the increase of the repulsive electric double layer forces between the membrane and the particles.

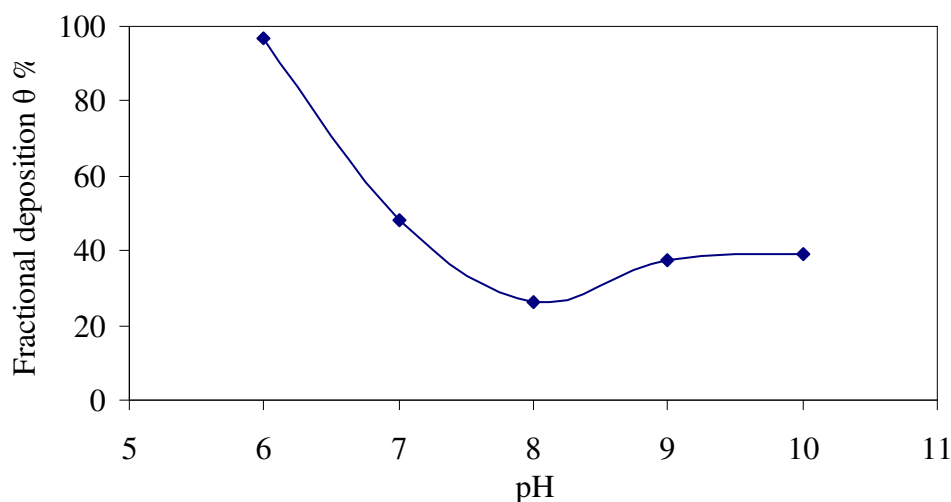


**Figure 7.9 Fractional deposition of the 3.0  $\mu\text{m}$  latex particles vs. pH with a concentration of 0.05 % vol. at CFV 0.2 m/s.**

Figure 7.10 shows the fractional depositions of the 5.0  $\mu\text{m}$  latex particles with a concentration of 0.05 % vol. as a function of crossflow velocity at pH 8.0. The fractional depositions of the 5.0  $\mu\text{m}$  latex particles decreased with the CFV. Table 7.2 shows the ratio of  $J_{crit}(\text{mass balance})$  to crossflow velocity and it was evident that fraction deposition (Figure 7.10) increased as  $J_{crit}(\text{mass balance})/\text{CFV}$  increased, or as ‘convective velocity’ increased and tangential shear velocity decreased. This was in qualitative agreement with Knutsen and Davis (2006).

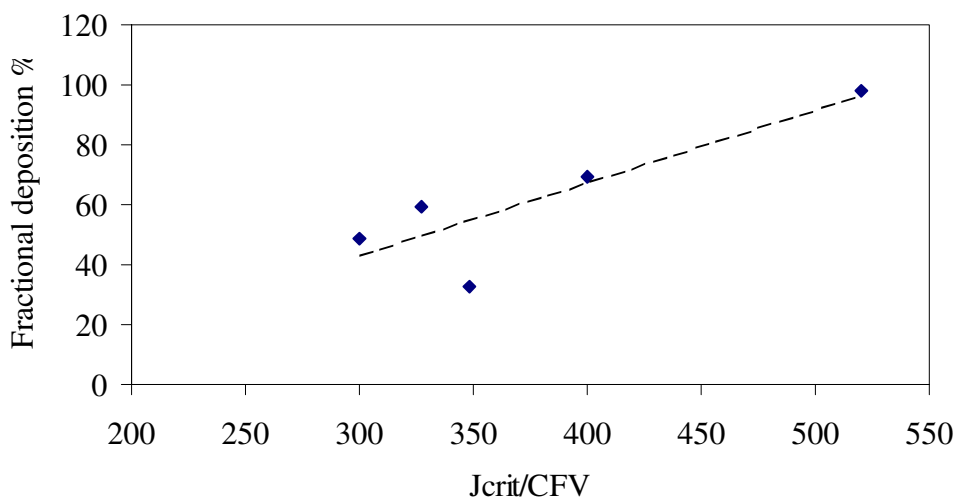


**Figure 7.10 Fractional deposition of the 5.0  $\mu\text{m}$  latex particles vs. CFVs with a concentration of 0.05 % vol. at pH 8.**

Shown in Figure 7.11 are the fractional depositions of the 10.0  $\mu\text{m}$  latex particles at various particle concentrations with a CFV of 0.2 m/s at pH 8. It was interesting to notice that the fractional depositions of the 10.0  $\mu\text{m}$  latex particles decreased when the particle concentrations were increased. Almost all the particles ( $\theta = 85\%$ ) deposited at the lowest concentration (0.005 % in this case) when above the critical flux. Two factors could explain the observed trends. Firstly, as particle concentration increased the critical flux decreased. Thus, at critical flux conditions the convective velocity (or ‘drag’ force) decreased as concentration increased ( $J_{crit}/\text{CFV}$  decreases). The decrease in this ratio was used to explain the cake trends in Figure 7.9. The other possible factor was that the suspension viscosity in the boundary layer would increase as suspension concentration increased, for example for dilute suspensions according to Belfort *et al.* (1994),

$$\mu = \mu_o(1 + 2.5c_s) \quad (7-20)$$

where  $c_s$  is suspension concentration and  $\mu_o$  is the viscosity of water.

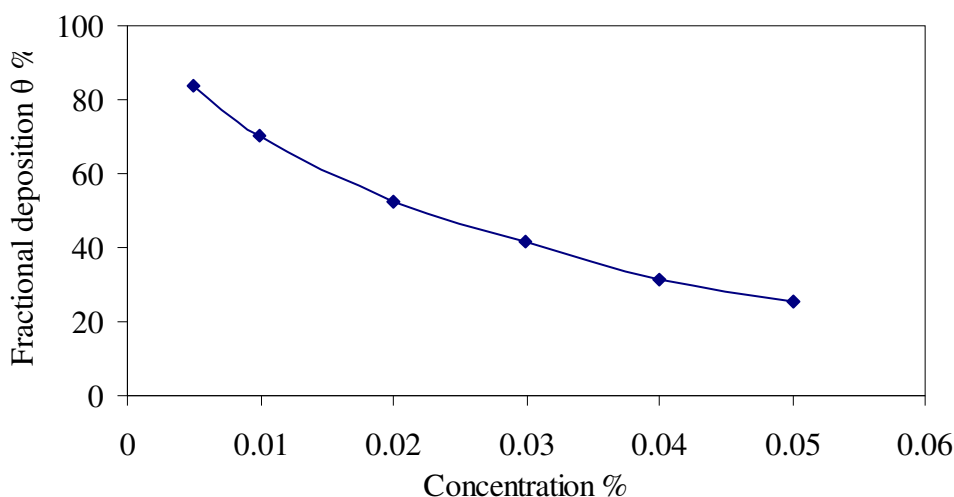


**Figure 7.11 Fractional deposition of the 10.0  $\mu\text{m}$  latex particles vs. concentrations with a CFV of 0.2 m/s at pH 8.**

An increase in viscosity would increase the shear stress at the membrane or cake surface, *i.e.*

$$\tau_{wall} = \mu \dot{\gamma}_{wall} \quad (7-21)$$

where  $\dot{\gamma}_{wall}$  is the local shear rate. Overall the fractional deposition would be expected to decrease as concentration increases.

Although the fractions of particle deposition declined with the feed concentration, it was possible that the total amount of the deposited particles increased with the concentration. Figure 7.12 is a re-plot of Figure 7.11 showing  $\theta^*c_b$  vs.  $c_b$ . The product of fractional deposition ( $\theta$ ) and bulk concentration ( $c_b$ ) could be used to show the actual amount of the deposited particles on the membrane surface when above the critical flux. It could be seen that the fouling amount increased with the bulk concentration and reached a plateau when the concentration was increased to a certain level. The cease of fouling on the membrane complied with the results in Figure 4.6 in Chapter 4 where the critical flux drop was lessened with the particle concentration.

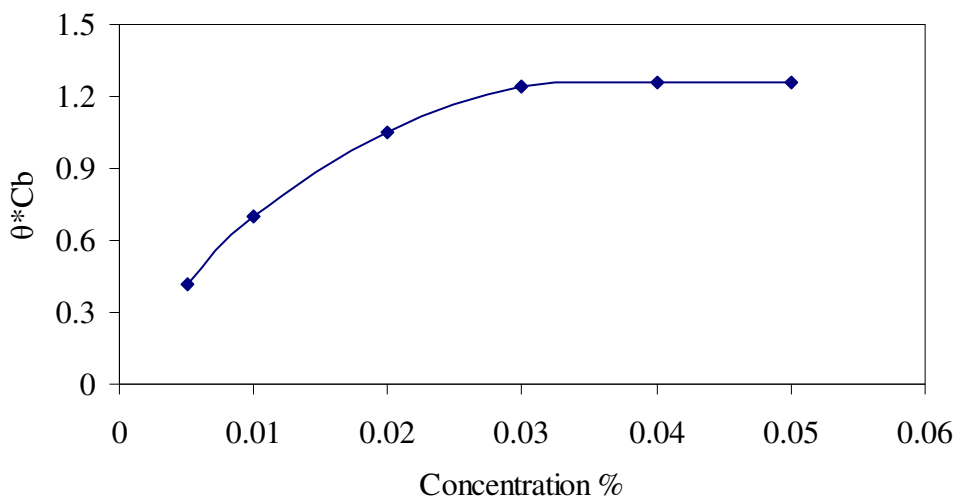


**Figure 7.12** Amount of deposited 10.0  $\mu\text{m}$  latex particles vs. concentrations with a CFV of 0.2 m/s at pH 8.



## 7.5 Summary

The reported methods for measuring the critical flux, *i.e.* TMP monitoring, mass balance and direct observation, were compared in this chapter. The limitations of the different methods were identified. A new method combining the mass balance and the DOTM technique was developed. The mass balance equation was modified to enable the estimation of the critical flux using the DOTM images. The mass balance analysis was further developed to evaluate the changes in critical flux when severe fouling occurred and hence the filtration properties were changed. The critical fluxes of the latex particles using the mass balance method combined with the DOTM image analysis were calculated. The critical fluxes obtained by this method were based on the assumption that all the particles carried to the membrane would deposit. Equation (7-14), developed from the mass balance, was modified by introducing the fractional deposition,  $\theta$ . The values of the fractional deposition were calculated at various conditions. The value of  $\theta$  declined as the ratio of  $J_{crit}$  to CFV decreased presumably due to the competing factors of convective drag and tangential shear stress. The critical fluxes obtained using this method were independent of the operation time as the deposition rates were always zero, and therefore were potentially more accurate than the DOTM values.

## **Chapter 8 Effect of electromagnetic field on critical flux of particles using DOTM**

### **8.1 Introduction and objectives**

It is well accepted that membrane fouling is an obstacle in the applications of membrane separation processes. Particle deposition and cake formation reduce water flux and cause pressure drops along the membrane. Recently, microbial fouling caused by bacteria has received more attention due to the complex fouling mechanisms involved. The bacteria play the role of colloidal particles and they can produce biopolymers that form a viscous biofilm on the membrane which causes severe fouling. Subsequently, bio-fouling can induce frequent chemical cleaning and even membrane replacement resulting in increased operating costs. Unless an efficient pretreatment is achieved and particle-free seawater is obtained, membrane fouling caused by colloidal particles and microorganisms are inevitable in membrane separation operations, especially in seawater desalination processes using RO membranes.

Many strategies were proposed to reduce the negative effects of the membrane fouling, (refer to Table 2.1 in Chapter 2). The conventional methods to reduce membrane fouling by increasing critical flux were to increase particle size by chemical flocculations, or to optimize hydrodynamic conditions to enhance the fluid back-transport. Among these strategies, physical treatments could have a more positive future since the regulations on the water treatment are getting more stringent. Recently, the use of electric fields to increase critical flux attracted some attention, including Akay *et al.* (1997) who used DC fields to increase the back transport of charged polymers.

GrahamTek introduced a novel technology involving an electromagnetic AC field around spiral wound RO membrane modules to reduce membrane fouling significantly during the desalination operation. It was proposed that the mechanisms could be due to the potential to cause particle aggregation on the moment in the AC

electromagnetic field. This postulation on how EMF device helped reduce membrane fouling is of interest in this study. However, another mechanism, in the form of an additional velocity vector to augment the shear-induced back diffusion was also a possible cause for the enhancement. The flow of ions near membrane surface could also interfere with the formation of crystallites, and hence reduce the membrane fouling.

The EMF device was wrapped around the pressure vessels holding the spiral wound modules and was applied throughout the length of each vessel and prevents fouling on the membrane surface (refer to [www.grahamtek.com](http://www.grahamtek.com)). This is an innovative application of magnetic treatment on reducing membrane fouling in membrane separation since most of the magnetic treatments are found in anti-scale formation. In addition to the claimed effects on scale-formation, the electromagnetic field is believed to reduce potential foulings.

This chapter reported a preliminary study on testing the effects of an electromagnetic field produced by three-phase AC currents flowing through copper coils wound around a flat-sheet membrane module in a ‘model’ system, *i.e.* well-controlled hydrodynamics, flux and feed properties (concentration, ionic strength and pH). Testing methods were developed according to the DOTM system. Measurements were made of the critical flux of particle suspensions in crossflow microfiltration using the non-invasive DOTM technique. Although most of the critical flux studies were applied to microfiltration, there is no reason why the phenomena will not be observed in RO. Critical flux was based on the competition between convection (permeate flux) and crossflow-induced back transport. For example, it was shown recently that critical flux could be measured in model RO systems with saline feed and colloidal silica foulant using the techniques developed and described by Chong *et al.* (2007). Critical flux behavior was also observed on large scale RO plants (Winters, 2007).

The objectives of this chapter include:

- (i) To measure the critical fluxes of organic and inorganic particles with and without EMF;
- (ii) To study the effects of placing the EMF device upstream or winding it around the membrane cell;
- (iii) To monitor the changes in particle size distribution after the EMF exposure;
- (iv) To optimize the operating conditions with EMF to enhance critical flux.

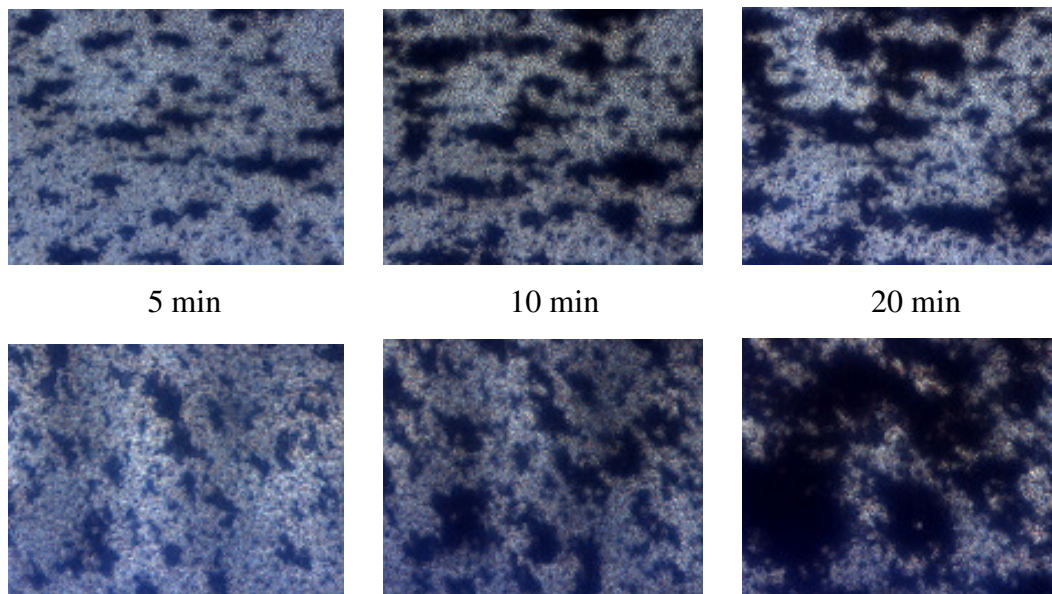
The experimental protocols described in Section 3.5.2, Chapter 3 were also applicable in this investigation. The EMF devices provided by GrahamTek were fixed at a frequency of 60 MHz for the EMF winding and 6 A for the EMF upstream due to the preliminary nature of this work and described in detail in Section 3.6, Chapter 3.

## **8.2 Results**

### **8.2.1 Hematite flocs with EMF winding**

Preliminary tests on the EMF winding were conducted using iron hematite particles. For a feed containing hematite flocs (prepared in our lab, refer to Chapters 3 and 6), the alignment of the flocs was changed by 90 degree compared to the non-EMF conditions. As a result, the nature of particle deposition was changed. However, the fouling was not alleviated when the EMF was applied. The fouling was heavier with the EMF device as shown in Figure 8.1. This established that the EMF had an effect on conductive materials, but under these conditions it did not alter the critical flux.

Without EMF (flow direction: right to left)



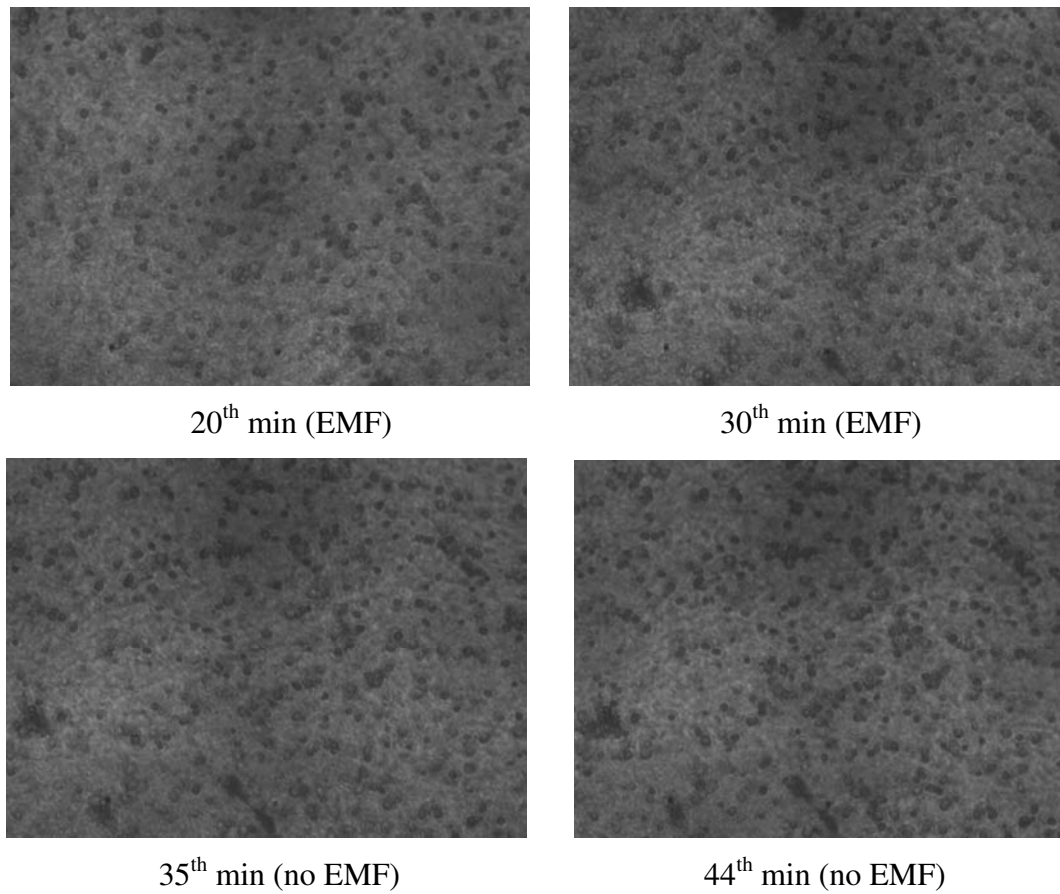
With EMF (flow direction: right to left)

**Figure 8.1 Hematite particle deposition pattern with and w/o EMF winding.**

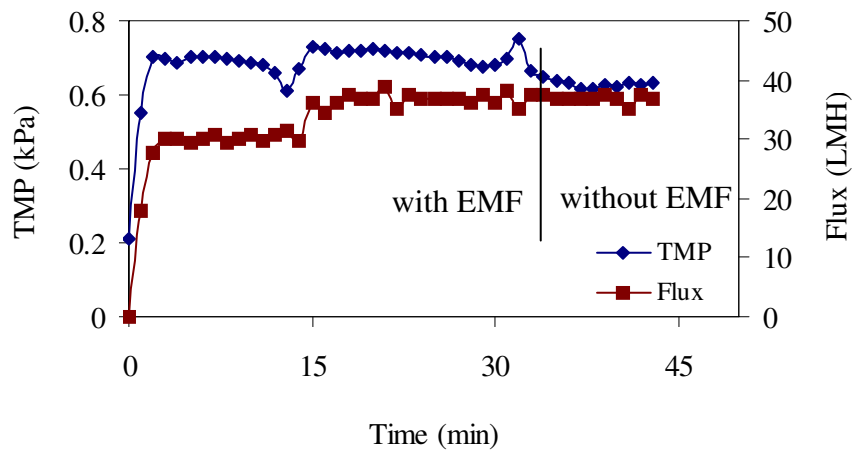
### 8.2.2 Yeast cells with EMF winding

The tests of sequentially switching on and off the EMF device were conducted to detect the changes in membrane fouling and investigate the effect of the EMF after the field was applied or removed.

Figure 8.2 shows the effect of the applied EMF (from 0-30 minutes), followed by a period (30-44 minutes) without EMF. Figure 8.2 (b) shows that at the 30<sup>th</sup> minute the imposed flux was 37 l/m<sup>2</sup>h which was higher than the critical flux of about 25 l/m<sup>2</sup>h without the EMF [note that the TMP values were very low and could not be taken as a true measurement of TMP changes]. The coverage of the membrane at 30 minutes (with EMF) was shown to be very low in Figure 8.2 (a). When the EMF was switched off there was no significant additional deposition. This might indicate that the yeast inventory was “pre-conditioned” by the EMF as it would have cycled an average 6 times through the field within the filtration loops.



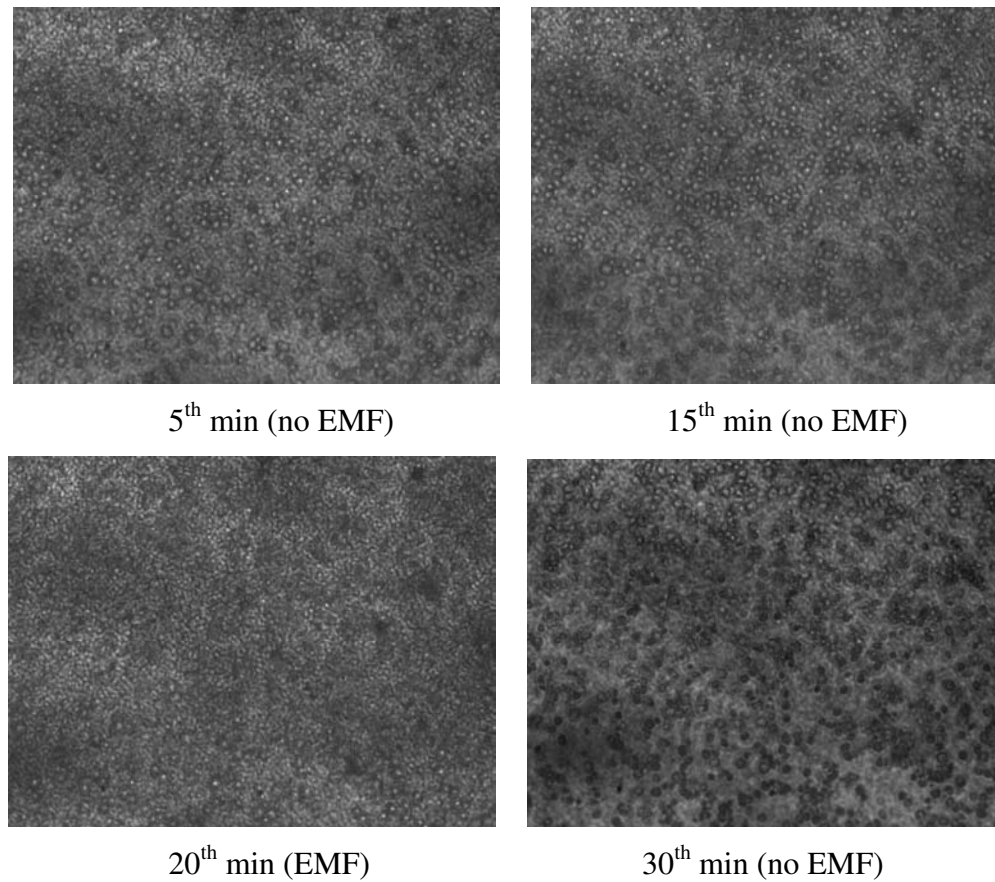
(a) Images of baker's yeast (with EMF before 30 min, without EMF after 30 min).



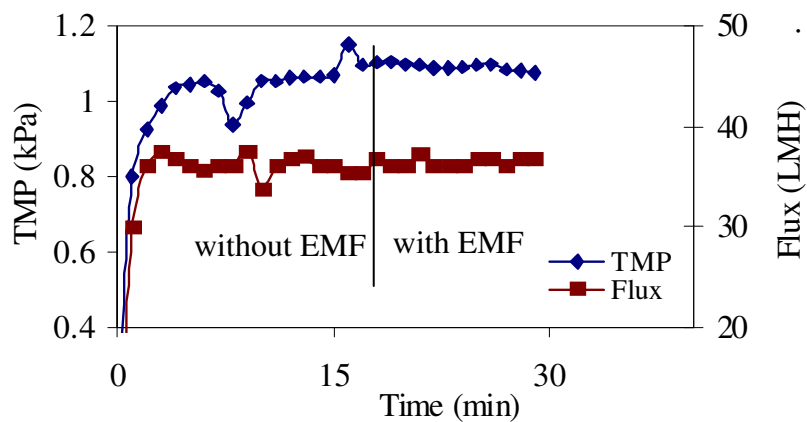
(b) TMP and Flux of the measurement of baker's yeast.

**Figure 8.2 Critical flux of baker's yeast with EMF at CFV 0.1 m/s, Concentration 0.525 g/l, pH 7.**





(a) Images of baker's yeast (without EMF before 15 min, with EMF after 15 min).



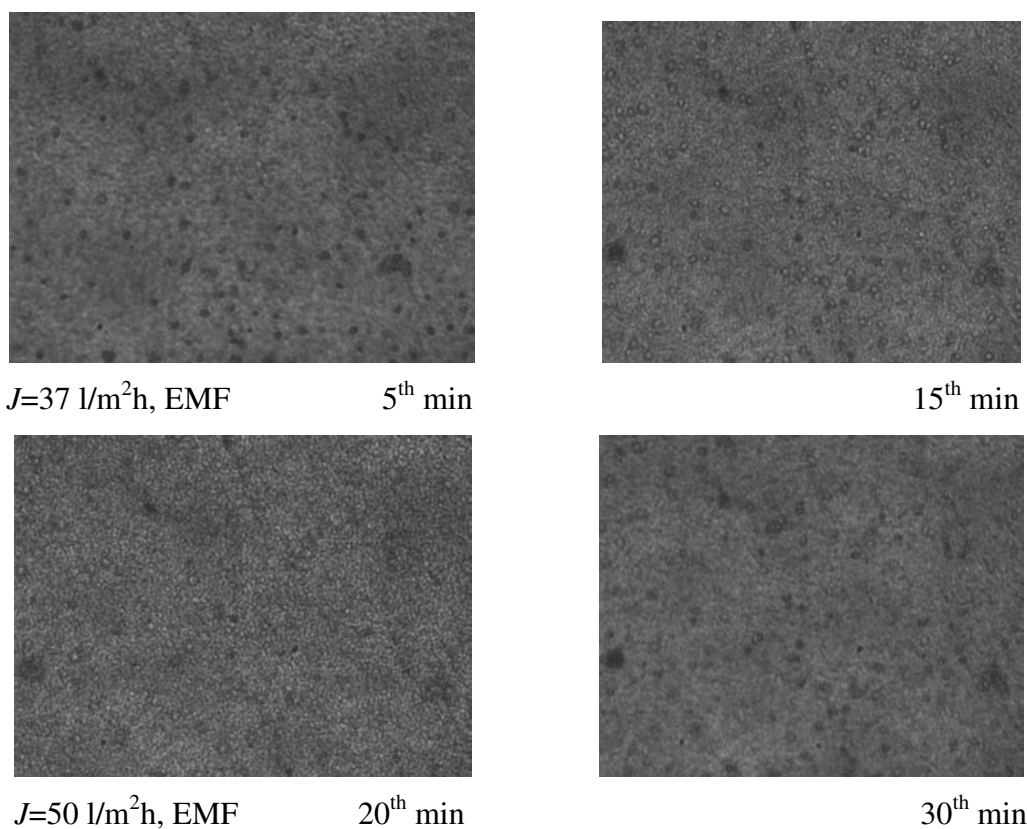
(b) TMP and Flux of the measurement of baker's yeast.

**Figure 8.3 Critical flux of baker's yeast with EMF at CFV 0.1 m/s, concentration 0.525g/l, pH 7.**

Figure 8.3 shows what happened without the EMF when the experiment was repeated with a fresh feed at a flux of 37 l/m<sup>2</sup>h, instead of starting with the EMF.

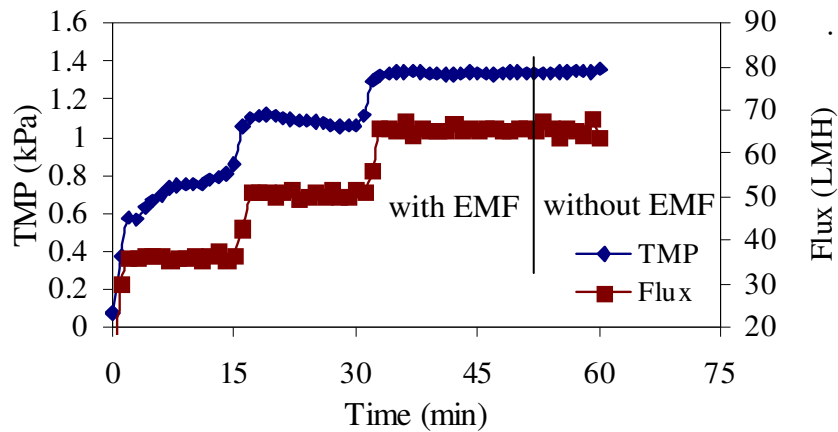
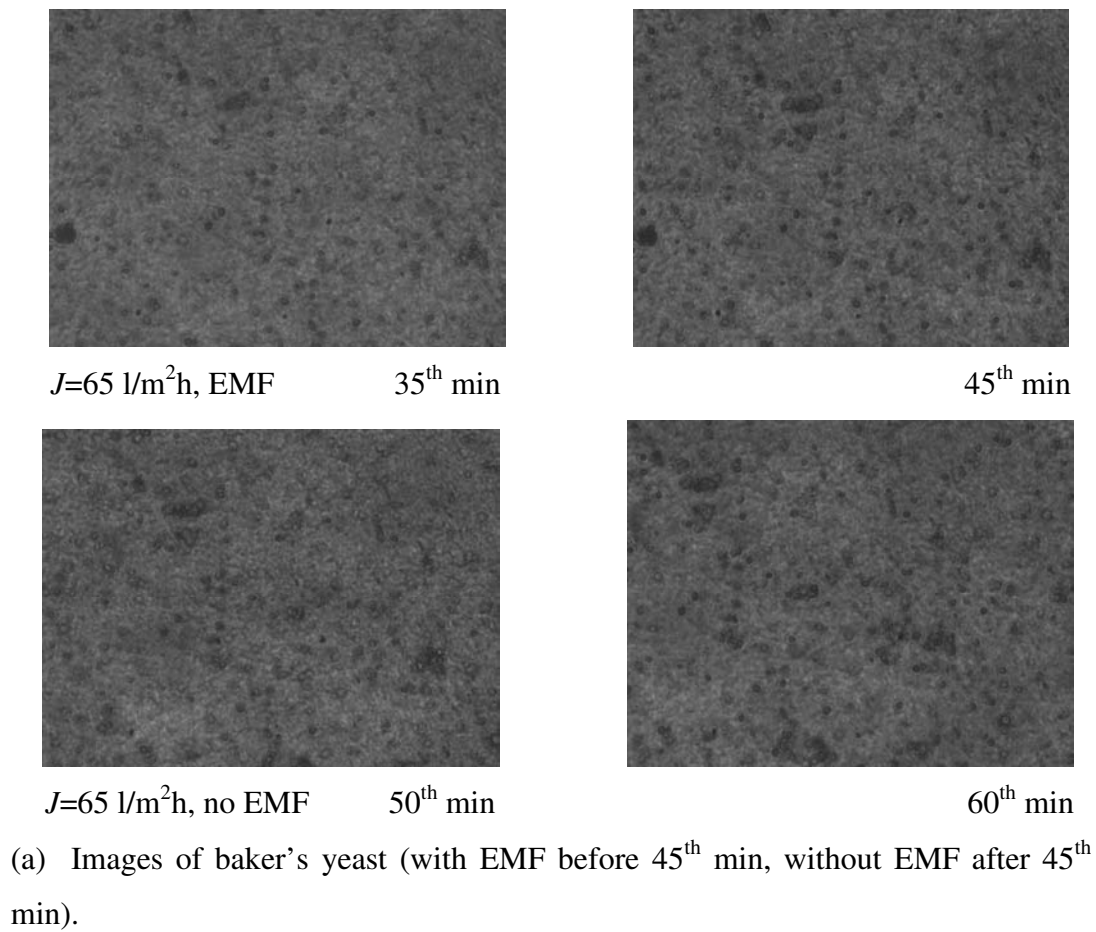
Figure 8.3 (a) shows that at the 15<sup>th</sup> minute there were more evident depositions of the yeast, as expected when operating above the critical flux. Between the 15<sup>th</sup> to 30<sup>th</sup> minute, the EMF was applied, and a close inspection of the Figure 8.3 (a) image at the 30<sup>th</sup> minute suggested some removal had occurred.

Figure 8.4 (a) shows the images at the 15<sup>th</sup>, 30<sup>th</sup> and 45<sup>th</sup> minute with the EMF at fluxes of 37, 52 and 65 l/m<sup>2</sup>h respectively. At all these supra-critical fluxes (measured as 25 l/m<sup>2</sup>h without EMF) the yeast deposition was sparse (compare with Figure 8.3 (a) at 15<sup>th</sup> minute). Figure 8.4 (a) also shows that when the EMF was switched off (images at 50<sup>th</sup> and 60<sup>th</sup> minute) the deposition did not increase. However, the yeast feed had already circulated an average 10 times through the EMF cell before the power was switched off. Again, this could imply some “pre-conditioning” had occurred.



(Figure 8.4 to be continued)

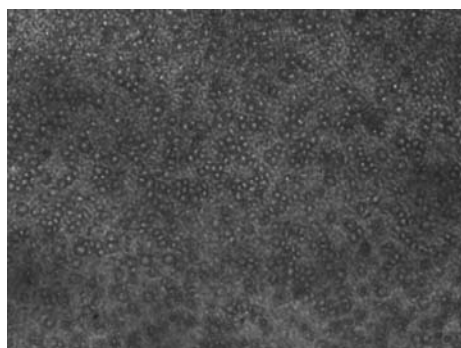




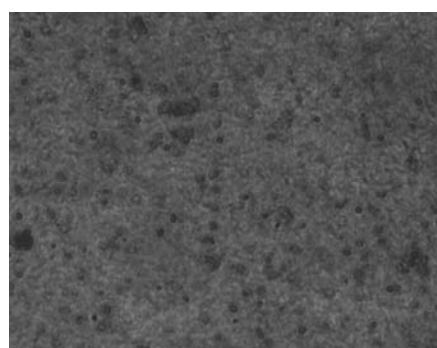
(b) TMP and Flux of the measurement of baker's yeast.

**Figure 8.4 Critical flux of baker's yeast with EMF at CFV 0.1 m/s, Concentration 0.525g/l, pH 7.**

Figure 8.5 shows more clearly the benefit of the EMF by contrasting the 15<sup>th</sup> minute in Figure 8.3 (no EMF) and 45<sup>th</sup> minute in Figure 8.4 (EMF). The images were processed on gray scale using the imaging software.



15<sup>th</sup> min in Figure 8.3  
( $J=37 \text{ l/m}^2\text{h}$ , no EMF)



60<sup>th</sup> min in Figure 8.4  
( $J=65 \text{ l/m}^2\text{h}$ , EMF)

**Figure 8.5 Comparison of two images on gray scale from Figures 8.3 and 8.4.**

Figure 8.6 shows the critical flux measurements of 0.525 g/l yeast suspensions under various pH values with and without the EMF. Both lines showed that the critical flux of the yeast suspensions increased with the pH values over a large range. The gap between the two lines was about 10 l/m<sup>2</sup>h of flux which means a significant increase in permeate flux was achieved with the EMF. The error bars shown were the results of three repeats of each experiment. The percentage increase in the critical flux was calculated and is shown in Table 8.1.

**Table 8.1 Increase in critical flux with EMF**

| pH           | 5  | 7  | 9  |
|--------------|----|----|----|
| no EMF (LMH) | 37 | 54 | 67 |
| EMF (LMH)    | 50 | 65 | 84 |
| Increase %   | 35 | 20 | 25 |

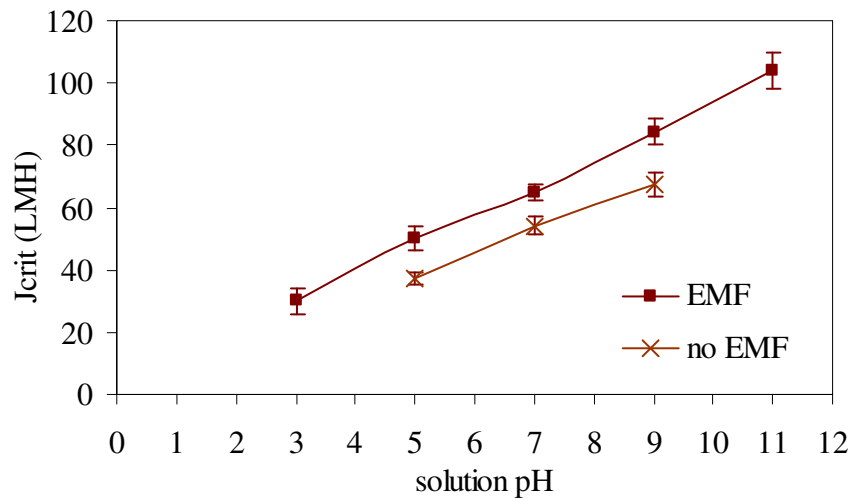


**Figure 8.6** Critical flux of 0.525 g/l yeast with EMF at various pH, CFV = 0.2 m/s.

Figure 8.7 shows the effect of the EMF on the critical fluxes of 0.525 g/l yeast suspensions in the presence of salt in the system at pH 7.0. The addition of salt caused lower critical fluxes compared with the same conditions without any salt where the critical flux was 60 l/m<sup>2</sup>h when the EMF was applied. Significant relative increases in the critical fluxes were found when the EMF was applied as shown in Table 8.2.

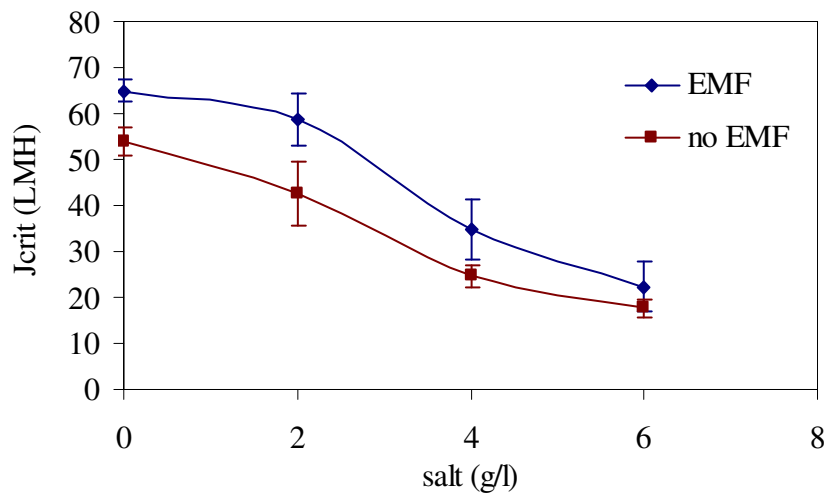


**Figure 8.7** Critical flux of 0.525 g/l yeast at various salt concentrations, at pH = 7, CFV = 0.2 m/s.

**Table 8.2 Increase in critical flux with EMF**

| Salt (g/l)   | 0  | 2  | 4  | 6    |
|--------------|----|----|----|------|
| no EMF (LMH) | 48 | 40 | 20 | 15   |
| EMF (LMH)    | 60 | 50 | 30 | 20   |
| Increase %   | 25 | 25 | 50 | 33.3 |

Figure 8.8 presents the critical fluxes of yeast at various concentrations in the presence of 2 g/l salt with and without EMF at a crossflow velocity of 0.2 m/s. It showed the anticipated trend that the critical flux decreased with the feed concentration (refer to Figure 4.8 in Section 4.3). This occurred with and without the EMF, but the critical fluxes were clearly enhanced by the EMF at all conditions. The improvement in the critical flux could be seen from Table 8.3.

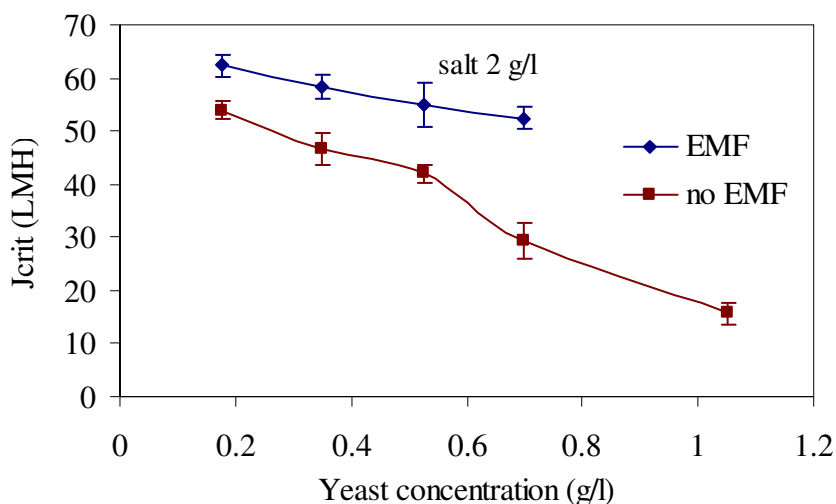


**Figure 8.8 Critical flux of yeast at different concentrations with presence of 2 g/l salt but with and without EMF at pH = 7, CFV = 0.2 m/s.**

**Table 8.3 Increase in critical flux with EMF**

| Yeast (g/l)  | 0.175 | 0.35 | 0.525 | 0.7 |
|--------------|-------|------|-------|-----|
| no EMF (LMH) | 54    | 47   | 42    | 30  |
| EMF (LMH)    | 62    | 58   | 55    | 52  |
| Increase %   | 15    | 23   | 31    | 73  |

### 8.2.3 Latex particles with EMF winding

Figure 8.9 shows the effect of the EMF cell device on the polystyrene latex particles with a concentration of 0.05% vol. in brackish water. All the tests were conducted at the iso-electric point of the membrane (pH 8) with a crossflow velocity of 0.2 m/s. The results showed that the critical flux decreased with the salt concentration in the solution. This was probably due to the decrease in the electrical double layer interaction between the particles caused by the presence of salt. It also could be seen that the critical fluxes resulting from the two situations, with and without the EMF, were comparable. The differences were within the experimental error. Although this was a null result, it did show the reproducibility of the measurement technique with error bars.

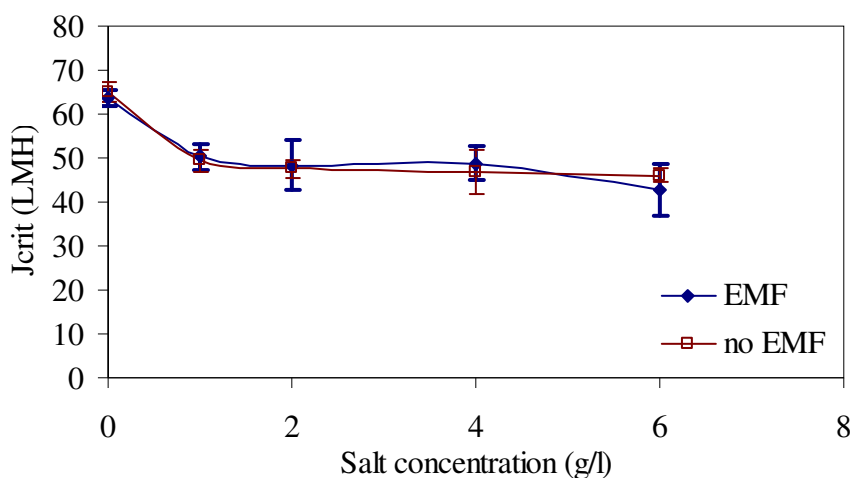


**Figure 8.9 Critical flux of 3.0  $\mu\text{m}$  latex in brackish water (0.05% vol., pH 8, CVF 0.2 m/s).**

Shown in Figure 8.10 are the results on the effect of the EMF cell device on the critical fluxes of polystyrene particles at various pH values in the absence of salt in

the suspension. The critical fluxes were all around 60 l/m<sup>2</sup>h for all pH values whether there was the EMF or not. At the iso-electric point of the membrane (pH 8), the critical flux might show a small peak. This implied that the effect of surface charge had no significant impact on the critical flux up to 3.0  $\mu$ m particles. Importantly, for this type of feed the EMF had no detectable effect on the critical flux. It was plausible that this material would respond to EMF at different frequencies, but unfortunately the system did not allow frequency variation in this study.

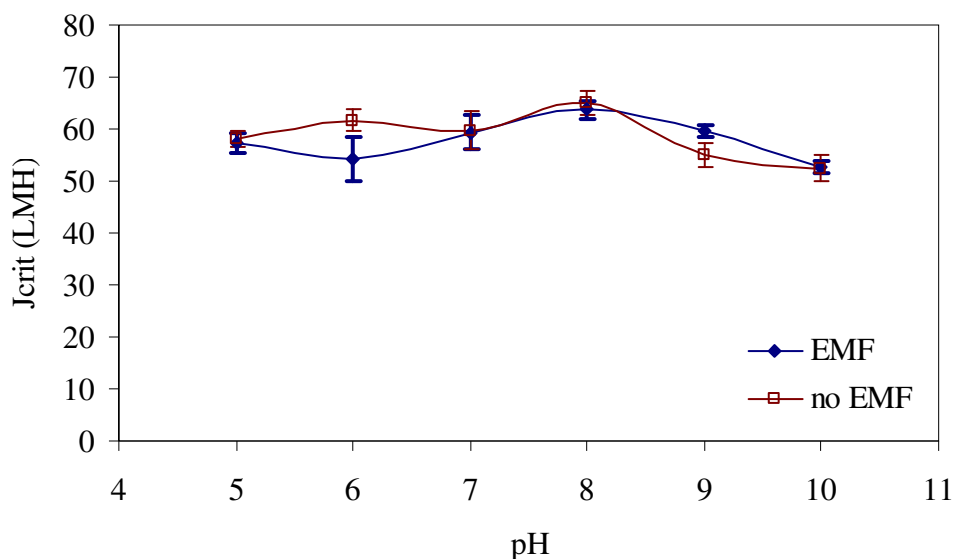


**Figure 8.10** Critical flux of 3.0  $\mu$ m latex at various pHs (no salt, 0.05% vol., CVF 0.2 m/s).

#### 8.2.4 Yeast cells with EMF upstream

The heat produced by the EMF upstream device was a challenge as the feed temperature had to be constant. Additional heat would affect the critical flux results and confuse with the enhancement achieved by the EMF. A circulating line with a water bath to control temperature was integrated into the DOTM filtration system. The details can be found in Section 3.6.2, Chapter 3. Figure 8.11 shows a summary

on the critical fluxes of 0.525 g/l washed bakers' yeast suspensions at various pH values when there was EMF, EMF 'upstream' and no EMF in the absence of salt. The critical flux increased when the EMF winding device was applied around the membrane cell. However, there was no significant improve in the critical flux when the EMF upstream device was used.

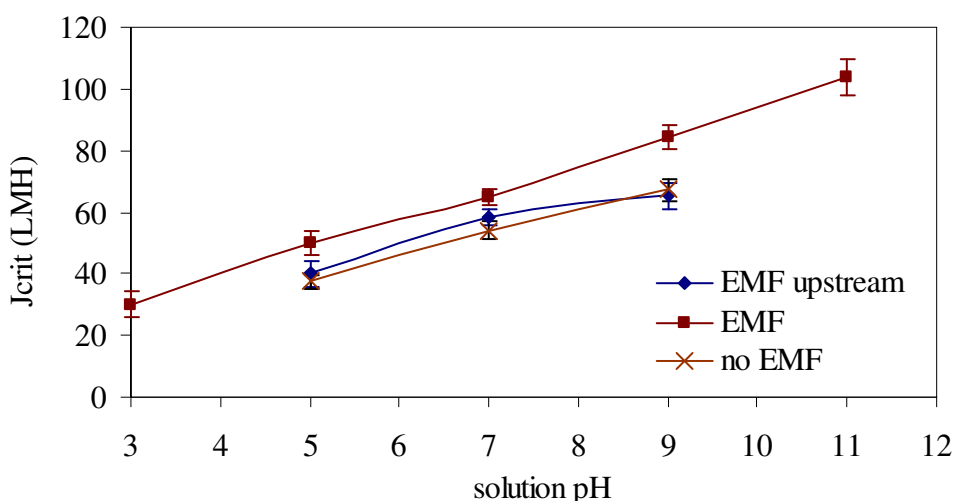


**Figure 8.11 Critical fluxes of 0.525 g/l yeast at different pH values without salt at CFV = 0.2 m/s.**

Shown in Figure 8.12 are critical fluxes of 0.525 g/l washed bakers' yeast suspensions at neutral pH in the presence of salt. Again the critical flux increased in the case of using the EMF winding; however, there was no significant change in the case of using the EMF upstream device.

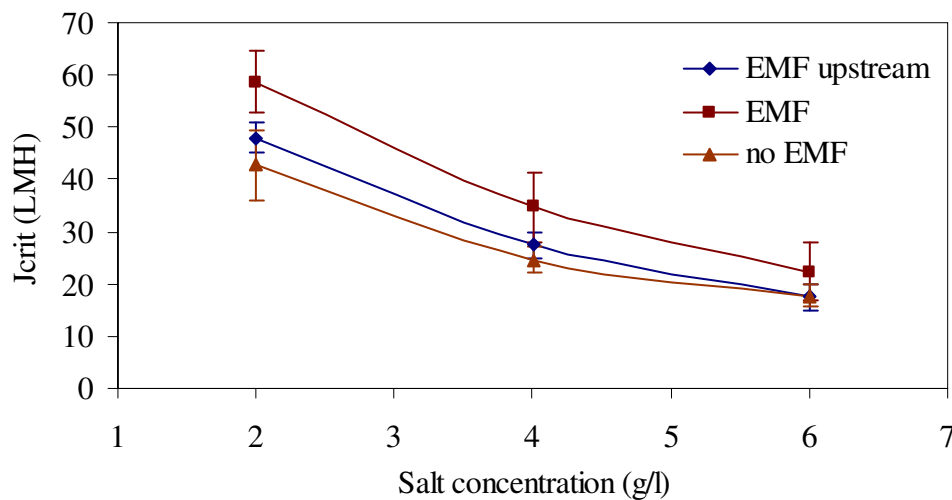


**Figure 8.12** Critical fluxes of 0.525 g/l yeast at different salt concentrations at pH = 7, CFV = 0.2 m/s.

### 8.3 Discussion

The results with the hematite particles and yeast cells showed that the AC field had an effect on particle deposition during the crossflow microfiltration. The critical fluxes of the yeast cell suspensions were increased by around 30 % with the AC field. Particle aggregation might not be the reason for the increase in the critical flux since the particle size distribution did not change noticeably after circulation through the EMF winding. However, particle aggregation could not be totally discounted as it was still possible that the particles aggregated only in the AC field and de-aggregated rapidly once outside the field (Coster, 2007). However, a more likely mechanism was dielectrophoretic mobility as an enhancement velocity for augmenting critical flux. Thus the film model becomes,

$$J_{crit} = k_S \ln(C_W / C_B) + V_E \quad (8-1)$$

where  $V_E$  is the enhancement velocity.

The electric field coupled with filtration, namely electro-filtration, was employed to reduce membrane fouling over the decades (Weigert *et al.*, 1999). The basic



principle of applying electric or other kind of force fields, such as ultrasonic fields, was to prevent particles from depositing on membrane surface under the extra forces in all kinds of fields. Based on this, dielectrophoresis was used to separate colloidal particles (Green *et al.*, 1998). In non-uniform AC fields, dielectric particles were mobile in their medium, usually water, due to the interaction of the induced dipoles. The interactions resulted in attractive or repulsive forces on particles depending on the difference in the polarizability of the particles and medium. When the particles were less polarizable than their suspending medium, *i.e.* the dielectric constant of the particles was smaller than that of their medium, the particles were repelled from the regions of high electric fields (Molla *et al.*, 2005). Therefore, when less dielectric particles passed by a membrane with embedded electrodes, the repulsive dielectric forces kept the particles suspending above the membrane, and the particles were swept away by the crossflow.

The fact that there was no significant change in the critical fluxes of the latex particles with the EMF did not necessarily invalidate this conclusion. The difference was probably due to the low dielectric constant of the latex particles (2.3-2.7). As found in the literature (Baker *et al.*, 1996; Coster *et al.*, 2002), the effect of the EMF depended on the material of the particles. Zeta potentials also influenced on the effect of the EMF. The presence of salt would compress the electrical double layers and suggested a double layer effect that was increased by the magnetic field. This could be seen from the experiments at various pH values and with the presence of salt in the feed solutions.

The EMF upstream was shown to be non-effective in the yeast experiments. One postulated mechanism of the EMF enhancement was particle aggregation, and this was not observed. If it had been an enhancement mechanism, the EMF upstream was expected to help. However, the absence of the effect of the EMF upstream supported the view that there might be transient particle aggregation only in the electromagnetic field. These results underlined the fact that we did not confirm the mechanisms at work with the EMF devices. Further work with the ability to vary frequency and power may reveal the mechanism(s).

## 8.4 Summary

Experiments on the lab-scale DOTM membrane system equipped with the GrahamTek EMF devices confirmed that under some conditions the AC field effect enhanced the critical flux of particles by up to 30%. The enhancement was observed for yeast suspensions with the EMF mounted around the membrane cell. It was not observed for the yeast suspensions with the EMF device located upstream of the membrane cell. The EMF effect was also not observed for the suspensions of latex particles with either EMF location. The different responses could be due to the differences in the dielectric constants of the particles and other properties. The enhancement mechanism was not clear but it was unlikely to be due to the aggregation and increased particle size. It was more likely due to a dielectrophoretic back-transport velocity. Although the results were obtained in a low-pressure membrane cell it was reasonable to assume that the phenomena could occur under some conditions in RO applications.

The EMF study was limited by the fixed frequency and power of the EMF devices provided. A more thorough assessment, leading to a mechanistic understanding and optimization required a tunable EMF device and a wider range of feed suspensions.

## **CHAPTER 9 Conclusions and Recommendations**

The demands for clean and economic water have been increasing around the world. Conventional separation processes cannot meet such huge demands. More environmental and efficient techniques to improve the situation are necessary and crucial. Membrane separation can help alleviate the problems. However, membrane fouling is one of the major challenges. The fouling phenomenon often leads to increasing energy requirement, more chemical cleaning, frequent membrane replacement, shortened operation period and increase in operation costs.

### **9.1 Conclusions**

This thesis presented the efforts to understand particle deposition on membrane surface during crossflow microfiltration and prolong the operation term. The direct observation through membrane (DOTM) technique was adopted and modified for the study of fouling mechanisms of mixed and flocculated suspensions. The mechanisms of particle deposition on membrane surface were visualized under the microscope of the DOTM. The critical fluxes of model mono- (latex and yeast), bi- (mixed latex) and poly-disperses (hematite flocs) suspensions were measured with the aid of the DOTM technique and were estimated more accurately with the image analysis based on the mass balance equation. The concept of critical flux was proved to be a useful tool in evaluating the filtration performance and provided the guidance on choosing operating conditions.

The investigation of the dominant factors of critical flux showed that particle deposition and membrane fouling were complex. Some properties of the feeds such as particle size distribution and porous floc structure made the situation even worse. Although the studies on model particles provided insights on fouling mechanisms, it was far from the real situations practiced in normal applications. Conventional filtration theories based on the assumption that the particles in the suspensions were compact spheres needed to be corrected for the complex mixed and flocculated feeds. The results showed that larger compact particles and higher crossflow

velocities were always desirable in crossflow filtration. But the costs followed had to be balanced with the benefits. The study on the channel height showed that the flow distribution was complicated and important in crossflow microfiltration. The fluid conditions should be well controlled.

The simulation of the mixed model particles turned out to be a successful transition from model suspensions to real flocculated feeds. The observation showed that the smaller particles dominated the deposited cake layer and their back transport diffusions were enhanced by the larger particles present in the mixed suspensions. The higher back diffusions of the larger particles could be contributed to the increase in the critical flux.

The pattern of particle deposition induced by the flocculated flocs was observed different from the model particles. The membrane was more easily fouled when separating the polydisperse suspensions due to the high proportion of small particles and their amorphous structures. However, the deposited clusters were readily to be removed due to the growth in particle size. Operation at sustainable flux was possible when the equilibrium between particle deposition and re-entry was achieved. The critical flux was shown to be dependent on not only the particle size distribution, but also the fractal property and increased with the fractal dimension. The particle size was less significant when the flocs were more porous (lower fractal dimension).

A quantitative method was developed combining the mass balance equation with the DOTM images. The critical fluxes were lower and more accurate compared with the values measured by the DOTM experimentally. The calculations of the fractional deposition showed that only partial particles deposited on the membrane surface above the critical flux.

The tests on the electro-magnetic field (EMF) showed that the particle interactions could be enhanced by external mechanisms and therefore the critical flux was increased. However, the benefits brought by the EMF were not universal for all

materials. It was a function of the dielectric constant of the materials as well as the ionic environment of the solutions.

## 9.2 Recommendations

Direct observation provided insightful information on particle deposition on membrane surface, especially for the non-destructive, in-situ observation technique like the DOTM. However, some modifications still could be done to refine this technique. The followings are suggested for further developments,

- The main drawback of the DOTM technique was that transparent membranes must be used. This type of membrane was usually fragile and not representative for the commonly used membranes in real practice. Advanced optical instruments (for example, confocal laser scanning microscope) could be adopted to observe any type of membrane surfaces clearly. Moreover, three-dimensional scanning of cake layer could provide more information on cake structures;
- The size and area of the specimen to be observed under the microscope were determined by the magnification of the objectives. In order to mount the membrane cell under the microscope to observe smaller particles and larger area, objectives with higher magnifications and longer working distances would be necessary;
- The transparent observing window confined the operational pressure. Transparent materials which can resist high pressure will enlarge the DOTM application to high pressure filtration, such as ultrafiltration;
- The DOTM technique was equipped with a crossflow circulating pipeline. More sensitive pressure transducers could be installed to detect any change in transmembrane pressure in order to compare the results;

- The data obtained by the DOTM were more qualitative. Quantitative methods would help interpret the DOTM images.
- Smaller particles in polydisperse suspensions were found to be the main reason for membrane fouling under idealized conditions by the DOTM. More complicated situations, such as polydisperse suspensions associated with different particle surface characteristics or dissolved organics or salts or even living microorganisms, could be suggested in order to figure out fouling mechanisms as more complex water is treated in current plants.
- The field flow in the testing cells was found very complicated. As a result, the observation could be affected by the hydrodynamic conditions. Further control and study to the field flow would be recommended.
- Fouling kinetics in terms of particle coverage was studied with the aid of imaging software. Further work, such as correlation with traditional relationships (*e.g.* Langmuir isotherm equation), would be suggested.
- The critical fluxes of the mixed suspensions were dependent on the content ratios. Various proportions in terms of volumetric concentrations were tested in this study. Some experiments with the same particle number or surface concentrations of different latex would also be useful for the investigation of particle interactions.
- The DOTM could only observe particles larger than 1  $\mu\text{m}$  in diameter under normal conditions. However, it might be possible to observe fluorescent submicron particles. Particle segregation, *i.e.* one of species in the mixed suspensions is smaller than membrane pore, could be insightful for fouling mechanisms.

## References:

Akay, G. and Wakeman, R. J. (1997), "Electric Field Enhanced Crossflow Microfiltration of Hydrophobically Modified Water Soluble Polymers", Journal of Membrane Science, Vol. 131, (1-2), pp. 229-236.

Altena, F. W. and Belfort, G. (1984), "Lateral Migration of Spherical Particles in Porous Flow Channels: Application to Membrane Filtration", Chemical Engineering Science, Vol. 39, (2), pp. 343-355.

Altmann, J. and Ripperger, S. (1997), "Particle Deposition and Layer Formation at the Crossflow Microfiltration", Journal of Membrane Science, Vol. 124, (1), pp. 119-128.

Bacchin, P., Aimar, P. and Sanchez, V. (1996), "Influence of Surface Interaction on Transfer During Colloid Ultrafiltration", Journal of Membrane Science, Vol. 115, (1), pp. 49-63.

Bacchin, P. (2004), "A Possible Link between Critical and Limiting Flux for Colloidal Systems: Consideration of Critical Deposit Formation Along a Membrane", Journal of Membrane Science, Vol. 228, (2), pp. 237-241.

Bacchin, P., Aimar, P. and Field, R. W. (2006), "Critical and Sustainable Fluxes: Theory, Experiments and Applications", Journal of Membrane Science, Vol. 281, (1-2), pp. 42-69.

Baker, R. J., Fane, A. G., Fell, C. J. D. and Yoo, B. H. (1985), "Factors Affecting Flux in Crossflow Filtration", Desalination, Vol. 53, (1-3), pp. 81-93.

Baker, J. S. and Judd, S. J. (1996), "Magnetic Amelioration of Scale Formation", Water Research, Vol. 30, (2), pp. 247-260.

Belfort, G., Davis, R. H. and Zydney, A. L. (1994), "The Behavior of Suspensions and Macromolecular Solutions in Crossflow Microfiltration", Journal of Membrane Science, Vol. 96, (1-2), pp. 1-58.

Bixler, H. J. and Rappe, G. C. (1970), "Ultrafiltration Process", U. S. P. 3, 541, 006.

Blake, N. J., Cumming, I. W. and Streat, M. (1992), "Prediction of Steady State Crossflow Filtration Using a Force Balance Model", Journal of Membrane Science, Vol. 68, (3), pp. 205-215.

Bos, R., van der Mei, H. C. and Busscher, H. J. (1999), "Physico-Chemistry of Initial Microbial Adhesive Interactions - Its Mechanisms and Methods for Study", FEMS Microbiology Reviews, Vol. 23, (2), pp. 179-229.

Chakraborti, R. K. (2003), "Application of Fractal Concepts for Analysis and Modeling of Particle Aggregation", Ph.D. Thesis, State University of New York at Buffalo, USA.

Chang, D.-J., Hsu, F.-C. and Hwang, S.-J. (1995), "Steady-State Permeate Flux of Cross-Flow Microfiltration", Journal of Membrane Science, Vol. 98, (1-2), pp. 97-106.

Chang, J. S., Tsai, L. J. and Vigneswaran, S. (1996), "Experimental Investigation of the Effect of Particle Size Distribution of Suspended Particles on Microfiltration", Water Science and Technology, Vol. 34, (9), pp. 133-140.

Chellam, S. and Wiesner, M. R. (1993), "Fluid Mechanics and Fractal Aggregates", Water Research, Vol. 27, (9), pp. 1493-1496.

Chellam, S. and Wiesner, M. R. (1998), "Evaluation of Crossflow Filtration Models Based on Shear-Induced Diffusion and Particle Adhesion: Complications Induced by Feed Suspension Polydispersivity", Journal of Membrane Science, Vol. 138, (1), pp. 83-97.



Chen, V., Fane, A. G., Madaeni, S. and Wenten, I. G. (1997), "Particle Deposition During Membrane Filtration of Colloids: Transition between Concentration Polarization and Cake Formation", Journal of Membrane Science, Vol. 125, (1), pp. 109-122.

Chen, J. C., Li, Q. and Elimelech, M. (2004a), "In Situ Monitoring Techniques for Concentration Polarization and Fouling Phenomena in Membrane Filtration", Advances in Colloid and Interface Science, Vol. 107, (2-3), pp. 83-108.

Chen, V., Li, H. and Fane, A. G. (2004b), "Non-Invasive Observation of Synthetic Membrane Processes - a Review of Methods", Journal of Membrane Science, Vol. 241, (1), pp. 23-44.

Childress, A. E. and Elimelech, M. (1996), "Effect of Solution Chemistry on the Surface Charge of Polymeric Reverse Osmosis and Nanofiltration Membranes", Journal of Membrane Science, Vol. 119, (2), pp. 253-268.

Choi, H., Zhang, K., Dionysiou, D. D., Oerther, D. B. and Sorial, G. A. (2005), "Influence of Cross-Flow Velocity on Membrane Performance During Filtration of Biological Suspension", Journal of Membrane Science, Vol. 248, pp. 189-199.

Chong T.H., Fane A.G. and Wong F.S., "Implications of critical flux and cake enhanced osmotic pressure (CEOP) on colloidal fouling in RO: experimental", (submitted to Journal of Membrane Science).

Connell, H. (1998), "Effect of Particle Shape on the Flux in Crossflow Microfiltration", Master Thesis, University of Western Ontario, Canada.

Connell, H., Zhu, J. and Bassi, A. (1999), "Effect of Particle Shape on Crossflow Filtration Flux", Journal of Membrane Science, Vol. 153, (1), pp. 121-139.

Coster, H. G. L. and Chilcott, T. C. (2002), "Electric Field Effects in Proteins in Membranes", Bioelectrochemistry, Vol. 56, pp. 141-146.

Coster H., (2007), Personal communication.

Dharmappa, H. B., Verink, J., Ben Aim, R., Yamamoto, K. and Vigneswaran, S. (1992), "A Comprehensive Model for Cross-Flow Filtration Incorporating Polydispersity of the Influent", Journal of Membrane Science, Vol. 65, (1-2), pp. 173-185.

Drew, D. A., Schonberg, J. A. and Belfort, G. (1991), "Lateral Inertial Migration of a Small Sphere in Fast Laminar Flow through a Membrane Duct", Chemical Engineering Science, Vol. 46, (12), pp. 3219-3224.

Eckstein, E. C., Bailey, D. G. and Shapiro, A. H. (1977), "Self-Diffusion of Particles in Shear Flow of a Suspension", Journal of Fluid Mechanics, Vol. 79, pp. 191-208.

Fane, A. G. (1984), "Ultrafiltration of Suspensions", Journal of Membrane Science, Vol. 20, (3), pp. 249-259.

Field, R. W., Wu, D., Howell, J. A. and Gupta, B. B. (1995), "Critical Flux Concept for Microfiltration Fouling", Journal of Membrane Science, Vol. 100, (3), pp. 259-272

Green, N. G. and Morgan, H. (1998), "Separation of Submicrometre Particles Using a Combination of Dielectrophoretic and Electrohydrodynamic Forces", Journal of Physics D: Applied Physics, Vol. 31, pp. 25-30.

Guan, J., Amal, R. and Waite, T. D. (2001), "Effect of Aggregate Size and Structure on Specific Resistance of Biosolids Filter Cakes", Water Science and Technology, Vol. 44, (10), pp. 215-220.

Ho, C.-C. and Zydney, A. L. (2000), "A Combined Pore Blockage and Cake Filtration Model for Protein Fouling During Microfiltration", Journal of Colloid and Interface Science, Vol. 232, (2), pp. 389-399.

Ho, W. S. W. and Sirkar, K. K. (2001). Membrane Handbook. USA, Kluwer Academic Publishers.

Hoek, E. M. V., Kim, A. S. and Elimelech, M. (2002), "Influence of Crossflow Membrane Filter Geometry and Shear Rate on Colloidal Fouling in Reverse Osmosis and Nanofiltration Separations", Environmental Engineering Science, Vol. 19, pp. 357-372.

Howell, J. A., Field, R. W. and Wu, D. (1993), "Yeast Cell Microfiltration: Flux Enhancement in Baffled and Pulsatile Flow Systems", Journal of Membrane Science, Vol. 80, (1), pp. 59-71.

Howell, J. A. (1995), "Sub-Critical Flux Operation of Microfiltration", Journal of Membrane Science, Vol. 107, (1-2), pp. 165-171.

Hughes, D., Tirlapur, U. K., Field, R. and Cui, Z. (2006), "In Situ 3d Characterization of Membrane Fouling by Yeast Suspensions Using Two-Photon Femtosecond near Infrared Non-Linear Optical Imaging", Journal of Membrane Science, Vol. 280, (1-2), pp. 124-133.

Huisman, I. H., Vellenga, E., Tragardh, G. and Tragardh, C. (1999), "The Influence of the Membrane Zeta Potential on the Critical Flux for Crossflow Microfiltration of Particle Suspensions", Journal of Membrane Science, Vol. 156, (1), pp. 153-158.

Johnson, C. P., Li, X. and Logan, B. E. (1996), "Settling Velociyies of Fractal Aggregates", Environmental Science and Technology, Vol. 30, (6), pp. 1911-1918.

Kang, S.-T., Subramani, A., Hoek, E. M. V., Deshusses, M. A. and Matsumoto, M. R. (2004), "Direct Observation of Biofouling in Cross-Flow Microfiltration: Mechanisms of Deposition and Release", Journal of Membrane Science, Vol. 244, (1-2), pp. 151-165.

Kawakatsu, T., Nakao, S. and Kimura, S. (1993), "Effects of Size and Compressibility of Suspended Particles and Surface Pore Size of Membrane on Flux in Crossflow Filtration", Journal of Membrane Science, Vol. 81, (1-2), pp. 173-190.

Kim, J. S., Akeprathumchai, S. and Wickramasinghe, S. R. (2001), "Flocculation to Enhance Microfiltration", Journal of Membrane Science, Vol. 182, (1-2), pp. 161-172.

Knutsen, J. S. and Davis, R. H. (2006), "Deposition of Foulant Particles During Tangential Flow Filtration", Journal of Membrane Science, Vol. 271, (1-2), pp. 101-113.

Kramadhati, N. N., Mondor, M. and Moresoli, C. (2002), "Evaluation of the Shear-Induced Diffusion Model for the Microfiltration of Polydisperse Feed Suspension", Separation and Purification Technology, Vol. 27, (1), pp. 11-24.

Kromkamp, J., van Domselaar, M., Schroen, K., van der Sman, R. and Boom, R. (2002), "Shear-Induced Diffusion Model for Microfiltration of Polydisperse Suspensions", Desalination, Vol. 146, (1-3), pp. 63-68.

Kromkamp, J. (2005), "Particle Separation and Fractionation by Microfiltration", Ph.D. Thesis, Wageningen University, Wageningen, The Netherlands.

Kromkamp, J., Faber, F., Schroen, K. and Boom, R. (2006), "Effects of Particle Size Segregation on Crossflow Microfiltration Performance: Control Mechanism for Concentration Polarisation and Particle Fractionation", Journal of Membrane Science, Vol. 268, (2), pp. 189-197.

Kwon, D. Y. and Vigneswaran, S. (1998), "Influence of Particle Size and Surface Charge on Critical Flux of Crossflow Microfiltration", Water Science and Technology, Vol. 38, (4-5), pp. 481-488.

Kwon, D. Y., Vigneswaran, S., Fane, A. G. and Aim, R. B. (2000), "Experimental Determination of Critical Flux in Cross-Flow Microfiltration", Separation and Purification Technology, Vol. 19, (3), pp. 169-181.

Le Clech, P., Jefferson, B., Chang, I. S. and Judd, S. J. (2003), "Critical Flux Determination by the Flux-Step Method in a Submerged Membrane Bioreactor", Journal of Membrane Science, Vol. 227, (1-2), pp. 81-93.

Green, N. G. and Morgan, H. (1998), "Separation of Submicrometre Particles Using a Combination of Dielectrophoretic and Electrohydrodynamic Forces", Journal of Physics D: Applied Physics, Vol. 31, pp. 25-30.

Lee, S. A., Fane, A. G., Aim, R. B. and Waite, T. D. (2003), "The Effect of Floc Size and Structure on Specific Cake Resistance and Compressibility in Dead-End Microfiltration", Separation Science and Technology, Vol. 38, (4), pp. 869-887.

Lee, S. A. (2005), "The Effect of Floc Properties on the Performance of Microfiltration Membranes for Water Treatment", Ph.D. Thesis, University of New South Wales, Australia.

Levy, P. F. and Earle, R. S. (1994), "The Effect of Channel Height and Channel Spacers on Flux and Energy Requirements in Crossflow Filtration", Journal of Membrane Science, Vol. 91, (1-2), pp. 135-143.

Li, H. (1996), "Mechanism Studies for Crossflow Microfiltration with Pulsatile Flow", Ph.D. Thesis, University of New South Wales, Australia.

Li, H., Fane, A. G., Coster, H. G. L. and Vigneswaran, S. (1998), "Direct Observation of Particle Deposition on the Membrane Surface During Crossflow Microfiltration", Journal of Membrane Science, Vol. 149, (1), pp. 83-97.

Li, H., Fane, A. G., Coster, H. G. L. and Vigneswaran, S. (2000), "An Assessment of Depolarisation Models of Crossflow Microfiltration by Direct Observation

through the Membrane”, Journal of Membrane Science, Vol. 172, (1-2), pp. 135-147.

Mackley, M. R. and Sherman, N. E. (1992), “Cross-Flow Cake Filtration Mechanisms and Kinetics”, Chemical Engineering Science, Vol. 47, (12), pp. 3067-3084.

Madaeni, S. S. and Fane, A. G. (1996), “Microfiltration of Very Dilute Colloidal Mixtures”, Journal of Membrane Science, Vol. 113, (2), pp. 301-312.

Madaeni, S. S. (1997a), “The Effect of Operation Conditions on Critical Flux in Membrane Filtration of Latexes”, Trans. IChemE., Vol. 75, pp. 266-269.

Madaeni, S. S. (1997b), “An Investigation of the Mechanism of Critical Flux in Membrane Filtration Using Electron Microscopy”, Journal of Porous Materials, Vol. 4, (4), pp. 239-244.

Madaeni, S. S. (1998), “Ultrafiltration of Very Dilute Colloidal Mixtures”, Colloids and Surfaces A: Physicochemical and Engineering Aspects, Vol. 131, (1-3), pp. 109-118.

Mairal, A. P., Greenberg, A. R. and Krantz, W. B. (2000), “Investigation of Membrane Fouling and Cleaning Using Ultrasonic Time-Domain Reflectometry”, Desalination, Vol. 130, (1), pp. 45-60.

Massey, B. S. (1989). Mechanics of Fluids. London, Van Nostrand Reinhold.

Matijevic, E. and Scheiner, P. (1978), “Ferric Hydrrous Oxide Sols: Iii. Preparation of Uniform Particles by Hydrolysis of Fe(III)-Chloride, -Nitrate, and -Perchlorate Solutions”, Journal of Colloid and Interface Science, Vol. 63, (3), pp. 509-524.

McDonogh, R. M., Fane, A. G. and Fell, C. J. D. (1989), "Charge Effects in the Cross-Flow Filtration of Colloids and Particulates", Journal of Membrane Science, Vol. 43, (1), pp. 69-85.

Mc Donogh, R. M., Bauser, H., Stroh, N. and Grauschopf, U. (1995), "Experimental in Situ Measurement of Concentration Polarisation During Ultra- and Micro-Filtration of Bovine Serum Albumin and Dextran Blue Solutions", Journal of Membrane Science, Vol. 104, (1-2), pp. 51-63.

Meakin, P. (1987), "Fractal Aggregates", Advances in Colloid and Interface Science, Vol. 28, pp. 249-331.

Mietton, M. and Aim, R. B. (1992), "Improvement of Crossflow Microfiltration Performances with Flocculation", Journal of Membrane Science, Vol. 68, (3), pp. 241-248.

Molla, S. H. and Bhattacharjee, S. (2005), "Prevention of Colloidal Membrane Fouling Employing Dielectrophoretic Forces on a Parallel Electrode Array", Journal of Membrane Science, Vol. 255, (1-2), pp. 187-199.

Moosemiller, M. D., Hill, C. G. and Anderson, M. A. (1989), "Physicochemical Properties of Supported  $\Gamma$ -Al<sub>2</sub>O<sub>3</sub> and TiO<sub>2</sub> Ceramic Membranes", Separation Science and Technology, Vol. 24, (9), pp. 641 - 657.

Mores, W. D. and Davis, R. H. (2001), "Direct Visual Observation of Yeast Deposition and Removal During Microfiltration", Journal of Membrane Science, Vol. 189, (2), pp. 217-230.

Mores, W. D. and Davis, R. H. (2002), "Direct Observation of Membrane Cleaning Via Rapid Backpulsing", Desalination, Vol. 146, (1-3), pp. 135-140.

Nazzal, F. F. and Wiesner, M. R. (1994), "Ph and Ionic Strength Effects on the Performance of Ceramic Membranes in Water Filtration", Journal of Membrane Science, Vol. 93, (1), pp. 91-103.

Ould-Dris, A., Jaffrin, M. Y., Si-Hassen, D. and Neggaz, Y. (2000), "Effect of Cake Thickness and Particle Polydispersity on Prediction of Permeate Flux in Microfiltration of Particulate Suspensions by a Hydrodynamic Diffusion Model", Journal of Membrane Science, Vol. 164, (1-2), pp. 211-227.

Penners, N. H. G. and Koopal, L. K. (1986), "Preparation and Optical Properties of Homodisperse Haematite Hydrosols", Colloids and Surfaces, Vol. 19, (2-3), pp. 337-349.

Petteys, M. P. and Schimpf, M. E. (1998), "Characterization of Hematite and Its Interaction with Humic Material Using Flow Field-Flow Fractionation", Journal of Chromatography A, Vol. 816, (2), pp. 145-158.

Redman, J. A., Estes, M. K. and Grant, S. B. (2001), "Resolving Macroscale and Microscale Heterogeneity in Virus Filtration", Colloids and Surfaces A: Physicochemical and Engineering Aspects, Vol. 191, pp. 57-70.

Richard Bowen, W. and Gan, Q. (1993), "Microfiltration of Protein Solutions at Thin Film Composite Membranes", Journal of Membrane Science, Vol. 80, (1), pp. 165-173.

Ripperger, S. and Altmann, J. (2002), "Crossflow Microfiltration - State of the Art", Separation and Purification Technology, Vol. 26, (1), pp. 19-31.

Sharma, M. M., Chamoun, H., Sarma, D. S. H. S. R. and Schechter, R. S. (1992), "Factors Controlling the Hydrodynamic Detachment of Particles from Surfaces", Journal of Colloid and Interface Science, Vol. 149, (1), pp. 121-134.



Shauly, A., Wachs, A. and Nir, A. (1998), "Shear-Induced Particle Migration in a Polydisperse Concentrated Suspension", Journal of Rheology, Vol. 42, (6), pp. 1329-1348.

Singh, G. and Song, L. (2005), "Quantifying the Effect of Ionic Strength on Colloidal Fouling Potential in Membrane Filtration", Journal of Colloid and Interface Science, Vol. 284, (2), pp. 630-638.

Smith, W. E. and Zukoski, C. F. (2004), "Flow Properties of Hard Structured Particle Suspensions", Journal of Rheology, Vol. 48, pp. 1375-1388.

Thiruvengkatachari, R., Ngo, H. H., Hagare, P., Vigneswaran, S. and Aim, R. B. (2002), "Flocculation--Cross-Flow Microfiltration Hybrid System for Natural Organic Matter (Nom) Removal Using Hematite as a Flocculent", Desalination, Vol. 147, (1-3), pp. 83-88.

Tragardh, G. (1989), "Membrane Cleaning", Desalination, Vol. 71, (3), pp. 325-335.

Wakeman, R. J. and Tarleton, E. S. (1991), "Colloidal Fouling of Microfiltration Membranes During the Treatment of Aqueous Feed Streams", Desalination, Vol. 83, (1-3), pp. 35-52.

Wakeman, R. J. and Williams, C. J. (2002), "Additional Techniques to Improve Microfiltration", Separation and Purification Technology, Vol. 26, (1), pp. 3-18.

Waite, T. D., Schafer, A. I., Fane, A. G. and Heuer, A. (1999), "Colloidal Fouling of Ultrafiltration Membranes: Impact of Aggregate Structure and Size", Journal of Colloid and Interface Science, Vol. 212, (2), pp. 264-274.

Wakeman, R. J. and Tarleton, E. S. (1991), "Colloidal Fouling of Microfiltration Membranes During the Treatment of Aqueous Feed Streams", Desalination, Vol. 83, (1-3), pp. 35-52.

Weigert, T., Altmann, J. and Ripperger, S. (1999), "Crossflow Electrofiltration in Pilot Scale", Journal of Membrane Science, Vol. 159, (1-2), pp. 253-262.

Winters H. (2007), Personal communication.

Winzeler, H. B. and Belfort, G. (1993), "Enhanced Performance for Pressure-Driven Membrane Processes: The Argument for Fluid Instabilities", Journal of Membrane Science, Vol. 80, (1), pp. 35-47.

Wu, D., Howell, J. A. and Field, R. W. (1999), "Critical Flux Measurement for Model Colloids", Journal of Membrane Science, Vol. 152, (1), pp. 89-98.

Yan, Y., Burns, J. L., Jameson, G. J. and Biggs, S. (2000), "The Structure and Strength of Depletion Force Induced Particle Aggregates", Chemical Engineering Journal, Vol. 80, (1-3), pp. 23-30.

Yusa, M. (1977), "Mechanics of Pelleting Flocculation", International Journal of Mineral Processing, Vol. 4, (4), pp. 293-305.

Zydney, A. L. and Colton, C. K. (1986), "A Concentration Polarization Model for the Filtrate Flux in Cross-Flow Microfiltration of Particulate Suspensions", Chemical Engineering Communications, Vol. 47, pp. 1-21.